LBNL-38886
UC-401

ERNEST ORLANDO LAWRENCE BERKELEY NATIONAL LABORATORY

Polarization Dependence of Two-Photon Transition Intensities in Rare-Earth Doped Crystals

A.-D. Le Nguyen
Chemical Sciences Division

May 1996
Ph.D. Thesis

REFERENCE COPY
Does Not
Circulate
Bldg. 50 Library.
LBNL-38886
Copy 1

DISCLAIMER

This document was prepared as an account of work sponsored by the United States Government. While this document is believed to contain correct information, neither the United States Government nor any agency thereof, nor the Regents of the University of California, nor any of their employees, makes any warranty, express or implied, or assumes any legal responsibility for the accuracy, completeness, or usefulness of any information, apparatus, product, or process disclosed, or represents that its use would not infringe privately owned rights. Reference herein to any specific commercial product, process, or service by its trade name, trademark, manufacturer, or otherwise, does not necessarily constitute or imply its endorsement, recommendation, or favoring by the United States Government or any agency thereof, or the Regents of the University of California. The views and opinions of authors expressed herein do not necessarily state or reflect those of the United States Government or any agency thereof or the Regents of the University of California.

LBNL-38886

Polarization Dependence of Two-Photon Transition Intensities in Rare-Earth Doped Crystals

An-Dien Le Nguyen
Ph.D. Thesis

Department of Physics
University of California, Berkeley

and

Chemical Sciences Division
Ernest Orlando Lawrence Berkeley National Laboratory
University of California
Berkeley, CA 94720

May 1996

This work was supported by the Director, Office of Energy Research, Office of Basic Energy Sciences, Chemical Sciences Division, of the U.S. Department of Energy under Contract No. DE-AC03-76SF00098.

Recycled Paper

Polarization Dependence of Two-Photon Transition Intensities in Rare-Earth Doped Crystals

by

An-Dien Le Nguyen

B.S. (University of California at Los Angeles) 1991

M.A. (University of California at Berkeley) 1995

A dissertation submitted in partial satisfaction of the

requirements for the degree of

Doctor of Philosophy

in

Physics

in the

GRADUATE DIVISION

of the

UNIVERSITY of CALIFORNIA at BERKELEY

Committee in charge:

Professor Sumner P. Davis, Chair

Professor Herbert L. Strauss

Professor Steven G. Louie

1996

Polarization Dependence of Two-Photon Transition Intensities in Rare-Earth Doped Crystals

Copyright © 1996

by

An-Dien Le Nguyen

The U.S. Department of Energy has the right to use this document
for any purpose whatsoever including the right to reproduce
all or any part thereof

Abstract

Polarization Dependence of Two-Photon Transition Intensities in Rare-Earth Doped Crystals

by

An-Dien Le Nguyen

Doctor of Philosophy in Physics

University of California at Berkeley

Professor Sumner P. Davis, Chair

A polarization dependence technique has been developed as a tool to investigate phonon scattering (PS), electronic Raman scattering (ERS), and two-photon absorption (TPA) transition intensities in vanadate and phosphate crystals. A general theory for the polarization dependence (PD) of two-photon transition intensities has been given. Expressions for the polarization dependent behavior of two-photon transition intensities have been tabulated for the 32 crystallographic point groups. When the wavefunctions for the initial and final states of a rare-earth doped in crystals are known, explicit PD expressions with no unknown parameters can be obtained.

A spectroscopic method for measuring and interpreting phonon and ERS intensities has been developed to study $PrVO_4$, $NdVO_4$, $ErVO_4$, and $TmVO_4$ crystals. Relative phonon intensities with the polarization of the incident and scattered light arbitrarily varied were accurately predicted and subsequently used for alignment and calibration in ERS measurements in these systems for the first time. Since ERS and PS

intensities generally follow different polarization curves as a function of polar angles, the two can be uniquely identified by comparing their respective polarization behavior. The most crucial application of the technique in ERS spectroscopy is the establishment of a stringent test for the Axe theory. For the first time, the F_1/F_2 ratio extracted from the experimental fits of the ERS intensities were compared with those predicted by theories which include both the second- and third-order contributions. Relatively good agreement between the fitted values of F_1/F_2 and the predicted values using the second-order theory has been found.

Two-photon absorption has been observed to the crystal-field levels of the $^5D_0$ and $^5D_2$ multiplets of Eu^{3+} in $LuPO_4$ as well as the $^6D_{7/2}$, $^6P_{5/2}$, and $^6D_{7/2}$' multiplets at 16800, 19900, and 27900 cm^{-1}, respectively, of Cm^{3+} in $LuPO_4$. Polarization isotropy and non-zero backgrounds have been observed in several TPA transitions in both materials. The theory of two-photon absorption was re-examined and extended beyond the electric-dipole approximation scheme to account for both the polarization isotropy and non-zero background observed. For the TPA transitions where non-zero background was not observed, second-order theory was adequate to account for the polarization dependent behavior and relative intensities among transitions.

Table of Contents

Acknowledgements xix

Introduction 1

Chapter 1: Fundamental Concepts in Rare-Earth Spectroscopy 5

1.1 Historical Background and Overview 5

1.2 Energy Levels and Wave Functions 9

1.2.1 The Free Ion 9

1.2.2 Ions in the Static Crystal Field 15

1.3 Intensities 17

1.3.1 One-Photon Spectroscopy 17

1.3.2 Two-Photon Spectroscopy 21

1.3.2.1 Two-Photon Absorption 22

1.3.2.2 Raman Scattering 22

1.3.2.3 Two-Photon Transition Intensities 30

Appendix A 35

References 38

Chapter 2: Theory of Polarization Dependence of Raman Scattering and TPA Intensities in Rare-Earth Crystals 42

2.1 Overview 42

2.2 Polarization Dependence - Second-Order Treatment 49

2.2.1 Electronic Raman Scattering Theory 49

2.2.2 Polarization Dependence 55

2.3 Polarization Dependence Theory - Higher-Order Contribution 68

2.3.1 Third-Order Contribution to Intra-Configurational Two-Photon Transition Intensities 68

2.3.1.1 Spin-Orbit Interaction 69

2.3.1.2 Crystal-Field Interaction 72

2.3.2 Fourth-Order Contribution to Intra-Configurational Two-Photon Transition Intensities - Spin-Orbit and Crystal-Field Interactions 75

2.3.3 Third-Order Contribution to Inter-Configurational Two-Photon Absorption Transition Intensities 77

2.3.4 Relative Magnitude of Higher-Order Contributions to Second-Order Contribution 82

2.4 Examples 83

2.4.1 Intra-Configurational TPA - Application to Sm^{2+} in BaClF 83

2.4.2 Inter-Configurational TPA - Application to Ce^{3+}:CaF_2 86

2.4.3 Electronic Raman Scattering and Phonon Raman Scattering 90

2.5 Summary 91

Appendix A 93

Appendix B 96

Appendix C 99

Appendix D 100

References 103

Chapter 3: Experimental Aspects 109

3.1 Polarization Dependence Spectroscopy - Overview 109

3.1.1 General Approach to Raman Spectroscopy 109

3.1.2 General Approach to TPA Spectroscopy 114

3.2 Applications to Polarization Dependent Intensities 115

3.2.1 Phonon Raman Scattering 115

3.2.2 Electronic Raman Scattering 117

3.2.3 Two-Photon Absorption 123

3.3 Raman Scattering - Experimental Aspects 124

3.3.1 Experimental Setup 124

3.3.1.1 Laser 125

3.3.1.2 Optics 127

3.3.1.3 Sample Crystal and Cryogenics 129

3.3.1.4 Spectrometer and Detection System 132

3.3.2 Experimental Procedure 135

3.4 Two-Photon Absorption - Experimental Aspects 138

3.4.1 Crystal Samples 138

3.4.2 Absorption Measurements 138

3.4.3 TPA Experimental Setup 139

References 143

Chapter 4: Polarization Dependence of Phonon Scattering and Electronic Raman Scattering Intensities in $PrVO_4$, $NdVO_4$, $ErVO_4$, and $TmVO_4$ 146

4.1 Raman Spectroscopy of $PrVO_4$ 146

4.1.1 Pr^{3+} - Selection Rules 146

4.1.2 Pr^{3+} - Polarization Dependence Functions 147

4.1.3 $PrVO_4$ - Experimental Raman Spectra 152

4.2 Raman Spectroscopy of $NdVO_4$ 165

4.2.1 Nd^{3+} - Selection Rules 165

4.2.2 Nd^{3+} - Polarization Dependence Functions 166

4.2.3 $NdVO_4$ - Experimental Raman Spectra 169

4.3 Raman Spectroscopy of $ErVO_4$ 184

4.3.1 Er^{3+} - Selection Rules 184

4.3.2 Er^{3+} - Polarization Dependence Functions 184

4.3.3 $ErVO_4$ - Experimental Raman Spectra 187

4.4 Raman Spectroscopy of $TmVO_4$ 201

4.4.1 Tm^{3+} - Selection Rules 201

4.4.2 Tm^{3+} - Polarization Dependence Functions 202

4.4.3 $TmVO_4$ - Experimental Raman Spectra 205

4.5 Summary 219

References 221

Chapter 5: Polarization Dependence of Two-Photon Absorption Transition Intensities in Eu^{3+}:$LuPO_4$ and Cm^{3+}:$LuPO_4$ 224

5.1 Introduction 224

5.2 TPA Spectroscopy of Eu^{3+} in $LuPO_4$ 226

5.2.1 Eu^{3+} - Selection Rules 226

5.2.2 Polarization Dependence Functions 227

5.2.3 Eu^{3+} in $LuPO_4$ -Experimental TPA Spectra 231

5.2.4 Conclusion 243

5.3 TPA Spectroscopy of Cm^{3+} in $LuPO_4$ 245

5.3.1 Cm^{3+} - Selection Rules 246

5.3.2 Polarization Dependence Functions 247

5.3.3 Cm^{3+} in $LuPO_4$ - Experimental TPA Spectra 252

5.3.3.1 $^8S_{7/2}$ - $^6D_{7/2}$ Transitions 252

5.3.3.2 $^8S_{7/2}$ - $^6P_{5/2}$ Transitions 257

5.3.3.3 $^8S_{7/2}$ - $^6D_{7/2}$' Transitions 260

5.3.4 Discussion 263

5.4 Summary 266

References 267

List of Figures

Fig. 1-1: Radial distributions of the 4f, 5s, 5p, and 5g orbitals for the Pr^{3+} free ion, from Hartree-Fock calculations 7

Fig. 1-2: Radial distributions of the 4f, 5s, 5p, 5d, and 5g orbitals for the Tm^{3+} free ion, from Hartree-Fock calculations 8

Fig. 1-3: Stokes and Anti-Stokes spectral lines in Raman scattering 24

Fig. 2-1 Polarization dependent behavior of the two-photon cross-section for the no-phonon transition of Ce^{3+}:CaF_2 at 6 K 89

Fig. 3-1: Crystal orientation in Raman experiments 116

Fig. 3-2: Experimental setup in ERS measurements 134

Fig. 3-3: Experimental setup in TPA intensity measurements 142

Fig. 4-1: Room temperature, unpolarized phonon spectra of $PrVO_4$, using the 514 nm excitation line 159

Fig. 4-2: Low temperature, unpolarized ERS spectra of $PrVO_4$, using the 514 nm excitation line 160

Fig. 4-3: Polarized phonon scattering spectra of $PrVO_4$ at 4.2 K, using the 514 nm excitation line 161

Fig. 4-4: Polarized ERS spectrum of $PrVO_4$ at 4.2 K, using the 514 nm excitation line 162

Fig. 4-5: Polarization dependence spectra of the phonon mode E_g at 807 cm^{-1} in $PrVO_4$ at 4.2 K 163

Fig. 4-6: Polarization dependence spectra of the ERS transition at 84 cm^{-1} of Pr^{3+} in $PrVO_4$ at 4.2 K 164

Fig. 4-7: Crystal-field levels of the $^4I_{9/2}$, $^2G_{9/2}$, $^2K_{13/2}$, and $^2K_{15/2}$ multiplets of Nd^{3+} in $NdVO_4$ 175

Fig. 4-8: Unpolarized ERS spectrum of $NdVO_4$ at 4.2 K, using the 476 nm excitation line 176

Fig. 4-9: Polarized phonon spectra of the A_{1g}^2 mode of $NdVO_4$ at 4.2 K, with excitation at 488 nm 177

Fig. 4-10: Polarized ERS spectra of the 101 cm^{-1} transition of Nd^{3+} in $NdVO_4$ at 4.2 K, with excitation at 488 nm 178

Fig. 4-11: Polarized ERS spectra of the 168 and 178 cm^{-1} transitions of Nd^{3+} in $NdVO_4$ at 4.2 K, with excitation at 488 nm 179

Fig. 4-12: Polarization dependence spectra of the phonon mode A_{1g}^2 at 875 cm^{-1} in $NdVO_4$ at 4.2 K 180

Fig. 4-13: Polarization dependence spectra of the 101 cm^{-1} transition of Nd^{3+} in $NdVO_4$ at 4.2 K 181

Fig. 4-14: Polarization dependent ERS spectra of the 169 cm^{-1} transition of Nd^{3+} in $NdVO_4$ at 4.2 K 182

Fig. 4-15: Polarization dependent ERS spectra of the 178 cm^{-1} transition of Nd^{3+} in $NdVO_4$ at 4.2 K.....183

Fig. 4-16: Unpolarized phonon spectrum of $ErVO_4$ at 297 K, using the excitation line at 496 nm..... 194

Fig. 4-17: Crystal-field levels of the $^4I_{15/2}$, $^2H_{11/2}$, $^4F_{7/2}$, and $^4F_{5/2}$ multiplets of Er^{3+} in $ErVO_4$.....195

Fig. 4.18: Low temperature, unpolarized ERS spectra of $ErVO_4$, using the 496 nm excitation line..... 196

Fig. 4-19: Polarized ERS spectra of the 43 cm^{-1} transition of Er^{3+} in $ErVO_4$ at 4.2 K, with excitation at 476 nm..... 197

Fig. 4-20: Polarized ERS spectra of the 252 cm^{-1} transition of Er^{3+} in $ErVO_4$ at 4.2 K, with excitation at 476 nm..... 198

Fig. 4-21: Unpolarized ERS spectra of the 252 cm^{-1} transition of Er^{3+} in $ErVO_4$ as a function of temperature.....199

Fig. 4-22: Polarization dependence spectra of the 43 cm^{-1} transition of Er^{3+} in $ErVO_4$ at 4.2 K.....200

Fig. 4-23: Unpolarized phonon spectra of $TmVO_4$ at 293 K, with the laser excitation at 514 nm and 488 nm..... 211

Fig. 4-24: Unpolarized phonon spectra of $TmVO_4$ at 4.2 K, with the laser excitation at 514 nm and 488 nm..... 212

Fig. 4-25: Unpolarized Raman spectra of $TmVO_4$ at 4.2 K, with the laser excitation at 497 nm and 488 nm 213

Fig. 4-26: Crystal-field levels of the $^3H_6$ and $^1G_4$ multiplets of Tm^{3+} in $TmVO_4$..... 214

Fig. 4-27: Polarized ERS spectra of the 115 cm^{-1} transition of Tm^{3+} in $TmVO_4$ at 4.2 K, with excitation at 488 nm 215

Fig. 4-28: Polarized Raman spectra of the 155 cm^{-1} transition of Tm^{3+} in $TmVO_4$ at 4.2 K, with excitation at 488 nm 216

Fig. 4-29: Polarization dependent phonon spectra of the E_g^2 mode at 155 cm^{-1} of $TmVO_4$ at 4.2 K 217

Fig. 4-30: Fig. 4-12: Polarization dependent ERS spectra of the 875 cm^{-1} transition of Tm^{3+} in $TmVO_4$ at 4.2 K 218

Fig. 5-1: Polarized spectra of the TPA transitions to the $^5D_2$ multiplet at 4.2 K ($\phi = 45°$) 233

Fig. 5-2: Polarized spectra of the TPA transitions to the $^5D_2$ multiplet at 4.2 K ($\phi = 23°$) 234

Fig. 5-3: Experimental and predicted polarization behavior of the $^7F_0$ - $^5D_0$ and $^5D_2$ transitions 235

Fig. 5-4: Experimental and predicted polarization behavior of the $^7F_0$ (1) - $^5D_0$ (1) and $^5D_2$ (3) transitions 239

Fig. 5-5: Pi and sigma polarized spectra of the TPA transitions to the $^6D_{7/2}$ multiplet 254

Fig. 5-6: Experimental and predicted polarization behavior of the $^8S_{7/2}$ - $^6D_{7/2}$ TPA transitions.....255

Fig. 5-7: Single-photon and two-photon absorption transitions to the four levels of the $^6D_{7/2}$ multiplet..... 256

Fig. 5-8: Pi and sigma polarized spectra of the TPA transitions to the $^6P_{5/2}$ mulitplet..... 258

Fig. 5-9: Experimental and predicted polarization behavior of the $^8S_{7/2}$ - $^6P_{5/2}$ TPA transitions.....259

Fig. 5-10: Pi and sigma polarized spectra of the TPA transitions to the $^6D_{7/2}$' mulitplet.....261

Fig. 5-11: Experimental and predicted polarization behavior of the $^8S_{7/2}$ - $^6D_{7/2}$' TPA transitions..... 262

Fig. 5-12: Experimental and fitted polarization behavior of the $^8S_{7/2}$ - $^6D_{7/2}$, $^6P_{5/2}$, and $^6D_{7/2}$' TPA transitions..... 265

List of Tables

Table 1.1: Cartesian Phonon Raman scattering tensors for the zircon structure (D_{4h}) 26

Table 1.2: Cartesian ERS tensors for D_{2d} 29

Table 2.1: Angular dependence functions for RE ERS and TPA transitions 64

Table 2.2: Calculated values of $D_q^{(t)}$ (k,n) 81

Table 3.1: Fitted parameters for RE^{3+} in $REVO_4$ or YVO_4 112

Table 3.2: Raman activity of D_{2d} point group 112

Table 3.3: Wavelengths and wavenumbers of argon-ion laser lines 126

Table 4.1: Selection rules and Raman activity of ERS transitions originating in the ground state of Pr^{3+} in $PrVO_4$ 147

Table 4.2: Polarization dependence functions for ERS transitions originating in the ground state of Pr^{3+} in $PrVO_4$ 148

Table 4.3: Wavefunctions for the ground multiplet of Pr^{3+} in $PrVO_4$ 148

Table 4.4: Polarization dependencies of ERS transition intensities in the $^3H_4$ ground multiplet of Pr^{3+} in $PrVO_4$ 149

Table 4.5: Predicted values of relative linestrengths of ERS transitions in the $^3H_4$ ground multiplet of Pr^{3+} in $PrVO_4$ 151

Table 4.6: Frequencies and symmetries of the Raman-active phonons in $PrVO_4$ at 297 and 4.2 K.....153

Table 4.7: Comparison between predicted and observed relative linestrengths of ERS transitions in the $^3H_4$ ground mulitplet of Pr^{3+} in $PrVO_4$ for the case $\tau = 1.03$.....155

Table 4.8: Relative magnitude of third-order spin-orbit to second-order contributions for ERS transitions in $PrVO_4$.....157

Table 4.9: Selection rules and Raman activity of ERS transitions originating in the ground state of Nd^{3+} in $NdVO_4$..... 166

Table 4.10: Polarization dependence functions for ERS transitions originating in the ground state of Nd^{3+} in $NdVO_4$.....167

Table 4.11: Wavefunctions for the ground multiplet of Nd^{3+} in $NdVO_4$.....167

Table 4.12: Polarization dependencies of ERS transition intensities in the $^4I_{9/2}$ ground multiplet of Nd^{3+} in $NdVO_4$.....168

Table 4.13: Predicted values of relative linestrengths of ERS transitions in the $^9I_{9/2}$ ground multiplet of Nd^{3+} in $NdVO_4$.....168

Table 4.14: Frequencies and symmetries of the Raman-active phonons in $NdVO_4$ at 297 and 4.2 K..... 170

Table 4.15: Comparison of the fitted and calculated values for the relative magnitudes of $\alpha_q^{(t)}$'s for the ERS transition in $NdVO_4$ at 101 cm^{-1}..... 172

Table 4.16: Comparison between predicted and observed relative ERS transition intensities in the $^4I_{9/2}$ ground mulitplet of Nd^{3+} in $NdVO_4$ for the case $\tau = 0.48$..... 173

Table 4.17: Relative magnitude of α_q^t for the ERS transition in $NdVO_4$ at 101 cm^{-1} 174

Table 4.18: Wavefunctions for the ground multiplet of Er^{3+} in YVO_4 185

Table 4.19: Polarization dependencies of ERS transition intensities in the $^4I_{15/2}$ ground multiplet of Er^{3+} in YVO_4 186

Table 4.20: Predicted values of relative linestrengths of ERS transitions in the $^9I_{15/2}$ ground multiplet of Er^{3+} in YVO_4 187

Table 4.21: Frequencies and symmetries of the Raman-active phonons in $ErVO_4$ at 297 and 4.2 K 189

Table 4.22: Comparison of the fitted and calculated values for the relative magnitudes of $\alpha_q^{(t)}$'s for the ERS transition in $ErVO_4$ at 43 cm^{-1} 190

Table 4.23: Comparison between predicted and observed relative ERS transition intensities in the $^4I_{15/2}$ ground mulitplet of Er^{3+} in $ErVO_4$ for the case $\tau = 1.0$ 192

Table 4.24: Relative magnitude of α_q^t for the ERS transition in $ErVO_4$ at 43 cm^{-1} ...193

Table 4.25: Selection rules and Raman activity of ERS transitions originating in the ground state of Tm^{3+} in $TmVO_4$ 201

Table 4.26: Polarization dependence functions for ERS transitions originating in the ground state of Tm^{3+} in $TmVO_4$ 202

Table 4.27: Wavefunctions for the ground multiplet of Tm^{3+} in $TmVO_4$ 203

Table 4.28: Polarization dependencies of ERS transition intensities in the $^3H_6$ ground multiplet of Tm^{3+} in $TmVO_4$ 204

Table 4.29: Predicted values of relative linestrengths of ERS transitions in the $^3H_6$ ground multiplet of Tm^{3+} in $TmVO_4$ 205

Table 4.30: Frequencies and symmetries of the Raman-active phonons in $TmVO_4$ at 297, 77, and 4.2 K 206

Table 4.31: Comparison of the fitted and calculated values for the relative linestrengths of ERS transitions in the $^3H_6$ ground multiplet of Tm^{3+} in $TmVO_4$ for the case $\tau = 0.072$ 209

Table 4.32: Comparison of the relative magnitudes of α_q^t obtained from calculation using the second-order theory, third-order spin-orbit, and from the fit for the transition at 150 cm^{-1} in $TmVO_4$ 210

Table 5.1: Selection rules and Raman activity of TPA transitions originating from the ground state of Eu^{3+} in $LuPO_4$ 227

Table 5.2: Polarization dependence functions for TPA $^7F_0$ - ^5D_J transitions of Eu^{3+} in $LuPO_4$ 228

Table 5.3: Wavefunctions for the $^7F_0$ and ^5D_J multiplets of Eu^{3+} in $LuPO_4$ 229

Table 5.4: Polarization dependencies of TPA intensities for the $^7F_0$ - ^5D_J transitions of Eu^{3+} in $LuPO_4$ (second-order contributions) 229

Table 5.5: Polarization dependencies of TPA intensities for the $^7F_0$ - ^5D_J transitions of Eu^{3+} in $LuPO_4$ (second- and third-order contributions) 230

Table 5.6: Predicted values of relative TPA intensities for the $^7F_0$ - ^5D_J transitions of Eu^{3+} in $LuPO_4$ for the case $\phi = 45°$ 231

Table 5.7: Predicted values of relative TPA intensities for the $^7F_0$ - ^5D_J transitions of Eu^{3+} in $LuPO_4$ for the case $n = \cos^2 \phi \neq 0$ 231

Table 5.8: Comparison of predicted and observed values of relative TPA intensities for the $^7F_0$ - ^5D_J transitions of Eu^{3+} in $LuPO_4$ for the case $\phi = 45°$ 238

Table 5.9: Comparison of predicted and observed values of relative TPA intensities for the $^7F_0$ - ^5D_J transitions of Eu^{3+} in $LuPO_4$ for the case $\phi = 23°$ and $35°$ 238

Table 5.10: Selection rules and Raman activity of TPA transitions originating from the ground state of Cm^{3+} in $LuPO_4$ 247

Table 5.11: Polarization dependence functions for TPA transitions originating in the ground state of Cm^{3+} in $LuPO_4$ 249

Table 5.12: Wavefunctions for various multiplets of Cm^{3+} in $LuPO_4$ 249

Table 5.13: Non-zero contributions of $\alpha_q^t = \langle i| \alpha_q^{(t)} |f\rangle$ for the $^8S_{7/2}$ - $^6D_{7/2}$, $^6P_{5/2}$, and $^6D_{7/2}$ transitions of Cm^{3+} in $LuPO_4$ ($\phi = 45°$) 251

Table 5.14: Polarization dependencies of TPA intensities for the $^8S_{7/2}$ - $^6D_{7/2}$, $^6P_{5/2}$, and $^6D_{7/2}$ transitions of Cm^{3+} in $LuPO_4$ ($\phi = 45°$) 252

"No mind can take one step without the aid of other minds."

C.S. Peirce

"What has been is what will be, and what has been done

is what will be done; there is nothing new under the sun."

Ecclesiastes 1.9

Acknowledgments

As life is full of surprise, being able to find a good research group, having found the right dissertation project, and successfully completing it with a reasonable amount of time have somewhat been beyond my expectation. To the completion of my thesis I am indebted to many people who have been monumental in guiding, helping, and supporting my graduate studies. First and foremost I would like to thank Norman Edelstein, my research supervisor, for being a great mentor and for the financial support for my research. I owed you all, Norm, for the suggestion of the dissertation topic, your prudent evaluation of my work and suggestions for improvement at every stage of my progress. I am also greatly indebted to Professor Sumner Davis, my advisor and mentor. Thanks for always being there, Sumner. It's great to know no matter what challenge you might face, your advisor is with you. Words can not describe how I greatly appreciate Sumner's mentorship and guidance, especially during my difficult days.

I would not have made my contributions to physics without the help of Professor Michael Downer and Dr. Gary Burdick. I would like to thank Mike for lending me the notes on third-order calculations of TPA intensities and for the warm host during my visit to Austin, Texas. I would like to thank Gary for his help with the theoretical questions I had. I really enjoyed the insightful discussion with you, Gary.

I have been very fortunate to have worked with the excellent LBNL staff and colleagues. My fruitful collaboration with Dr. Keith Murdoch on the TPA experiments has been a memorable experience for me. Thanks, Keith, for all the help and critiques. At

least I could finally convince you on the polarization dependence theory! I would like to thank Jerry Bucher for the assistance during my initial encounter with the ERS experimental challenge. Despite appearing to be a complete wet blanket, Jerry is not really one. Thanks, Jerry, for being the only person I can count on when I looked for the relics from the previous lab work. I would also like to thank Dr. Joost Sytsma, for giving me the confidence in electronics during his transition back to his home country in the Netherlands. Finally I would like to thank Ken Osborne for his help with the high vacuum problems and for accompanying me in social activities.

Besides academic research, I really enjoyed the warm atmosphere fostered by my research group at LBNL. It has been exciting to meet and work with people from different parts the world who have passed through LBNL. Besides Joost Sytsma from the Netherlands and Keith Murdoch from New Zealand, my exchange with Dr. Solange Hubert, Ronan Cavellec and Dr. Myriam Illemassene from France have been uniquely interesting. Sorry for my poor French, Myriam. I also enjoy talking with Dr. David Shuh, Dr. Pat Allen, and Geoff Siemering at lunch.

Finally I am deeply grateful to the support and encouragement from my family, especially my mother, during my busy days of graduate school. I would like to thank my sister and brother in law, Henry, for checking on my thesis progress and for offering assistance. I would also like to express my gratitude to my friends David, Raymond, and Monique, for the valuable friendship and support. Without all of you I could not make it.

This work was supported by the Department of Energy Office of Basic Energy Sciences, Chemical Sciences Division under contract number DE-AC03-76SF00098.

Introduction

Crystals doped with rare-earth (RE) ions play an important role in applied physics and optical technologies. The sharp intra-configurational f-f transitions of RE impurities in insulators and semiconductors are utilized for developing lasers and amplifiers in the near UV, visible, and IR regions. The short-decay time characteristics of the electric-dipole allowed f-d transition levels in several RE ions have made wide band-gap insulators doped with these RE ions potential candidates for scintillators for medical-imaging and high-energy physics detection applications. RE orthophosphates have been a potential advanced-ceramic medium for the encapsulation and permanent disposal of high-level radioactive wastes, due to their long-term stability [1,2]. Because of these technologically important implications, we have investigated the electronic energy levels and transition intensities in RE ions doped in crystals using two-photon spectroscopy.

The main achievement of this dissertation is the accurate prediction of the Raman scattering and two-photon absorption transition intensities in vanadate and phosphate crystals, using a theoretical formalism proposed in chapter two. In particular, a polarization dependence (PD) theory has been developed as a tool to study two-photon processes such as two-photon absorption (TPA), phonon scattering (PS), and electronic Raman scattering (ERS) which take place between Stark levels in rare-earth doped crystals. The PD expressions have been tabulated for all 32 crystallographic point

groups. When applied to a crystal of a particular symmetry with known wavefunctions for the initial and final states, explicit PD expressions with no unknown parameters can be obtained.

Following the PD theory, a new spectroscopic method has been suggested for accurate measurement and interpretation of the PS and ERS intensities. The new method is significant in a number of ways. Firstly, for the first time relative phonon intensities of incident and scattered light with polarization arbitrarily varied in spherical polar coordinates are predicted, measured, and subsequently used for alignment and calibration in ERS intensity measurements. Secondly, the method offers a reliable way to identify ERS transitions. Since ERS and PS intensities generally follow different polarization curves as a function of the polar angles associated with the polarization unit vectors, the two can be distinctly identified by comparing their respective polarization behaviors. Finally, the PD technique offers a stringent test for the Judd-Ofelt-Axe theory, which has been the foundation for quantitative studies of two-photon spectroscopy in rare-earth materials [3-5]. This is in fact the most crucial application of the new technique in rare-earth spectroscopy.

The thesis contains two main parts. The first part is the theoretical development of the PD theory for PS, ERS, and TPA processes. The results are applied to study the PD intensities in various RE crystals in the second part. The first two chapters of this thesis provide the theoretical background for the study of the PD technique. The next three chapters are devoted to the experimental verification of the theory from observed ERS and PS data in $PrVO_4$, $NdVO_4$, $ErVO_4$, and $TmVO_4$, and from observed TPA data in Eu^{3+}:$LuPO_4$, and Cm^{3+}:$LuPO_4$. For Pr^{3+}, Nd^{3+}, Er^{3+}, and Tm^{3+} in vanadate crystals,

second-order perturbation theory is sufficient to explain the two-photon intensities. But for Eu^{3+} and Cm^{3+} in $LuPO_4$ one has to include third-order contributions in order to adequately explain the data. A revisited TPA theory is given in chapter five to explain the isotropy and a non-zero background observed in the intensities of several TPA transitions of Eu^{3+} and Cm^{3+} in $LuPO_4$.

References

[1] L. A. Boatner and B.C. Sales, Monazite, in "Radioactive Waste Forms for the Future," editted by W. Lutze and R.C. Ewing (North Holland, Amsterdam, 1988), page 495.

[2] B.C. Sales, M. Petek, and L.A. Boatner, in "Scientific Basis for Nuclear Waste Management VI," vol. **15**, edited by D. G. Brookins (North Holland, Amsterdam, 1983) vol. 15, p 495.

[3] B. R. Judd, Phys. Rev. **127**, 750 (1962).

[4] G. S. Ofelt, J. Chem. Phys. **37**, 511 (1962).

[5] J. D. Axe, Phys. Rev. **136A**, 42 (1964).

Chapter 1

Fundamental Concepts in Rare-Earth Spectroscopy

1.1 Historical Background and Overview

The rare earth elements, also known as the lanthanides, begin with the element cerium (Z = 57) and end with the element lutetium (Z = 71). The lanthanides are associated with the filling of the 4f-shells of their electronic configurations. The neutral lanthanides possess the common core of a xenon structure of electrons ($1s^2 2s^2 2p^6 3s^2 3p^6 3d^{10} 4s^2 4p^6 4d^{10} 5s^2 5p^6$) with two or three outer electrons ($6s^2$ or $5d6s^2$). In a crystalline environment containing rare earth ions, the rare earth ion commonly exists in the trivalent state, in which two electrons in the outer $6s^2$ shell and one in the $4f^{N+1}$ (N = 0,...,13) or 5d shell are removed. The electronic configuration of the trivalent rare earth ion in its ground state is thus $[Xe]4f^N$ (N=0,...13).

The distinctive sharpness of the spectral lines of rare earth salts was probably first noticed by J. Becquerel in the early 1900's [1-4]. For the first time, it was possible to recognize that the absorption spectra of some of the rare earths consist not of bands, as expected for most solids, but of lines approximating in sharpness the absorption and emission lines of gases. Linewidths as narrow as a tenth of a wavenumber at helium temperature, and a few wave numbers at room temperature, are commonly observed in

the absorption and emission spectra. The theoretical explanation for the unusual sharpness of rare earth spectral lines, however, had not been available until the advance of quantum mechanics.

By applying the Thomas-Fermi model of atomic theory into the 4f group elements, in 1941, Maria Mayer [5] and, in following years, others [6,7] have shown that the energy and spatial extension of the 4f-eigenfunctions dramatically drop at the commencement of the lanthanides. From the calculation of the effective radial potential in the Thomas-Fermi model, Mayer found that at the commencement of the lanthanides a potential well developed near the nucleus becomes deep and large enough that it draws the 4f-electrons from the outer shells of the atom into the interior. The contraction increases throughout the entire $4f^N$-shell as the effective nuclear charge increases. The so-called lanthanide contraction arises from the imperfect shielding of one 4f-electron by another 4f-electron [8]. The contraction remarkably reduces the interactions between the 4f-electrons with neighboring atoms. As a result the 4f-electrons have very little tendency to participate in chemical bond formation and thus possess atomic-like spectral structures.

The first excited configurations of rare earth ions is $4f^{N-1}5d^1$. Figures 1.1 and 1.2 shows the radial distribution functions of the 4f, 5s, 5p, 5d, and 5g orbitals for the Pr^{3+} and Tm^{3+} free ions, respectively, as obtained from Hartree-Fock calculations [9]. The radial distribution function is defined as the square of the radial wavefunction times the squared radius. In contrast to the ground configuration, the 5d and 5g orbitals are spread

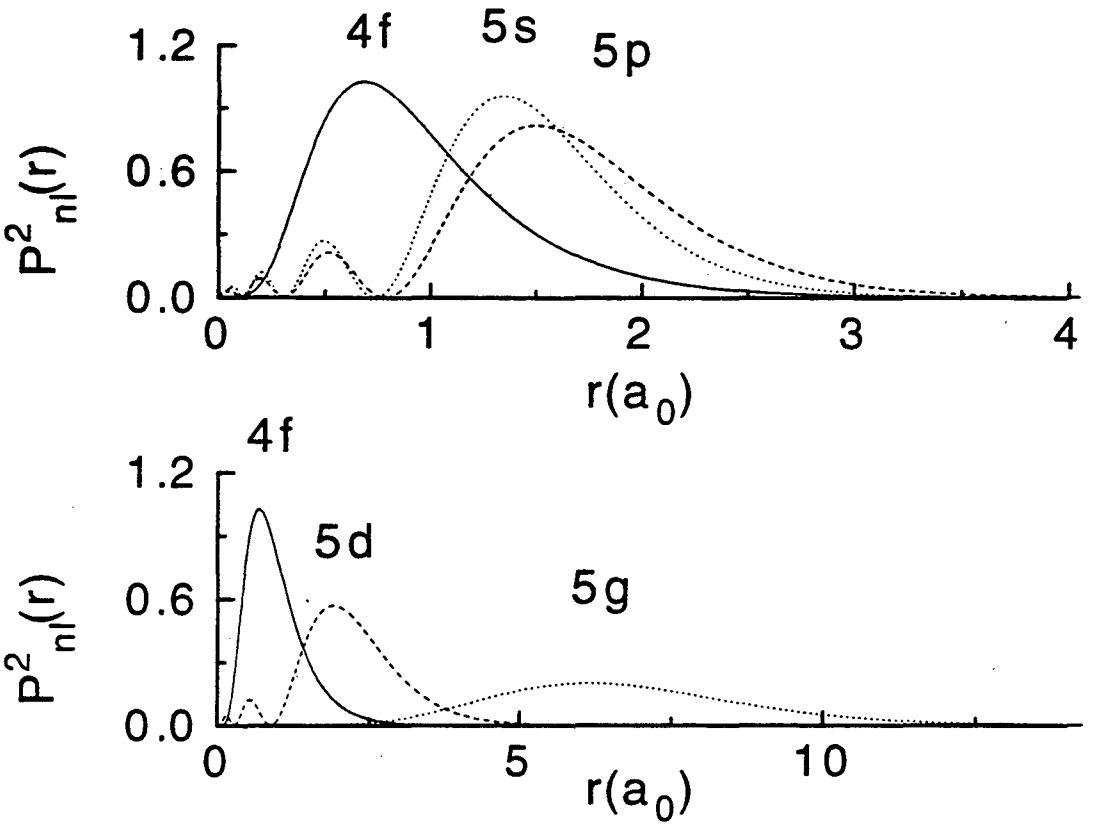

Fig. 1-1: Radial distributions of the 4f, 5s, 5p, 5d, and 5g orbitals for the Pr^{3+} free ion, from Hartree-Fock calculations [9]. Top: 4f, 5s, and 5p orbitals of the ground configuration $4f^2 5s^2 5p^6$. Bottom: 4f, 5d, and 5g orbitals of the configurations 4f5d, and 4f5g, respectively.

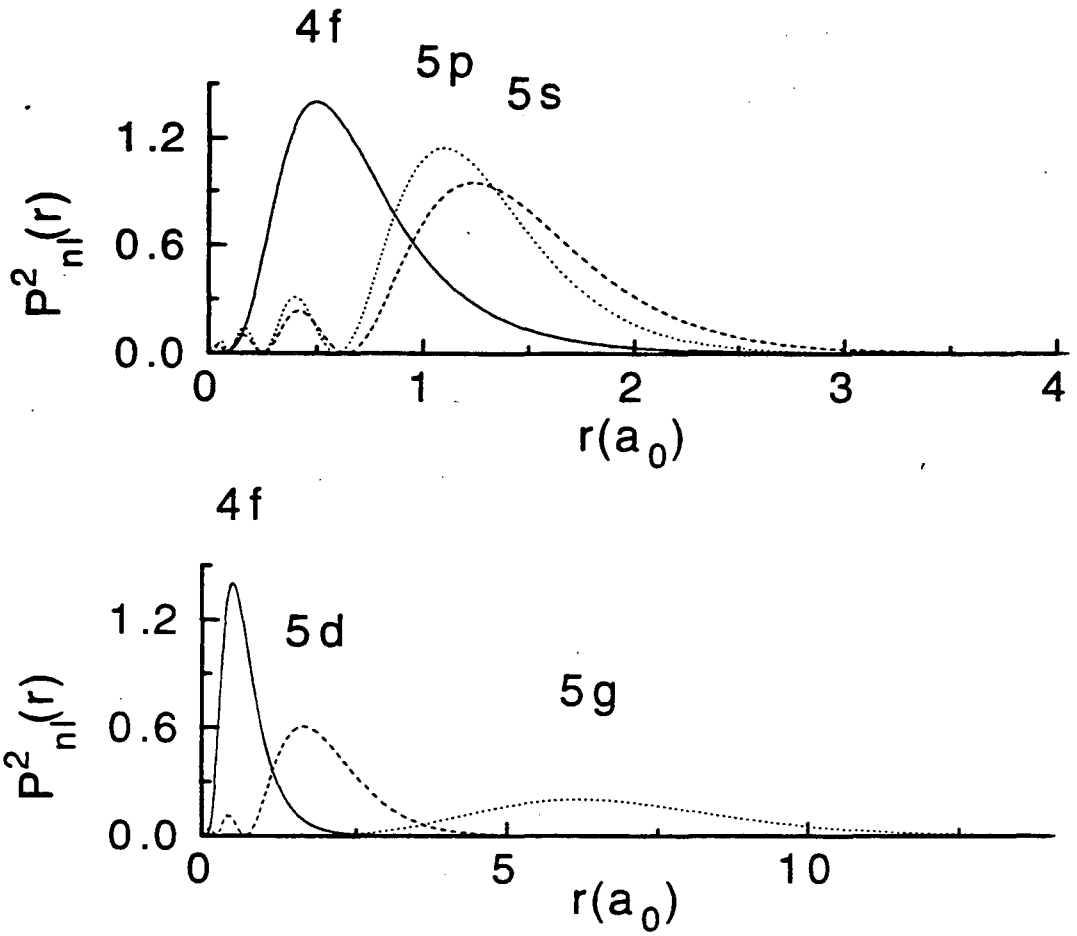

Fig. 1-2: Radial distributions of the 4f, 5s, 5p, 5d, and 5g orbitals for the Tm^{3+} free ion, from Hartree-Fock calculations [9]. Top: 4f, 5s, and 5p orbitals of the ground configuration $4f^{12}5s^{2}5p^{6}$. Bottom: 4f, 5d, and 5g orbitals of the configurations $4f^{11}5d$, and $4f^{11}5g$, respectively.

out over a broad range relatively far from the nucleus. The mean radial position of a 4f electron is shown to be closer to the nucleus than that of a 5s or 5p electron.

1.2 Energy Levels and Wave Functions

1.2.1 The Free Ion

The free-ion Hamiltonian that determines the 4f energy level can be written as [10]:

$$H_{FI} = -\frac{\hbar^2}{2m}\sum_{i=1}^{N}\Delta_i - \sum_{i=1}^{N}\frac{Z^* e^2}{r_i} + \sum_{i<j}^{N}\frac{e^2}{r_{ij}} + \sum_{i=1}^{N}\zeta(r_i)\mathbf{s}_i \cdot \mathbf{l}_i, \tag{1.1}$$

where N=1,...,14 is the number of the 4f electrons, $Z^* e$ the screened charge of the nucleus, and $\zeta(r_i)$ the spin-orbit coupling function

$$\zeta(r_i) = \frac{\hbar^2}{2m^2c^2 r_i}\frac{dU(r_i)}{dr_i}, \tag{1.2}$$

where $U(r_i)$ is the potential in which the electron is moving.

The Hamiltonian (1.1) can be rewritten:

$$H_{FI} = H_o + H_c + H_{so}, \tag{1.3}$$

where H_o is the first two terms in (1.1), the first of which represents the kinetic energy of the 4f electrons and the second their Coulomb interaction with the nucleus; H_c and H_{so} are the third and fourth terms in (1.1), which represents the mutual Coulomb interaction of the 4f electrons and their spin-orbit interaction, respectively.

When H_{so} is small compared to H_c, we have the so-called Russell-Saunders coupling, where the spin-orbit interaction is treated as a small perturbation on the

energy level structure which has been determined from the diagonalization of H_c. The good quantum numbers for the Russell-Saunders coupling scheme are L and S. For rare earth ions, however, H_c and H_{so} are of approximately equal magnitude and the energy level calculations involve simultaneous diagonalization of both H_c and H_{so}. It is the common practice to use a basis set of Russell-Saunders eigenfunctions for the diagonalization. The new eigenfunctions are now a linear combination of states (terms) with different L and S but the same J, since the Hamiltonian $H_c + H_{so}$ is diagonal in J. Without the presence of a crystalline environment the new states are still degenerate in M_J. Sometimes a new quantum number τ is introduced to distinguish configurations with the same L and S that occur more than once [11].

We can now proceed to calculate the energy levels of the rare earth ions. The first term in (1.3), H_o, contributes to the energy shifts that are the same for all the levels belonging to a given configuration without affecting the energy-level structure of the configuration. The second and third terms, H_c and H_{so}, will be different for different states of the same configuration. We first consider the repulsive Coulomb interaction of the $4f^N$ electron, H_c.

The matrix elements corresponding to H_c is written [12]:

$$(\tau, SLJM|\sum_{i<j}\frac{e^2}{r_{ij}}|\tau', S'L'J'M'). \tag{1.4}$$

Since the electrostatic Hamiltonian commutes with the angular momentum operators corresponding to $\mathbf{L}^2$, $\mathbf{S}^2$, $\mathbf{J}$, and $\mathbf{M}$, the matrix elements will be diagonal in L and S (although not in τ) and independent of J and M. Thus (1.4) becomes

$$(\tau, SL|\sum_{i<j}\frac{e^2}{r_{ij}}|\tau', SL). \tag{1.5}$$

The interaction between each pair of electrons can be expanded using Legendre polynomials of the cosine of the angle θ_{ij} between the vectors from the nucleus to the two electrons [13]:

$$\frac{e^2}{r_{ij}} = e^2\sum_k \frac{r_<^k}{r_>^{k+1}} P_k(\cos\theta_{ij}), \tag{1.6}$$

where $r_<$ is the distance from the nucleus to the nearer electron and $r_>$ the distance from the nucleus to the further away electron. Using the spherical harmonic addition theorem [13] we can write

$$\begin{aligned} P_k(\cos\theta_{ij}) &= \frac{4\pi}{2k+1}\sum_q Y^*_{kq}(\theta_i,\phi_i)Y_{kq}(\theta_j,\phi_j) \\ &= \sum(-1)^q (C^{(k)}_{-q})_i (C^{(k)}_q)_j = (C^{(k)}_i C^{(k)}_j), \end{aligned} \tag{1.7}$$

where the $C_q^{(k)}$ are defined by

$$C_q^{(k)} = \left(\frac{4\pi}{2k+1}\right)^{1/2} Y_{kq}. \tag{1.8}$$

Expression (1.5) becomes

$$\sum_k e^2(\tau SL|\sum_{i<j}\frac{r_<^k}{r_>^{k+1}}(C_i^{(k)}\cdot C_j^{(k)})|\tau' SL). \tag{1.9}$$

The evaluation of (1.9) can be made by use of the tensor operator methods of Racah [14]. We only consider here the simple problem of 2-electron configuration. The extensions to more complex configurations can be found in reference [12]. The matrix element of electrostatic interaction between the two configurations can be written as

$$(n_a l_a, n_b l_b; SL|\frac{e^2}{r_{12}}|n_c l_c, n_d l_d; SL) = \sum_k [f_k(l_a, l_b; l_c, l_d) R^k(n_a l_a, n_b l_b; n_c l_c, n_d l_d) + g_k(l_a, l_b; l_d, l_c) R^k(n_a l_a, n_b l_b; n_d l_d, n_c l_c)], \tag{1.10}$$

where the f_k and g_k represent the angular parts of the matrix elements of Eq. (1.10) and the R^k's, the Slater radial integrals, arise from the radial parts of the one-electron eigenfunctions. The angular factors can be expressed as

$$f_k(l_a, l_b; l_c, l_d) = (-1)^{l_b + l_c + L} (l_a \| C_1^{(k)} \| l_c)(l_b \| C_2^{(k)} \| l_d) \begin{Bmatrix} l_a & l_c & k \\ l_d & l_b & L \end{Bmatrix}, \tag{1.11}$$

and

$$g_k(l_a, l_b; l_d, l_c) = (-1)^S (l_a \| C_1^{(k)} \| l_d)(l_b \| C_2^{(k)} \| l_c) \begin{Bmatrix} l_a & l_d & k \\ l_c & l_b & L \end{Bmatrix}, \tag{1.12}$$

where the reduced matrix element $(l \| C^{(k)} \| l')$ is defined by

$$(l \| C^{(k)} \| l') = (-1)^l [(2l+1)(2l'+1)]^{1/2} \begin{pmatrix} l & k & l' \\ 0 & 0 & 0 \end{pmatrix}. \tag{1.13}$$

The last factor in equations (1.11) and (1.12) are the 6-j symbols, and the last factor in equation (1.13) is the 3-j symbol. Properties of these symbols can be found in Appendix A. The numerical values of the 3-j and 6-j symbols have been tabulated by Rotenberg et al [15].

The Slater radial integrals R^k are defined by [13]

$$R^k(n_a l_a, n_b l_b; n_c l_c, n_d l_d) = e^2 \int_0^\infty \int_0^\infty \frac{r_<^k}{r_>^{k+1}} R_{n_a l_a}(r_1) R_{n_b l_b}(r_2) R_{n_c l_c}(r_3) R_{n_d l_d}(r_4) dr_1 dr_2. \tag{1.14}$$

We thus have obtained general formulas for the evaluation of the electrostatic interaction matrix elements within and between all possible two-elecctron configurations. A complete tabulation of the electrostatic energy matrices for all the f^N

configurations has been made by Nelson and Koster [16]. In their tabulation, however, the matrix elements are expressed in terms of four parameters, E^k (k = 0,...,3):

$$E = \sum_{k=0}^{3} e_k E^k, \tag{1.15}$$

where e_k's are the angular parts and E^k are radial parts which are related to the Slater integrals F^k in the following expression [16]:

$$E^0 = F^0 - 2F^2/45 - F^4/33 - 50F^6/1287$$

$$E^1 = 14F^2/405 + 7F^4/297 + 350F^6/11583$$

$$E^2 = F^2/2025 - F^4/3267 + 175F^6/1656369$$

$$E^3 = F^2/135 + 2F^4/1089 - 175F^6/42471, \tag{1.16}$$

and

$$F^k(n_a l_a, n_b l_b) = R^k(n_a l_a, n_b l_b; n_c l_c, n_d l_d). \tag{1.17}$$

We now consider the spin-orbit interaction, H_{so}. The spin-orbit coupling Hamiltonian $\sum_{i=1}^{N} \zeta(r_i)\mathbf{s}_i \cdot \mathbf{l}_i$ is a tensor product of two rank-one tensors, one of which acts only on the spin, the other only on the orbit. Using formulas (A7) and (A9) in Appendix A, we obtain the matrix elements of spin-orbit interaction in an l^N configuration:

$$\begin{aligned}(l^N \alpha SLJM|\zeta_{nl}\sum_{i=1}^{N}(s_i \cdot l_i)|l^N \alpha' S' L' J' M') &= \zeta_{nl}(-1)^{J+L+S'}\begin{Bmatrix} L & L' & 1 \\ S' & S & J \end{Bmatrix} \\ &\times [l(l+1)(2l+1)]^{1/2}\left(l^N \alpha SL\middle|V^{(11)}\middle|l^N \alpha' S' L'\right),\end{aligned} \tag{1.18}$$

Here the double tensor $V^{(1x)}$ is defined as

$$V^{(1x)} = \sum_i (su^x)_i, \tag{1.19}$$

where u^x is a unit irreducible tensor operator, which operates on the spatial coordinates and is normalized such that [14]

$$(l\|u^{(k)}\|l) = 1 \tag{1.20}$$

An example for k even is

$$u_q^{(k)} = \frac{C_q^{(k)}}{(l\|C^{(k)}\|l)}. \tag{1.21}$$

The complete $V^{(11)}$ matrices for all f^N configurations has been tabulated by Nielson and Koster [16].

Having constructed the energy matrices of a particular configuration we can obtain the energy level of that entire configuration, if the Slater and the spin-orbit radial integrals are known. In the absence of reliable wave functions, the radial integrals have traditionally been treated as adjustable parameters. In a least-squares method, the parameters are usually chosen to fit the few known levels of the configuration being studied. The resulting energy-level scheme is then used to make further level assignments, after which the parameters may be refined. A correct fit should also yield eigenfunctions that can be used to calculate other physical observables with a comparable precision.

The Coulomb and the spin-orbit interactions are the most important ones for describing rare earth free ion energy levels. Discrepancies of the order of 100 cm^{-1}, however, still remain in comparing experimental and theoretical results [10]. In order to reduce these discrepancies, additional interactions need to be taken into account. The most important one is the configuration interaction via the Coulomb interaction. It can be put into parameter form with three two-body integrals, denoted by α, β, γ [17], and

six three-body integrals, denoted by T^2 to T^8 [18]. The next additional interactions are the spin-spin interaction and the spin-other-orbit interaction, which are absorbed into three parameters, M^0, M^2, and M^4. Finally because of the configuration interaction, the spin-orbit coupling can no longer be described by a single constant ζ, and this effect can be put into three parameters, P^2, P^4, P^6[19, 1.20]. Altogether, we have up to 21 parameters with which to describe the free ion spectra.

1.2.2 Ions in the Static Crystal Field

For a free ion, each energy level is (2J+1) fold degenerate because of the spherical symmetry. On placing the ion in a crystal, the ion experiences the crystal field, which is produced by the charge distribution in the crystal. The crystal field destroys the spherical symmetry and removes the M_j degeneracy of the free ion energy levels. The symmetry about the ion will be reduced from spherical symmetry to the symmetry of the position the ion occupies in the crystal. The free ion levels will split into a number of sublevels that may be characterized by the irreducible representations of the group associated with the point symmetry of the ion in the crystal. If the point symmetry is well defined, the new basis for the perturbed Hamiltonian will be $|\alpha SLJ\ {}^{\delta}\Gamma_r)$, where ${}^{\delta}\Gamma_r$ are the irreducible representations of the point group.

The extent of the removal of the M_j degeneracy depends on the crystal symmetry. The number of levels into which free ion J terms are split in a crystal field of a given symmetry is completely known and well-documented (see, for example,

references [12] and [21]). We are now only concerned with the problem of calculating the actual size of the crystal field splitting.

The Hamiltonian for an ion placed in a crystal field may be written as:

$$H = H_F + V, \tag{1.22}$$

where H_F is the Hamiltonian of the free ion and V the potential provided by the crystal environment about the ion being studied. We will assume that the eigenvalues and eigenfunctions of H_F are known and regard V as a perturbation. The unperturbed eigenfunctions will have complete spherical symmetry, and we will try to expand V in terms of spherical harmonics. We may expand the potential in terms of the tensor operators $C_q^{(k)}$ to give

$$V = \sum_{k,q,i} B_q^k (C_q^{(k)})_i, \tag{1.23}$$

where the summation involving i is over all the electrons of the ion of interest. The quantities B_q^k can be regarded as coefficients of expansion to be determined empirically from the experimental data without assuming any details of the model. For the f^N configuration the matrix elements of V is given by

$$\left(f^N \alpha SLJM|V|f^N \alpha' S' L' J' M'\right) = \sum_{k,q} B_q^k (f^N \alpha SLJM|U_q^{(k)}|f^N \alpha' S' L' J' M')(f||C^{(k)}||f) \tag{1.24}$$

where $U^{(k)}$ is a symmetric unit tensor operator defined as [22]

$$U^{(k)} \equiv \sum_{i=1}^{N} u_i^{(k)} \tag{1.25}$$

Equation (1.24) can be further evaluated using (1.13), (A10), and the Wigner-Eckart theorem, (A4):

$$\left(f^N\alpha SLJM|V|f^N\alpha' S'L'J'M'\right) = -7[J,J']^{1/2}\sum_{k,q} B_q^k(-1)^{S+L'+k+2J-M}\partial(S,S')$$
$$\times\begin{pmatrix} J & k & J' \\ -M & q & M' \end{pmatrix}\begin{pmatrix} 3 & k & 3 \\ 0 & 0 & 0 \end{pmatrix}\begin{Bmatrix} J & J' & k \\ L' & L & S \end{Bmatrix}(f^N\alpha SL\|U^{(k)}\|f^N\alpha' SL'). \tag{1.26}$$

The reduced matrix elements of $U^{(k)}$ may be obtained directly from the tables of Nielson and Koster [16]. From the symmetry properties of the 3-j symbol in (1.26) we can immediately see that the matrix elements of V are non-zero only if k is even and $k \leq 6$. The number of nonzero terms (k,q) of the series is further restricted by the point symmetry at the site of the rare-earth ion of the crystal. In experimental spectroscopy, B_q^k are treated as adjustable parameters. In an actual crystal field analysis, the observed energy levels are fitted to a Hamiltonian that contains the free parameters, ζ, F_2, F_4, F_6, etc., and the crystal field parameters B_q^k's. Except for cases of very low symmetry, involving a great many crystal field parameters, there are generally more experimental data than crystal field parameters and therefore a reliable set of crystal field parameters can be obtained.

1.3 Intensities

1.3.1 One-Photon Spectroscopy

The one-photon intensities of an absorption or emission radiative transition are often expressed in terms of oscillator strengths, f_{nm}, where n and m are initial and final states of the transition. In purely atomic transitions, f_{nm} is defined as

$$f_{nm} = \frac{8\pi^2 m\nu}{h} |(n|P|m)|^2 \tag{1.27}$$

for electric or magnetic dipole transitions, and

$$f_{nm} = \frac{12\pi^4 m\nu^4}{he^2c^2} |(n|Q|m)|^2 \tag{1.28}$$

for electric quadrupole transitions, where ν is the frequency of the transition i->f, ***P*** the electric dipole or magnetic dipole moment, and ***Q*** the quadrupole moment tensor.

For allowed transitions in free atoms, the electric dipole oscillator strengths are of the order of magnitude one in the visible, and the magnetic dipole or electric quadrupole oscillator strengths are of the order 10^{-5} or smaller. The electric dipole transitions between the levels of the $4f^N$ configurations, which are responsible for the free ion spectra, are forbidden, because the electric dipole operator has odd parity and the transition matrix element must have even parity (Laporte selection rule). The experimental data on the crystal spectra of rare-earths, however, show that the radiative transitions are mostly electric dipole in nature, though in some cases the magnetic dipole transitions are also observed. Van Vleck [23] was first to point out that electric dipole radiation can occur if the $4f^N$ states have admixtures of $4f^{N-1}nl$ configurations, where $4f^{N-1}nl$ are chosen such that it has opposite parity from $4f^N$. The admixture of the $4f^{N-1}$ wavefunctions into the $4f^N$ wavefunctions is produced by interactions that have odd parity. In crystals where rare earth ions occupy noncentrosymmetric sites, odd parity components of the crystal field mix states from opposite parity configurations into the $4f^N$ wave functions. This mechanism of "forbidden electric dipole transitions", as first proposed by Van Vleck, turned out to be the dominant source for the one-photon intensities in the rare earth spectra.

Van Vleck's proposal of forbidden electric dipole transitions was developed into a quantitative theory of rare earth transition intensities in 1962 by Judd [24] and Ofelt [25]. Using first order perturbation theory, the $4f^N$ initial |i) and final |f) state wavefunctions of the rare earth ion can be expressed as:

$$
\begin{aligned}
(i| &= (f^N \alpha JM| + \sum_j \frac{(f^N \alpha JM|V_{CF}^{odd}|j)(j|}{E_{ji}}, \\
|f) &= |f^N \alpha' J' M') + \sum_j \frac{|j)(j|V_{CF}^{odd}|f^N \alpha' J' M')}{E_{jf}},
\end{aligned}
\tag{1.29}
$$

where the symbol $\sum_j$ stands for the sum over the |α'',J'',M'') states of the n''l'' excited configuration whose parity is opposite to that of the f^N configuration. Here the unprime, prime, and double prime symbols denote the initial, final, and intermediate states, respectively, α denotes the quantum numbers other than total angular momentum J and the azimuthal component of angular momentum M needed to completely specify the wave functions in the intermediate coupling scheme, and $E_{jx}=E_j-E_x$, where x = i or f.

For an electric dipole transition from crystal field state |i) to |f) the oscillator is given as [24]

$$
f_{if} = \frac{8\pi^2 m\nu}{h} \chi |(i|D_q^{(1)}|f)|^2, \tag{1.30}
$$

where $\chi = n(n^2 + 2)^2/9$, a correction for the refractive index n of the crystal, and $D_q^{(1)}$ is the electric dipole operator, defined by

$$
D_q^1 = \sum_j r_j C_q^{(1)}(\theta_j, \varphi_j), \tag{1.31}
$$

where $C_q^{(k)}$ is defined in (1.8).

For transitions between energy levels i and f in an anisotropic medium eq. (1.31) is written

$$f_{if} = \frac{8\pi^2 m\nu}{3h(2J+1)} \chi \sum_{i,f,q} |(i|D_q^{(1)}|f)|^2 \tag{1.32}$$

In any case the oscillator strength is proportional to

$$|(i|D_q^{(1)}|f)|^2 = \Big| \sum_j \frac{(\alpha JM|V_{CF}^{odd}|j)(j|D_q^{(1)}||\alpha' J' M')}{E_{ji}} + \sum_j \frac{(\alpha JM|D_q^{(1)}|j)(j|V_{CF}^{odd}|\alpha' J' M')}{E_{jf}} \Big|^2 \tag{1.33}$$

in the electric dipole approximation.

The explicit computation of the sum in (1.33) is unmanageable because of the infinite number of levels in the intermediate configurations. If the denominators in (1.33) are regarded as constant, however, the closure relation $\sum_j |j)(j| = 1$ can be invoked. This closure approximation was introduced by Judd and Ofelt in 1962 in order to transform (1.33) into a more tractable form. In its mildest form the closure approximation regards all excited configurations E(n''l'',α'' J'') as independent of J'', as the splittings within multiplets of the excited configurations are supposed to be negligible compared with the energies that the configuration as a whole lie above l^N[24], and the sums in (1.33) can be performed over J'' and M''. In its most sweeping form the closure approximation simply regards all excited configurations as completely degenerate, leaving only a single constant energy denominator. A common approximation regards the lowest energy configuration $4f^{N-1}5d$ as degenerate and most significant, and neglects the contribution of other intermediate configurations. After the summations are performed we obtain [24]

$$f^{ed} = \frac{8\pi m\nu}{3h(2J+1)}\chi \sum_{\lambda=2,4,6}\Omega_\lambda (f^N\alpha J\|U^{(\lambda)}\|f^N\alpha' J')^2, \tag{1.34}$$

where

$$\Omega_\lambda = (2\lambda+1)\sum_{k,q}\frac{|B_q^k|^2\,|H_\lambda^k|^2}{2k+1}$$

and (1.35)

$$H_\lambda^k = \frac{2}{E_{l'l}}\sum_{n'l'}\begin{Bmatrix}1 & \lambda & k\\ f & l' & f\end{Bmatrix}(f|r|n'l')(f\|C^{(1)}\|l')(f\|C^{(k)}\|l').$$

Equation (1.33) is key to quantitative study of radiative one-photon processes. The reduced matrix elements of $U^{(\lambda)}$ in equation (1.34) can be evaluated in the same manner as mentioned in section 1.2.2. The coefficients Ω_λ are called the Judd-Ofelt (JO) parameters, as their values are usually determined by fitting experimental oscillator strengths. Typically a single set of Ω_λ are used to fit all observed oscillator strengths of a particular rare earth ion in a given host crystal or solution. The oscillator strengths of numerous one-photon transitions in all trivalent rare earth ions have been analyzed according to such a fitting. The phenomenological treatment has successfully accounted for the intensities of a majority of transitions in each rare earth ion. The most extensive work has been done by Carnall et al. [26,27] on the aqueous solutions of trivalent rare earths. References on analyses of rare earth oscillator strengths can be found in review papers such as that of Peacock [28].

1.3.2 Two-Photon Spectroscopy

Unlike one-photon spectroscopy, which had been well-established by the commencement of this century, most of the studies of two-photon spectroscopy had to

await the advance of lasers. Two-photon transitions are second-order processes, and are therefore much weaker than their one-photon counterpart. We will discuss two different mechanisms contributing to two-photon processes.

1.3.2.1 Two-Photon Absorption

One of the two-photon processes is two photon absorption (TPA), a process in which two photons are simultaneously absorbed. TPA has been used to locate and determine the symmetry of the crystal field wavefunctions and their energy levels in the UV and near-UV region [29]. Since the selection rules for two-photon absorption processes are different from those for single-photon processes, transitions that are forbidden in linear absorption may be explored by two-photon absorption. The first observation of two-photon absorption was the experiment of Kaiser and Garrett [30]. Since then two-photon absorption has been used as an important tool to study phonons, polaritons, excitons, and intra- and inter-configurational electronic transitions in a wide variety of solids [29, 1.31].

1.3.2.2 Raman Scattering

Another two-photon process is Raman scattering, which includes phonon scattering and electronic Raman scattering. This light scattering phenomenon was first discovered by Raman in 1928 [32]. He investigated light scattered from a clear substance and found that its frequency was shifted in such a way to correspond to the rotational and vibrational energy characteristic of the substance. The amount of the scattered light is quite small compared to that of the light passing through the material without deflection. Furthermore, most of the scattered light was frequency unshifted - the so-called Rayleigh scattering. Only approximately one percent of the scattered light was frequency shifted - the Raman scattering. For a liquid sample only 10^{-5} to 10^{-7} of

the amount of the incident light beam is scattered as Raman light. This explains the difficulty in detection and measurement of the Raman scattering technique in the early days. However, with the advance of the intense and highly coherent light produced by a laser, Raman spectroscopy has become one of the powerful techniques in determining the rotational, vibrational, and electronic energy levels of molecules, which traditionally had been determined only by infrared spectroscopy.

If the scattered light frequency is shifted to the lower energies, the spectral line is called the Stokes line. The spectrum line corresponding to the higher energies is called the anti-Stokes line (fig. 1.3). The Stokes lines come from the inelastic collision of the incident light and the molecule of the excited sample material bringing the molecule to a higher energy level. In the quantum language the molecule absorbs a photon coming from the laser, jumps to an excited level, and induces a photon of lower frequency, with the difference in frequency corresponding exactly to the difference in energy between the initial and final states of the molecule. The anti-Stokes lines result from the deexciting the molecule from a higher to a lower energy level. Thus Raman scattering is a two-photon phenomenon, one photon being destroyed and the other created out of the vacuum.

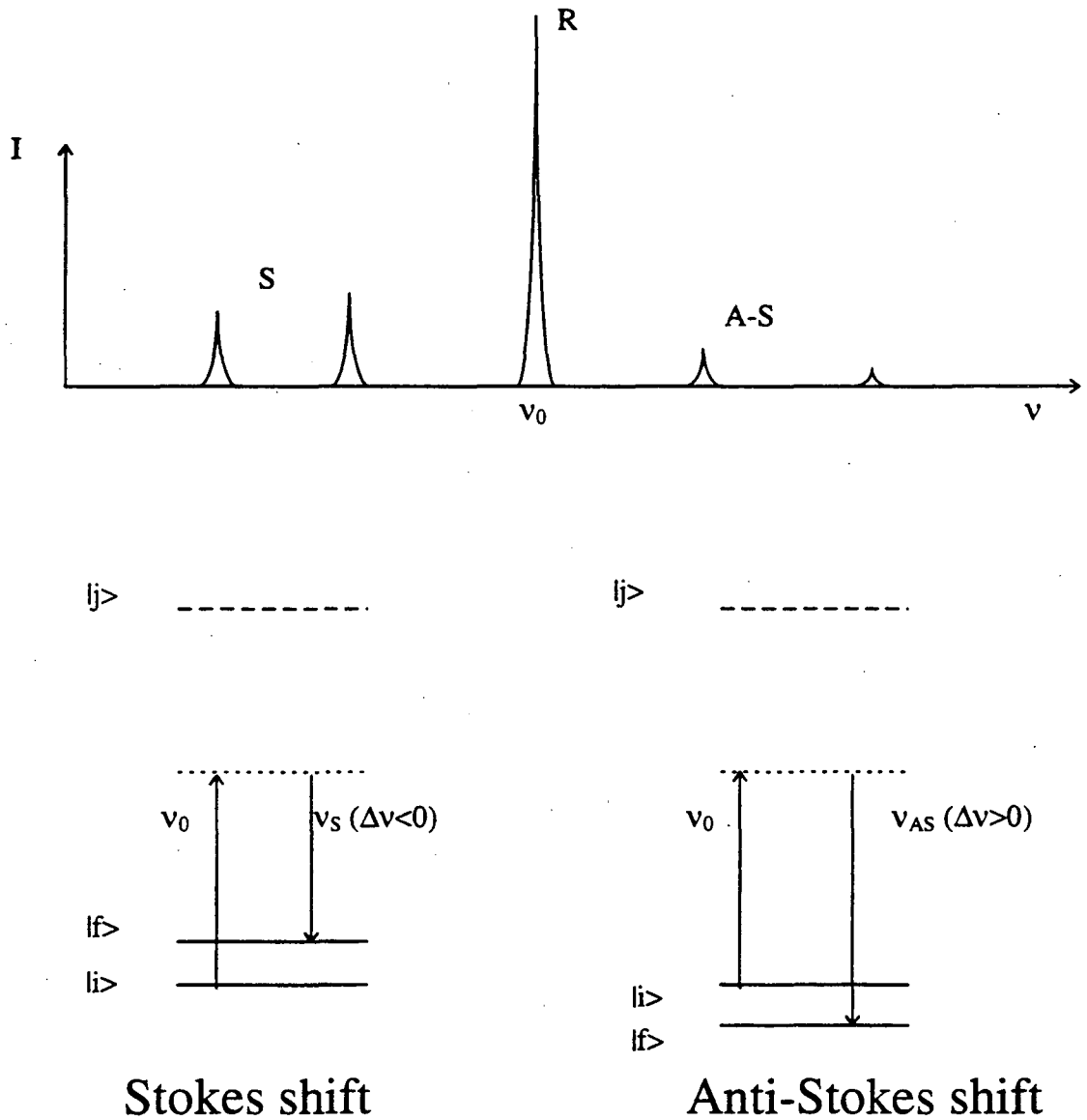

Fig. 1.3: Stokes and Anti-Stokes spectral lines in Raman scattering. In a Stokes shift, the molecules are excited to a state of higher energy. In an Anti-Stokes shift, the molecules are deexcited to a state of lower energy.

a. Phonon Raman Scattering

If the molecule is excited to a new vibrational level of the same electronic state, the scattering is called phonon scattering. It is merely the interaction between the incoming light and the phonons of the medium. In solids there are optical and acoustic modes of vibration. Only optical modes can be Raman active, due to their ability to interact with light via induced dipole moments. For non-resonant phonon scattering - in which the incoming light frequency does not match any electronic level of the medium- the phonon modes have to be symmetric to be Raman active.

b. Electronic Raman Scattering

When a Raman scattering transition occurs between two electronic states of the medium, the transition is called the electronic Raman transition. Rare earth crystals are good candidates for the electronic Raman technique because their crystal field energy levels of the ground multiplet are generally quite sharp and fall well into the infrared region. Thus a laser with an optical frequency can probe the low-lying levels of a multiplet (usually the ground multiplet) to reveal the energy separation between these crystal field levels. The first electronic Raman scattering experiment was reported by Hougen and Singh in 1963 [33]. From the measured intensities of the electronic Raman transitions, one can study the mechanisms of the interaction between the lanthanide ion and the radiation field [34].

c. Selection Rules and Symmetry in Raman Spectroscopy

The selection rules for the vibrational and electronic Raman scattering processes are determined by the symmetry of the crystal lattice. The phonons of the rare earth

vanadate crystal medium are classified by the irreducible representations of the group D_{4h}, which is the symmetry group of the unit cell [35]. The electronic levels are classified by the irreducible representations of the point group D_{2d}, which is the site symmetry group of the lanthanide ion in the zircon structure crystal lattice. In Raman scattering processes, in which an incident light wave of polarization σ is inelastically scattered into a light wave of polarization ρ, the amplitude of a Raman scattering transition is determined by $\alpha_{\rho\sigma}$, where ρ and σ commonly represent Cartesian coordinates [36].

i) Selection rules in phonon scattering:

For $(RE)VO_4$ crystals there are two molecules per primitive cell; hence there are 36 phonon modes, 33 of which are optical. Of these 12 are Raman active: $2A_{1g}+4B_{1g}+B_{2g}+5E_g$. Except the E_g mode, which is doubly degenerate, all other modes are non-degenerate. The polarization dependence of these Raman modes is contained in their respective Cartesian Raman tensors listed below in Table 1.1 [37].

Table 1.1: Cartesian Phonon Raman scattering tensors for the zircon structure (D_{4h}).

$A_{1g}\begin{pmatrix} a & 0 & 0 \\ 0 & a & 0 \\ 0 & 0 & b \end{pmatrix}$	$B_{1g}\begin{pmatrix} c & 0 & 0 \\ 0 & -c & 0 \\ 0 & 0 & 0 \end{pmatrix}$	$B_{2g}\begin{pmatrix} 0 & d & 0 \\ d & 0 & 0 \\ 0 & 0 & 0 \end{pmatrix}$
$E_g\begin{pmatrix} 0 & 0 & e \\ 0 & 0 & 0 \\ e & 0 & 0 \end{pmatrix}$	and	$\begin{pmatrix} 0 & 0 & 0 \\ 0 & 0 & f \\ 0 & f & 0 \end{pmatrix}$

ii) Selection rules in electronic Raman scattering:

The symmetry of the electronic Raman Cartesian tensor $\alpha_{\rho\sigma}$ is determined by requiring that the direct product $\Gamma_i \otimes \Gamma(\alpha_{\rho\sigma}) \otimes \Gamma_f$ contain the totally symmetric representation, where Γ_i and Γ_f are the irreducible representations of the initial and final electronic states, and σ and ρ are the polarizations of the incident and scattered light, respectively. Here the notation used for the irreducible representations is that of Koster et al [21]. This means that the allowed tensor is given by the decomposition of $\Gamma_i \otimes \Gamma_f$ into irreducible representations. In practice Γ_i is usually known from absorption data, $\Gamma(\alpha_{\rho\sigma})$ is determined from the experiment, and Γ_f is found by the requirement stated above.

The electronic levels of the rare earth (RE) ion in the vanadate crystal host are classified by the irreducible representations of the point group D_{2d}, which is the site symmetry group of the lanthanide ion in the zircon structure $(RE)VO_4$ crystal lattice. The Cartesian electronic Raman scattering tensors are listed in Table 1.2. Note that a transformation is needed to express the scattering tensors in the crystallographic X, Y, Z frame, which can be readily observed from the experiment, while the symmetry properties of the scattering tensors are derived in the local D_{2d} symmetry (the x, y, z frame). A scattering tensor $\alpha_{\rho\sigma}$ observed in the X,Y,Z frame is related to the tensor $\alpha_{\lambda\mu}$ expressed in the rotated x,y,z frame by the equation:

$$\alpha_{\rho\sigma} = R^t \alpha_{\lambda\mu} R \qquad (1.36)$$

where R is the matrix of a 45° rotation about the Z axis, R^t its transpose, $\rho,\sigma = X,Y,Z$, and $\lambda,\mu = x, y, z$

$$R = \begin{pmatrix} \cos(\pi/4) & \sin(\pi/4) & 0 \\ -\sin(\pi/4) & \cos(\pi/4) & 0 \\ 0 & 0 & 1 \end{pmatrix} \tag{1.37}$$

The z axis is parallel to the Z axis, and the x and y axes are rotated in the X-Y plane by 45° relative to the X and Y axis. In the Cartesian coordinates, x and y (X and Y) are completely interchangeable for D_{2d} symmetry. The effect of the rotation of the tensors is that some tensors having diagonal elements may be transformed into tensors having elements equal to zero, and vice-versa. Note also that since x and y are equivalent one must have

$$f^{*} = e^{i\phi} f \text{ and } \quad g^{*} = e^{i\phi} g. \tag{1.38}$$

Table 1.2: Cartesian electronic Raman scattering tensors for D_{2d}

Symmetry labels	Axes x,y,z	Axes X,Y,Z
Γ_1	$\begin{pmatrix} a & 0 & 0 \\ 0 & a & 0 \\ 0 & 0 & b \end{pmatrix}$	$\begin{pmatrix} a & 0 & 0 \\ 0 & a & 0 \\ 0 & 0 & b \end{pmatrix}$
Γ_2	$\begin{pmatrix} 0 & c & 0 \\ -c & 0 & 0 \\ 0 & 0 & 0 \end{pmatrix}$	$\begin{pmatrix} 0 & c & 0 \\ -c & 0 & 0 \\ 0 & 0 & 0 \end{pmatrix}$
Γ_3	$\begin{pmatrix} d & 0 & 0 \\ 0 & -d & 0 \\ 0 & 0 & 0 \end{pmatrix}$	$\begin{pmatrix} 0 & d & 0 \\ d & 0 & 0 \\ 0 & 0 & 0 \end{pmatrix}$
Γ_4	$\begin{pmatrix} 0 & e & 0 \\ e & 0 & 0 \\ 0 & 0 & 0 \end{pmatrix}$	$\begin{pmatrix} e & 0 & 0 \\ 0 & -e & 0 \\ 0 & 0 & 0 \end{pmatrix}$
Γ_5 (symmetric)	$\begin{pmatrix} 0 & 0 & f \\ 0 & 0 & 0 \\ f & 0 & 0 \end{pmatrix}$ $\begin{pmatrix} 0 & 0 & 0 \\ 0 & 0 & f^* \\ 0 & f^* & 0 \end{pmatrix}$	$\begin{pmatrix} 0 & 0 & f/\sqrt{2} \\ 0 & 0 & -f/\sqrt{2} \\ f/\sqrt{2} & -f/\sqrt{2} & 0 \end{pmatrix}$ $\begin{pmatrix} 0 & 0 & f^*/\sqrt{2} \\ 0 & 0 & f^*/\sqrt{2} \\ f^*/\sqrt{2} & f^*/\sqrt{2} & 0 \end{pmatrix}$
Γ_5 (antisymmetric)	$\begin{pmatrix} 0 & 0 & g \\ 0 & 0 & 0 \\ -g & 0 & 0 \end{pmatrix}$ $\begin{pmatrix} 0 & 0 & 0 \\ 0 & 0 & g^* \\ 0 & -g^* & 0 \end{pmatrix}$	$\begin{pmatrix} 0 & 0 & g/\sqrt{2} \\ 0 & 0 & -g/\sqrt{2} \\ -g/\sqrt{2} & g/\sqrt{2} & 0 \end{pmatrix}$ $\begin{pmatrix} 0 & 0 & g^*/\sqrt{2} \\ 0 & 0 & g^*/\sqrt{2} \\ -g^*/\sqrt{2} & -g^*/\sqrt{2} & 0 \end{pmatrix}$

1.3.2.3 Two-Photon Transition Intensities

The derivation of two-photon transition intensities in the framework of time dependent perturbation theory can be found in advanced textbooks on quantum mechanics (see, for example, references [38] and [39]), and a rather detailed discussion on its application to rare-earth ions was given in Downer's thesis [40]. We will only discuss important results for rare-earth ions which will be useful for our theoretical treatment of two-photon transition intensities in subsequent chapters.

The total Hamiltonian of N atomic electrons of the configuration f^N interacting with electromagnetic radiation can be written:

$$H = H_0 + V_0, \tag{1.39}$$

where the H_0 term includes the central field term, the $p^2/2m$ term, the Coulomb interaction, spin-orbit interaction, crystal field interaction, and other terms not included in radiative interaction term. The V_0 term represents the interaction Hamiltonian, which can be written:

$$V_0 = \frac{e}{mc}\sum_{n=1}^{N}\mathbf{A}(\mathbf{r}_n)\cdot\mathbf{p}_n + \frac{e^2}{2mc^2}\sum_{n=1}^{N}[\mathbf{A}(\mathbf{r}_n)]^2, \tag{1.40}$$

where the vector potential $\mathbf{A}(\mathbf{r}_n)$ satisfies the transversality condition $\nabla\cdot\mathbf{A} = 0$, often known as the Coulomb gauge. In a general two photon process the vector potential can be regarded as superposition of two plane waves of frequencies ω_1 and ω_2 and unit polarization $\hat{\mathbf{e}}_1$ and $\hat{\mathbf{e}}_2$:

$$\mathbf{A}(\mathbf{r}_n) = \frac{1}{2}[\hat{\mathbf{e}}_1 A_1 e^{i(\mathbf{k}_1\mathbf{r}_n - i\omega_1 t)} + \hat{\mathbf{e}}_2 A_2 e^{i(\mathbf{k}_2\mathbf{r}_n - i\omega_2 t)}] \tag{1.41}$$

In the time-dependent perturbation language, the linear (**A.p**) term in (1.40) makes no contribution in first order to a two-photon process. The first-order TPA transition amplitude from i to f thus comes only from the quadratic (**A.A**) term in (1.40):

$$c^{(1)}(t) = \frac{1}{4\hbar}\frac{e^2}{2mc^2}(\hat{\mathbf{e}}_1 \cdot \hat{\mathbf{e}}_2)A_1A_2 < i|\sum_n e^{i(\mathbf{k}_1+\mathbf{k}_2)\cdot\mathbf{r}_n}|f > g(t), \tag{1.42}$$

$$\text{where } g(t) = \frac{1}{\omega_{if} - \omega_1 - \omega_2}[e^{i(\omega_{if}-\omega_1-\omega_2)t} - 1]. \tag{1.43}$$

The signs in front of **k** and ω for two-photon emission, would be opposite to those for TPA. For Raman scattering, one photon is absorbed and the other emitted, thus the signs would alternate. The exponential operator in (1.42) can be expanded in the series

$$e^{i(\mathbf{k}_1+\mathbf{k}_2)\cdot\mathbf{r}_n} = 1 + i(\mathbf{k}_1 + \mathbf{k}_2)\cdot\mathbf{r}_n - \frac{1}{2}[\mathbf{k}_1 + \mathbf{k}_2)\cdot\mathbf{r}_n]^2 + \ldots \tag{1.44}$$

In the expansion (1.44) the first term only contributes to Raleigh scattering. For rare-earth transitions between states of the 4f configuration, the second term of the approximation is smaller than the first term by approximately a factor of 10^{-5}. This is because $(\mathbf{k}_1 + \mathbf{k}_2)\cdot < 4f|\sum_n \mathbf{r}_n|5d >$ is on the order of 10^{-2} for excitation in the optical range and assuming $< 4f|\sum_n \mathbf{r}_n|5d >$ to be of the same magnitude as atomic level spacings. In addition, due to the small amount of opposite-parity configurational mixing of the 5d states into the 4f states, the matrix element $< 4f|\sum_n \mathbf{r}_n|4f >$ is smaller than $< 4f|\sum_n \mathbf{r}_n|5d >$ by a factor of 10^{-3}, but non-zero, making the total magnitude of

$(\mathbf{k}_1 + \mathbf{k}_2) \cdot < 4f | \sum_n \mathbf{r}_n | 4f >$ to be approximately 10^{-5}. The last term also gives a contribution on the order of 10^{-5}. Both of these latter terms turn out to be negligible compared to the second-order contributions to the two-photon transition probability. It should be noted that although having the same magnitude order, the second term differs from the third term in (1.44) by an imaginary factor.

The **A.p** term in (1.41) can be taken twice in the second order to give a contribution to two-photon amplitude. The second-order transition amplitude $c^{(2)}(t)$ for a TPA process between states i and f is given by

$$c^{(2)}(t) = -\frac{1}{\hbar}\frac{e^2}{m^2c^2} g(t) \sum_j \left[\frac{M_{ij}^{(1)} M_{jf}^{(2)}}{\hbar(\omega_{jf} - \omega_2)} + \frac{M_{ij}^{(2)} M_{jf}^{(1)}}{\hbar(\omega_{jf} - \omega_1)} \right], \tag{1.45}$$

where the summation is performed over all intermediate states j, and

$$M_{ab}^{(q)} = \frac{A_q}{2} < a | \sum_n e^{i\mathbf{k}_q \cdot \mathbf{r}_n} \hat{\mathbf{e}}_q \cdot \mathbf{p}_n | b >, \tag{1.46}$$

where q is 1, 2, a is i, j, and b is j, f.

In the case of resonant excitation where $\omega_{jf} - \omega_2 \cong 0$ (or $\omega_{jf} - \omega_1 \cong 0$), the denominator in (1.45) must be modified to include the linewidth of the excited state, i.e. $\hbar(\omega_{jf} - \omega_2 - i\Gamma_j / 2)$ (or $\hbar(\omega_{jf} - \omega_1 - i\Gamma_j / 2)$).

The exponential operator in (1.46) can again be expanded via (1.44). The first term in the expansion can be written

$$< a | \hat{\mathbf{e}}_q \cdot \sum_n \mathbf{p}_n | b > = -\frac{im\omega}{e} < a | \hat{\mathbf{e}}_q \cdot \mathbf{D} | b >, \tag{1.47}$$

where $\mathbf{D} = \sum_n \mathbf{r}_n$. An approximation in which only the $\hat{\mathbf{e}}.\mathbf{p}$ term is kept is called the electric dipole (E1) approximation. When the electric dipole term is sufficiently small, the second term of (1.44) may be taken into account:

$$< a|\sum_n i(\mathbf{k}_q \cdot \mathbf{r}_n)(\hat{\mathbf{e}}_q \cdot \mathbf{p}_n)|b >= \frac{m\omega^2}{2c}\hat{\mathbf{k}}_q \cdot < a|\mathbf{DD}|b > \cdot \hat{\mathbf{e}}_q + \frac{im\omega}{e} < a|(\hat{\mathbf{k}}_q \times \hat{\mathbf{e}}_q) \cdot \mathbf{m}|b >, \tag{1.48}$$

where the first term on the right hand side of (1.48) is the quadrupolar term (E2) and the second term the magnetic dipolar term (M1). These are the terms responsible for the electric quadrupole and magnetic dipole transition in one-photon absorption. The transition probabilities corresponding to these terms are of the order 10^{-4} smaller than for the electric-dipole term. The E2 term is in general out of phase with the E1 term and M1 term, except in the case of circular polarization, in which the magnetic dipole term is also out of phase with the electric dipole term, since $(\hat{\mathbf{k}} \times \hat{\mathbf{e}}_\pm) = \mp i\hat{\mathbf{e}}_\pm$, where $\hat{\mathbf{e}}_+$ and $\hat{\mathbf{e}}_-$ are the polarization vectors of right (+) and left (-) circularly polarized light. In most cases where the second-order electric dipole term is sufficiently large, the electric quadrupole and magnetic dipole terms can be neglected.

The quantitative study of two-photon processes began when Axe [31], using the Judd-Ofelt closure approximation, derived an explicit expression for the second-order two-photon line strength, in a manner analogous to Judd and Ofelt's formula for single-photon line strength. The expression for two-photon absorption line strength, however, generally contains only one parameter, instead of three, as in the one-photon expression. As a result, the ratio of the line strengths of two-photon transitions can be computed without the need for phenomenological parameters. Experimental measurements of line

strength ratios and polarization dependence of line strengths therefore provide rigorous tests of the second order theory of two-photon absorption. More details of the quantitative derivations of the two-photon absorption and electronic Raman scattering are provided in the next chapter, where the treatment of the polarization dependence of the two-photon transition intensities in crystals is given.

We have just built the foundation for understanding the energy levels of a rare earth ion in a crystal and the corresponding crystal field eigenfunctions. We have also provided the theoretical framework for one-photon intensities of rare-earth transitions, and contrasted the two-photon with the one-photon spectroscopy. In the next chapter we will study the quantitative two-photon transition intensities in crystals and provide the theoretical analysis for the polarization dependence technique.

Appendix A

The following definitions and formulas have been used in the tensor operator recoupling techniques. We will employ the following abbreviated notation:

$[j] = 2j+1$

$[j_1, j_2, \ldots] = (2j_1+1)(2j_2+1)\ldots$

1. Definition of the 3-j Symbol

$$\begin{pmatrix} j_1 & j_2 & j \\ m_1 & m_2 & m \end{pmatrix} = (-1)^{j_1-j_2-m}[j]^{-1/2}\left(j_1 m_1 j_2 m_2 | j_1 j_2 j - m\right) \tag{A1}$$

2. Definition of the 6-j Symbol

$$\begin{Bmatrix} j_1 & j_2 & j_{12} \\ j_3 & j & j_{23} \end{Bmatrix} = (-1)^{j_1+j_2+j_3+j}[j_{12}, j_{23}]^{-1/2}\left((j_1 j_2) j_{12} j_3 j | j_1 (j_2 j_3) j_{23} j\right) \tag{A2}$$

3. Definition of the 9-j Symbol

$$\begin{Bmatrix} j_1 & j_2 & j_{12} \\ j_3 & j_4 & j_{34} \\ j_{13} & j_{24} & j \end{Bmatrix} = (-1)^{j_1+j_2+j_3+j}[j_{12}, j_{34}, j_{13}, j_{24}]^{-1/2} \times\left((j_1 j_2) j_{12} (j_3 j_4) j_{34} j | (j_1 j_3) j_{13} (j_2 j_4) j_{24} j\right) \tag{A3}$$

Symmetry properties of the 3-j, 6-j, and 9-j symbols can be found in many textbook references on tensor operators such as [11],[16], and [22].

4. The Wigner-Eckart Theorem

a. Single Tensor Operators

$$(\alpha j m | \mathbf{T}_q^{(k)} | \alpha' j' m') = (-1)^{j'-m+j}(\alpha j \| \mathbf{T}^{(k)} \| \alpha' j') \begin{pmatrix} j & k & j' \\ -m & q & m' \end{pmatrix} \tag{A4}$$

b. Double Tensor Operators

$$(\alpha s m_s l m_l | \mathbf{T}^{(kk')}_{qq'} | \alpha' s' m_s' l_l' m_l') = (-1)^{s+l-m_s-m_l}$$
$$\times \begin{pmatrix} s & k & s' \\ -m_s & q & m' \end{pmatrix} \begin{pmatrix} l & k' & l' \\ -m_l & q' & m' \end{pmatrix} (\alpha s l \,||\mathbf{T}^{(kk')}||\alpha' s' l') \tag{A5}$$

5. Product of Tensor Operators

$$(\alpha j_1 j_2 j || (\mathbf{T}^{(k_1)} \times \mathbf{U}^{(k_2)})^{(K)} || \alpha' j_1' j_2' j') = \sum_{\alpha''} (\alpha j_1 || \mathbf{T}^{(k_1)} || \alpha'' j_1')(\alpha'' j_2 || \mathbf{U}^{(k_2)} || \alpha' j_2')$$
$$\times [j, j', k]^{1/2} \begin{Bmatrix} j_1 & j_1' & k_1 \\ j_2 & j_2' & k_2 \\ j & j' & K \end{Bmatrix} \tag{A6}$$

6. Scalar Product of Two Tensor Operators

$$\mathbf{T}^{(k)} \cdot \mathbf{U}^{(k)} = \sum_q (-1)^q \mathbf{T}^{(k)}_q \mathbf{U}^{(k)}_{-q}$$
$$= (-1)^k (2k+1)^{1/2} (\mathbf{T}^{(k)} \times \mathbf{U}^{(k)})^{(0)} \tag{A7}$$

Setting K = 0 and $k_1 = k_2 = k$ in (A.6) we get

$$(\alpha j_1 j_2 j m | (\mathbf{T}^{(k)} \cdot \mathbf{U}^{(k)}) | \alpha' j_1' j_2' j' m') = \delta(j, j')\delta(m, m')(-1)^{j_1'+j_2+j}$$
$$\times \begin{Bmatrix} j_1 & j_1' & k \\ j_2' & j_2 & j \end{Bmatrix} \sum_{\alpha''} (\alpha j_1 || \mathbf{T}^{(k)} || \alpha'' j_1')(\alpha'' j_2 || \mathbf{U}^{(k)} || \alpha' j_2') \tag{A8}$$

Setting $k_2 = 0$ and then $k_1 = 0$ in (A.6) we get

$$(\alpha j_1 j_2 j || \mathbf{T}^{(k)} || \alpha' j_1' j_2' j') = \delta(j_2, j'_2)(-1)^{j_1+j_2+j'+k} [j, j']^{1/2}$$
$$\times \begin{Bmatrix} j & j' & k \\ j_1' & j_1 & j_2 \end{Bmatrix} (\alpha j_1 || \mathbf{T}^{(k)} || \alpha'' j_1') \tag{A9}$$

and

$$(\alpha j_1 j_2 j \| \mathbf{U}^{(k)} \| \alpha' j_1' j_2' j') = \delta(j_1, j'_1)(-1)^{j_1+j_2'+j+k}[j, j']^{1/2}$$
$$\times \begin{Bmatrix} j & j' & k \\ j_2' & j_2 & j_1 \end{Bmatrix} (\alpha j_2 \| \mathbf{U}^{(k)} \| \alpha'' j_2') \tag{A10}$$

7. Useful Reduced Matrix Elements

a. $$(l \| \mathbf{l} \| l') = [l(l+1)(2l+1)]^{1/2}\, \delta(l,l') \tag{A11}$$

b. $$(s \| \mathbf{s} \| s') = [s(s+1)(2s+1)]^{1/2} \delta(s,s') \tag{A12}$$

c. $$(l \| \mathbf{C}^{(k)} \| l') = (-1)^{l}[l,l']^{1/2} \begin{pmatrix} l & k & l' \\ 0 & 0 & 0 \end{pmatrix} \tag{A13}$$

8. Useful Formulas for Reduced Matrix Elements

$$(\alpha j_1 j_2 j \| \mathbf{W}^{(11)K} \| \alpha' j_1' j_2' j') = (\alpha j_1 j_2 \| \mathbf{W}^{(11)} \| \alpha' j_1' j_2')[j, j', k]^{1/2} \begin{Bmatrix} j_1 & j_1' & 1 \\ j_2 & j_2' & 1 \\ j & j' & K \end{Bmatrix}$$

(A14)

$$(l^N \alpha SLJ \| (\mathbf{U}^{(t)} \mathbf{W}^{(11)0}) \| l^N \alpha' S' L' J')$$
$$= [J]^{-1/2} \sum_{\psi''} (l^N \alpha SLJ \| \mathbf{U}^{(t)} \| l^N \alpha'' SL' J'')(l^N \alpha'' SL'' J' \| \mathbf{W}^{(11)0} \| l^N \alpha' S' L' J')$$

(A15)

$$(l^N \alpha SL \| \mathbf{W}^{(11)} \| l^N \alpha' S' L') = \sqrt{6}(l^N \alpha SL \| \mathbf{V}^{(11)} \| l^N \alpha' S' L') \tag{A16}$$

References

[1] J. Becquerel, C.R. Acad. Sci. **142**, 775 (1906).

[2] J. Becquerel, Le Radium **4**, 328 (1907).

[3] J. Becquerel and H. Kammerlingh Onnes, Proc. Acad. Amsterdam **10**, 592 (1908).

[4] J. Becquerel and H. Kammerlingh Onnes, Le Radium **5**, 227 (1908).

[5] M. Mayer, Phys. Rev. **60**, 184 (1941).

[6] R. Latter, Phys. Rev. **99**, 510 (1955).

[7] C. A. Coulson and C. S. Sharma, Proc. Phys. Soc. (London), **79**, 920 (1962).

[8] C. K. Jørgensen, J. Inorg. Nuclear Chem., **1**, 301 (1955).

[9] N. Edelstein (private communication).

[10] S. Hüfner, *Optical Spectra of Rare Earth Compounds* (Academic Press, New York, 1978).

[11] B. R. Judd, *Operator Techniques in Atomic Spectroscopy* (McGraw-Hill Book Co., New York, 1963).

[12] B. G. Wybourne, *Spectroscopic Properties of Rare Earths* (Interscience Publishers, New York, 1965).

[13] E. U. Condon and G. H. Shortley, *The Theory of Atomic Spectra* (Cambridge University Press, Cambridge,1935).

[14] G. Racah, Phys. Rev. **62**, 438 (1942).

[15] Rotenberg, Bivins, Metropolis, and Wooten, *The 3-j and 6-j Symbols* (M.I.T. Press, Princeton, 1959).

[16] C. W. Nielson and G. F. Koster, *Spectroscopic Coefficients of the p^n, d^n, and f^n Configurations* (The M.I.T. Press, Cambridge, Massachusetts, 1963).

[17] K. Rajnak and B. G. Wybourne, Phys. Rev. **132**, 280 (1963).

[18] B. R. Judd, Phys. Rev. **141**, 4 (1966).

[19] B. R. Judd, H. M. Crosswhite, and H. Crosswhite, Phys. Rev. **169**, 130 (1968).

[20] H. Crosswhite, H. M. Crosswhite, and B. R. Judd, Phys. Rev. **174**, 89 (1968).

[21] G. F. Koster, J. O. Dimmock, R. G. Wheeler, and H. Statz, *Properties of the Thirty-Two Point Groups* (M. I. T. Press, Cambridge, Massachusetts, 1963).

[22] R. D. Cowan, *The theory of Atomic Structure and Spectra* (University of California Press, Berkeley and Los Angeles, California, 1981).

[23] J. H. van Vleck, J. Phys. Chem. **41**, 67 (1937).

[24] B. R. Judd, Phys. Rev. **127**, 750 (1962).

[25] G. S. Ofelt, J. Chem. Phys. **37**, 511 (1962).

[26] W. T. Carnall, H. Crosswhite, and H. M. Crosswhite, *Energy Level Structure and Transition Probabilities of Trivalent Lanthanides in* LaF_3 (Argonne National Laboratory Report, 1977).

[27] W. T. Carnall, Pr. Fields, and B. G. Wybourne, J. Chem. Phys. **42**, 3797 (1965).

[28] R. D. Peacock: Struc. Bonding **22**, 83 (1975).

[29] M. Downer, in *Laser Spectroscopy of Solids II*, edited by W. M. Yen (Springer Verlag, New York, 1989).

[30] W. Kaiser and C. G. B. Garrett, Phys. Rev. Lett. **7**, 229 (1960).

[31] J. D. Axes, Phys. Rev. **136A**, 42, (1964).

[32] C. V. Raman and R. S. Krishnan, Nature **121**, 501 (1928).

[33] J. T. Houghen and S. Singh, Phys. Rev. Lett. **10**, 406 (1963).

[34] R. J. H. Clark and T. T. Dines, in *Advances in Infrared and Raman Spectroscopy*, edited by R. J. H. Clark and R. E. Hester (Heyden, London, 1982), Vol. 9, p. 282.

[35] M. Cardona, in *Light Scattering in Solids II* (Springer-Verlag, Berlin, 1982), p. 19.

[36] J. A. Koningstein, *Introduction to the Theory of the Raman Effect* (D. Reidel Publishing Company, Dordrecht, Holland, 1972).

[37] R. Loudon, Adv. in Phys. **13**, 423 (1964).

[38] J.J. Sakurai, *Advanced Quantum Mechanics* (Addison-Wesley Publishing Company, Inc., Redwood City, California, 1987).

[39] R. Loudon, *The Quantum Theory of Light* (Clarendon Press, Oxford, 1983).

[40] M.C. Downer, Ph.D. thesis, Harvard University, Cambridge, 1983.

Chapter 2

Theory of Polarization Dependence of Raman Scattering and TPA Intensities in Rare-Earth Doped Crystals

2.1 Overview

Two-photon spectroscopy has emerged as an important tool in the study of electronic states of ions in crystals. There are two types of two-photon spectroscopy. The first type is two-photon absorption (TPA), in which both photons are simultaneously absorbed by the ion. The second type is electronic Raman scattering (ERS), in which a photon is inelastically scattered from an ion such that the ion is excited to a different electronic state. Both types of spectroscopy are considered complementary to linear spectroscopy. TPA has provided access to higher energy absorption bands than single-photon absorption, and ERS has been used to probe low energy levels near the ground state. Since the selection rules for two-photon processes are different from those for single-photon processes, transitions that are forbidden in linear absorption may be explored by TPA. The freedom to independently vary each of the two polarizations in two-photon processes has provided a powerful tool to study the symmetries of the initial and final states in a transition. Among the important

applications of two-photon spectroscopy one may include the study of phonons, polaritons, excitons, and intra- and inter- configurational electronic transitions in a wide variety of solids [1-4].

The theory of two-photon processes owes much of its origin to the theory of one-photon processes. The quantitative theory of single-photon transition intensities was developed by Judd [2] and Ofelt [3] in 1962. By introducing the so-called "Judd-Ofelt closure approximation" Judd and Ofelt were able to derive an expression in which the oscillator strengths of the one-photon transitions of rare earth (RE) ions in host lattice crystals are described in terms of a radial factor, which can be estimated for a particular rare earth, and only three parameters. The values of these so-called Judd-Ofelt parameters are usually determined by fitting experimental oscillator strengths. Typically, a single set of Judd-Ofelt parameters are used to fit all observed oscillator strengths of a particular RE ion in a given host crystal or solution. The phenomenological treatment has successfully accounted for the intensities of a majority of transitions for each RE ion. The most extensive work has been done by Carnall et al. [5,6] on the aqueous solutions of trivalent RE's. References on analyses of RE oscillator strengths can be found in review papers such as that of Peacock [7].

The quantitative study of two-photon processes began when Axe [4], using the Judd-Ofelt closure approximation, derived an expression for the second-order two-photon line strength, in a manner analogous to Judd and Ofelt's formula for single-photon line strength. The expression for TPA line strength, however, generally contains only one parameter, instead of three, as in the one-photon expression. As a result, the

ratio of the line strengths of two-photon transitions can be computed without the need for phenomenological parameters. Experimental measurements of line strength ratios and the polarization dependence of line strengths therefore provide rigorous tests of the second order theory of TPA. Axe's theory, however, is traditionally applied to intra-configurational transitions from one multiplet to another, with the polarization of the excitation photons being either parallel or perpendicular to the z-axis of the lanthanide complex, where the z-axis is the highest symmetry [8].

The overwhelming success of the Judd-Ofelt theory when applied to RE materials has been the motivation for the intensive study of two-photon intensities using Judd-Ofelt-Axe's theory. Strong disagreement, however, was found when Axe's theory was applied to Gd^{3+} ions in a number of RE hosts. In particular, the experimental results in Gd^{3+}:LaF_3 reported by Dagenais, Downer, Neumann, and Bloembergen [9] showed that two-photon transitions from the ground level $^8S_{7/2}$ of Gd^{3+} to the first three excited levels, $^6P_{7/2}$, $^6P_{5/2}$ and $^6P_{3/2}$, were anomalously strong with respect to the predictions of a second-order theory, and that the angular momentum selection rule $\Delta J \leq 2$ broke down in several transitions ($^8S_{7/2} \rightarrow {}^6I_{13/2,15/2,17/2}$, $^6D_{1/2}$). In order to account for the anomalous intensity observed for $^8S_{7/2} \rightarrow {}^6P_{7/2}$ in Gd^{3+}, Judd and Pooler expanded Axe's second-order theory of TPA to include third-order terms involving the spin-orbit interaction [10]. Downer and coworkers [11,12] later showed that the inclusion of third-order terms involving the crystal-field interaction among intermediate states could explain the anomalous intensity of the $^8S_{7/2} \rightarrow {}^6I_J$ lines in Gd^{3+}. A fuller analysis of the experimental results for the integrated and crystal component intensities for the $^8S \rightarrow {}^6I$

transitions in the Gd^{3+} ion using expressions which include up to the fourth order contributions involving spin-orbit and/or crystal-field interactions was given by Downer et al [12,13]. Ceulemans and Vandenberghe later presented a more general expression which can be applied to any RE ion [14].

Other third-order mechanisms in two-photon processes were also investigated by several workers. Reid and Richardson [15], for example, estimated the ligand-polarization contribution in two-photon processes. Sztucki and Strek [16,17], expanding Reid and Richardson's idea, proposed the third-order contributions to the TPA processes from the static and dynamic coupling mechanisms developed within the independent systems model. Smentek-Mielczarek et al. [18,19] examined the third-order electron-correlation and crystal-field contributions to the two-photon amplitude within the framework of double perturbation theory [20,21].

All of the mechanisms mentioned above have been applied to intra-configurational two-photon transitions, where the initial and final states both belong to the f^N configurations and the two-photon processes are therefore allowed because of the parity rule. TPA transitions from the $4f^N$ to the $4f^{N-1}5d$ have also been observed for Ce^{3+} ions in various crystals [22-26]. These transitions are parity forbidden in the second-order and thus are directly the effect of third-order contributions. A theoretical description of the cross section of the two-photon f-d transitions based on the perturbation coming from the rank-one component of the crystal field was first proposed by Gayen et al [24]. Their calculated polarization anisotropy for the zero-phonon transition in Ce^{3+}:CaF_2, however, were far from the observed values. Using the second

quantization techniques, Leavitt [27] later derived the static and dynamic contributions to the TPA cross section and applied the results to the lowest 4f->5d two-photon transition in Ce^{3+}:CaF_2. Leavitt's calculated values were closer to the experiment, compared with Gayen et al's value, but were still not satisfactory. Expanding the TPA cross-section theory to include arbitrary polarizations in spherical polar coordinates, Makhanek et al [28,29] showed that good agreement between calculated and observed values for the polarization anisotropy might be obtained if the third-rank component of the crystal field were the dominant term. Sztucki and Strek [17], using the independent systems model to describe the influence of crystal field and ligand polarization on the f-d two-photon transitions, obtained a cross-section value of the same magnitude as the experimental one, if the value of the magnitude of the crystal-field component $B_0^{(1)}$ was properly chosen. From the values obtained for the polarization anisotropy, they concluded that the first-rank component of the crystal field should be the dominant term, in contradiction to the Makhanek et al's result. Finally, using the symmetry adaptation techniques developed by Kibler [30,31], Daoud and Kibler developed a formalism to determine the intensity of interconfigurational two-photon transitions. The model was then applied to the case of the Ce^{3+} ion in CaF_2 and $LuPO_4$ with reasonable agreement with observed data [32].

Except the derivations proposed by Makhanek et al [28,29] and Daoud et al [32], all of two-photon studies up to the fourth order mentioned above have been applied in the framework of the Cartesian coordinates or circular polar coordinates. The general study of polarization dependence behavior of the thirty two crystallographic

point groups was initiated by Inoue and Toyozawa [33]. Bader and Gold [34] later revised the theory and tabulated the results for TPA transitions between Stark levels. These are the most general polarization dependence formulas for two-photon intensities, in which the polarization vectors are described in the spherical polar coordinates. The major disadvantage of the Bader and Gold formalism is the presence of a number of phenomenological parameters, which in some cases weaken the predictive power.

In addition to the second-order theory of polarization dependence of TPA cross-sections developed by Manakhek [28,29], Kibler, Gâcon and coworkers [33-40] have recently published a number of results in which the polarization dependence of the reported intra-configurational two-photon Stark transitions were compared with a new theory which made use of the symmetry adaptation technique and of the Judd-Ofelt approximation. The Manakhek's and Gâcon -Kibler's formalisms are generally more useful than that of Bader-Gold's formalism, since in the former cases the two-photon intensities between Stark-levels and their corresponding polarization dependence expressions for a particular system contain only one or two parameters, which in turn can be further evaluated if the radial factors are known. Their polarization dependence expressions are in good agreement with the more general forms given by Bader and Gold, once the parameters' values in the latter's expression are appropriately assigned. The major disadvantage of the Gâcon-Kibler theory is that its computation appears to be complicated. As a consequence, the theory has been applied to only a few particular systems, rather than being tabulated for the 32 crystallographic point groups as did Bader and Gold.

In this chapter another formalism for obtaining the polarization dependent behavior of two-photon intensities between the Stark levels is developed. The general expressions for the polarization dependent two-photon intensities are tabulated for the 32 point groups, whose parameters can be calculated explicitly when applied to a particular system. The proposed theory is derived from a formalism in which the two-photon scattering tensors in polar coordinates are expressed in terms of the irreducible representation of the scattering tensors. The explicit expressions for the irreducible scattering tensors can be obtained by applying the second-order theory of Axe for the TPA processes within the framework of the electric-dipole-interaction perturbation theory [43-45] and/or by expanding perturbation theories which include higher-order mechanisms [10-21]. Since Axe's theory is based on the Judd-Ofelt approximation, the theory provides a stringent test for the Judd-Ofelt theory. When applied to a given system, the expressions for the polarization dependent behavior of the TPA transition intensities are identical to those of Gâcon et al. The calculation using this proposed method is, however, much more straightforward than that of Gâcon et al [36,38]. The second-order intensity calculations using this new method are given in the electronic Raman framework, but can be applied to the TPA with little modification.

Intensity calculations involving the irreducible scattering tensors in the proposed theory are straightforward and have been routinely practiced in ERS work. When explicit forms for the irreducible scattering tensors are not available, such as in the case of Raman phonon scattering, the table of the polarization dependent behavior for two-photon intensities are particularly useful, since this table was derived using the group-

theoretical selection rules for two photon transitions and the special properties of the second-rank irreducible tensors without eliciting its explicit forms for a particular transition.

By use of the irreducible representation of the scattering tensors, the proposed polarization dependence theory can be readily extended to include higher order interactions contributing to two-photon transition intensities. Using the standard tensor coupling technique, the explicit polarization dependence formulas for the third- and fourth- order contributions to the second-order two-photon intensities are obtained for the first time. The third-order contributions including the spin-orbit interaction, crystal-field interaction are discussed. The fourth-order treatment includes the spin-orbit and crystal field interactions. The polarization dependence of other higher-order interactions can be applied in the same manner. In addition the polarization dependence expressions for inter-configurational two-photon transition intensities are also given.

2.2 Polarization Dependence - Second-Order Treatment

2.2.1 Electronic Raman Scattering Theory

We employ the conventional set up for the two-photon processes. In the ERS experiment, one beam is incident on the crystal, and the scattered light is collected at 90° with respect to the incident beam. In the TPA experiment, two light beams are incident on the crystal. The z-axis is assumed to be parallel to the z-axis of the center ion. For a uniaxial crystal, the z-axis is the crystallographic c-axis. In the TPA case we

define by $\hat{\mathbf{e}}_1$ and $\hat{\mathbf{e}}_2$ the polarization unit vectors of the first and second beams, respectively. In the ERS case we use the commonly employed notation [43-45] in which $\hat{\mathbf{e}}_1$ denotes the polarization of the incident beam and $\hat{\mathbf{e}}_2$ the polarization of the scattered light.

The ERS amplitude for a transition from state |i> to state |f> is given by [46]

$$(\alpha_{21})_{if} = -\sum_j \left[\frac{\langle i|\hat{\mathbf{e}}_2 \cdot \mathbf{D}|j\rangle\langle j|\hat{\mathbf{e}}_1 \cdot \mathbf{D}|f\rangle}{\hbar\omega_j - \hbar\omega_1} + \frac{\langle i|\hat{\mathbf{e}}_1 \cdot \mathbf{D}|j\rangle\langle j|\hat{\mathbf{e}}_2 \cdot \mathbf{D}|f\rangle}{\hbar\omega_j + \hbar\omega_2} \right], \tag{2.1}$$

where i,j, and f are the respective initial, intermediate, and final Stark levels of the two-photon transition, 1 and 2 represent the polarizations of the incident and scattered photons [47], $\hat{\mathbf{e}}_i \cdot \mathbf{D}$ is the electric dipole operator of the ith polarization vector, $\hbar\omega_1$, $\hbar\omega_2$ are the energies of the incident and scattered photons, and $\hbar\omega_j$ are the energies of the intermediate Stark levels.

The TPA amplitude for a transition from state |i> to state |f> is given by the second-order tensor:

$$(\alpha_{21})_{if} = -\sum_j \left[\frac{\langle i|\hat{\mathbf{e}}_2 \cdot \mathbf{D}|j\rangle\langle j|\hat{\mathbf{e}}_1 \cdot \mathbf{D}|f\rangle}{\hbar\omega_j - \hbar\omega_1} + \frac{\langle i|\hat{\mathbf{e}}_1 \cdot \mathbf{D}|j\rangle\langle j|\hat{\mathbf{e}}_2 \cdot \mathbf{D}|f\rangle}{\hbar\omega_j - \hbar\omega_2} \right]. \tag{2.2}$$

The result for the TPA intensity is the same as that for the ERS intensity, with a change of sign for $\hbar\omega_2$ in the denominator in the second term of expression (2.2). We thus only consider here the ERS theory and give the modification for the TPA theory at the end.

In the second-order quantized form the electric-dipole operator for a transition between the shell (nl) and the shell (n'l') can be expressed as [1]

$$\hat{\mathbf{e}}\cdot\mathbf{D}=\hat{\mathbf{e}}\cdot\sum_i \bar{\mathbf{r}}_i=(-1)^{l'}(2)^{\frac{1}{2}}\left[\frac{(2l+1)(2l'+1)}{3}\right]^{\frac{1}{2}}\begin{pmatrix} l & 1 & l' \\ 0 & 0 & 0 \end{pmatrix}\langle nl|r|n'l'\rangle\hat{\mathbf{e}}\cdot\left[(\mathbf{a}^{\dagger}\mathbf{b})^{(01)}-(\mathbf{b}^{\dagger}\mathbf{a})^{(01)}\right], \tag{2.3}$$

where i denotes the electron participating in the transition, $\hat{\mathbf{e}}$ is the unit polarization vector, $\mathbf{D}$ is the sum $\sum_i \bar{\mathbf{r}}_i$ of the position vectors for all elecrons i in the nl configuration [48], $\mathbf{a}^{\dagger}$ and $\mathbf{a}$ are the creation and annihilation operators for the (nl) shell, and $\mathbf{b}^{\dagger}$ and $\mathbf{b}$ are those for the (n'l') shell. This expression results from the rules obtained by Judd [49] for finding the second quantized form of an atomic one-particle operator. For an initial and a final state belonging to the (nf) shell and intermediate states belonging to the (n'l') shell $\mathbf{a}^{\dagger}$ and $\mathbf{a}$ become $\mathbf{f}^{\dagger}$ and $\mathbf{f}$, respectively, and l = 3. The radius operator $\mathbf{D}$ becomes

$$\mathbf{D}=(2)^{\frac{1}{2}}\left[\frac{7(2l'+1)}{3}\right]^{\frac{1}{2}}\begin{pmatrix} 3 & 1 & l' \\ 0 & 0 & 0 \end{pmatrix}\times\langle nf|r|n'l'\rangle\left[(\mathbf{f}^{\dagger}\mathbf{b})^{(01)}-(\mathbf{b}^{\dagger}\mathbf{f})^{(01)}\right]. \tag{2.4}$$

Substituting (2.4) into (2.2) we get

$$(\alpha_{21})_{fi}=-\sum_{n'l'}C(n'l')\sum_j\left[\frac{\langle i|[(\mathbf{f}^{\dagger}\mathbf{b})^{(01)}-(\mathbf{b}^{\dagger}\mathbf{f})^{(01)}].\mathbf{e}_2{}^{(01)}|j\rangle\langle j|[(\mathbf{f}^{\dagger}\mathbf{b})^{(01)}-(\mathbf{b}^{\dagger}\mathbf{f})^{(01)}].\mathbf{e}_1{}^{(01)}|f\rangle}{\hbar\omega_j-\hbar\omega_1}\right.$$
$$\left.+\frac{\langle i|[(\mathbf{f}^{\dagger}\mathbf{b})^{(01)}-(\mathbf{b}^{\dagger}\mathbf{f})^{(01)}].\mathbf{e}_1{}^{(01)}|j\rangle\langle j|[(\mathbf{f}^{\dagger}\mathbf{b})^{(01)}-(\mathbf{b}^{\dagger}\mathbf{f})^{(01)}].\mathbf{e}_2{}^{(01)}|f\rangle}{\hbar\omega_j+\hbar\omega_2}\right], \tag{2.5}$$

where $\mathbf{e}_i$ (i = 1,2) denotes the unit polarization vector, j denotes any excited state different from the initial and final states, and

$$C(n'l') = \left[\frac{14(2l'+1)}{3}\right] \times \begin{pmatrix} 3 & 1 & l' \\ 0 & 0 & 0 \end{pmatrix}^2 \times \langle nf|r|n'l'\rangle^2. \tag{2.6}$$

The Judd-Ofelt closure approximation [2,3] is now applied:

$$\begin{aligned}(\alpha_{21})_{fi} \approx \sum_{n'l'} C(n'l')\Big[& \frac{1}{E_{n'l'} - \hbar\omega_1}\langle i|[\mathbf{e}_2^{(01)}.(\mathbf{f}^\dagger\mathbf{b})^{(01)}][\mathbf{e}_1^{(01)}.(\mathbf{b}^\dagger\mathbf{f})^{(01)}]|f\rangle \\ & + \frac{1}{E_{n'l'} + \hbar\omega_2}\langle i|[\mathbf{e}_1^{(01)}.(\mathbf{f}^\dagger\mathbf{b})^{(01)}][\mathbf{e}_2^{(01)}.(\mathbf{b}^\dagger\mathbf{f})^{(01)}]|f\rangle\Big],\end{aligned} \tag{2.7}$$

where $E_{n'l'}$ is the average energy of the n'l' configuration.

Through standard recoupling procedure we obtain the familiar result for the scattering tensor [44, 50]:

$$\begin{aligned}\alpha_{21} = & \sum_{nf^{N-1}n'l'} 7(2l'+1)\begin{pmatrix} 3 & 1 & l' \\ 0 & 0 & 0 \end{pmatrix}^2 \langle nf|r|n'l'\rangle^2 \\ & \times \sum_t (2t+1)^{\frac{1}{2}} \begin{Bmatrix} 1 & 3 & l' \\ 3 & 1 & t \end{Bmatrix} \left[\frac{1}{E_{n'l'} - \hbar\omega_1} + \frac{(-1)^t}{E_{n'l'} + \hbar\omega_2}\right] (\mathbf{e}_2\mathbf{e}_1)^{(t)}.\mathbf{U}^{(t)},\end{aligned} \tag{2.8}$$

where $\mathbf{U}^{(t)}$ is the unit tensor of rank t.

In equation (2.8), the only non-vanishing terms occur for t = 0, 1 and 2. Other values of t vanish during the recoupling procedure.

If we let

$$F_t = (-1)^t \sum_{nf^{N-1}n'l'} 7(2l'+1)\begin{pmatrix} 3 & 1 & l' \\ 0 & 0 & 0 \end{pmatrix}^2 \langle nf|r|n'l'\rangle^2$$
$$\times (2t+1)^{\frac{1}{2}} \begin{Bmatrix} 1 & 3 & l' \\ 3 & 1 & t \end{Bmatrix} \left[\frac{1}{E_{n'l'} - \hbar\omega_1} + \frac{(-1)^t}{E_{n'l'} + \hbar\omega_2} \right] \tag{2.9}$$

then $\alpha_{21} = \sum_t (-1)^t F_t (\mathbf{e}_2\mathbf{e}_1)^{(t)} \cdot \mathbf{U}^{(t)}$. (2.10)

The F_t parameter, first introduced by Koningstein and Mortensen [43], can be treated as a phenomenological constant, which is dependent only on the energy of the n'l' configurations and the radial overlap between the n'l' and nl configurations. For the TPA transitions the expression of F_t is the same as in (2.9), with the minus sign in front of $\hbar\omega_2$.

For intensity calculations the ERS tensors in the Cartesian coordinates are expressed in terms of the irreducible representation of the spherical scattering tensors defined by Mortensen and Koningstein [43] :

$$
\begin{cases}
\alpha_{xx} = -\frac{1}{\sqrt{3}}\alpha_0^{(0)} + \frac{1}{2}\alpha_2^{(2)} + \frac{1}{2}\alpha_{-2}^{(2)} - \frac{1}{\sqrt{6}}\alpha_0^{(2)} \\
\alpha_{yy} = -\frac{1}{\sqrt{3}}\alpha_0^{(0)} - \frac{1}{2}\alpha_2^{(2)} - \frac{1}{2}\alpha_{-2}^{(2)} - \frac{1}{\sqrt{6}}\alpha_0^{(2)} \\
\alpha_{zz} = -\frac{1}{\sqrt{3}}\alpha_0^{(0)} + \frac{2}{\sqrt{6}}\alpha_0^{(2)} \\
\alpha_{xy} = -i\frac{1}{\sqrt{2}}\alpha_0^{(1)} - i\frac{1}{2}\alpha_2^{(2)} + i\frac{1}{2}\alpha_{-2}^{(2)} \\
\alpha_{xz} = -\frac{1}{2}\alpha_1^{(1)} - \frac{1}{2}\alpha_{-1}^{(1)} - \frac{1}{2}\alpha_1^{(2)} + \frac{1}{2}\alpha_{-1}^{(2)} \\
\alpha_{yz} = i\frac{1}{2}\alpha_1^{(1)} - i\frac{1}{2}\alpha_{-1}^{(1)} + i\frac{1}{2}\alpha_1^{(2)} + i\frac{1}{2}\alpha_{-1}^{(2)} \\
\alpha_{yx} = i\frac{1}{\sqrt{2}}\alpha_0^{(1)} - i\frac{1}{2}\alpha_2^{(2)} + i\frac{1}{2}\alpha_{-2}^{(2)} \\
\alpha_{zx} = \frac{1}{2}\alpha_1^{(1)} + \frac{1}{2}\alpha_{-1}^{(1)} - \frac{1}{2}\alpha_1^{(2)} + \frac{1}{2}\alpha_{-1}^{(2)} \\
\alpha_{zy} = -i\frac{1}{2}\alpha_1^{(1)} + i\frac{1}{2}\alpha_{-1}^{(1)} + i\frac{1}{2}\alpha_1^{(2)} + i\frac{1}{2}\alpha_{-1}^{(2)},
\end{cases}
\tag{2.11}
$$

where the irreducible spherical scattering tensor has the simple form (see Appendix A)

$$\alpha_q^{(t)} = F_t \mathbf{U}_q^{(t)}. \tag{2.12}$$

We now can determine the ERS amplitude for the transition between intermediate coupling states |i> and |f>. We write the initial state as

$$|i\rangle = \sum_{\alpha SLJJ_z} a(i; nf^N \alpha SLJJ_z)|nf^N \alpha SLJJ_z\rangle, \tag{2.13}$$

and the final state is written

$$|f\rangle = \sum_{\alpha' S' L' J' J'_z} a'(f; nf^N \alpha' S' L' J' J'_z)|nf^N \alpha' S' L' J' J'_z\rangle. \tag{2.14}$$

The ERS amplitude for the transition between states |i> and |f> is given in terms of the matrix elements of the irreducible scattering tensor operators:

$$\langle i|\alpha_q^{(t)}|f\rangle = F_t \sum_{\alpha SLJJ_z} \sum_{\alpha' S' L' J' J'_z} a(i;nf^N\alpha SLJJ_z)a'(f;nf^N\alpha' S' L' J' J'_z)$$
$$\times \langle nf^N\alpha SLJJ_z|\mathbf{U}_q^{(t)}|nf^N\alpha' S' L' J' J_z'\rangle, \tag{2.15}$$

where

$$\langle nf^N\alpha SLJJ_z|\mathbf{U}_q^{(t)}|nf^N\alpha' S' L' J' J_z'\rangle =$$
$$(-1)^{2J+S+L'+t-J_z}[(2J'+1)(2J+1)]^{\frac{1}{2}}\begin{pmatrix} J & t & J' \\ -J_z & q & J_z' \end{pmatrix}\begin{Bmatrix} L & J & S \\ J' & L' & t \end{Bmatrix}\langle SL\|\mathbf{U}^{(t)}\|SL'\rangle\delta(S,S'). \tag{2.16}$$

The values of the reduced matrix elements $\langle SL\|\mathbf{U}^{(t)}\|SL'\rangle$ are tabulated by Nielson and Koster [8]. The Raman amplitude can be readily evaluated once the coefficients of the initial and final intermediate coupling wavefunctions are known. These wavefunctions can be obtained from the crystal-field fits which are based on absorption and/or fluorescence spectra.

The scattering intensity is proportional to the square of the absolute values of the scattering tensor:

$$(I_{21})_{fi} = C(\omega_O + \omega_{fi})^4|(\alpha_{21})_{fi}|^2, \tag{2.17}$$

where C is a constant, ω_0 is the laser's frequency and $\omega_{fi} = \omega_f - \omega_i$ is the frequency corresponding to the energy difference between the initial and final states [51].

These equations are generally used in ERS calculations, where the intensities are measured in the Cartesian coordinates. We can now express these equations in polar coordinates and obtain the polarization dependent forms for TPA and ERS intensities.

2.2.2 Polarization Dependence

We consider the general case in which both polarization unit vectors are oriented in an arbitrary direction and independent of each other. In spherical coordinates a unit polarization vector is written

$$\hat{\mathbf{e}} = \hat{\mathbf{z}}\cos\theta + \hat{\mathbf{y}}\sin\theta\sin\varphi + \hat{\mathbf{x}}\sin\theta\cos\varphi. \tag{2.18}$$

By substitution of (2.18) into a general expression of the two-photon scattering tensor α_{21} (e.g. equation (2.5)), it can be shown that the scattering tensor expressed in the polar coordinates has the form:

$$\begin{aligned}\alpha_{e_2e_1} = {} & \alpha_{zz}\cos\theta_2\cos\theta_1 + \alpha_{yy}\sin\theta_2\sin\theta_1\sin\varphi_2\sin\varphi_1 + \alpha_{xx}\sin\theta_2\sin\theta_1\cos\varphi_2\cos\varphi_1 \\ & + \alpha_{zy}\cos\theta_2\sin\theta_1\sin\varphi_1 + \alpha_{yz}\sin\theta_2\sin\varphi_2\cos\theta_1 \\ & + \alpha_{zx}\cos\theta_2\sin\theta_1\cos\varphi_1 + \alpha_{xz}\sin\theta_2\cos\varphi_2\cos\theta_1 \\ & + \alpha_{yx}\sin\theta_2\sin\varphi_2\sin\theta_1\cos\varphi_1 + \alpha_{xy}\sin\theta_2\cos\varphi_2\sin\theta_1\sin\varphi_1,\end{aligned} \tag{2.19}$$

or, in a more compact form,

$$\begin{aligned}\alpha_{e_2e_1} = {} & n_2n_1\alpha_{zz} + m_2m_1\alpha_{yy} + l_2l_1\alpha_{xx} + n_2m_1\alpha_{zy} + m_2n_1\alpha_{yz} \\ & + n_2l_1\alpha_{zx} + l_2n_1\alpha_{xz} + m_2l_1\alpha_{yx} + l_2m_1\alpha_{xy},\end{aligned} \tag{2.20}$$

where we have used the same notation as given in Inoue and Toyozawa [33], in which

$$(l, m, n) = (\sin\theta\cos\varphi, \sin\theta\sin\varphi, \cos\theta). \tag{2.21}$$

In terms of the irreducible spherical scattering tensors:

$$
\begin{aligned}
\alpha_{e_2 e_1} = & (-\frac{1}{\sqrt{3}}\alpha_0^{(0)} + \frac{2}{\sqrt{6}}\alpha_0^{(2)}) n_2 n_1 \\
& + (-\frac{1}{\sqrt{3}}\alpha_0^{(0)} - \frac{1}{2}\alpha_2^{(2)} - \frac{1}{2}\alpha_{-2}^{(2)} - \frac{1}{\sqrt{6}}\alpha_0^{(2)}) m_2 m_1 \\
& + (-\frac{1}{\sqrt{3}}\alpha_0^{(0)} + \frac{1}{2}\alpha_2^{(2)} + \frac{1}{2}\alpha_{-2}^{(2)} - \frac{1}{\sqrt{6}}\alpha_0^{(2)}) l_2 l_1 \\
& + (-i\frac{1}{2}\alpha_1^{(1)} + i\frac{1}{2}\alpha_{-1}^{(1)} + i\frac{1}{2}\alpha_1^{(2)} + i\frac{1}{2}\alpha_{-1}^{(2)}) n_2 m_1 \\
& + (i\frac{1}{2}\alpha_1^{(1)} - i\frac{1}{2}\alpha_{-1}^{(1)} + i\frac{1}{2}\alpha_1^{(2)} + i\frac{1}{2}\alpha_{-1}^{(2)}) m_2 n_1 \\
& + (\frac{1}{2}\alpha_1^{(1)} + \frac{1}{2}\alpha_{-1}^{(1)} - \frac{1}{2}\alpha_1^{(2)} + \frac{1}{2}\alpha_{-1}^{(2)}) n_2 l_1 \\
& + (-\frac{1}{2}\alpha_1^{(1)} - \frac{1}{2}\alpha_{-1}^{(1)} - \frac{1}{2}\alpha_1^{(2)} + \frac{1}{2}\alpha_{-1}^{(2)}) l_2 n_1 \\
& + (i\frac{1}{\sqrt{2}}\alpha_0^{(1)} - i\frac{1}{2}\alpha_2^{(2)} + i\frac{1}{2}\alpha_{-2}^{(2)}) m_2 l_1 \\
& + (-i\frac{1}{\sqrt{2}}\alpha_0^{(1)} - i\frac{1}{2}\alpha_2^{(2)} + i\frac{1}{2}\alpha_{-2}^{(2)}) l_2 m_1 .
\end{aligned}
\tag{2.22}
$$

The scattering tensor can be rewritten

$$
\begin{aligned}
\alpha_{e_2e_1} = & (-\frac{1}{\sqrt{3}})[n_2n_1 + m_2m_1 + l_2l_1]\alpha_0^{(0)} \\
& + \frac{1}{\sqrt{6}}[2n_2n_1 - m_2m_1 - l_2l_1]\alpha_0^{(2)} \\
& + \frac{1}{2}[(n_2m_1 + m_2n_1)i - (n_2l_1 + l_2n_1)]\alpha_1^{(2)} \\
& + \frac{1}{2}[(n_2m_1 + m_2n_1)i + (n_2l_1 + l_2n_1)]\alpha_{-1}^{(2)} \\
& + \frac{1}{2}[(l_2l_1 - m_2m_1) - (l_2m_1 + m_2l_1)i]\alpha_2^{(2)} \\
& + \frac{1}{2}[(l_2l_1 - m_2m_1) + (l_2m_1 + m_2l_1)i]\alpha_{-2}^{(2)} \\
& + \frac{i}{\sqrt{2}}[m_2l_1 - l_2m_1]\alpha_0^{(1)} \\
& + \frac{1}{2}[(m_2n_1 - n_2m_1)i + (n_2l_1 - l_2n_1)]\alpha_1^{(1)} \\
& + \frac{1}{2}[(-m_2n_1 + n_2m_1)i + (n_2l_1 - l_2n_1)]\alpha_{-1}^{(1)}.
\end{aligned}
\tag{2.23}
$$

or, in a more compact form,

$$
\alpha_{21} = \sum_{t=0}^{2} \sum_{q=-t}^{t} \lambda_q^t \alpha_q^{(t)} , \tag{2.24}
$$

where the polarization dependent coefficients λ_q^t's are defined by

$$\lambda_0^0 = -\frac{1}{\sqrt{3}}[n_2 n_1 + m_2 m_1 + l_2 l_1]$$

$$\lambda_{-1}^1 = \frac{1}{2}[(-m_2 n_1 + n_2 m_1)i + (n_2 l_1 - l_2 n_1)]$$

$$\lambda_0^1 = \frac{i}{\sqrt{2}}[m_2 l_1 - l_2 m_1]$$

$$\lambda_1^1 = \frac{1}{2}[(m_2 n_1 - n_2 m_1)i + (n_2 l_1 - l_2 n_1)]$$

$$\lambda_{-2}^2 = \frac{1}{2}[(l_2 l_1 - m_2 m_1) + (l_2 m_1 + m_2 l_1)i]$$

$$\lambda_{-1}^2 = \frac{1}{2}[(n_2 m_1 + m_2 n_1)i + (n_2 l_1 + l_2 n_1)]$$

$$\lambda_0^2 = \frac{1}{\sqrt{6}}[2n_2 n_1 - m_2 m_1 - l_2 l_1]$$

$$\lambda_1^2 = \frac{1}{2}[(n_2 m_1 + m_2 n_1)i - (n_2 l_1 + l_2 n_1)]$$

$$\lambda_2^2 = \frac{1}{2}[(l_2 l_1 - m_2 m_1) - (l_2 m_1 + m_2 l_1)i]. \tag{2.25}$$

Putting (2.12) into (2.24) we obtain the polarization dependence expression for second-order two-photon transition intensities:

$$(\alpha_{21})^{2nd} = \sum_{t=0}^{2} \sum_{q=-t}^{t} \lambda_q^t F_t \mathbf{U}_q^{(t)} . \tag{2.26}$$

Equation (2.24) is the most general polarization dependence expression of two-photon transition intensities between Stark levels. Further applications of (2.24) such as in the case of circular polarization and with various functional forms of $\alpha_q^{(t)}$ can be found in Appendices B and C. For clarity purpose we will use the symbol α_q^t to denote the matrix element of the irreducible scattering tensor $\alpha_q^{(t)}$. For a particular transition between Stark levels only certain α_q^t are non zero, according to the Raman activity of the group corresponding to the Stark levels [51,52]. In particular, the following

comments apply. First, since $\alpha_0^{(0)}$ is proportional to $\mathbf{U}_0^{(0)}$ in the second order approximation, where $\mathbf{U}_0^{(0)}$ is a number operator proportional to $-N/(14)^{1/2}$ for the f^N configuration, α_0^0 is exactly zero for different initial and final states used in Raman transitions. We therefore will omit all α_0^0's for second-order calculations. As will be explained in the next section on the third-order theory of two-photon intensities, the third-order contribution associated with the $\alpha_0^{(0)}$ term is not always zero, but in fact might be dominant for certain transitions. One must include the $\alpha_0^{(0)}$ term in the third-order calculation in order to obtain meaningful results. Secondly, in the case of TPA where the two beams come from the same source, the $\alpha_q^{(1)}$ terms vanish.

Table 2.1 gives the angular dependence functions for ERS and TPA transitions for all 32 crystallographic point groups. In table 2.1, we have labeled the irreducible representations by the usual symbols for molecular representations, in order to facilitate comparison with Bader and Gold [34]. In RE intensity calculations, however, the irreducibe representations of a point group G often appear [53] as Γ_i, where i denotes the ith representation of group G. Only transitions of the type $\Gamma_1 <-> \Gamma_j$, where Γ_1 is the totally symmetric representation and Γ_j any irreducible representation, are considered. Other transitions can be calculated using the fact that the triple product $\Gamma_{\psi_f} \otimes \Gamma_{\alpha_{21}} \otimes \Gamma_{\psi_i}$ of any of the 32 point groups must contain the totally symmetric representation. The three terms appearing in the triple product are the irreducible representations of the final state, the Raman tensor, and the initial state. For a transition to an n-fold degenerate level the total intensity is proportional to the sum of the squares of each scattering amplitude corresponding to each degenerate state. In table 2.1 only contributions from

one of the degenerate levels is listed. The total contribution is the sum of each contribution coming from one of the n-fold degenerate levels. If the states of these levels are Kramers states, the two-photon contribution from an initial Kramers state (Ψ_i) to a final Kramers state(Ψ_f) is different from the two-photon contribution from (Ψ_i) to the Kramers conjugate state of the final state (Ψ_f^K), i.e. $|\alpha_{21}(\Psi_i \rightarrow \Psi_f)|^2 \neq |\alpha_{21}(\Psi_i \rightarrow \Psi_f^K)|^2$; the two-photon contribution from Ψ_i to Ψ_f is however exactly equal to the two-photon contribution from Ψ_i^K to Ψ_f^K, i.e. $|\alpha_{21}(\Psi_i \rightarrow \Psi_f)|^2 = |\alpha_{21}(\Psi_i^K \rightarrow \Psi_f^K)|^2$. For transitions between non-Kramers state, the TPA contributions from a singlet (Ψ_i) to each state of a doubly degenerate level (Ψ_{fx} or Ψ_{fy}) are equal, i.e. $|\alpha_{21}(\Psi_i \rightarrow \Psi_{fx})|^2 = |\alpha_{21}(\Psi_i \rightarrow \Psi_{fy})|^2$ (see proof in Appendix D).

It can be noted that table 2.1 agrees with Bader and Gold [34], since the expression for the polarization dependence of the intensities of transitions between Stark levels only depends on the Cartesian Raman tensors and their corresponding irreducible spherical tensors whose non-zero values are predicted by group theory. No approximation has been required to derive the relationship between the intensities and the general form of the irreducible spherical Raman tensors $\alpha_q^{(t)}$, which replace the parameters λ_i's in Bader and Gold's theory. The explicit second-order expressions for $\alpha_q^{(t)}$ in (2.26), in terms of F_t and $\mathbf{U}_q^{(t)}$, however, are derived using the Judd-Ofelt-Axe theory. Since $\mathbf{U}_q^{(t)}$ can be calculated for a particular transition, the expression for the intensities for two photon processes in terms of F_t provides a stringent test for the Axe theory. In the case of TPA from the same source only F_2 would appear in the expression

for intensities. Thus relative intensities between Stark levels can be calculated and compared with experimental values. For a single two-photon transition the polarization dependence of the intensities on θ and φ can be directly compared with experimental data.

Another test for the second-order theory of Axe may come from the ratio F_1/F_2, as first demonstrated by Becker et al. in the case of $TmPO_4$ and $ErVO_4$ [54]. Using Cartesian coordinates it is common to obtain ERS intensities corresponding to at most four polarization states. Asymmetry [44] can be measured by the ratio of two of these intensities, I_{XZ} (or I_{YZ}) and I_{ZX} (or I_{ZY}), from which the value of F_1/F_2 can be obtained. From the Raman scattering intensities of light with incident and scattered polarizations being arbitrarily varied, a better fit for the ratio F_1/F_2 may be obtained. Thus this new analysis method should provide a more reliable value for the ratio F_1/F_2.

In general the two-photon scattering tensor α_{21} is related to the irreducible representation of the scattering tensor $\alpha_q^{(t)}$ by the relation

$$(\alpha_{21}) = \sum_{t=0}^{2} \sum_{q=-t}^{t} (-1)^{t+q} (\mathbf{e}_2\mathbf{e}_1)^t_{-q} (\alpha_q^{(t)}) , \qquad (2.27)$$

where $(\mathbf{e}_2\mathbf{e}_1)^t_{-q}$ is the coupled form of the polarization unit vectors. Equation (2.27) was derived by the use of the standard method of tensor operators. The complete derivation is given in Appendix B. The expression for the TPA amplitude in the case of circular polarization incident beams is also given in Appendix B. We will use this tensor coupling method when we derive the polarization dependence expressions for third-order and fourth-order terms involving spin-orbit and crystal field interactions in the

next section. The same procedure can readily be applied to other third-order interactions such as ligand-polarization [15-17] and electron correlation [18-21]. The polarization dependence expression for interconfigurational TPA intensities will also be discussed in the next section.

Table 2.1. Angular-dependence functions for RE ERS and TPA transitions. The symbols are defined in the text.

$C_1 \quad C_i$

$$A \leftrightarrow A \quad A_g \leftrightarrow A_g \quad |(-\frac{1}{\sqrt{3}})[n_2n_1 + m_2m_1 + l_2l_1]\alpha_0^0 + (-\frac{1}{\sqrt{6}})[-2n_2n_1 + m_2m_1 + l_2l_1]\alpha_0^2$$

$$+\frac{1}{2}[(n_2m_1 + m_2n_1)i - (n_2l_1 + l_2n_1)]\alpha_1^2 + \frac{1}{2}[(n_2m_1 + m_2n_1)i + (n_2l_1 + l_2n_1)]\alpha_{-1}^2$$

$$+\frac{1}{2}[(l_2l_1 - m_2m_1) - (l_2m_1 + m_2l_1)i]\alpha_2^2 + \frac{1}{2}[(l_2l_1 - m_2m_1) + (l_2m_1 + m_2l_1)i]\alpha_{-2}^2$$

$$+\frac{i}{2}[m_2l_1 - l_2m_1]\alpha_0^1 + \frac{1}{2}[(m_2n_1 - n_2m_1)i + (n_2l_1 - l_2n_1)]\alpha_1^1$$

$$+\frac{1}{2}[(-m_2n_1 + n_2m_1)i + (n_2l_1 - l_2n_1)]\alpha_{-1}^1|^2$$

$C_2 \quad C_s \quad C_{2h}$

$$A \leftrightarrow A \quad A \leftrightarrow A \quad A_g \leftrightarrow A_g \quad |(-\frac{1}{\sqrt{3}})[n_2n_1 + m_2m_1 + l_2l_1]\alpha_0^0 + (-\frac{1}{\sqrt{6}})[-2n_2n_1 + m_2m_1 + l_2l_1]\alpha_0^2$$

$$+\frac{i}{2}[m_2l_1 - l_2m_1]\alpha_0^1 + \frac{1}{2}[(l_2m_1 + m_2l_1)i](\alpha_{-2}^2 - \alpha_2^2) + \frac{1}{2}[l_2l_1 + m_2m_1](\alpha_{-2}^2 + \alpha_2^2)|^2$$

$$A \leftrightarrow B \quad A' \leftrightarrow A'' \quad A_g \leftrightarrow B_g \quad |n_2m_1(\frac{\alpha_1^2 - \alpha_1^1}{2}) + m_2n_1(\frac{\alpha_1^2 + \alpha_1^1}{2})|^2 + |n_2l_1(\frac{\alpha_1^2 - \alpha_1^1}{2}) + l_2n_1(\frac{\alpha_1^2 + \alpha_1^1}{2})|^2$$

$$+|n_2m_1(\frac{\alpha_{-1}^2 + \alpha_{-1}^1}{2}) + m_2n_1(\frac{\alpha_{-1}^2 - \alpha_{-1}^1}{2})|^2 + |n_2l_1(\frac{\alpha_{-1}^2 + \alpha_{-1}^1}{2}) + l_2n_1(\frac{\alpha_{-1}^2 - \alpha_{-1}^1}{2})|^2$$

C_3, C_{3i}

$$A \leftrightarrow A \quad |(-\frac{1}{\sqrt{3}})[n_2n_1 + m_2m_1 + l_2l_1]\alpha_0^0 + (-\frac{1}{\sqrt{6}})[-2n_2n_1 + m_2m_1 + l_2l_1]\alpha_0^2 + \frac{i}{2}[m_2l_1 - l_2m_1]\alpha_0^1|^2$$

$$A \leftrightarrow E \quad |\frac{1}{2}[n_2l_1 - l_2n_1](\alpha_{-1}^1 + \alpha_1^1) + \frac{1}{2}[n_2l_1 + l_2n_1](\alpha_{-1}^2 - \alpha_1^2)$$

$$+\frac{1}{2}[l_2l_1 - m_2m_1](\alpha_2^2 + \alpha_{-2}^2)|^2 + |\frac{1}{2}[l_2m_1 + m_2l_1](\alpha_{-2}^2 - \alpha_2^2)$$

$$+\frac{1}{2}[n_2m_1 - m_2n_1](\alpha_{-1}^1 - \alpha_1^1) + \frac{1}{2}[n_2m_1 + m_2n_1](\alpha_1^2 + \alpha_{-1}^2)|^2$$

C_4, C_{4h}, S_4

$A \leftrightarrow A$ $\quad |(-\frac{1}{\sqrt{3}})[n_2n_1 + m_2m_1 + l_2l_1]\alpha_0^0 + (-\frac{1}{\sqrt{6}})[-2n_2n_1 + m_2m_1 + l_2l_1]\alpha_0^2 + \frac{i}{2}[m_2l_1 - l_2m_1]\alpha_0^1|^2$

$A \leftrightarrow B$ $\quad |\frac{1}{2}[(l_2l_1 - m_2m_1) - (l_2m_1 + m_2l_1)i]\alpha_2^2 + \frac{1}{2}[(l_2l_1 - m_2m_1) + (l_2m_1 + m_2l_1)i]\alpha_{-2}^2|^2$

$A \leftrightarrow E$ $\quad |n_2m_1(\frac{\alpha_1^2 - \alpha_1^1}{2}) + m_2n_1(\frac{\alpha_1^2 + \alpha_1^1}{2})|^2 + |n_2l_1(\frac{\alpha_1^2 - \alpha_1^1}{2}) + l_2n_1(\frac{\alpha_1^2 + \alpha_1^1}{2})|^2$

$$+|n_2m_1(\frac{\alpha_{-1}^2 + \alpha_{-1}^1}{2}) + m_2n_1(\frac{\alpha_{-1}^2 - \alpha_{-1}^1}{2})|^2 + |n_2l_1(\frac{\alpha_{-1}^2 + \alpha_{-1}^1}{2}) + l_2n_1(\frac{\alpha_{-1}^2 - \alpha_{-1}^1}{2})|^2$$

C_{3h} $\quad C_6(C_{6h})$

$A' \leftrightarrow A'$ $\quad A \leftrightarrow A$ $\quad |(-\frac{1}{\sqrt{3}})[n_2n_1 + m_2m_1 + l_2l_1]\alpha_0^0 + (-\frac{1}{\sqrt{6}})[-2n_2n_1 + m_2m_1 + l_2l_1]\alpha_0^2 + \frac{i}{2}[m_2l_1 - l_2m_1]\alpha_0^1|^2$

$A' \leftrightarrow E'$ $\quad A \leftrightarrow E_1$ $\quad |\frac{1}{2}[l_2l_1 - m_2m_1](\alpha_2^2 + \alpha_{-2}^2)|^2 + |\frac{1}{2}[l_2m_1 + m_2l_1](\alpha_{-2}^2 - \alpha_2^2)|^2$

$A' \leftrightarrow E''$ $\quad A \leftrightarrow E_2$ $\quad |n_2m_1(\frac{\alpha_1^2 - \alpha_1^1}{2}) + m_2n_1(\frac{\alpha_1^2 + \alpha_1^1}{2})|^2 + |n_2l_1(\frac{\alpha_1^2 - \alpha_1^1}{2}) + l_2n_1(\frac{\alpha_1^2 + \alpha_1^1}{2})|^2$

$$+|n_2m_1(\frac{\alpha_{-1}^2 + \alpha_{-1}^1}{2}) + m_2n_1(\frac{\alpha_{-1}^2 - \alpha_{-1}^1}{2})|^2 + |n_2l_1(\frac{\alpha_{-1}^2 + \alpha_{-1}^1}{2}) + l_2n_1(\frac{\alpha_{-1}^2 - \alpha_{-1}^1}{2})|^2$$

C_{2v} $\quad D_2$ $\quad D_{2h}(D_{2h} = D_2 x C_i)$

$A_1 \leftrightarrow A_1$ $\quad A \leftrightarrow A$ $\quad |(-\frac{1}{\sqrt{3}})[n_2n_1 + m_2m_1 + l_2l_1]\alpha_0^0 + (-\frac{1}{\sqrt{6}})[-2n_2n_1 + m_2m_1 + l_2l_1]\alpha_0^2$

$$+\frac{1}{2}[l_2l_1 - m_2m_1](\alpha_2^2 + \alpha_{-2}^2)|^2$$

$A_1 \leftrightarrow A_2$ $\quad A \leftrightarrow B_1$ $\quad |\frac{1}{2}[m_2l_1 - l_2m_1]\alpha_0^1 + \frac{1}{2}[l_2m_1 + m_2l_1](\alpha_{-2}^2 - \alpha_2^2)|^2$

$A_1 \leftrightarrow B_1$ $\quad A \leftrightarrow B_2$ $\quad |\frac{1}{2}[n_2l_1 + l_2n_1](\alpha_{-1}^2 - \alpha_1^2) + \frac{1}{2}[n_2l_1 - l_2n_1](\alpha_1^1 + \alpha_{-1}^1)|^2$

$A_1 \leftrightarrow B_2$ $\quad A \leftrightarrow B_3$ $\quad |-\frac{1}{2}[n_2m_1 + m_2n_1](\alpha_1^2 + \alpha_{-1}^2) + \frac{1}{2}[m_2n_1 - n_2m_1](\alpha_1^1 - \alpha_{-1}^1)|^2$

$D_3,\quad C_{3v},\qquad D_{3d}(D_{3d}=D_2xC_i)$

$A_1 \leftrightarrow A_1$ $\qquad |(-\frac{1}{\sqrt{3}})[n_2n_1+m_2m_1+l_2l_1]\alpha_0^0+(-\frac{1}{\sqrt{6}})[-2n_2n_1+m_2m_1+l_2l_1]\alpha_0^2|^2$

$A_1 \leftrightarrow A_2$ $\qquad |\frac{i}{2}[m_2l_1-l_2m_1]\alpha_0^1|^2$

$A_1 \leftrightarrow E$ $\qquad |\frac{1}{2}[n_2l_1-l_2n_1](\alpha_{-1}^1+\alpha_1^1)+\frac{1}{2}[n_2l_1+l_2n_1](\alpha_{-1}^2-\alpha_1^2)$

$+\frac{1}{2}[l_2l_1-m_2m_1](\alpha_2^2+\alpha_{-2}^2)|^2+|\frac{1}{2}[l_2m_1+m_2l_1](\alpha_{-2}^2-\alpha_2^2)$

$+\frac{1}{2}[n_2m_1-m_2n_1](\alpha_{-1}^1-\alpha_1^1)+\frac{1}{2}[n_2m_1+m_2n_1](\alpha_1^2+\alpha_{-1}^2)|^2$

$D_4, C_{4v}, D_{2d},\qquad D_{4h}(D_{4h}=D_4xC_i)$

$A_1 \leftrightarrow A_1$ $\qquad |(-\frac{1}{\sqrt{3}})[n_2n_1+m_2m_1+l_2l_1]\alpha_0^0+(-\frac{1}{\sqrt{6}})[-2n_2n_1+m_2m_1+l_2l_1]\alpha_0^2|^2$

$A_1 \leftrightarrow A_2$ $\qquad |\frac{i}{2}[m_2l_1-l_2m_1]\alpha_0^1|^2$

$A_1 \leftrightarrow B_1$ $\qquad |\frac{1}{2}[l_2l_1-m_2m_1](\alpha_2^2+\alpha_{-2}^2)|^2$

$A_1 \leftrightarrow B_2$ $\qquad |-\frac{i}{2}[l_2m_1+m_2l_1](\alpha_2^2-\alpha_{-2}^2)|^2$

$A_1 \leftrightarrow E$ $\qquad |n_2m_1(\frac{\alpha_1^2-\alpha_1^1}{2})+m_2n_1(\frac{\alpha_1^2+\alpha_1^1}{2})|^2+|n_2l_1(\frac{\alpha_1^2-\alpha_1^1}{2})+l_2n_1(\frac{\alpha_1^2+\alpha_1^1}{2})|^2$

$+|n_2m_1(\frac{\alpha_{-1}^2+\alpha_{-1}^1}{2})+m_2n_1(\frac{\alpha_{-1}^2-\alpha_{-1}^1}{2})|^2+|n_2l_1(\frac{\alpha_{-1}^2+\alpha_{-1}^1}{2})+l_2n_1(\frac{\alpha_{-1}^2-\alpha_{-1}^1}{2})|^2$

$D_5, C_{5v}\qquad D_{5h}(D_{5h}=D_5xC_i),$

$D_6, C_{6v}\quad D_{3h}\qquad D_{6h}(D_{6h}=D_6xC_i)$

D_{4d}

$A_1 \leftrightarrow A_1\quad A'_1 \leftrightarrow A'_1\quad A_1 \leftrightarrow A_1\quad |(-\frac{1}{\sqrt{3}})[n_2n_1+m_2m_1+l_2l_1]\alpha_0^0+(-\frac{1}{\sqrt{6}})[-2n_2n_1+m_2m_1+l_2l_1]\alpha_0^2|^2$

$A_1 \leftrightarrow A_2\quad A'_1 \leftrightarrow A'_2\quad A_1 \leftrightarrow A_2\quad |\frac{i}{2}[m_2l_1-l_2m_1]\alpha_0^1|^2$

$A_1 \leftrightarrow E_1\quad A_1 \leftrightarrow E''\quad A'_1 \leftrightarrow E_3\quad |n_2m_1(\frac{\alpha_1^2-\alpha_1^1}{2})+m_2n_1(\frac{\alpha_1^2+\alpha_1^1}{2})|^2+|n_2l_1(\frac{\alpha_1^2-\alpha_1^1}{2})+l_2n_1(\frac{\alpha_1^2+\alpha_1^1}{2})|^2$

$+|n_2m_1(\frac{\alpha_{-1}^2+\alpha_{-1}^1}{2})+m_2n_1(\frac{\alpha_{-1}^2-\alpha_{-1}^1}{2})|^2+|n_2l_1(\frac{\alpha_{-1}^2+\alpha_{-1}^1}{2})+l_2n_1(\frac{\alpha_{-1}^2-\alpha_{-1}^1}{2})|^2$

$A'_1 \leftrightarrow E_2\quad A_1 \leftrightarrow E'\quad A'_1 \leftrightarrow E_2\quad |\frac{1}{2}[l_2l_1-m_2m_1](\alpha_2^2+\alpha_{-2}^2)|^2+|\frac{1}{2}[l_2m_1+m_2l_1](\alpha_{-2}^2-\alpha_2^2)|^2$

$O, T_d, \qquad O_h (O_h = OxC_i)$

$A_1 \leftrightarrow A_1 \qquad |(-\frac{1}{\sqrt{3}})[n_2 n_1 + m_2 m_1 + l_2 l_1]\alpha_0^0|^2$

$A_1 \leftrightarrow E \qquad |(-\frac{1}{\sqrt{6}})[-2n_2 n_1 + m_2 m_1 + l_2 l_1]\alpha_0^2 + \frac{1}{2}[l_2 l_1 - m_2 m_1](\alpha_2^2 + \alpha_{-2}^2)|^2$

$A_1 \leftrightarrow T_1 \qquad |\frac{i}{2}[m_2 l_1 - l_2 m_1]\alpha_0^1 + \frac{i}{2}[m_2 n_1 - n_2 m_1](\alpha_1^1 - \alpha_{-1}^1)|^2 + |\frac{1}{2}[n_2 l_1 - l_2 n_1](\alpha_1^1 + \alpha_{-1}^1)|^2$

$A_1 \leftrightarrow T_2 \qquad |\frac{i}{2}[n_2 m_1 + m_2 n_1](\alpha_1^2 + \alpha_{-1}^2) + \frac{i}{2}[l_2 m_1 + m_2 l_1](\alpha_{-2}^2 - \alpha_2^2)|^2 + |\frac{1}{2}[-(n_2 l_1 + l_2 n_1)](\alpha_1^2 - \alpha_{-1}^2)|^2$

T, T_h

$A \leftrightarrow A \qquad |(-\frac{1}{\sqrt{3}})[n_2 n_1 + m_2 m_1 + l_2 l_1]\alpha_0^0|^2$

$A_1 \leftrightarrow E \qquad |(-\frac{1}{\sqrt{6}})[-2n_2 n_1 + m_2 m_1 + l_2 l_1]\alpha_0^2 + \frac{1}{2}[l_2 l_1 - m_2 m_1](\alpha_2^2 + \alpha_{-2}^2)|^2$

$A_1 \leftrightarrow T^b \qquad |\frac{i}{2}[m_2 l_1 - l_2 m_1]\alpha_0^1 + \frac{i}{2}[m_2 n_1 - n_2 m_1](\alpha_1^1 - \alpha_{-1}^1)|^2 + |\frac{1}{2}[n_2 l_1 - l_2 n_1](\alpha_1^1 + \alpha_{-1}^1)|^2$

$A_1 \leftrightarrow T^a \qquad |\frac{i}{2}[n_2 m_1 + m_2 n_1](\alpha_1^2 + \alpha_{-1}^2) + \frac{i}{2}[l_2 m_1 + m_2 l_1](\alpha_{-2}^2 - \alpha_2^2)|^2 + |\frac{1}{2}[-(n_2 l_1 + l_2 n_1)](\alpha_1^2 - \alpha_{-1}^2)|^2$

2.3 Polarization Dependence Theory - Higher-order Contribution

2.3.1 Third-Order Contribution to Intra-Configurational Two-Photon Transition Intensities

The line strength of a two-photon transition from an initial state |i) to a final state |f) shown up to the third-order is proportional to

$$\left| -\sum_i \frac{(i|\boldsymbol{E}\cdot\boldsymbol{D}|j)(j|\boldsymbol{E}\cdot\boldsymbol{D}|f)}{E_j} + \sum_{j,k} \frac{(i|V_1|j)(j|V_2|k)(k|V_3|f)}{E_j E_k} - \ldots \right|^2, \quad (2.28)$$

where E_j and E_k are the average energy of the excited j and k configurations.

Depending on the specific details of the interaction V_i (i = 1, 2, or 3) and the initial and final states, expression (2.28) represents different third-order contributions to the two-photon intensities. If the initial and final states are crystal field states belonging to the $4f^N$ configuration, $V_1 = V_3 = \boldsymbol{E}\cdot\boldsymbol{D}$, and $V_2 = H_{SO}$, expression (2.28) represents the third-order spin-orbit contribution. If $V_2 = H_{CF}$, however, the third-order contribution comes from the interaction between intermediate configurations via the crystal-field potential. When the wave functions i, j, k, and f are products of lanthanide and ligand wave functions, and $V_2 = H_C$, where H_C is the Coulomb interaction between the electrons in the lanthanide ion and the ligand excited states, expression (2.28) represents the ligand-polarization third-order contribution [15-17]. This ion-ligand excitation mechanism is called the dynamic mechanism to distinguish it from the static mechanism

as it involves ligand excited states. Finally, a third-order contribution can come from electron correlation, if $V_2 = V_c^{non\text{-}central}$, where $V_c^{non\text{-}central}$ denotes the noncentral part of the Coulomb interaction:

$$V_c^{non\text{-}central} = V_C - U, \tag{2.29}$$

where U stands for the potential of the central field approximation [18-21].

In the independent systems model [15-17] and in the double perturbation model [18-21], the third-order terms in which V_2 is interchanged with V_1 or V_3 also arise, and the electric dipole operator $\boldsymbol{E} \cdot \boldsymbol{D}$ may represent the light-central ion or light-ligand interaction.

2.3.1.1 Spin-Orbit Interaction

Following Judd and Pooler [10], Downer and Bivas [11], and Ceulemans and Vandenberghe [14] the third-order spin-orbit operator can be expressed as

$$\begin{aligned}
&3[l(l+1)(2l+1)]^{1/2}\frac{\zeta_l(nl|r|nl')^2}{E_{l'l}^2}\sum_t\begin{Bmatrix}1 & l & l'\\ l & 1 & t\end{Bmatrix}(\mathbf{e}_2\mathbf{e}_1)^{(t)}\cdot(\mathbf{a}^\dagger\mathbf{a})^{(0t)t}(\mathbf{a}^\dagger\mathbf{a})^{(11)0}\\
&-3[l(l+1)(l+1/2)]^{1/2}\frac{\zeta_l(nl|r|nl')^2}{E_{l'l}^2}\sum_{t,\lambda}(-1)^{\lambda+1}(2\lambda+1)^{1/2}\begin{Bmatrix}1 & l & l\\ l & 1 & \lambda\end{Bmatrix}\begin{Bmatrix}1 & l & l'\\ l & 1 & t\end{Bmatrix}\\
&\qquad\qquad\times(\mathbf{e}_2\mathbf{e}_1)^{(t)}\cdot(\mathbf{a}^\dagger\mathbf{a})^{(1\lambda)t}\\
&-3[l'(l'+1)(l'+1/2)]^{1/2}\frac{\zeta_{l'}(nl|r|nl')^2}{E_{l'l}^2}\sum_{t,\lambda}(-1)^{\lambda+1}(2\lambda+1)^{1/2}\begin{Bmatrix}1 & l & l'\\ 1 & l & l'\\ t & \lambda & 1\end{Bmatrix}\\
&\qquad\qquad\times(\mathbf{e}_2\mathbf{e}_1)^{(t)}\cdot(\mathbf{a}^\dagger\mathbf{a})^{(1\lambda)t}.
\end{aligned} \tag{2.30}$$

where ζ_l, $\zeta_{l'}$ are the spin-orbit coupling constants for l and l' electrons, respectively.

In expression (2.30) the only non-vanishing terms occur for t = 0, 1, and 2 and for λ=1, 2, and 3. The expression for the third-order two-photon scattering tensor can be recast in a more compact form:

$$(\alpha_{21})^{3rd} = \sum_t (-1)^t (\mathbf{e}_2\mathbf{e}_1)^{(t)} \cdot \left[H(t)\,(\mathbf{a}^\dagger\mathbf{a})^{(0t)t}(\mathbf{a}^\dagger\mathbf{a})^{(11)0} + \sum_\lambda G(t,\lambda)\,(\mathbf{a}^\dagger\mathbf{a})^{(1\lambda)t} \right], \quad (2.31)$$

where

$$H(t) = 3(-1)^t [l(l+1)(2l+1)]^{1/2} \frac{\zeta_l (nl|r|nl')^2}{E_{l'l}^2} \begin{Bmatrix} 1 & l & l' \\ l & 1 & t \end{Bmatrix}, \quad (2.32)$$

and

$$G(t,\lambda) = -3(-1)^t [l(l+1)(l+1/2)]^{1/2} \frac{\zeta_l (nl|r|nl')^2}{E_{l'l}^2} (-1)^{\lambda+1} (2\lambda+1)^{1/2} \begin{Bmatrix} 1 & l & l \\ l & 1 & \lambda \end{Bmatrix} \begin{Bmatrix} 1 & l & l' \\ l & 1 & t \end{Bmatrix}$$
$$-3(-1)^t [l'(l'+1)(l'+1/2)]^{1/2} \frac{\zeta_{l'} (nl|r|nl')^2}{E_{l'l}^2} (-1)^{\lambda+1} (2\lambda+1)^{1/2} \begin{Bmatrix} 1 & l & l' \\ 1 & l & l' \\ t & \lambda & 1 \end{Bmatrix}. \quad (2.33)$$

Applying the procedure given in Appendix B, we obtain the two-photon scattering amplitude expressed in the third order:

$$(\alpha_{21})^{3rd} = \sum_{t=0}^{2} \sum_{q=-t}^{t} \lambda_q^t (\alpha_q^{(t)})^{3rd}, \quad (2.34)$$

where λ_q^t's are the polarization dependent coefficients defined in equations (2.25) and $(\alpha_q^{(t)})^{3rd}$ is the third-order irreducible scattering tensor operator defined by

$$(\alpha_q^{(t)})^{3rd} = H(t)\,(\mathbf{a}^\dagger\mathbf{a})_q^{(0t)t}(\mathbf{a}^\dagger\mathbf{a})^{(11)0} + \sum_\lambda G(t,\lambda)\,(\mathbf{a}^\dagger\mathbf{a})_q^{(1\lambda)t} \quad . \tag{2.35}$$

The matrix element of the third-order irreducible scattering tensor is given by

$$\begin{aligned}(f^N LSJM|(\alpha_q^{(t)})^{3rd}|f^N L'S'J'M') \\ = (-1)^{J-M}\begin{pmatrix} J & t & J' \\ -M & q & M' \end{pmatrix}(f^N LSJ||(\alpha^{(t)})^{3rd}||f^N L'S'J'),\end{aligned} \tag{2.36}$$

where

$$\begin{aligned}(f^N SLJ||(\alpha^{(t)})^{3rd}||f^N S'L'J') = H(t)\,(f^N SLJ||(\mathbf{a}^\dagger\mathbf{a})^{(0t)t}(\mathbf{a}^\dagger\mathbf{a})^{(11)0}||f^N S'L'J') \\ + \sum_\lambda G(t,\lambda)\,(f^N SLJ||(\mathbf{a}^\dagger\mathbf{a})^{(1\lambda)t}||f^N S'L'J').\end{aligned} \tag{2.37}$$

For l=3 and l'=2 we have the following values for $H(t)$ and $G(t,\lambda)$:

$$\begin{aligned}&H(0)=\frac{6\zeta_f}{E_{df}^2}(f|r|d)^2, \quad H(2)=\frac{6\sqrt{6}\,\zeta_f}{5E_{df}^2}(f|r|d)^2, \\ &G(0,1)=\frac{(6\zeta_f-4\zeta_d)}{\sqrt{14}E_{df}^2}(f|r|d)^2, \quad G(2,1)=\frac{(-18\zeta_f+8\zeta_d)}{\sqrt{1400}E_{df}^2}(f|r|d)^2, \\ &G(2,2)=\frac{-3\sqrt{42}\,\zeta_f}{70E_{df}^2}(f|r|d)^2, \quad G(2,3)=\frac{3\sqrt{42}(\zeta_f-\zeta_d)}{35E_{df}^2}(f|r|d)^2.\end{aligned} \tag{2.38}$$

The reduced matrix elements in expression (2.36) can be evaluated by using the following formulas [49,55]

$$(\alpha j_1 j_2 j||\mathbf{W}^{(11)k}||\alpha' j_1' j_2' j') = (\alpha j_1 j_2||\mathbf{W}^{(11)}||\alpha' j_1' j_2')[j,j',k]^{1/2}\begin{Bmatrix} j_1 & j_1' & 1 \\ j_2 & j_2' & 1 \\ j & j' & k \end{Bmatrix} \tag{2.39}$$

$$\begin{aligned}&(l^N\alpha SLJ||(\mathbf{U}^{(t)}\mathbf{W}^{(11)0})||l^N\alpha' S'L'J') \\ &\quad = [J']^{-1/2}\sum_{\psi''}(l^N\alpha SLJ||\mathbf{U}^{(t)}||l^N\alpha'' SL'' J')(l^N\alpha'' SL'' J''||\mathbf{W}^{(11)0}||l^N\alpha' S'L'J')\end{aligned} \tag{2.40}$$

$$(l^N\alpha SL\|\mathbf{W}^{(11)}\|l^N\alpha' S' L') = \sqrt{6}(l^N\alpha SL\|\mathbf{V}^{(11)}\|l^N\alpha' S' L') \tag{2.41}$$

$$(\mathbf{a}^\dagger\mathbf{a})^{(1\lambda)t} = -\mathbf{W}^{(1\lambda)t} \tag{2.42}$$

and

$$(\mathbf{a}^\dagger\mathbf{a})^{(0t)t} = -\left(\frac{2t+1}{2}\right)^{1/2}\mathbf{U}^{(t)} \tag{2.43}$$

where the values of the reduced matrix elements of $\mathbf{W}^{(1\lambda)}$ and $\mathbf{V}^{(11)}$ can be found in literature [8,12].

Since the third order spin-orbit contribution to two-photon intensities can be expressed in terms of the second rank irreducible tensor form, with the same polarization dependent coefficients as the second-order contribution, one can just add the results for α_q^t calculated in the third order into the second-order results in (2.26) and square the resulting total amplitude $(\alpha_{21})^{total}$ to obtain the TPA transition intensities calculated up to the third order involving spin-orbit coupling. Note from expression (2.37), because of the presence of the operator $(\mathbf{a}^\dagger\mathbf{a})^{(11)0}$, the scattering tensor $\alpha_0^{(0)}$ is not a scalar, and its corresponding matrix elements are no longer zero for different initial and final states as in the case of the second order theory. It should also be noted H(0) is generally the largest term in equations (2.38). For this reason the third-order contribution corresponding to the $\alpha_0^{(0)}$ term may be dominant in transitions where its matrix elements have non-zero values [10].

2.3.1.2 Crystal-Field Interaction

The original expression for the third-order TPA operator involving crystal-field interaction has been worked out by Downer and coworkers [12,13]. Its full expression has the following tensorial form:

$$-(-1)^{l+l'}[(2l+1)(2l'+1)^2]\frac{(nl\|r\|nl')^2}{\sqrt{2}E_{l'l}^2}\begin{pmatrix} l & 1 & l' \\ 0 & 0 & 0 \end{pmatrix}^2$$
$$\times\sum_{t,k,h}(-1)^k(2k+1)^{1/2}(2t+1)^{1/2}\begin{pmatrix} l' & h & l' \\ 0 & 0 & 0 \end{pmatrix}\begin{Bmatrix} l & 1 & l' \\ h & l' & k \end{Bmatrix}\begin{Bmatrix} 1 & l & l' \\ l & k & t \end{Bmatrix}(\mathbf{e}_2^{(1)}(\mathbf{B}^{(h)}\mathbf{e}_1^{(1)})^{(k)})^{(t)}\cdot(\mathbf{U})^{(t)}, \tag{2.44}$$

where h, k, t are tensor ranks and $B^{(h)}$ is the crystal field tensor corresponding to the third-order crystal field interaction acting between excited configurations |j> and |k> in expressions (2.28).

Specific results for f^N transitions, with intermediate states $f^{N-1}d$, can be readily obtained by substituting l=3 and l'=2 in equation (2.44). The matrix element of the third order crystal-field tensor is given by

$$(i|(\alpha)^{3rd}|f) = (i|\sum_{t,k,h}K(h,k,t)(\mathbf{e}_2^{(1)}(\mathbf{B}^{(h)}\mathbf{e}_1^{(1)})^{(k)})^{(t)}\cdot(\mathbf{U})^{(t)}|f), \tag{2.45}$$

where

$$K(h,k,t) = -(-1)^{l+l'}[(2l+1)(2l'+1)^2]\frac{(nl\|r\|nl')^2}{\sqrt{2}E_{l'l}^2}\begin{pmatrix} l & 1 & l' \\ 0 & 0 & 0 \end{pmatrix}^2$$
$$\times(-1)^k(2k+1)^{1/2}(2t+1)^{1/2}\begin{pmatrix} l' & h & l' \\ 0 & 0 & 0 \end{pmatrix}\begin{Bmatrix} l & 1 & l' \\ h & l' & k \end{Bmatrix}\begin{Bmatrix} 1 & l & l' \\ l & k & t \end{Bmatrix}. \tag{2.46}$$

As can be seen from expression (2.44), the crystal field tensor operator $B^{(h)}$ is coupled to the electric field vectors. By further recoupling the electric field tensors, Ceulemans and Vandenberghe have obtained an expression in which the electric field tensors are directly coupled and all the 6-j symbols are combined into a single 9-j symbol [14]. We neverththeless will develop the polarization dependent form for Downer et al's expression, so that comparison can readily be made between the two theories in the case of parallel and circular polarized beams. Since the unit polarization vectors are coupled to the crystal-field tensor, $B^{(h)}$, in expression (2.44), we have to resort to the method of tensor operators to derive the polarization dependence for the third-order crystal-field term. The decoupling procedure for all possible values of h, k, and q is, however, quite tedious; we therefore only consider the special case in which the only crystal-field term appearing in (2.45) is the fourth rank crystal field term $B_0^{(4)}$. Putting h = 4, l = 3, and l' = 2, expression (2.45) becomes [13]

$$(il(\alpha)^{3rd}|f) = (il\sum_{t,k} L(t,k)(\mathbf{e}_2^{(1)}(\mathbf{B}^{(4)}\mathbf{e}_1^{(1)})^{(k)})^{(t)} \cdot (\mathbf{U})^{(t)}|f), \tag{2.47}$$

where

$$L(t,k) = \frac{15(nl|r|nl')^2}{\sqrt{35}E_{l'l}^2}(-1)^{l+k}(2k+1)^{1/2}(2t+1)^{1/2}\begin{Bmatrix}1 & 3 & 2\\ 3 & t & k\end{Bmatrix}\begin{Bmatrix}3 & 1 & 2\\ 4 & 2 & t\end{Bmatrix}. \tag{2.48}$$

For k = 5 and t = 6, the tensor operator in (2.47) can be written

$$\begin{aligned}(\mathbf{e}_2^{(1)}(\mathbf{B}^{(4)}\mathbf{e}_1^{(1)})^{(5)})^{(6)} \cdot \mathbf{U}^{(6)} &= (-1)^2(\mathbf{e}_2^{(1)}(\mathbf{B}^{(4)}\mathbf{e}_1^{(1)})^{(5)})_2^{(6)}\mathbf{U}_{-2}^{(6)}\\ &+(-1)^1(\mathbf{e}_2^{(1)}(\mathbf{B}^{(4)}\mathbf{e}_1^{(1)})^{(5)})_1^{(6)}\mathbf{U}_{-1}^{(6)} + (-1)^0(\mathbf{e}_2^{(1)}(\mathbf{B}^{(4)}\mathbf{e}_1^{(1)})^{(5)})_0^{(6)}\mathbf{U}_0^{(6)}\\ &+(-1)^{-1}(\mathbf{e}_2^{(1)}(\mathbf{B}^{(4)}\mathbf{e}_1^{(1)})^{(5)})_{-1}^{(6)}\mathbf{U}_1^{(6)} + (-1)^{-2}(\mathbf{e}_2^{(1)}(\mathbf{B}^{(4)}\mathbf{e}_1^{(1)})^{(5)})_{-2}^{(6)}\mathbf{U}_2^{(6)}.\end{aligned} \tag{2.49}$$

After decoupling and rearranging, the right-hand side of (2.49) has the form:

$$B_0^{(4)}\{(14/99)^{1/2}(\mathbf{e}_2)_1(\mathbf{e}_1)_1\mathbf{U}_{-2}^{(6)}-(35/198)^{1/2}[(\mathbf{e}_2)_0(\mathbf{e}_1)_1+(\mathbf{e}_2)_1(\mathbf{e}_1)_0]\mathbf{U}_{-1}^{(6)}$$
$$+(5/66)^{1/2}[(\mathbf{e}_2)_{-1}(\mathbf{e}_1)_1+(\mathbf{e}_2)_1(\mathbf{e}_1)_{-1}+2(\mathbf{e}_2)_0(\mathbf{e}_1)_0]\mathbf{U}_0^{(6)} \qquad (2.50)$$
$$-(35/198)^{1/2}[(\mathbf{e}_2)_0(\mathbf{e}_1)_{-1}+(\mathbf{e}_2)_{-1}(\mathbf{e}_1)_0]\mathbf{U}_1^{(6)}+(14/99)^{1/2}(\mathbf{e}_2)_{-1}(\mathbf{e}_1)_{-1}\mathbf{U}_2^{(6)}\}.$$

Using (B5) we have the final polarization dependent form for the crystal-field third-order contribution:

$$B_0^{(4)}\{\frac{1}{3\sqrt{11}}\{\sqrt{14}\lambda_{-2}^2\mathbf{U}_{-2}^{(6)}+\sqrt{35}\lambda_{-1}^2\mathbf{U}_{-1}^{(6)}+3\sqrt{5}\lambda_0^2\mathbf{U}_0^{(6)}+\sqrt{35}\lambda_1^2\mathbf{U}_1^{(6)}+\sqrt{14}\lambda_2^2\mathbf{U}_2^{(6)}\},(2.51)$$

where λ_q^t 's are defined in (B7).

The crystal-field third-order contribution is proportional to $(10/33)^{1/2}$ $\langle i|\mathbf{U}_0^{(6)}|f\rangle$ and $(14/99)^{1/2}$ $\langle i|\mathbf{U}_{-2}^{(6)}|f\rangle$ for parallel and circular polarization, respectively. For the $^8S_{7/2}$ -> ^6I_J transitions in Gd^{3+}:LaF_3, the ratio of the integrated two-photon line strength corresponding to parallel polarization to that corresponding to circular polarization is 15/7, in exact agreement with Downer et al. [13].

2.3.2 Fourth-Order Contribution to Intra-Configurational Two-Photon Transition Intensities - Spin-Orbit and Crystal-Field Interactions

The fourth-order contribution to two photon intensities is expressed as

$$-\sum_{j,h,k}\frac{(i|\boldsymbol{E}\cdot\boldsymbol{D}|j)(j|V|h)(h|V'|k)(k|\boldsymbol{E}\cdot\boldsymbol{D}|f)}{E_jE_kE_h}$$
$$-\sum_{j,h,k}\frac{(i|\boldsymbol{E}\cdot\boldsymbol{D}|j)(j|V'|h)(h|V|k)(k|\boldsymbol{E}\cdot\boldsymbol{D}|f)}{E_jE_kE_h}. \qquad (2.52)$$

Downer and Bivas [13] have explored the fourth-order terms with $V=H_{SO}$ and $V'=H_{CF}$ for the case of $^8S \rightarrow {}^6I$. A more general expression was later given by Ceulemans and Vandenberghe [14]. Following Ceulemans and Vandenberghe's results, the expression for the fourth-order scattering tensor amplitude between states |i> and |f> taking into account spin-orbit and crystal field interactions can be written

$$
\begin{aligned}
(i|(\alpha_{21})^{4th}|f) = (i|\sum_{t,k,n} ((\mathbf{e}_2\mathbf{e}_1)^{(t)} B^{(k)})^{(n)} \cdot [\ & M(t,k,n)\,(\mathbf{a}^\dagger\mathbf{a})^{(0n)n}(\mathbf{a}^\dagger\mathbf{a})^{(11)0} \\
+\sum_{\lambda} N(t,k,n,\lambda)\,(\mathbf{a}^\dagger\mathbf{a})^{(1\lambda)n} + \sum_{\lambda even} & P(t,k,n,\lambda)\,(\mathbf{a}^\dagger\mathbf{a})^{(1\lambda)n}\ ]|f),
\end{aligned}
\tag{2.53}
$$

where t, k, n, and λ are tensor ranks, $B^{(k)}$ is the crystal field tensor,

$$
\begin{aligned}
M(t,k,n) = 2(-1)^{l'} & \frac{\zeta_l(2l+1)(2l'+1)^2(nl|r|nl')^2}{E^3_{l'l}} \begin{pmatrix} l & 1 & l' \\ 0 & 0 & 0 \end{pmatrix}^2 \\
& \times [l(l+1)(2l+1)]^{1/2}(-1)^{n+k}(2t+1)^{1/2} \begin{pmatrix} l' & k & l' \\ 0 & 0 & 0 \end{pmatrix} \begin{Bmatrix} 1 & l' & l \\ 1 & l' & l \\ m & k & n \end{Bmatrix},
\end{aligned}
\tag{2.54}
$$

$$
\begin{aligned}
N(t,k,n,\lambda) = 2^{1/2}(-1)^{l'+n+\lambda+k} & \frac{\zeta_l[l(l+1)]^{1/2}(2l+1)^{3/2}(2l'+1)^2(nl|r|nl')^2}{E^3_{l'l}} \begin{pmatrix} l & 1 & l' \\ 0 & 0 & 0 \end{pmatrix}^2 \\
& \times [(2\lambda+1)(2t+1)]^{1/2} \begin{pmatrix} l' & k & l' \\ 0 & 0 & 0 \end{pmatrix} \begin{Bmatrix} 1 & l' & l \\ 1 & l' & l \\ t & k & n \end{Bmatrix} \begin{Bmatrix} 1 & \lambda & n \\ l & l & l \end{Bmatrix},
\end{aligned}
\tag{2.55}
$$

and

$$P(t,k,n,\lambda)=2^{1/2}(-1)^{l'+n+\lambda+k}\frac{\zeta_{l'}(2l+1)[l'(l'+1)]^{1/2}(2l'+1)^{5/2}(nl|r|nl')^2}{E^3_{l'l}}\begin{pmatrix} l & 1 & l' \\ 0 & 0 & 0 \end{pmatrix}^2$$
$$\times[(2\lambda+1)(2t+1)]^{1/2}\begin{pmatrix} l' & k & l' \\ 0 & 0 & 0 \end{pmatrix}\begin{Bmatrix} 1 & 1 & t & n \\ l & l & \lambda & l' \\ l' & l' & k & 1 \end{Bmatrix}, \qquad (2.56)$$

where $\zeta_{l'}$ and ζ_l are the spin-orbit coupling constants for l and l' electrons.

As in the third-order crystal field analysis, we only consider the special case in which the only crystal-field term appearing in (2.53) is the fourth rank crystal field term $B_0^{(4)}$. Appendix C and table 2.2 provide the decomposition of $((\mathbf{e}_2\mathbf{e}_1)^{(t)}B^{(k)})^{(n)}\cdot O^{(n)}$ for different values of t and n corresponding to k = 4, where $O^{(n)}$ represents the tensor operator in the square bracket of equation (2.53). The corresponding polarization dependence expression is given therein.

2.3.3 Third-Order Contribution to Inter-Configurational Two-Photon Absorption Transition Intensities

The theory of static and dynamic contributions to the two-photon f-d transitions has been developed by several workers [27, 32, 42]. Most of these works were developed for the special case of 4f →5d two-photon transition in Ce^{3+}:CaF_2. We will discuss the models given by R. C. Leavitt [27] and Sztucki and Strek [17]. Following Leavitt's result for Ce^{3+}:CaF_2, the static contribution is given by

$$(\psi_{nf}|\alpha_q^{(r)}|\psi_{n'd})=\frac{h^2e^2}{\varepsilon r_0^2}(f\|C^{(1)}\|d)^3(R_{nf}|r|R_{n'd})^3(\psi_{nf}|\sum_k S_q^{l}U_q^{(k)}|\psi_{n'd}), \qquad (2.57)$$

where

$$
\begin{aligned}
S_q^t = & \sum_k \frac{(2t+1)^{1/2}(2k+1)}{2(E_d+E_v)E_v}(-1)^{t+q}\begin{Bmatrix} 3 & 3 & t \\ 1 & 1 & 2 \end{Bmatrix}\begin{Bmatrix} 3 & 3 & t \\ k & 1 & 2 \end{Bmatrix}\begin{pmatrix} t & 1 & k \\ q & 0 & -q \end{pmatrix} \\
& + \sum_k \frac{(2t+1)^{1/2}(2k+1)}{E_d E_v}(-1)^{t+q}\begin{Bmatrix} 2 & 2 & t \\ 1 & 1 & 3 \end{Bmatrix}\begin{Bmatrix} 2 & 2 & t \\ k & 1 & 3 \end{Bmatrix}\begin{pmatrix} t & 1 & k \\ -q & 0 & q \end{pmatrix} \\
& + \sum_k \frac{(2t+1)^{1/2}(2k+1)}{(E_d+E_v)E_v}(-1)^{t+q}\begin{Bmatrix} 1 & 1 & t \\ 2 & 3 & k \\ 3 & 2 & 1 \end{Bmatrix}\begin{pmatrix} t & 1 & k \\ -q & 0 & q \end{pmatrix}
\end{aligned}
\tag{2.58}
$$

In expression (2.57), ε is the effective dielectric constant, r_0 is the magnitude of ligand position $\mathbf{r}_0$, $\mathbf{C}^{(1)}$ is a spherical tensor depending on the RE electron postion, and t can take the values 0, 1, or 2. In equation (2.58), the dominant configurations are assumed to be nf and n'd, and E_d and E_v are the energies of the n'd configuration and the excitation beam. In Leavitt's derivation of the static effect, the RE ion and the nearby interstitial ligands (the charge compensating F^- ions in this case) are treated as static point charges. Odd-parity crystal field effects arise from interaction between the RE ion and these ligand ions.

When the interaction between the ligand-electrons and RE electrons are taken into account, we have the ligand dependent effect [15]. Leavitt's expression for the dynamic coupling contribution to TPA intensities is given as follows

$$
(\psi_{nf}|\alpha_q^{(t)}|\psi_{n'd}) = \frac{h\sqrt{105}E_{\bar{v}}}{\varepsilon r_0^4(E_v+E_{\bar{v}})}(d\|C^{(1)}\|f)(R_{nf}|r|R_{n'd})\ \bar{\alpha}_L(\psi_{nf}|\sum_k D_q^t U_q^{(k)}|\psi_{n'd}),
\tag{2.59}
$$

where $\bar{\alpha}_L$ is the charge compensating interstitial ligand polarizability, $E_{\bar{v}}$ is its the average excitation energy, and

$$D_q^t = (d\|C^{(2)}\|f)(R_{nf}|r^2|R_{n'd}) \sum_k \frac{(2t+1)^{1/2}(2k+1)}{(E_f - E_v)}(-1)^{1+t+q}$$
$$\times \begin{Bmatrix} 1 & 2 & k \\ 3 & 2 & 3 \end{Bmatrix} \begin{Bmatrix} 1 & 1 & t \\ k & 3 & 2 \end{Bmatrix} \begin{Bmatrix} k & k & 0 \\ 1 & 1 & 1 \end{Bmatrix} \begin{pmatrix} t & 3 & k \\ -q & 0 & q \end{pmatrix}$$
$$+ (d\|C^{(2)}\|d)(R_{n'd}|r^2|R_{n'd}) \sum_k \frac{(2t+1)^{1/2}(2k+1)}{(E_d - E_v)}(-1)^{q} \tag{2.60}$$
$$\times \begin{Bmatrix} 1 & 2 & k \\ 2 & 3 & 2 \end{Bmatrix} \begin{Bmatrix} 1 & 1 & t \\ k & 3 & 2 \end{Bmatrix} \begin{Bmatrix} k & k & 0 \\ 1 & 1 & 1 \end{Bmatrix} \begin{pmatrix} t & 3 & k \\ -q & 0 & q \end{pmatrix}$$

Expressions (2.57) and (2.59) already have the second-rank irreducible tensor form. Their corresponding polarization dependence expression is therefore given by equation (2.23), with $\alpha_q^{(t)}$ being replaced by expression (2.57) for static contribution and expression (2.59) for dynamic contribution.

The general formulae for the static and dynamic TPA transition amplitude can be described within the framework of the independent systems model [17]:

$$(\psi_f|\alpha_S|\psi_d) = [(\mathbf{e}_2\mathbf{e}_1)^{(t)} B_{fd}^k]^{(n)} \cdot \{ (M_i(f)|\mathbf{U}^{(n)}|M_f(d))$$
$$\times \sum_{\substack{t=0,2 \\ odd\ k\le 5}} \sum_{n\le 5} 6(35[t][n])^{1/2} E_{df}^{-2} \begin{pmatrix} 2 & k & 3 \\ 0 & 0 & 0 \end{pmatrix} (f|r^2|d) \tag{2.61}$$
$$\times \left[(-1)^n \begin{Bmatrix} 2 & 1 & 3 \\ 1 & 2 & t \end{Bmatrix} \begin{Bmatrix} 2 & t & 2 \\ k & 3 & n \end{Bmatrix} - \begin{Bmatrix} 3 & 1 & 2 \\ 1 & 3 & t \end{Bmatrix} \begin{Bmatrix} 3 & t & 3 \\ k & 2 & n \end{Bmatrix} + (-1)^n 2 \begin{Bmatrix} 1 & 1 & t \\ 2 & 3 & k \\ 3 & 2 & n \end{Bmatrix} \right] \},$$

and

$$(\psi_f|\alpha_D|\psi_d) = [(\mathbf{e}_2\mathbf{e}_1)^{(t)} T^{(k+1)}]^{(n)} \cdot \{ (M_i(f)|\mathbf{U}^{(n)}|M_f(d))$$
$$\times \sum_{\substack{t=0,2 \\ even\ k\le 6}} \sum_{n\le 5} (-1)^{k+n+1} 6[\frac{2}{35}(k+1)[k+1][k][t][n]]^{1/2} E_{df}^{-1} \overline{\alpha} \begin{Bmatrix} t & k+1 & n \\ k & 1 & 1 \end{Bmatrix} (f|r|d) \tag{2.62}$$
$$\times \left[(-1)^{n+1} 3 \begin{pmatrix} 3 & k & 3 \\ 0 & 0 & 0 \end{pmatrix} \begin{Bmatrix} 2 & 1 & 3 \\ k & 3 & n \end{Bmatrix} (f|r^k|f) + 2 \begin{pmatrix} 2 & k & 2 \\ 0 & 0 & 0 \end{pmatrix} \begin{Bmatrix} 3 & 1 & 2 \\ k & 2 & n \end{Bmatrix} (d|r^k|d) \right] \}$$

where α_S and α_D are the static and dynamic two-photon f-d transition amplitude, $\bar{\alpha}$ is the average polarizability, $|M_j)$ is the free-ion eigenstates of the RE ion (denoted by M), which is related to $|L_j)$, the free-ion eigenstates of the ligands (denoted by L), and $|\phi_j)$, the zeroth-order states of the system, by the expression

$$|\phi_j) = |M_j)\,|L_j), \tag{2.63}$$

B^k_{fd} are the crystal-field parameters, and T^{k+1} is the geometrical tensor defined by

$$B^k_{fd} = \sum_L T^{(k)}_L (nf|r^k|n'd). \tag{2.64}$$

The polarization dependence of the static and dynamic two-photon f-d transition amplitude given by the Sztucki and Strek's model can be found by decomposition of $((\mathbf{e}_2\mathbf{e}_1)^{(1)}B^{(k)})^{(n)} \cdot O_S^{(n)}$ and $((\mathbf{e}_2\mathbf{e}_1)^{(1)}T^{(k+1)})^{(n)} \cdot O_D^{(n)}$, where O_S and O_D represent the tensor operators in the square brackets of equations (2.61) and (2.62), respectively. For a system such as Ce^{3+}:CaF_2, only terms associated with $B_0^{(1)}$, $B_0^{(3)}$, and $T_0^{(3)}$ are relevant. The decomposition procedure for the case of k = 1 and 3 is given in Appendix C and table 2.2.

Table 2.2: Calculated values of $D_q^{(t)}(k,n)$

k	n	$D_2^{(2)}$	$D_1^{(2)}$	$D_0^{(2)}$	$D_1^{(1)}$	$D_0^{(1)}$	$D_0^{(0)}$
1	3	$\frac{1}{\sqrt{3}}$	$2\sqrt{\frac{2}{15}}$	$\sqrt{\frac{3}{5}}$	0	0	0
	2	$-\sqrt{\frac{2}{3}}$	$-\frac{1}{\sqrt{6}}$	0	$-\frac{1}{\sqrt{2}}$	$-\sqrt{\frac{2}{3}}$	0
	1	0	$-\sqrt{\frac{3}{10}}$	$-\sqrt{\frac{2}{5}}$	$\sqrt{\frac{5}{6}}$	0	1
	0	0	0	0	0	$\frac{1}{\sqrt{3}}$	0
3	5	$\frac{1}{\sqrt{6}}$	$2\sqrt{\frac{2}{21}}$	$\sqrt{\frac{10}{21}}$	0	0	0
	4	$-\sqrt{\frac{3}{7}}$	$-\sqrt{\frac{3}{14}}$	0	$-\sqrt{\frac{5}{14}}$	$-\frac{2}{\sqrt{7}}$	0
	3	$\frac{1}{\sqrt{3}}$	$-\frac{1}{\sqrt{30}}$	$-\frac{2}{\sqrt{15}}$	$\frac{1}{\sqrt{2}}$	0	1
	2	$-\frac{1}{\sqrt{14}}$	$\sqrt{\frac{2}{7}}$	0	$-\frac{1}{\sqrt{7}}$	$\sqrt{\frac{3}{7}}$	0
	1	0	$-\sqrt{\frac{3}{35}}$	$\frac{3}{\sqrt{35}}$	0	0	0
4	6	$\frac{1}{3}\sqrt{\frac{14}{11}}$	$\frac{1}{3}\sqrt{\frac{35}{11}}$	$\sqrt{\frac{5}{11}}$	0	0	0
	5	$-\frac{1}{3}\sqrt{\frac{7}{2}}$	$-\frac{\sqrt{2}}{3}$	0	$-\frac{1}{\sqrt{3}}$	$-\frac{\sqrt{5}}{3}$	0
	4	$3\sqrt{\frac{3}{77}}$	$-\sqrt{\frac{3}{154}}$	$-2\sqrt{\frac{5}{77}}$	$\frac{1}{\sqrt{2}}$	0	1
	3	$-\frac{1}{3}$	$\frac{1}{3}\sqrt{\frac{5}{2}}$	0	$-\frac{1}{\sqrt{6}}$	$\frac{2}{3}$	0
	2	$\frac{1}{3\sqrt{14}}$	$\frac{2}{3}\sqrt{\frac{2}{7}}$	$\sqrt{\frac{2}{7}}$	0	0	0

where

$D_q^{(t)}(k,n) = (-1)^t\,(t\ {-q}\ k\ 0 \mid n\ {-q}) = (-1)^{t+k+n}\,D_{-q}^{(t)}(k,n)$

2.3.4 Relative Magnitude of Higher-Order Contributions to Second-Order Contribution

Finally, we consider the relative magnitude of the third (and fourth) order contribution to the second-order contribution. Using the intermediate coupling states we have

$$\frac{<\Psi\,|(\alpha_q^{(t)})^{nth}|\Psi'>}{<\Psi\,|(\alpha_q^{(t)})^{2nd}|\Psi'>}=$$

$$\frac{\sum_{SLJ,S'L'J'} a(SLJM)a'(S'L'J'M')\begin{pmatrix} J & t & J' \\ -M & q & M' \end{pmatrix}(-1)^{(J-M)} < SLJ||(\alpha^{(t)})^{nth}||S'L'J'>}{\sum_{SLJ,S'L'J'} a(SLJM)a'(S'L'J'M')\begin{pmatrix} J & t & J' \\ -M & q & M' \end{pmatrix}(-1)^{(J-M)} < SLJ||(\alpha^{(t)})^{2nd}||S'L'J'>}, \quad (2.65)$$

where nth can be 3, 4, or any higher order contribution taken into account.

If the SLJ mixing are negligible for the states Ψ and Ψ' the coefficients a(SLJM) and a'(S'L'J'M') are functions of J and M, i.e., a(SLJM) = a(JM), a'(S'L'J'M') = a'(J'M'). We then have

$$\frac{<\Psi\,|(\alpha_q^{(t)})^{nth}|\Psi'>}{<\Psi\,|(\alpha_q^{(t)})^{2nd}|\Psi'>}=$$

$$\frac{< SLJ||(\alpha^{(t)})^{nth}||S'L'J'> \sum_{SLJ,S'L'J'} a(JM)a'(J'M')\begin{pmatrix} J & t & J' \\ -M & q & M' \end{pmatrix}(-1)^{(J-M)}}{< SLJ||(\alpha^{(t)})^{2nd}||S'L'J'> \sum_{SLJ,S'L'J'} a(JM)a'(J'M')\begin{pmatrix} J & t & J' \\ -M & q & M' \end{pmatrix}(-1)^{(J-M)}} \quad (2.66)$$

$$=\frac{< SLJ||(\alpha^{(t)})^{nth}||S'L'J'>}{< SLJ||(\alpha^{(t)})^{2nd}||S'L'J'>},$$

which is independent of q. For a TPA process with a single laser excitation wavelength, $\alpha_q^{(1)}$ vanishes, and $\alpha_0^{(0)}$ also vanishes if J' is different from J. In this case the polarization dependence and relative amplitudes of TPA Stark intensities, which now depend only on $\alpha_q^{(t)}$, would not change when higher order contribution were included. We now apply the polarization dependence theory into a number of cases including intra- and inter-configurational TPA.

2.4 Examples

2.4.1 Intra-Configurational TPA - Application to Sm^{2+} in BaClF

In the second-order approximation the polarization dependence functions of the TPA intensities are expressed in terms of $\alpha_q^{(t)}$'s, which can be further evaluated in terms of the parameters F_t's when one applies equations (2.12) - (2.16) to a particular TPA transition. The final polarization dependence functions are thus expressed in terms of the parameter F_t's and can be compared directly with observed data. In this section we will provide examples on how to apply the master formula (2.23) to TPA transitions in a particular system.

We now apply formulae (2.15) and (2.16) to the transition $^7F_0 \rightarrow {}^5D_2$ for Sm^{2+} in BaClF (C_{4v} site symmetry). Using the crystal-field parameters given by Gâcon et al [38], we can obtain the crystal-field wavefunctions and coefficients for the initial and final states.

The initial state, which is the ground state, can be expressed as [56]

$$|\Gamma_1\rangle = .97\ {}^7F(0,0) - .17\ {}^5D1(0,0), \tag{2.67}$$

where we have used the ${}^{2S+1}Li(J,J_z)$ notation.

The final states are

$$|\Gamma_1\rangle = -.74\ [{}^5D3(2,0)] + .6[\ {}^5D1(2,0)]$$

$$|\Gamma_3\rangle = -.74[\frac{1}{\sqrt{2}}\ {}^5D3(2,2) + \frac{1}{\sqrt{2}}\ {}^5D3(2,-2)] + .6[\frac{1}{\sqrt{2}}\ {}^5D1(2,2) + \frac{1}{\sqrt{2}}\ {}^5D1(2,-2)]$$

$$|\Gamma_4\rangle = -.74[-\frac{1}{\sqrt{2}}\ {}^5D3(2,2) + \frac{1}{\sqrt{2}}\ {}^5D3(2,-2)] + .6[-\frac{1}{\sqrt{2}}\ {}^5D1(2,2) + \frac{1}{\sqrt{2}}\ {}^5D1(2,-2)]$$

$$|\Gamma_{5x}\rangle = -.74[-\ {}^5D3(2,1)] + .6[-\ {}^5D1(2,1)]$$

$$|\Gamma_{5y}\rangle = -\ .74[-\ {}^5D3(2,-1)] + .6[-\ {}^5D1(2,-1)], \tag{2.68}$$

where Γ_{5x} and Γ_{5y} are the two components of the doubly degenerate Γ_5 states.

For Sm^{2+} ($4f^6$) we have

$$\langle\Gamma_1|\alpha_q^{(2)}|\Gamma_1\rangle = \begin{cases} \frac{.079}{5}F_2 & \text{for} \quad q = 0 \\ 0 & \text{for} \quad q \neq 0 \end{cases}$$

$$\langle\Gamma_1|\alpha_q^{(2)}|\Gamma_3\rangle = \begin{cases} \frac{.079}{5\sqrt{2}}F_2 & \text{for} \quad q = \pm 2 \\ 0 & \text{for} \quad q \neq \pm 2 \end{cases}$$

$$\langle\Gamma_1|\alpha_q^{(2)}|\Gamma_4\rangle = \begin{cases} \mp\frac{.079}{5\sqrt{2}}F_2 & \text{for} \quad q = \pm 2 \\ 0 & \text{for} \quad q \neq \pm 2 \end{cases}$$

$$\langle\Gamma_1|\alpha_q^{(2)}|\Gamma_{5x}\rangle = \begin{cases} -\frac{.079}{5}F_2 & \text{for} \quad q = 1 \\ 0 & \text{for} \quad q \neq 1 \end{cases}$$

$$<\Gamma_1|\alpha_q^{(2)}|\Gamma_{5y}> = \begin{cases} -\frac{.079}{5}F_2 & \text{for} \quad q=-1 \\ 0 & \text{for} \quad q \neq -1, \end{cases}$$

(2.69)

Equation (2.23) can be rewritten for the case of TPA from the same source:

$$\alpha_{r_2r_1} = (\frac{3\cos^2\theta - 1}{\sqrt{6}})\alpha_0^{(2)} - (\frac{e^{-i\varphi}}{2}\sin 2\theta)\alpha_1^{(2)} + (\frac{e^{i\varphi}}{2}\sin 2\theta)\alpha_{-1}^{(2)} + (\frac{e^{-2i\varphi}}{2}\sin^2\theta)\alpha_2^{(2)} + (\frac{e^{2i\varphi}}{2}\sin^2\theta)\alpha_{-2}^{(2)} \tag{2.70}$$

$$<\Gamma_1|\alpha_{r_2r_1}|\Gamma_1> = \frac{1}{\sqrt{6}}(3\cos^2\theta - 1) <\Gamma_1|\alpha_0^{(2)}|\Gamma_1> = \frac{a_2}{\sqrt{3}}(3\cos^2\theta - 1)$$

$$<\Gamma_1|\alpha_{r_2r_1}|\Gamma_3> = \frac{e^{-2i\varphi} <\Gamma_1|\alpha_2^{(2)}|\Gamma_3> + e^{2i\varphi} <\Gamma_1|\alpha_{-2}^{(2)}|\Gamma_3>}{2}(\sin^2\theta) = a_2 \sin^2\theta\cos\ 2\varphi$$

$$<\Gamma_1|\alpha_{r_2r_1}|\Gamma_4> = \frac{e^{-2i\varphi} <\Gamma_1|\alpha_2^{(2)}|\Gamma_4> + e^{2i\varphi} <\Gamma_1|\alpha_{-2}^{(2)}|\Gamma_4>}{2}(\sin^2\theta) = ia_2 \sin^2\theta\sin 2\varphi$$

$$<\Gamma_1|\alpha_{r_2r_1}|\Gamma_{5x}> = -\frac{e^{-i\varphi} <\Gamma_1|\alpha_1^{(2)}|\Gamma_{5x}>}{2}(\sin 2\theta) = \frac{a_2}{\sqrt{2}}(\sin 2\theta)e^{-i\varphi}$$

$$<\Gamma_1|\alpha_{r_2r_1}|\Gamma_{5y}> = \frac{e^{i\varphi} <\Gamma_1|\alpha_{-1}^{(2)}|\Gamma_{5y}>}{2}(\sin 2\theta) = -\frac{a_2}{\sqrt{2}}(\sin 2\theta)e^{i\varphi},$$

(2.71)

where $a_2 = \frac{.079}{5\sqrt{2}}F_2$. (2.72)

The angular dependence of the TPA line strengths can be expressed in terms of the overall strength S_0 of the $^7F_0 \rightarrow {}^5D_2$ two-photon transition:

$$S(\Gamma_1 \rightarrow \Gamma_1) = \frac{1}{3} S_0 (3\cos^2\theta - 1)^2$$

$$S(\Gamma_1 \rightarrow \Gamma_3) = S_0 \sin^4\theta \cos^2 2\varphi$$

$$S(\Gamma_1 \rightarrow \Gamma_4) = S_0 \sin^4\theta \sin^2 2\varphi$$

$$S(\Gamma_1 \rightarrow \Gamma_5) = S_0 \sin^4 2\theta. \tag{2.73}$$

Note that we can equivalently obtain (2.62) by using table 2.1 for the case of C_{4v} and substitute the nonvanishing values of $\alpha_q^{(t)}$ given in (2.69) into the polarization functions for each two-photon transition. Table 2.1 is particularly useful when the intermediate coupling coefficients of the wavefunctions for the initial and final states are unknown. Once these coefficients are obtained, and the corresponding $\alpha_q^{(t)}$'s are determined, the master formula (2.23) can be used instead. The results in (2.73) are identical with those of Gâcon et al [38], which were shown to agree well with experiment. As pointed out by Gâcon et al, the results given in (2.73) agree with the results of Bader and Gold and, furthermore, complete their results.

2.4.2 Inter-Configurational TPA - Application to Ce^{3+}:CaF_2

We can apply equation (2.23) to calculate the dependence of the TPA cross-section on the directions of the electric field vector $\hat{\mathbf{e}}$ and the wave vector $\vec{\mathbf{k}}$ of the incident laser beam. For the Ce^{3+} ion in CaF_2 with site symmetry C_{4v}, the TPA cross-

section σ for the zero-phonon transition from the 4f ground state to the lowest 5d state of the Ce^{3+} ion is proportional to

$$\left(-\frac{1}{\sqrt{3}}\alpha_0^0+(\frac{3\cos^2\theta-1}{\sqrt{6}})\alpha_0^2\right)^2+\left((\frac{e^{-i\varphi}}{2}\sin 2\theta)\alpha_1^2\right)^2 \tag{2.74}$$

For the case where $\vec{\mathbf{k}} \parallel [100]$ and $\hat{\mathbf{e}} \parallel [010]$ we have

$$\sigma \propto 1+C\sin^2 2\theta, \tag{2.75}$$

where $C = (2b-1/2)/(3a^2-2a+1)$, (2.76)

with $a = \frac{1}{3}+\frac{\sqrt{2}}{3}\frac{\alpha_0^0}{\alpha_0^2}$ and $b = \frac{1}{6}\left(\frac{\alpha_1^2}{\alpha_0^2}\right)^2$. (2.77)

Similarly, we obtain

$$\sigma \propto 1+\frac{3C}{4}\sin^2 2\theta + C\sin^2\theta \quad \text{for the case where } \vec{\mathbf{k}} \parallel [110] \text{ and } \hat{\mathbf{e}} \parallel [001], \tag{2.78}$$

and

$$\sigma \propto 1+C \quad \text{for the case where } \vec{\mathbf{k}} \parallel [111] \text{ and } \hat{\mathbf{e}} \parallel [110]. \tag{2.79}$$

The fitted curves for (2.75), (2.78), and (2.79) are shown in Fig. 2.1. The best fit for C is found to be 1.774. The polarization anisotropy for the case where $\vec{\mathbf{k}} \parallel [100]$ and $\hat{\mathbf{e}} \parallel [010]$ is

$$A=\frac{\sigma(45^0)-\sigma(0^0)}{\sigma(45^0)+\sigma(0^0)}=\frac{C}{2+C}, \tag{2.80}$$

is 0.47, in good agreement with the observed value, which is 0.5 in this case.

The value for A calculated by Gayen et al [24] is 0.076. Taking into account only the $B_0^{(3)}$ component of the crystal field and ignoring the dynamic effect, Makhanek et al. [28] obtained a value of 0.47. Leavitt's calculated value for A is 0.32 [27]. Finally, Sztucki and Strek found A = 0.55, 0.15 and 0.52 for the static terms proportional to $B_0^{(1)}$, $B_0^{(3)}$, and the dynamic one, respectively. A recalculation based on the treatment given in section 2.3.3 of this chapter however shows that Leavitt's model gives A equal to 0.17 and 0.16 for the static and dynamic contributions, respectively. The reason of the discrepancies stem from the fact that the number of α_1^2's was being overcounted in expression 13b of ref. [27] . This is because α_1^2 and α_{-1}^2 can not be both nonzero in one TPA transition from one component of a Kramers doublet to another. We also found that Sztucki and Strek's model [17] gives A equal to 0.815, 0.51, and 0.16 for the static terms proportional to $B_0^{(1)}$, $B_0^{(3)}$, and the dynamic one, respectively. We conclude that the third-rank component of the crystal field was in fact the dominant term in the TPA transition intensity from the 4f ground state to the lowest 5d state of the Ce^{3+} ion in CaF_2, as was claimed by Makhanek et al.

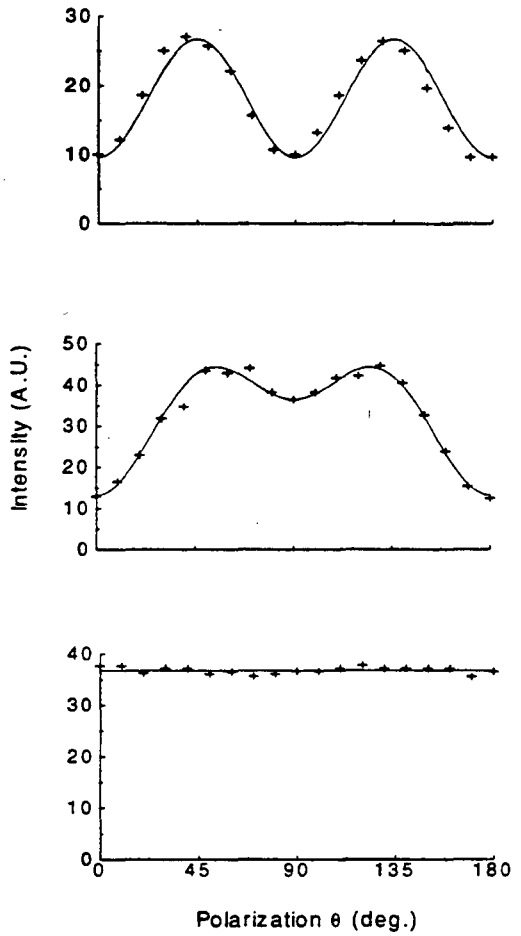

Fig. 2-1: Polarization dependent behavior of the two-photon cross-section for the no-phonon transition of Ce^{3+}:CaF_2 at 6-K. The solid crosses represent the experimental measurements given in ref. [24] and the solid lines are the fits to the data using the angular functions described in equations (2.75), (2.78), and (2.79).

2.4.3 Electronic Raman Scattering and Phonon Raman Scattering

As in the case of two-photon absorption, the polarization dependence functions for ERS and phonon intensities are expressed in terms of the non-vanishing values of the matrix elements of the irreducible representation of the scattering tensors, α_q^t. These polarization dependence functions can be directly compared with the observed intensities, from which the fitted values of α_q^t can be obtained. In the ERS case, the more explicit expressions of α_q^t in terms of the parameters F_t, which arise in the second-order theory of Axe, can then be obtained from equation (2.12). In the second-order approximation, the final polarization dependence functions depend only on two parameters, namely, F_1 and F_2, which in general are simpler than the original polarization dependence functions expressed in terms of α_q^t. The simple expressions of the final polarization dependence thus provide a crucial test for Axe's second-order theory. Another sensitive test for Axe's theory come from the ratio F_1/F_2, which can be derived from the ratio $\alpha_q^1/\alpha_{q'}^2$ obtained from the fit mentioned above. The ratio F_1/F_2 is predicted from the Axe theory to be aprroximately the same for all ERS transitions of a particular rare earth ion. Deviation from the value of the ratio F_1/F_2 would provide insight to further revision of the second-order theory of Axe. Examples and applications of the master equation (2.23) in ERS and phonon Raman scattering processes are given in Chapter 3, where all the experimental Raman scattering data given have been obtained by our group.

2.5 Summary

We have proposed a theoretical framework for obtaining the polarization dependence formulae for two-photon transition intensities of rare-earths doped in crystals. The theory was developed based on the properties of the irreducible representation of the scattering tensors calculated up to the fourth order. A table of angular dependence functions for two-photon transitions for 32 crystallographic point groups was given. Our third-order expression for the TPA scattering tensor taking into account the crystal field interaction agrees with Downer et al's expression for the case of parallel and circular polarization [13]. We have applied our second-order polarization dependence formulae to the $^7F_0$->$^5D_2$ TPA transitions, and the results are identical with those given by Gacon et al [38]. Third-order inter-configurational two-photon absorption was also treated. Its applications in the case of Ce^{3+} in CaF_2 were given. An excellent fit to the experimental polarization dependence curves was obtained. From the fit we have calculated the polarization anisotropy using Sztucki and Strek's model, and we were able to show the dominance of the 4f-5d third-rank crystal field term in contributing to the 4f-5d TPA amplitude in the case of Ce^{3+} in CaF_2, which was in agreement with Makhanek et al [28].

The properties of the irreducible scattering tensor, $\alpha_q^{(t)}$, have been exploited to derive the relationship between the two-photon scattering tensor, α_{21}, and the coupled form of the unit polarization vectors, $(e_2e_1)^{(t)}$. This relationship has been particularly useful in deriving the explicit expression for the intra-configurational two-photon amplitude including the Judd-Ofelt-Axe's second-order term [2-4], Judd-Pooler's third-

order spin-orbit term [10], Downer-Bivas's third-order crystal field term [11-13], Ceulemans-Vandenberghe's fourth order spin-orbit and crystal-field term [14], as well as the inter-configurational TPA amplitude using models given by Leavitt, and Sztucki and Strek [17, 27]. The relative magnitude of higher order contributions to the second order contribution was also discussed based on the properties of $\alpha_q^{(t)}$ and the Wigner-Eckart theorem. Finally, employing the properties of $\alpha_q^{(t)}$ and using the time-reversal invariance properties of the Hamiltonian, we have derived the general theorem proving the equality in magnitude for two-photon transition amplitude calculated either from a Kramers doublet pair or from its conjugate pair in the case of a system of odd number of electrons. Similarly, we have proved for the case of a system of even number of electrons the equal magnitude for two-photon transition amplitude calculated either from a singlet to a state of a doublet or from the singlet to the other state of that doublet.

Appendix A

Using the standard tensor transformation [49] one can write

$$(\mathbf{e}_2\mathbf{e}_1)^{(t)}.\mathbf{U}^{(t)} = \sum_q (-1)^q (\mathbf{e}_2\mathbf{e}_1)^{(t)}.\mathbf{U}_{-q}^{(t)} = \sum_q \sum_{q_1 q_2} (-1)^q (1q_1 1q_2 | 1 1tq)(\mathbf{e}_2)_{q_1}(\mathbf{e}_1)_{q_2}\mathbf{U}_{-q}^{(t)}. \quad \text{(A1)}$$

The scattering tensor (2.10) would then be expressed as

$$\alpha_{21} = \sum_t (-1)^t F_t \sum_q \sum_{q_1 q_2} (-1)^q (1q_1 1q_2 | 1 1tq)(\mathbf{e}_2)_{q_1}(\mathbf{e}_1)_{q_2}\mathbf{U}_{-q}^{(t)}. \quad \text{(A2)}$$

By making the changes q_1->-q_1, q_2->-q_2, and q->q we obtain

$$\alpha_{21} = \sum_{q_1 q_2} \left\{ \sum_t (-1)^t F_t \sum_q \mathbf{U}_q^{(t)} (1-q_1 1-q_2 | 1 1t-q) \right\} (-1)^q (\mathbf{e}_2)_{-q_1}(\mathbf{e}_1)_{-q_2}. \quad \text{(A3)}$$

The transformation from Cartesian to spherical coordinates for the scattering tensor in equation (2.10) is given by

$$\alpha_{21} = \sum_{q_1 q_2} (-1)^q \alpha_{q_1 q_2} (\mathbf{e}_2)_{-q_1}(\mathbf{e}_1)_{-q_2}, \quad \text{(A4)}$$

where $q_1+q_2 = -q$.

Comparing (A3) and (A4) we obtain the following expression for the scattering tensor expressed in the spherical coordinates:

$$\alpha_{q_1 q_2} = \sum_{t,q} (-1)^t F_t \mathbf{U}_q^{(t)} (1-q_1 1-q_2 | 1 1t-q). \quad \text{(A5)}$$

The standard coupling technique of irreducible tensor operators gives

$$\alpha_q^{(t)} = \sum_{q_1 q_2} (1q_1 1q_2 | 1 1tq)\alpha_{q_1 q_2}, \tag{A6}$$

where $\alpha_q^{(t)}$ is a coupled form of the scattering tensor. We then have

$$\alpha_q^{(t)} = \sum_{q_1 q_2} (-1)^{t'} (1q_1 1q_2 | 1 1tq) \sum_{t' q'} F_{t'} \mathbf{U}_{q'}^{(t')} (1-q'_1 1-q'_2 | 1 1t' -q'). \tag{A7}$$

Using the properties of the 3-J symbols, we can write this as

$$\alpha_q^{(t)} = \sum_{t' q'} (-1)^{t'} F_{t'} \mathbf{U}_{q'}^{(t')} \sum_{q_1 q_2} (1q_1 1q_2 | 1 1tq)(1q'_1 1q'_2 | 1 1t' q')(-1)^{t'+2}. \tag{A8}$$

The irreducible scattering tensor now becomes

$$\alpha_q^{(t)} = \sum_{t' q'} (-1)^{t'} (-1)^{t'} F_{t'} \mathbf{U}_q^{(t)} \delta(t,t') \delta(q,q') = F_t \mathbf{U}_q^{(t)}. \tag{A9}$$

Note the compact expression of the irreducible representation of the Raman scattering tensor. In order to obtain this compact form, a factor $(-1)^t$ is present in the expression for F_t. Leaving out this factor in the expression for F_t has led to a sign error for the ratio F_1/F_2 in several papers written by Smentek-Mielczarek [57-59]. The derivation for expression (A9) can also be found in Becker's thesis [50], in which Becker made an error in expression (8), where $(\mathbf{e}_2\mathbf{e}_1)^t$ was given as $(\mathbf{e}_1\mathbf{e}_2)^t$, which is a factor of $(-1)^t$ different from $(\mathbf{e}_2\mathbf{e}_1)^t$. In equation (A4), however, Becker made another error, which accidentally cancels out the previous error he made. In the expression (A9),

$(\mathbf{e}_2)_{-q}(\mathbf{e}_1)_{-q'}$ was written as $(\mathbf{e}_1)_{-q}(\mathbf{e}_2)_{-q'}$, where the latter is equal to the former multiplied by a factor of $(-1)^t$.

Appendix B

Consider the two-photon scattering tensor of the form

$$\begin{aligned}\alpha_{2i} &= \sum_{t=0}^{2}(-1)^t(\mathbf{e}_2\mathbf{e}_1)^{(t)}\cdot \boldsymbol{O}^{(t)} = (\mathbf{e}_2\mathbf{e}_1)^{(0)}\cdot \boldsymbol{O}^{(0)} - (\mathbf{e}_2\mathbf{e}_1)^{(1)}\cdot \boldsymbol{O}^{(1)} + (\mathbf{e}_2\mathbf{e}_1)^{(2)}\cdot \boldsymbol{O}^{(2)} \\ &= (\mathbf{e}_2\mathbf{e}_1)_0^{(0)}\boldsymbol{O}_0^{(0)} + (\mathbf{e}_2\mathbf{e}_1)_{-1}^{(1)}\boldsymbol{O}_1^{(1)} - (\mathbf{e}_2\mathbf{e}_1)_0^{(1)}\boldsymbol{O}_0^{(1)} + (\mathbf{e}_2\mathbf{e}_1)_1^{(1)}\boldsymbol{O}_{-1}^{(1)} \\ &+ (\mathbf{e}_2\mathbf{e}_1)_{-2}^{(2)}\boldsymbol{O}_2^{(2)} - (\mathbf{e}_2\mathbf{e}_1)_{-1}^{(2)}.\boldsymbol{O}_1^{(2)} + (\mathbf{e}_2\mathbf{e}_1)_0^{(2)}\boldsymbol{O}_0^{(2)} - (\mathbf{e}_2\mathbf{e}_1)_1^{(2)}\boldsymbol{O}_{-1}^{(2)} + (\mathbf{e}_2\mathbf{e}_1)_2^{(2)}\boldsymbol{O}_{-2}^{(2)}.\end{aligned} \tag{B1}$$

Decoupling $(\mathbf{e}_2\mathbf{e}_1)_q^{(t)}$ in the circular polar coordinates gives

$$\begin{aligned}
(\mathbf{e}_2\mathbf{e}_1)_0^{(0)} &= (3)^{-1/2}(\mathbf{e}_2)_1^{(1)}(\mathbf{e}_1)_{-1}^{(1)} + (3)^{-1/2}(\mathbf{e}_2)_{-1}^{(1)}(\mathbf{e}_1)_1^{(1)} - (3)^{-1/2}(\mathbf{e}_2)_0^{(1)}(\mathbf{e}_1)_0^{(1)} \\
(\mathbf{e}_2\mathbf{e}_1)_{-1}^{(1)} &= (2)^{-1/2}(\mathbf{e}_2)_0^{(1)}(\mathbf{e}_1)_{-1}^{(1)} - (2)^{-1/2}(\mathbf{e}_2)_{-1}^{(1)}(\mathbf{e}_1)_0^{(1)} \\
(\mathbf{e}_2\mathbf{e}_1)_0^{(1)} &= (2)^{-1/2}(\mathbf{e}_2)_1^{(1)}(\mathbf{e}_1)_{-1}^{(1)} - (2)^{-1/2}(\mathbf{e}_2)_{-1}^{(1)}(\mathbf{e}_1)_1^{(1)} \\
(\mathbf{e}_2\mathbf{e}_1)_1^{(1)} &= (2)^{-1/2}(\mathbf{e}_2)_1^{(1)}(\mathbf{e}_1)_0^{(1)} - (2)^{-1/2}(\mathbf{e}_2)_0^{(1)}(\mathbf{e}_1)_1^{(1)} \\
(\mathbf{e}_2\mathbf{e}_1)_{-2}^{(2)} &= (\mathbf{e}_2)_{-1}^{(1)}(\mathbf{e}_1)_{-1}^{(1)} \\
(\mathbf{e}_2\mathbf{e}_1)_{-1}^{(2)} &= (2)^{-1/2}(\mathbf{e}_2)_0^{(1)}(\mathbf{e}_1)_{-1}^{(1)} + (2)^{-1/2}(\mathbf{e}_2)_{-1}^{(1)}(\mathbf{e}_1)_0^{(1)} \\
(\mathbf{e}_2\mathbf{e}_1)_0^{(2)} &= (6)^{-1/2}(\mathbf{e}_2)_{-1}^{(1)}(\mathbf{e}_1)_1^{(1)} + (6)^{-1/2}(\mathbf{e}_2)_{-1}^{(1)}(\mathbf{e}_1)_1^{(1)} + (2/3)^{1/2}(\mathbf{e}_2)_0^{(1)}(\mathbf{e}_1)_0^{(1)} \\
(\mathbf{e}_2\mathbf{e}_1)_1^{(2)} &= (2)^{-1/2}(\mathbf{e}_2)_1^{(1)}(\mathbf{e}_1)_0^{(1)} + (2)^{-1/2}(\mathbf{e}_2)_0^{(1)}(\mathbf{e}_1)_1^{(1)} \\
(\mathbf{e}_2\mathbf{e}_1)_2^{(2)} &= (\mathbf{e}_2)_1^{(1)}(\mathbf{e}_1)_1^{(1)}.
\end{aligned} \tag{B2}$$

From (B1) and (B2) we can obtain the transition intensity expressions for circular and parallel ($\mathbf{E}\|\hat{\mathbf{z}}$) polarizations. For right circular polarization beams in TPA processes, all terms except $(\mathbf{e}_2)_1^{(1)}$ $(\mathbf{e}_2)_1^{(1)}$ in (B2) vanish. For left circular polarization, only $(\mathbf{e}_2)_{-1}^{(1)}$ $(\mathbf{e}_2)_{-1}^{(1)}$ term is non-zero in (B2). For parallel polarization, only $(\mathbf{e}_2)_0^{(1)}$ $(\mathbf{e}_2)_0^{(1)}$ term is non-zero. The two-photon scattering tensor becomes

$$\boldsymbol{O}_{-2}^{(2)}(\mathbf{e}_2)_1^{(1)}(\mathbf{e}_1)_1^{(1)} \qquad \text{for right circular polarization,} \tag{B3}$$

$$\boldsymbol{O}_{2}^{(2)}(\mathbf{e}_2)_{-1}^{(1)}(\mathbf{e}_1)_{-1}^{(1)} \qquad \text{for left circular polarization,} \tag{B4}$$

and $\quad (\sqrt{\frac{2}{3}}O_0^{(2)} - \frac{1}{\sqrt{3}}O_0^{(0)})(\mathbf{e}_2)_0^{(1)}(\mathbf{e}_1)_0^{(1)} \qquad$ for parallel polarization (B5)

The spherical polar unit vectors are related to the circular polar unit vectors according to the transformation:

$$(\mathbf{e})_1^{(1)} = -(2)^{-1/2}(l + im), \quad (\mathbf{e})_0^{(1)} = n, \quad (\mathbf{e}_1)_{-1}^{(1)} = (2)^{-1/2}(l - im), \tag{B6}$$

where we have used the (l, m, n) notation given in (2.21).

We now substitute (B6) into (B1) to get

$$\begin{aligned}\sum_{t=0}^{2} (-1)^t (\mathbf{e}_2\mathbf{e}_1)^{(t)} \cdot O^{(t)} &= \sum_{t=0}^{2} \sum_{q=-t}^{t} \lambda_q^t O_q^{(t)} \\ &= \lambda_0^{(0)}O_0^{(0)} + \lambda_{-1}^{(1)}O_{-1}^{(1)} + \lambda_0^{(1)}O_0^{(1)} + \lambda_1^{(1)}O_1^{(1)} \\ &+ \lambda_{-2}^{(2)}O_{-2}^{(2)} + \lambda_{-1}^{(2)}.O_{-1}^{(2)} + \lambda_0^{(2)}O_0^{(2)} + \lambda_1^{(2)}O_1^{(2)} + \lambda_2^{(2)}O_2^{(2)},\end{aligned} \tag{B7}$$

where the coefficients λ_q^t 's are defined by

$$\lambda_q^t = (-1)^{t+q}(\mathbf{e}_2\mathbf{e}_1)_{-q}^t, \tag{B8}$$

and

$$\lambda_0^0 = -\frac{1}{\sqrt{3}}[n_2 n_1 + m_2 m_1 + l_2 l_1]$$

$$\lambda_{-1}^1 = \frac{1}{2}[(-m_2 n_1 + n_2 m_1)i + (n_2 l_1 - l_2 n_1)]$$

$$\lambda_0^1 = \frac{i}{\sqrt{2}}[m_2 l_1 - l_2 m_1]$$

$$\lambda_1^1 = \frac{1}{2}[(m_2 n_1 - n_2 m_1)i + (n_2 l_1 - l_2 n_1)]$$

$$\lambda_{-2}^2 = \frac{1}{2}[(l_2 l_1 - m_2 m_1) + (l_2 m_1 + m_2 l_1)i]$$

$$\lambda_{-1}^2 = \frac{1}{2}[(n_2 m_1 + m_2 n_1)i + (n_2 l_1 + l_2 n_1)]$$

$$\lambda_0^2 = \frac{1}{\sqrt{6}}[2n_2 n_1 - m_2 m_1 - l_2 l_1]$$

$$\lambda_1^2 = \frac{1}{2}[(n_2 m_1 + m_2 n_1)i - (n_2 l_1 + l_2 n_1)]$$

$$\lambda_2^2 = \frac{1}{2}[(l_2 l_1 - m_2 m_1) - (l_2 m_1 + m_2 l_1)i], \tag{B9}$$

which is identical to (2.25).

Appendix C

Consider the two-photon scattering tensor of the form

$$\alpha_{21} = \sum_{n,k,t} [(\mathbf{e}_2\mathbf{e}_1)^t B^k]^{(n)} \cdot O^{(n)}(k,t,n) = \sum_{n,k,t} \sum_{w} (-1)^w [(\mathbf{e}_2\mathbf{e}_1)^t B^k]^n_{-w} O^{(n)}_w(k,t,n)$$

$$= \sum_{n,k,t} \sum_{w} \left[\sum_{q,l} (\mathbf{e}_2\mathbf{e}_1)^t_q B^k_l (t\ q\ k\ l \mid n\ \ -w) \right] (-1)^w O^{(n)}_w(k,t,n) \qquad \text{(C1)}$$

$$= \sum_{n,k,t} \sum_{q} \sum_{l} \lambda^t_{-q} (-1)^{t-l} B^k_l (t\ q\ k\ l \mid n\ \ (q+l))\, O^{(n)}_{-q-l}(k,t,n),$$

where we have used (B8) and the relation w = -q-l to obtain the last step in (C1).

If we make the change q -> -q in (C1) and define

$$D_q^{(t)}(k,n,l) = (-1)^{t-l}\, (t\ -q\ k\ l \mid n\ -q+l) \qquad \text{(C2)}$$

and

$$\alpha_q^{(t)}(k,t,n) = \sum_l B^k_l D^{(t)}_q(k,n,l) O^{(n)}_{q-l}(k,t,n), \qquad \text{(C3)}$$

we then get the familiar polarization dependence relation

$$\sum_n \sum_{t=0}^{2} [(\mathbf{e}_2\mathbf{e}_1)^t B^k]^{(n)} \cdot O^{(n)} = \sum_n \sum_{t=0}^{2} \sum_{q=-t}^{t} \lambda^t_q \alpha^{(t)}_q(k,t,n), \qquad \text{(C4)}$$

where the two-photon scattering tensor has been expressed in terms of the polarization dependence functions λ^t_q's defined in (B9) and the irreducible scattering tensor $\alpha_q^{(t)}$'s defined in (C3).

For l=0 the irreducible scattering tensor becomes

$$\alpha_q^{(t)}(k,t,n) = B^k_0 D^{(t)}_q(k,n)\, O^{(n)}_q(k,t,n).$$

The values for $D_q^{(t)}(k,n)$ for k = 1,3, and 4 are tabulated in table 2.2.

Appendix D

We will use the property of the time-reversal invariance T to prove the relation $|\alpha_{21}(\Psi_i \to \Psi_f)|^2 = |\alpha_{21}(\Psi_i^K \to \Psi_f^K)|^2$ and $\alpha_{21}(\Psi_i \to \Psi_{fx})|^2 = |\alpha_{21}(\Psi_i \to \Psi_{fy})|^2$

By definition, the time-reversal operator T is defined by

$$T\Psi(\mathbf{r}_i, \sigma_{zi}, t) = \Psi^*(\mathbf{r}_i, \sigma_{zi}, -t), \tag{D1}$$

where r_i, σ_{zi} represent the electron coordinates and t represents time. The time reversal operator T transforms an eigenfunction of the form

$$\Psi(\mathbf{r}_i, \sigma_{zi}, -t) = \psi(\mathbf{r}_i, \sigma_{zi}) \exp(-iEt/\hbar) \tag{D2}$$

into

$$T\Psi(\mathbf{r}_i, \sigma_{zi}, t) = \psi^*(\mathbf{r}_i, \sigma_{zi}) \exp(-iEt/\hbar), \tag{D3}$$

so that both Ψ and $T\Psi$ belong to the same energy level E. If Ψ and $T\Psi$ are distinct eigenfunctions of the Hamiltonian which is time-reversal invariant, then the eigenstate $T\Psi$ is called the Kramers conjugate state of Ψ and is denoted by Ψ^K. Applying T to the spherical harmonics Y_{lm} we get

$$TY_{lm} = (Y_{lm})^* = (-1)^m Y_{l-m} \tag{D4}$$

or, in the (J,M) basis,

$$T|\alpha,J,M\rangle = |\alpha,J,-M\rangle(-1)^{p+J-M}, \tag{D5}$$

where p is the sum of the parities of the orbitals making up the state $|\alpha,J,M\rangle$, namely

$$p = \sum_{i=1}^{N} l_i \tag{D6}$$

For an odd electron system, Ψ and Ψ^K are related by the relation

$$\Psi\,(K) = \sum_{J,M} |J,-M\rangle\, a^*(J,M)\,(-1)^{J-M}, \tag{D7}$$

$$\text{where } \Psi = \sum_{J,M} |J,M\rangle\, a(J,M). \tag{D8}$$

For an even electron system, Ψ_x and Ψ_y are related by the relation

$$\Psi_x = \sum_{J,M} |J,-M\rangle\, a(J,M), \tag{D9}$$

$$\text{where } \Psi_y = \sum_{J,M} |J,M\rangle\, a(J,M). \tag{D10}$$

A corrollary of (D8) and (D9) is that if Ψ is a singlet, then

$$a(J,M) = a(J,-M) \tag{D11}$$

We consider next the properties of $\langle\Psi_i|\alpha_q^{(t)}|\,\Psi_f\rangle$ and $\langle\Psi_i^K|\alpha_q^{(t)}|\,\Psi_f^{\,K}\rangle$, where $|\Psi\rangle$ represents the $|SLJM\rangle$ intermediate coupling states. It can be shown that

$$\frac{<\Psi\,|\alpha_q^{(t)}|\Psi'>}{<\Psi^K|\alpha_{-q}^{(t)}|\Psi'^K>} =$$

$$\frac{\sum_{SLJ,S'L'J'} a(SLJM)a'(S'L'J'M')\begin{pmatrix} J & t & J' \\ -M & q & M' \end{pmatrix}(-1)^{(J-M)} < SLJ||\alpha^{(t)}||S'L'J'>}{\sum_{SLJ,S'L'J'} a^K(SLJM)a'^K(S'L'J'M')\begin{pmatrix} J & t & J' \\ M & -q & -M' \end{pmatrix}(-1)^{(J+M)} < SLJ||\alpha^{(t)}||S'L'J'>}$$

$$= (-1)^{2(J+J'+M-M')+t} = (-1)^t.$$

(D12)

Combining (D12) and (26) we get $|\alpha_{21}(\Psi_i \to \Psi_f)|^2 = |\alpha_{21}(\Psi_i^K \to \Psi_f^K)|^2$.

Similarly, it can be shown

$$\frac{<\Psi\,|\alpha_q^{(t)}|\Psi'_x>}{<\Psi\,|\alpha_{-q}^{(t)}|\Psi'_y>} =$$

$$\frac{\sum_{SLJ,S'L'J'} a(SLJM)a_x'(S'L'J'M')\begin{pmatrix} J & t & J' \\ -M & q & M' \end{pmatrix}(-1)^{(J-M)} < SLJ||\alpha^{(t)}||S'L'J'>}{\sum_{SLJ,S'L'J'} a(SLJ-M)a_y'(S'L'J'M')\begin{pmatrix} J & t & J' \\ M & -q & -M' \end{pmatrix}(-1)^{(J+M)} < SLJ||\alpha^{(t)}||S'L'J'>}$$

$$= (-1)^t.$$

(D13)

Combining (D13) and (26) we get $|\alpha_{21}(\Psi \to \Psi_x')|^2 = |\alpha_{21}(\Psi \to \Psi_y')|^2$.

References

[1] M. Downer, in *Laser Specroscopy of Solids II*, edited by W. M. Yen (Springer Verlag, New York, 1989).

[2] B. R. Judd, Phys. Rev. **127**, 750 (1962).

[3] G. S. Ofelt, J. Chem. Phys. **37**, 511 (1962).

[4] J. D. Axe, Phys. Rev. **136A**, 42 (1964).

[5] W. T. Carnall, H. Crosswhite, and H. M. Crosswhite, *Energy Level Structure and Transition Probabilities of Trivalent Lanthanides in* LaF_3 (Argonne National Laboratory Report, 1977).

[6] W. T. Carnall, Pr. Fields, and B. G. Wybourne, J. Chem. Phys. **42**, 3797 (1965).

[7] R. D. Peacock, Struc. Bonding **22**, 83 (1975).

[8] C. W. Nielson and G. F. Koster, *Spectroscopic Coefficients of the* p^n, d^n, *and* f^n *Configurations* (The M.I.T. Press, Cambridge, Massachussetts, 1963).

[9] M. Dagenais, M. Downer, R. Neumann, and N. Bloembergen, Phys. Rev. Lett. **46**, 561 (1981).

[10] B. R. Judd and D. R. Pooler, J. Phys. C **15**, 591 (1982).

[11] M. C. Downer, A. Bivas, and N. Bloembergen, Opt. Commun. **41**, 335 (1982).

[12] M. C. Downer, Ph. D. thesis, Harvard University, 1983.

[13] M. C. Downer and A. Bivas, Phys. Rev. B **28**, 3677 (1983).

[14] A. Celemans and G. M. Vandengberghe, J. Chem. Phys. **98**, 9372 (1993).

[15] M. F. Reid and F. Richardson, Phys. Rev. B **29**, 2830 (1984).

[16] J. Sztucki and W. Strek, Phys. Rev. B **34**, 3120 (1986).

[17] J. Sztucki and W. Strek, Chem. Phys. Lett. **125**, 520 (1986).

[18] K. Jankowski and L. Smentek-Mielczarek, Mol. Phys. **60**, 1211 (1987).

[19] L. Smentek-Mielczarek and B. Andes Hess, Jr., Phys. Rev. B **36**, 1811 (1987).

[20] K. Jankowski and L. Smentek-Mielczarek, Mol. Phys. **38**, 1445 (1979).

[21] L. Smentek-Mielczarek and K. Jankowski, Mol. Phys. **38**, 1459 (1979).

[22] S. K. Gayen and D. S. Hamilton, Phys. Rev. B **28**, 3706 (1983).

[23] S. K. Gayen, G. J. Pogatshnik, and D. S. Hamilton, J. Lumin. **31/32**, 260 (1984).

[24] S. K. Gayen, D. S. Hamilton, and R. H. Bartram, Phys. Rev. B **34**, 7517 (1986).

[25] C. Pedrini et al., J. Phys. Condens. Matter **4**, 5461 (1992).

[26] J. Sytsma et al., Phys. Rev. B **47**, 14786 (1993).

[27] R. C. Leavitt, Phys. Rev. B **35**, 9271 (1987).

[28] A. G. Makhanek, V. S. Korolkov, and L. A. Yuguryan, Phys. Stat. Sol. B **149**, 231 (1988).

[29] A. G. Makhanek and V. S. Korolkov, *Analytical Methods in Perturbation Theory of Quantum Mechanics* (Izd. Nauka I Tekhnika, Minsk 1982).

[30] M. Kibler, in *Symmetry and Structural Properties of Condensed Matter*, edited by W. Florek, T. Lulek, and D. Lipinski (World Scientific, Singapore, 1991).

[31] M. R. Kibler, in *Recent Advances in Group Theory and Their Applications to Spectroscopy*, edited by J. C. Donini (Plenum, New York, 1979).

[32] M. Daoud and M. Kibler, Laser Phys. **2**, 704 (1992).

[33] M. Inoue and Y. Toyozawa, J. Phys. Soc. Japan **20**, 363 (1965).

[34] T. R. Bader and A. Gold, Phys. Rev. **171**, 997 (1968).

[35] J. Sztucki, M. Daoud, and M. Kibler, Phys. Rev. B **45**, 2023 (1992).

[36] J. C. Gâcon, G. W. Burdick, B. Moine, and H. Bill, Phys. Rev. B **47**, 11712 (1993).

[37] J. C. Gâcon, B. Jacquier, J. F. Marcerou, M. Bouazaoui and M. Kibler, J. Lum. **45**, 162 (1990).

[38] J. C. Gâcon, G. Grenet, J. C. Souillat, and M. Kibler, J. Chem. Phys. **69**, 868 (1978).

[39] J. C. Gâcon, J. F. Marcerou, M. Bouazaoui, B. Jacquier, and M. Kibler, Phys. Rev. B **40**, 2070 (1989).

[40] M. Kibler and J. C. Gâcon, Croat. Chem. Acta **62**, 783 (1989).

[41] J. C. Gâcon, M. Bouazaoui, B. Jacquier, M. Kibler, L. A. Boatner, and M. M. Abraham, Eur. J. Solid State Inorg. Chem. **28**, 113 (1991).

[42] J. Sztucki and W. Strek, Chem. Phys. **143**, 347 (1990).

[43] J. A. Koningstein and O. S. Mortensen, Phys. Rev. **168**, 75 (1968).

[44] O. S. Mortensen and J. A. Koningstein, J. Chem. Phys. **48**, 3971 (1968).

[45] J. A. Koningstein and O. S. Mortensen, J. Opt. Soc. Am. **58**, 1208 (1968).

[46] G. Placzek, *Handbuch der Radiologie* (Leipzig, 1934), Vol. VI, Part II, p. 205.

[47] In our expression for the two-photon scattering amplitude, the initial state is written on the left, the final state on the right, and the scattered photon's electric field vector is written to the left of that for the incident photon. This notation is different

from that used by Becker and coworkers, in which the initial state was written on the right, the final state on the left.

[48] We have used Downer's expression for **D**, given in Ref. 1, in which the matrix element used to evaluate **D** is written from left to right:

$$\mathbf{D} = \langle nl \mid r\, \mathbf{C}^{(1)} \mid n'l' \rangle,$$

where $\mathbf{C}^{(1)}$ is a spherical tensor depending on the rare-earth electron coordinates.

[49] B. R. Judd, *Operator Techniques in Atomic Spectroscopy* (New York, McGraw-Hill, 1963).

[50] P. C. Becker, Ph.D. thesis, University of California, Berkeley, 1986.

[51] J. A. Koningstein, *Introduction to the theory of the Raman Effect* (D. Reidel Publishing Company, Dordrecht-Holland, 1972).

[52] B. Gachter, J. Mol. Spec. **63**, 1 (1976).

[53] G. Koster, J. Dimmock, R. Wheeler, and H. Statz, *Properties of the thirty-two point groups* (The M.I.T. Press, Cambridge, Massachussetts, 1963).

[54] P. C. Becker, N. Edelstein, G. M. Williams, J. J. Bucher, R. E. Russo, J. A. Koningstein, L. A. Boatner, and M. M. Abraham, Phys. Rev. B **31**, 8102 (1985).

[55] B. R. Judd, *Second Quantization and Atomic Spectroscopy* (The Johns Hopins Press, Baltimore, 1967).

[56] Here we have used Koster et al's notation (24). To compare with table 2.1, we make the following changes for the case of C_{4v} site symmetry: $\Gamma_1 = A_1$, $\Gamma_3 = B_1$, $\Gamma_4 = B_2$, and $\Gamma_5 = E$.

[57] L. Smentek-Mielczarek, Phys. Rev. B **46**, 14467 (1992).

[58] L. Smentek-Mielczarek, J. Chem. Phys. **94**, 5369 (1991).

[59] L. Smentek-Mielczarek, Phys. Rev. B **40**, 6499 (1989).

Chapter 3

Experimental Aspects

This chapter and subsequent chapters present the experimental verification for the proposed polarization dependence theory given in chapter two. Most of the experimental work on phonon scattering and ERS has been done by myself, but the experiments on two-photon absorption have been the collaboration between myself and Dr. Keith Murdoch. This chapter deals with the experimental aspect of the polarization dependence method used in ERS and TPA experiments. Phonon scattering and ERS experimental results for $PrVO_4$, $NdVO_4$, $ErVO_4$, and $TmVO_4$ are discussed together in chapter four. TPA experimental results for Eu^{3+} and Cm^{3+} in $LuPO_4$ are discussed in chapter five.

3.1 Polarization Dependence Spectroscopy - Overview

3.1.1 General Approach to Raman Spectroscopy

As discussed in chapters one and two, major developments of quantitative two-photon spectroscopic studies of rare-earth materials have been built upon the Judd-Ofelt-Axe theory. It is therefore an important undertaking to verify Axe's theory. The aim of this section is to discuss a reliable method for the test of this theory using the ERS polarization dependence technique which is a modified version of Becker et al.'s

technique [1,2]. The results will be applied to $PrVO_4$, $NdVO_4$, $ErVO_4$, and $TmVO_4$ in the following chapter.

Becker et al's sensitive test of Axe's theory [3] comes from comparison between the observed and calculated intensities of the ERS transitions in rare-earth doped crystals. Following Koningstein and Mortensen [4], who observed that ERS spectra display asymmetric features (e.g., $I_{XZ} \neq I_{ZY}$, where the first and second subscripts indicate the polarizations of the scattered and incident photons, respectively), Becker et al showed that the ratio of the intensity corresponding to XZ or YZ polarization to the intensity corresponding to ZX or ZY polarization may provide a sensitive test of the second-order theory. This is because this ratio is related to the ratio F_1/F_2, which in turn can be directly estimated by Axe's theory. The value of F_1/F_2 obtained from experiment can then be compared with the value obtained ab initio using the second order theory of Axe. Becker et al's extensive study of ERS in rare-earth phosphate crystals, nevertheless, indicate poor agreements between calculated and experimental intensity results [2]. This inadequacy of the second-order theory motivated further theoretical investigations in the third-order regime by Smentek-Mielczarek [5]. Even with the extension to the third-order theory, only moderate agreement with observed data was found.

We have listed in chapter 2 the expressions for the polarization dependent behavior of the ERS and two-photon absorption transition intensities. The results can also be applied to phonon scattering, and a tabulation for two photon polarization dependence functions for the 32 crystallographic point groups has been produced. The

new results, when applied to a particular system, yield expressions of polarization functions that depend only on two parameters F_1 and F_2, which in turn depend only on the properties of the ion being considered and which can be treated as phenomenological constants or can be estimated if the energies of the excited configurations and the overlap integrals of the excited and ground configurations are known. These factors immediately suggest a new, more reliable method to obtain a fit for the value of the ratio $\tau = F_1/F_2$. From the old method used by Becker and coworkers, this ratio was extracted from only two data points, namely I_{XZ} and I_{ZX} at 0° and 90° (parallel and perpendicular to the crystal axis). The new method, however, allows the extraction of the ratio from an unlimited number of ERS data points associated with $I(\theta_i,\phi_i)$ and $I(\theta_s,\phi_s)$, where θ_i, ϕ_i, θ_s, and ϕ_s describe the polarization states of the incoming and scattered photons, which can be arbitrarily varied. These ERS data points, furthermore, can be calibrated using phonon polarization dependent intensities to yield more accurate ERS polarization information. The calibration procedure will be described in detail in section 3.3.2.

In order to extract the experimental values of $\tau = F_1/F_2$ for Pr^{3+}, Nd^{3+}, Er^{3+}, and Tm^{3+} in $PrVO_4$, $NdVO_4$, $ErVO_4$, and $TmVO_4$, respectively, the crystal field wavefunctions for the ground multiplet of these ions must be known. The wavefunctions used in this work come from results published elsewhere or from crystal field fits whose crystal field parameters used as input have been taken from literature. Table 3.1 lists the parameters for crystal field fits for RE^{3+} in $REVO_4$ or YVO_4, where RE represent Pr, Nd, Er, and Tm. Most of these crystal field parameters were derived

from diluted crystals, in which the rare earth ion in consideration has been doped into YVO_4. It is however expected that the energy level structure and wavefunctions of the diluted crystals will be approximately the same as that of the pure vanadate crystals, as it has been the case for phosphate crystals [2].

Table 3.1: Fitted parameters for RE^{3+} in $REVO_4$ or YVO_4

RE^{3+}	$4f^N$	Crystal field parameters (cm^{-1})					Spin-orbit	References
		B_0^2	B_0^4	B_0^6	B_4^4	B_4^6	ζ_{4f} (cm^{-1})	
Pr^{3+}	$4f^2$	-77	71	-68	970	-200	739 (*)	[6,7]
Nd^{3+}	$4f^3$	302	273	-1245	-777	-109	880	[8]
Er^{3+}	$4f^{11}$	-218	322	-702	917	10	2366	[7,9]
Tm^{3+}	$4f^{12}$	-175	337	-612	832	-50	2642	[10]

(*)derived from $RE^{3+}:YPO_4$

Table 3.2: Raman activity of D_{2d} point group

Symmetry of electronic transition (D_{2d} point group)	Raman activity $\alpha_q^t = \langle\Gamma_i\|\alpha_q^{(t)}\|\Gamma_f\rangle$
Γ_1	α_0^0, α_0^2
Γ_2	α_0^1
Γ_3	$\alpha_2^2, \alpha_{-2}^2$
Γ_4	$\alpha_2^2, \alpha_{-2}^2$
$\Gamma_{5x}^{(*)}$	α_1^2, α_1^1
$\Gamma_{5y}^{(*)}$	$\alpha_{-1}^2, \alpha_{-1}^2$

(*)Γ_{5x} and Γ_{5y} represent the crystal field states of the Γ_5 doublet.

Once the crystal field wavefunctions have been obtained, the explicit expressions for the matrix elements of the irreducible scattering tensors α_q^t's in terms of F_t can be determined. In general selection rules can be used to determine which α_q^t's are non-zero. The point group symmetry for Pr^{3+}, Nd^{3+}, Er^{3+}, and Tm^{3+} in pure vanadate

crystals is D_{2d}. Using table 2.1 we obtain the Raman activity for a rare-earth ion of point group symmetry D_{2d} listed in table 3.2.

From the selection rules given in chapter 1 and the Raman activity in table 3.2, the polarization dependence function for each ERS transition can be determined. The observed polarization dependence curves can then be fitted with the predicted curves. The relative values of α_q^{t}'s can be extracted, from which the experimental value of τ can be determined. The procedure stated above is summarized in the following diagram:

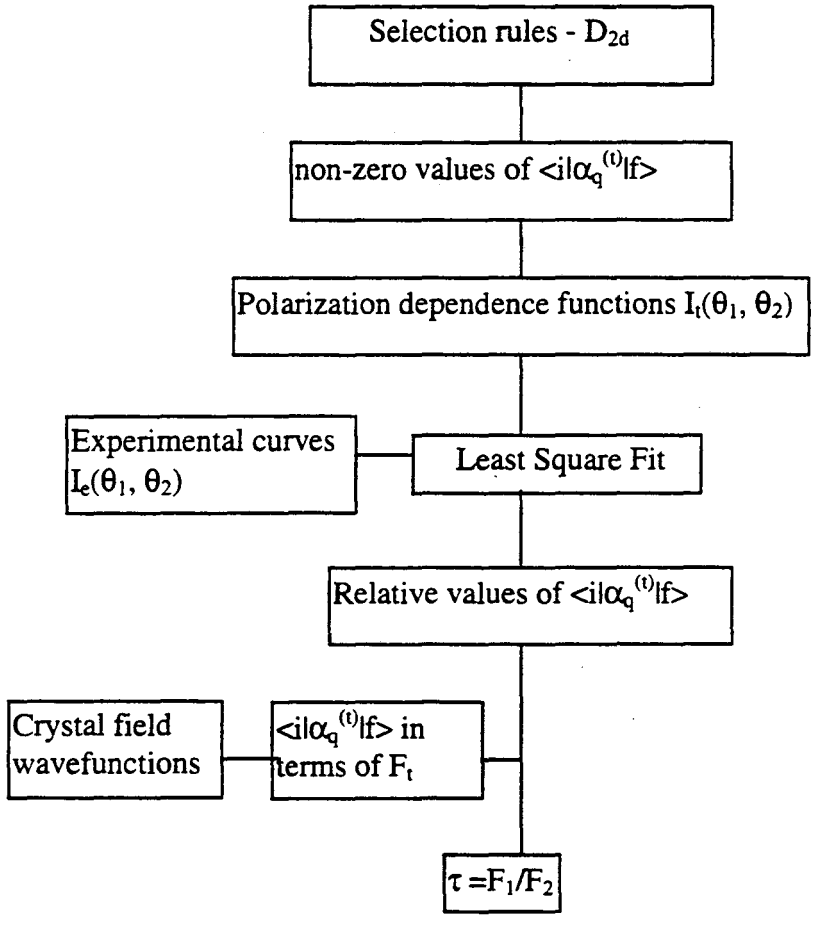

3.1.2 General Approach to TPA Spectroscopy

The experimental and data analysis procedures for polarization dependent TPA experiments are similar to that for ERS experiments. For the case of TPA from the same excitation source, $\alpha_q^1 = 0$ for all transitions. The polarization dependence functions for TPA transitions can thus be expressed in terms of α_q^2. The Raman activity listed in table 2.1 can be used to determine the nonzero α_q^2 in TPA transitions for a rare-earth ion of point group symmetry D_{2d}. With the crystal field wavefunctions provided, α_q^2's can be expressed in terms of F_2. The observed polarization dependence curves will then be fitted with the predicted curves. The observed relative TPA intensities for different transitions can be compared with prediction. For a rare-earth ion with an even number of electrons in the outer shell, the polarization dependence formulas generally depend on only one nonzero values of α_q^2. The polarization dependence expressions for this system would look the same regardless of whether or not α_q^2 can be further expressed in terms of F_2. The relative intensities among different transitions predicted from the second order theory, however, would depend only on F_2, which is the same for all transitions of a particular system. The ratio of these intensities therefore would not contain any unknown parameters and could be compared with observation. For a transition with more than one nonzero α_q^2 (such as a transition between Kramers states), the observed intensities can be fitted first with the theoretical polarization dependence expressions, which now depend on more than one nonzero α_q^2. The ratio of the relative values of α_q^2 for different q can be extracted from the fit and compared with the calculated values. Both the fitted values of the relative α_q^2 and the observed polarization

dependence of TPA intensities for each transition will provide a sensitive test for Axe's second order theory.

3.2 Applications to Polarization Dependent Intensities

3.2.1 Phonon Raman Scattering

The polarization dependence functions corresponding to phonon scattering intensities can be found in table 2.1. We denote by e_1 and e_2 the incident and scattered unit polarization vectors, respectively. Taking into account the 45° rotation of the RE^{3+} center about the Z axis and the scattering geometry, in which scattered light is detected at 90° with respect to the incident beam (fig. 3.1), the required coordinate transformations are given by:

$$\theta_1 \to \theta_1, \quad \theta_2 \to \theta_2, \quad \varphi_1 \to -45^\circ, \quad \varphi_2 \to 45^\circ. \tag{3.1}$$

Noting that in nonresonant scattering, α_q^1's vanish for all phonon modes, the formulas corresponding to the D_{4h} point group become

A_{1g} mode: $|\alpha_{21}(A_{1g})|^2 = \cos^2\theta_1 \cos^2\theta_2 \left(\frac{-\alpha_0^0 + \sqrt{2}\alpha_0^2}{\sqrt{3}}\right)^2$

B_{1g} mode: $|\alpha_{21}(B_{1g})|^2 = \sin^2\theta_1 \sin^2\theta_2 \left(\frac{\alpha_2^2 + \alpha_{-2}^2}{2}\right)^2$

B_{2g} mode: $|\alpha_{21}(B_{2g})|^2 = 0$

E_g mode: $|\alpha_{21}(E_{1g})|^2 = \left(\frac{\alpha_1^2}{2}\right)^2 [\sin^2(\theta_1 - \theta_2) + \sin^2(\theta_2 + \theta_1)]$ (3.2)

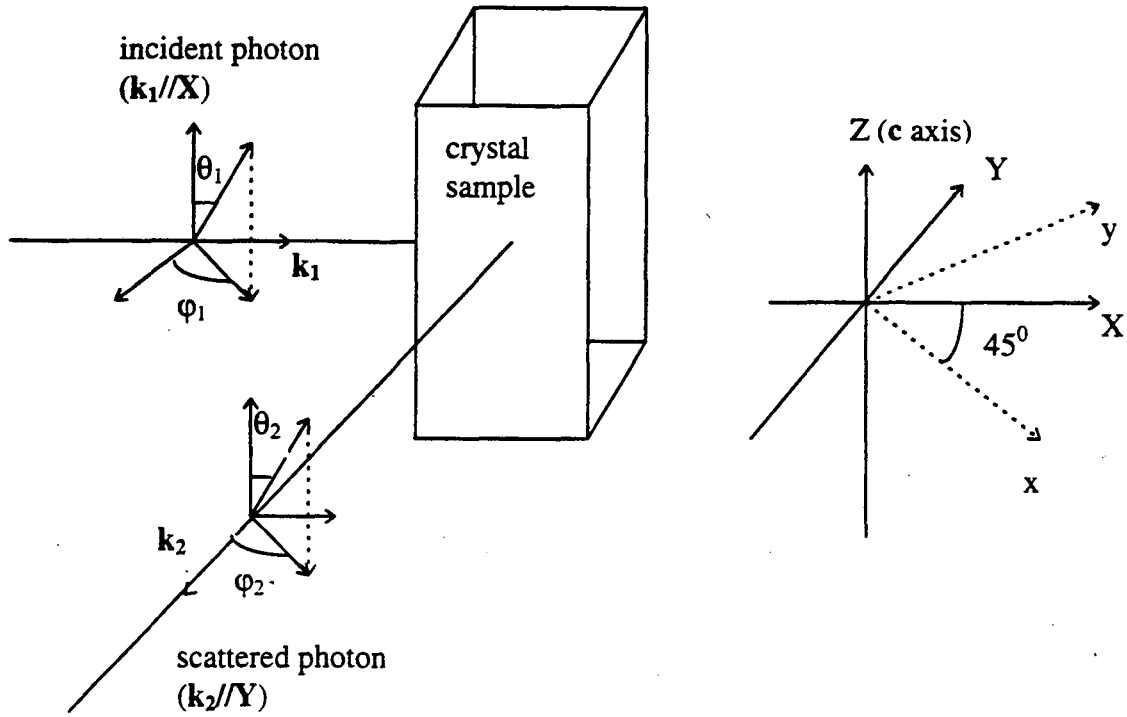

Fig. 3-1: Crystal orientation in Raman experiments. X,Y,Z represent the crystallographic axes; x,y,z represent the symmetry axes.

The polarization dependence functions corresponding to E_g modes at fixed values of θ_1 have the following simple forms:

$$f(\theta_2,0) = [(\alpha_1^2)^2 / 2]\sin^2\theta_2$$

$$f(\theta_2,\pm 22.5^o) = [(\alpha_1^2)^2 / 2](.85\sin^2\theta_2 + .15\cos^2\theta_2)$$

$$f(\theta_2,\pm 45^o) = [(\alpha_1^2)^2 / 2]$$

$$f(\theta_2,\pm 67.5^o) = [(\alpha_1^2)^2 / 2](.85\cos^2\theta_2 + .15\sin^2\theta_2)$$

$$f(\theta_2,\pm 90^o) = [(\alpha_1^2)^2 / 2]\cos^2\theta_2 \qquad (3.3)$$

A particularly interesting case for E_g mode is when $\theta_1 = 45^0$ the scattering intensity is a constant, independent of θ_2, and vice versa. This can be conveniently used as a guide to check the crystal alignment at both room and low temperature.

3.2.2 Electronic Raman Scattering

Following the development in chapter two, the general formula for the polarization dependence of the Raman scattering tensor is given by

$$
\begin{aligned}
\alpha_{e_2e_1} = & (-\frac{1}{\sqrt{3}})[n_2n_1 + m_2m_1 + l_2l_1]\alpha_0^{(0)} \\
& + (-\frac{1}{\sqrt{6}})[-2n_2n_1 + m_2m_1 + l_2l_1]\alpha_0^{(2)} \\
& + \frac{1}{2}[(n_2m_1 + m_2n_1)i - (n_2l_1 + l_2n_1)]\alpha_1^{(2)} \\
& + \frac{1}{2}[(n_2m_1 + m_2n_1)i + (n_2l_1 + l_2n_1)]\alpha_{-1}^{(2)} \\
& + \frac{1}{2}[(l_2l_1 - m_2m_1) - (l_2m_1 + m_2l_1)i]\alpha_2^{(2)} \\
& + \frac{1}{2}[(l_2l_1 - m_2m_1) + (l_2m_1 + m_2l_1)i]\alpha_{-2}^{(2)} \\
& + \frac{i}{2}[m_2l_1 - l_2m_1]\alpha_0^{(1)} \\
& + \frac{1}{2}[(m_2n_1 - n_2m_1)i + (n_2l_1 - l_2n_1)]\alpha_1^{(1)} \\
& + \frac{1}{2}[(-m_2n_1 + n_2m_1)i + (n_2l_1 - l_2n_1)]\alpha_{-1}^{(1)}
\end{aligned}
\tag{3.4}
$$

In equation (3.4), the terms $\alpha_q^{(t)}$'s, where t = 0, 1, 2 and q = -2, -1, ... , 2, are the irreducible second-rank tensors, and

$$(l_i, m_i, n_i) = (\sin\theta_i \cos\varphi_i, \sin\theta_i \sin\varphi_i, \cos\theta_i), \tag{3.5}$$

where (θ_i, φ_i) are the polar angles of the unit polarization vector $\boldsymbol{e}_i$ with respect to the crystallographic c-axis.

The initial and final crystal-field levels can be written in terms of Russell-Saunders coupled wave functions:

$$
\begin{aligned}
|i\rangle &= \sum_{\alpha SLJJ_z} a(i; nf^N \mu SLJJ_z)|nf^N \mu SLJJ_z\rangle, \\
|f\rangle &= \sum_{\alpha' S'L'J'J'_z} a'(f; nf^N \mu' S'L'J'J'_z)|nf^N \mu' S'L'J'J'_z\rangle,
\end{aligned}
\tag{3.6}
$$

The electronic Raman amplitude for the transition between states |i> and |f> is given by

$$\langle i|\alpha_q^{(t)}|f\rangle = F_t^{ERS} \sum_{\alpha SLJJ_z} \sum_{\alpha' S'L'J'J'_z} a(i;nf^N\mu SLJJ_z)a'(f;nf^N\mu' S'L'J'J_z') \times \langle nf^N\mu SLJJ_z|\mathbf{U}_q^{(t)}|nf^N\mu' S'L'J'J_z'\rangle, \tag{3.7}$$

where

$$\langle nf^N\mu SLJJ_z|\mathbf{U}_q^{(t)}|nf^N\mu' S'L'J'J_z'\rangle = (-1)^{2J'+S+L'+t-J_z}[(2J'+1)(2J+1)]^{\frac{1}{2}}\begin{pmatrix} J & t & J' \\ -J_z & q & J_z' \end{pmatrix}\begin{Bmatrix} L & J & S \\ J' & L' & t \end{Bmatrix}\langle SL||\mathbf{U}^{(t)}||SL'\rangle\delta(S,S'). \tag{3.8}$$

and

$$F_t^{ERS} = (-1)^t \sum_{nf^{N-1}n'l'} 7(2l'+1)\begin{pmatrix} 3 & 1 & l' \\ 0 & 0 & 0 \end{pmatrix}^2 \langle nf|r|n'l'\rangle^2 \times (2t+1)^{\frac{1}{2}}\begin{Bmatrix} 1 & 3 & l' \\ 3 & 1 & t \end{Bmatrix}\left[\frac{1}{E_{n'l'}-\hbar\omega_1} + \frac{(-1)^t}{E_{n'l'}+\hbar\omega_2}\right], \tag{3.9}$$

It is instructive to examine the explicit expressions of F_1 and F_2. Making the approximations $\omega_i \approx \omega_s = \omega$ and $\omega_i << E_{df}$ we have

$$F_1^{ERS} = -7(3)^{\frac{1}{2}} \sum_{4f^{N-1}n'l'} (2l'+1)\langle 4f|r|n'l'\rangle^2 \begin{pmatrix} 3 & 1 & l' \\ 0 & 0 & 0 \end{pmatrix}^2 \begin{Bmatrix} 1 & 3 & l' \\ 3 & 1 & 1 \end{Bmatrix} \frac{2\hbar\omega}{E_{l'}^2},$$

and

$$F_2^{ERS} = 7(5)^{\frac{1}{2}} \sum_{4f^{N-1}n'l'} (2l'+1)\langle 4f|r|n'l'\rangle^2 \begin{pmatrix} 3 & 1 & l' \\ 0 & 0 & 0 \end{pmatrix}^2 \begin{Bmatrix} 1 & 3 & l' \\ 3 & 1 & 2 \end{Bmatrix} \frac{2}{E_{l'}}. \tag{3.10}$$

We now compare separately the contributions of the d and g orbital configurations.

For the d orbitals:

$$F_{1d}^{ERS} = \frac{\sqrt{6}}{\sqrt{7}} \sum_{4f^{N-1}5d} \langle 4f|r|5d\rangle^2 \frac{2\hbar\omega}{E_d^2},$$

and $$F_{2d}^{ERS} = \frac{3\sqrt{2}}{\sqrt{35}} \sum_{4f^{N-1}5d} \langle 4f|r|5d\rangle^2 \frac{2}{E_d}. \tag{3.11}$$

For the g orbitals:

$$F_{1g}^{ERS} = -\frac{2\sqrt{3}}{\sqrt{14}} \sum_{4f^{N-1}5g} \langle 4f|r|5g\rangle^2 \frac{2\hbar\omega}{E_g^2},$$

and $$F_{2g}^{ERS} = \frac{2\sqrt{5}}{3\sqrt{14}} \sum_{4f^{N-1}5g} \langle 4f|r|5g\rangle^2 \frac{2}{E_g}. \tag{3.12}$$

Assuming the degeneracy of the g- and d- orbital configuration energy levels, the ratio F_1/F_2 is given by the simple relation:

$$\tau = \frac{F_1}{F_2} = \frac{F_{1d} + F_{1g}}{F_{2d} + F_{2g}} = \frac{\sqrt{3}}{\sqrt{5}} \hbar\omega \frac{\left(\frac{1}{E_d^{\,2}} - \frac{R}{E_g^{\,2}}\right)}{\left(\frac{3}{5E_d} + \frac{R}{3E_g}\right)}, \tag{3.13}$$

where $$R = \frac{|\langle 4f|r|5g\rangle|^2}{|\langle 4f|r|5d\rangle|^2}. \tag{3.14}$$

The irreducible scattering tensor corresponding to the third order spin orbit interaction has the form

$$(\alpha_q^{(t)})^{3rd} = H(t)\,(\mathbf{a}^\dagger\mathbf{a})_q^{(0t)t}(\mathbf{a}^\dagger\mathbf{a})^{(11)0} + \sum_\lambda G(t,\lambda)\,(\mathbf{a}^\dagger\mathbf{a})_q^{(1\lambda)t}, \tag{3.15}$$

where $\mathbf{a}^{\dagger}$, $\mathbf{a}$ represent creation and annihilation tensors, t can be 0, 1, or 2, and $H(t)$, $G(t,\lambda)$ have the following expressions for l=3 and l'=2:

$$
\begin{aligned}
&H(0)=\frac{6\zeta_{sf}}{E_{df}^2}(f|r|d)^2,\ H(1)=\frac{2\sqrt{6}\zeta_{sf}}{E_{df}^2}(f|r|d)^2,\ H(2)=\frac{6\sqrt{6}\zeta_{sf}}{5E_{df}^2}(f|r|d)^2,\\
&G(0,1)=\frac{(6\zeta_{sf}-4\zeta_{sd})}{\sqrt{14}E_{df}^2}(f|r|d)^2,\ G(1,1)=\frac{-\zeta_{sf}}{\sqrt{14}E_{df}^2}(f|r|d)^2,\ G(1,2)=\frac{(5\zeta_{sf}-4\zeta_{sd})\sqrt{3}}{\sqrt{70}E_{df}^2}(f|r|d)^2,\\
&G(2,1)=\frac{(-18\zeta_{sf}+8\zeta_{sd})}{\sqrt{1400}E_{df}^2}(f|r|d)^2,\ G(2,2)=\frac{-3\sqrt{42}\zeta_{sf}}{70E_{df}^2}(f|r|d)^2,\\
&G(2,3)=\frac{3\sqrt{42}(\zeta_{sf}-\zeta_{sd})}{35E_{df}^2}(f|r|d)^2.
\end{aligned}
\tag{3.16}
$$

The first term of the right hand side of equation (3.15) is a scalar product of coupled tensors. Since this term can connect non-identical initial and final states, the matrix elements of $\alpha_q^{(0)}$ no longer vanish. For t = 0, we have two contributions

$$i)S_{00}=H(0)\,(\mathbf{a}^{\dagger}\mathbf{a})_0^{(00)0}(\mathbf{a}^{\dagger}\mathbf{a})^{(11)0} \tag{3.17}$$

Since the eigenvalue of $(\mathbf{a}^{\dagger}\mathbf{a})_0^{(00)0}$ is $-N(14)^{-1/2}$ when sandwiched between (l^NSLJJ$_z$| and |l^NS'L'J'J$_z$'), the first term of $\alpha_0^{(0)}$ becomes $N(14)^{-1/2}\,H(0)\mathbf{W}_0^{(11)0}$, where $\mathbf{W}_0^{(11)0}$ represents the standard sum of single-particle double-tensor operators.

$$ii)S_{01}=G(0,1)(\mathbf{a}^{\dagger}\mathbf{a})_0^{(11)0}$$

The total third order contribution for the case t=0 is

$$
\begin{aligned}
&(l^N SLJM|(\alpha_0^0)^{3rd}|l^N S'L'J'M')=(l^N SLJM|S_{00}+S_{01}|l^N S'L'J'M')\\
&[\frac{N}{\sqrt{14}}H(0)-G(0,1)](-1)^{J-M}\begin{pmatrix} J & 0 & J' \\ -M & 0 & M' \end{pmatrix}(l^N SLJ||\mathbf{W}^{(11)0}||l^N S'L'J').
\end{aligned}
\tag{3.18}
$$

For t=1, we have three contributions

$$i) S_{10} = H(1)\,(\mathbf{a}^{\dagger}\mathbf{a})_q^{(01)1}(\mathbf{a}^{\dagger}\mathbf{a})^{(11)0} = H(1)\mathbf{W}^{(11)0}\sqrt{\frac{3}{2}}\mathbf{U}_q^{(1)}$$

$$\begin{aligned}
&(l^N\alpha SLJM|S_{10}|l^N\alpha' S'L'J'M') = \sqrt{\frac{3}{2}}H(1)(-1)^{J-M}\begin{pmatrix} J & 1 & J' \\ -M & q & M' \end{pmatrix}[J']^{-1/2} \\
&\times\sum_{\alpha''L''}(l^N\alpha SLJ||\mathbf{U}^{(1)}||l^N\alpha'' SL''J')(l^N\alpha'' SL''J'||\mathbf{W}^{(11)0}||l^N\alpha' S'L'J') \\
&= \sqrt{\frac{3}{2}}H(1)(-1)^{J-M}\begin{pmatrix} J & 1 & J' \\ -M & q & M' \end{pmatrix}[J']^{-1/2} \\
&\times(l^N\alpha SLJ||\mathbf{U}^{(1)}||l^N\alpha SLJ)(l^N\alpha SLJ||\mathbf{W}^{(11)0}||l^N\alpha' S'L'J')
\end{aligned} \tag{3.19}$$

$$ii) S_{11} = G(1,1)(\mathbf{a}^{\dagger}\mathbf{a})_q^{(11)1} \tag{3.20}$$

$$iii) S_{12} = G(1,2)(\mathbf{a}^{\dagger}\mathbf{a})_q^{(12)1}. \tag{3.21}$$

For t=2, we have several contributions

$$i) S_{20} = H(2)\,(\mathbf{a}^{\dagger}\mathbf{a})_q^{(02)2}(\mathbf{a}^{\dagger}\mathbf{a})^{(11)0} = H(2)\mathbf{W}^{(11)0}\sqrt{\frac{5}{2}}\mathbf{U}_q^{(2)}$$

$$\begin{aligned}
&(l^N\alpha SLJM|S_{20}|l^N\alpha' S'L'J'M') = \sqrt{\frac{5}{2}}H(2)(-1)^{J-M}\begin{pmatrix} J & 2 & J' \\ -M & q & M' \end{pmatrix}[J']^{-1/2} \\
&\sum_{\alpha''L''}(l^N\alpha SLJ||\mathbf{U}^{(2)}||l^N\alpha'' SL''J')(l^N\alpha'' SL''J'||\mathbf{W}^{(11)0}||l^N\alpha' S'L'J')
\end{aligned} \tag{3.22}$$

$$ii) S_{21} = G(2,1)(\mathbf{a}^{\dagger}\mathbf{a})_q^{(11)2} \tag{3.23}$$

$$iii) S_{22} = G(2,2)(\mathbf{a}^{\dagger}\mathbf{a})_q^{(12)2} \tag{3.24}$$

$$iv) S_{23} = G(2,3)(\mathbf{a}^{\dagger}\mathbf{a})_q^{(13)2} \tag{3.25}$$

As explained in chapter two, the most significant third-order spin-orbit contribution comes from the terms for which t=0, when the matrix elements

corresponding to these term do not vanish. Since the third order spin-orbit contribution to two-photon intensities can be expressed in terms of the second-rank irreducible tensor form, the third order polarization dependence functions have the same forms as the second order. We therefore can just add the results for α_q^t calculated in the third order into the second-order results and square the final result to obtain the final intensities calculated up to the third order involving spin-orbit coupling.

3.2.3 Two-Photon Absorption

For the case of two-photon absorption from the same source, the two photon scattering tensor corresponding to linearly polarized incident photons has the general form

$$\begin{aligned}\alpha_{\mathrm{TPA}} = & -\frac{1}{\sqrt{3}}\alpha_0^{(0)} + (\frac{3\cos^2\theta - 1}{\sqrt{6}})\alpha_0^{(2)} - (\frac{e^{-i\varphi}}{2}\sin 2\theta)\alpha_1^{(2)} + (\frac{e^{i\varphi}}{2}\sin 2\theta)\alpha_{-1}^{(2)} \\ & + (\frac{e^{-2i\varphi}}{2}\sin^2\theta)\alpha_2^{(2)} + (\frac{e^{2i\varphi}}{2}\sin^2\theta)\alpha_{-2}^{(2)}\end{aligned} \tag{3.26}$$

where the values of θ and ϕ describe the orientation of the incident photon polarization in the polar coordinates, with the z axis being parallel to the crystallographic c-axis of the crystal.

The two photon intensity is directly related to the matrix elements of the scattering tensor by

$$(I_{TPA})_{fi} = C(\omega_O + \omega_{fi})^4 |(\alpha_{TPA})_{fi}|^2, \tag{3.27}$$

where C is a constant, ω_0 is the laser's frequency and $\omega_{fi} = \omega_f - \omega_i$ is the frequency corresponding to the energy difference between the initial and final states *i* and *f*.

In the second order approximation the irreducible tensor $\alpha_q^{(t)}$'s appearing in equation (3.26) are related to the standard unit tensor $U_q^{(t)}$ by

$$(\alpha_q^{(t)})^{(2nd)} = F_t^{TPA} U_q^{(t)}. \tag{3.28}$$

where t can be 0 or 2 for the case of TPA from a single source, q can take the values -t, -t+1, ..., t, and

$$\begin{aligned} F_t^{TPA} = (-1)^t \sum_{nf^{N-1}n'l'} & 7(2l'+1)\begin{pmatrix} 3 & 1 & l' \\ 0 & 0 & 0 \end{pmatrix}^2 \langle 5f|r|n'l'\rangle^2 \\ & \times (2t+1)^{\frac{1}{2}} \begin{Bmatrix} 1 & 3 & l' \\ 3 & 1 & t \end{Bmatrix} \left[\frac{1}{E_{n'l'} - \hbar\omega} \right] \end{aligned} \tag{3.29}$$

where $E_{n'l'}$ is the average energy of the n'l' configuration and ω is the angular frequency of the incident photon.

The irreducible scattering tensor corresponding to third order spin orbit TPA amplitude is the same for that corresponding to the ERS amplitude given in equation (3.15), except that the terms associated with t = 1 vanish for the case of two-photon absorption from the same source.

3.3 Raman Scattering - Experimental Aspects

3.3.1 Experimental Setup

Figure 3.2 describes the experimental set up for our Raman study. Incoming light with varied polarization is incident on the crystal sample, and the scattered light is collected for analysis at angle 90° with respect to the input beam direction. The main components of the set up consist of i)an argon cw laser; ii)a series of optical devices

including a polarization rotator, focusing and collimating lenses, a polarization analyser, a Dove prism, and a polarization scrambler; iii)a cryogenic system; iv)a spectrometer and a detection system including a photomultiplier, a preamplifier, and a photon counter connected to a PC.

3.3.1.1 Laser

The excitation for the ERS experiment is provided by a Coherent Innova model 306 cw argon-ion laser. The laser can operate in multi-line operation or single-line operation. The single-line operation is achieved by placing a prism in the laser cavity. For ERS scans only the single-line configuration was chosen, with the output power strongest for the single-line 514 nm and single-line 488 nm. These are the two single-lines most commonly used in our ERS work. Other single-lines were also used for verification of the nature of the spectral lines, to determine whether they are truly Raman peaks, whose spectral positions are at a fixed distance with respect to the excitation spectral line. Weak plasma lines coming from the laser's plasma tube were also observed in 488 nm, 501 nm, and 496 nm excitation lines. These plasma lines have their own fixed polarization dependent behavior and therefore were readily catalogued for identification. Except for ERS transitions in $NdVO_4$, none of these plasma lines interfered with the reported transitions in our ERS work. The wavelengths and wavenumbers of the argon-ion laser lines are given in Table 3.3.

The linewidth of an argon laser line is approximately 0.2 cm^{-1}. An intracavity etalon can be placed in the laser cavity to further reduce the laser linewidth and produce a single-mode output. This was unnecessary for our ERS work on vanadate crystals

since the linewidth of most of the ERS transitions are on the order of 3 cm^{-1} or above. The beam diameter is about 1.5 mm at the output mirror, and the virtual beam waist diameter is approximately 1.4 mm, with a beam divergence of 0.5 mrad. In the case that tight focusing is desired, the beam can be focused to a spot size as small as 50 microns at the center of the crystal sample, using a combination of a microscope and achromatic doublet lenses. This will be discussed in more detail in the next section.

Table 3.3: Wavelengths and wavenumbers of argon-ion laser lines.

Wavelength (nm)	Wavenumber (cm^{-1})	
	Air	Vacuum
514.53	19435.1	19429.7
501.71	19931.6	19926.0
496.51	20140.6	20135.0
487.99	20492.4	20486.7
476.49	20986.9	20981.0
465.79	21468.7	21462.7
457.94	21837.1	21831.0

The polarization of the output beam is primarily vertical, with approximately less than one percent horizontal leakage. The small intensity coming from this horizontal polarization leakage was one of the main causes for polarization leakage problems in our polarization dependent work. Other sources for polarization leakage include imperfect crystal alignment or multiple scattering of the laser beam along the beam path inside the crystal. The latter problem can be alleviated by choosing an appropriate set of collection optics so that only the narrow beam path on the crystal can

be imaged and analysed while stray light from multiple scattering or specular reflection inside the crystal is rejected.

3.3.1.2 Optics

a. Polarization Rotator: A Spectra Physics model 310-21 polarization rotator was chosen to vary the beam's polarization between 0 and 360 degree. This polarization rotator was preferred to a Soleil Babinet Compensator, since the former is known to give an output with fixed intensity and direction when the beam polarization is varied. A slight motion of the beam path on the crystal when beam polarization is changed, which usually occurs when a Soleil Babinet Compensator is used, can immensely affect ERS signals, whose intensities are extremely weak and sensitive to the beam path along the crystal.

b. Focusing and Collimating Optics: In Raman scattering, signal coming from Raman light is much weaker than signal coming from Rayleigh and reflected light. In order to obtain the maximum amount of the wanted Raman light and reject most of the unwanted, great care needs to be exercised in arranging a suitable optical system. Two observations are made for attaining such a system.

First, the system has to be prepared in such a way that good alignment can be achieved and reproduced with little effort. To meet this goal we have mounted every optical component that may be moved in the alignment procedure such as lenses and prisms in a two-dimensional translation stage which can be adjusted by a micrometer. It was found that collected signal is sometimes greatly enhanced with only a minute adjustment of the optics.

Secondly, most Raman signals are concentrated on the thin, narrow laser beam path on the crystal. The beam waist and beam diameter of the focused spot has to be chosen such that the beam path's image can fill the diffraction grating of the spectrometer. The spectrometer's slit widths are normally set at 250 microns in order to obtain maximum signal. Experimentally, we found that desired signal level can be obtained with a beam diameter of the focused spot between 50 and 200 microns and by choosing a collection optics with a magnification of less than or equal to 7. A beam diameter of 200 μm can be obtained by simply using an achromatic doublet focusing lens L_1 with a focal length of 15 cm, which actually was used in a majority of ERS experiments. When smaller beam diameters are desired, we used a series of components including a Newport Research Corporation model 900 spatial filter, which acts as an inverted microscope with a 0.5 cm focal length objective, to expand the laser beam size, an achromatic doublet with a 15 cm focal length to collimate the beam, and another achromatic doublet with a 15 cm focal length to focus the beam to a spot size below 50 microns. The beam diameter can be estimated by projecting the crystal image on a wall, and the size of the beam spot can be compared with respect to the size of the enlarged crystal image. The collection optics we have chosen were composed of two lenses L_2 and L_3, one collimating and one focusing, respectively. The sample is placed at the focal point of L_2, which is a Nikon camera lens with focal length of 5 cm and diameter of 4 cm. The collimated light with an aperture of 4 cm coming from L_2 is focused on the spectrometer entrance slit by L_3, which is an achromatic doublet with focal length of 33 cm and diameter of 4 cm. L_3 was so chosen to match the spectrometer's entrance f-

number of 7.8. With a magnification of 6.6 coming from our collection optics, the scattered light image may overfill the spectrometer's entrance slits, and some signal may be lost. The signal level obtained, however, is sufficient for most of our Raman study.

c. Polarization Analyser: A polarization sheet is placed right after the collimating lens to select and analyze the polarization of the scattered light. This polarization analyser is mounted on a rotator with marks from 0 to 360° for accurate polarization selection.

d. Dove prism: We have so far ignored one important fact in our discussions above. In our current setup, the laser path is horizontal, while the spectrometer's slit is vertical. In order to fix this problem, a Dove prism was used to rotate the laser path image by 90 degree. Two major problems arise when a Dove prism is used. Firstly, it functions well only with parallel light. For this reason we placed the Dove prism between the collimating lens, L_2, and the focusing lens, L_3. Since light coming from L_2 is parallel, the beam's image using the Dove prism would not be distorted. Secondly, due to multiple reflection, a Dove prism responds differently to the polarization of light being passed through, in a similar fashion that a spectrometer's diffraction grating would respond with respect to light. To eliminate this problem, the Dove prism was placed behind the polarization analyser, and a depolarizer was placed between the Dove prism and the polarization analyser. The depolarizer consists of a 2° crystal quartz wedge with a second compensating fused silica wedge.

3.3.1.3 Sample Crystal and Cryogenics

a. Crystal Sample

The samples used were grown by L. A. Boatner and M. M. Abraham from the Oak Ridge National Laboratory. All crystal samples have the form of a plate, with typical dimensions 1mm × 1mm × 4mm. The host crystal belongs to the D_{4h} symmetry. The RE^{+3} ion is at a D_{2d} -symmetry site. The x and y axes, which are the two-fold C_2 axes, are rotated in the X-Y crystallographic plane by 45° relative to the X and Y axes (fig. 3-1). The z axis is parallel to the crystallographic Z axis.

All ERS spectra were taken at approximately 4.2 K, the liquid He temperature. At this temperature, only the ground state is populated for most rare-earth ions, and the scattering intensities come primarily from Stokes transitions, which originate from the ground state and end in the excited states of the ground multiplet. When the temperature is raised significantly above 4.2 K, the intensities corresponding to these Raman transitions are reduced according to the Boltzmann factor, due to thermal population. In addition to Stokes peaks, anti-Stokes can also be observed at high temperature. These anti-Stokes peaks arise from ERS transitions originating from excited levels.

The cryogenics equipments required to maintain the crystal at 4.2 K are provided by Oxford Instruments. These equipments include a CF1204 continuous flow cryostat, a TTL low loss transfer tube, a VC30 flow control console, and a ITCV4 temperature controller.

b. Cryostat: The CF1204 cryostat contains a sample tube, a radiation shield, and a vacuum space. In the sample space enclosed by the sample tube, the sample is top-loaded through an access port on top of the cryostat. This port is sealed by a plug

against an 'O' ring, and the crystal sample is suspended from this plug by a rod of material with high thermal resistance. During an experiment, the sample space is evacuated and then filled with He exchange gas. The sample tube is surrounded by a radiation shield which intercepts room temperature radiation. Next to this radiation shield is the outer vacuum case, where high vacuum is kept at all time in order to maintain the thermal isolation of the liquid helium. The sample tube, radiation shield and outer vacuum case have positions for four radial and axial quartz windows. The clear diameters of these windows are 13 mm for the inner, 15 mm for the shield, and 25 mm for the outer. It is recommended that these windows be checked for polarization behavior before each polarization measurement is taken. At one time we discovered that one of these windows behaved like a birefringent crystal, which is capable of changing the polarization of light passing through. The cause for such behavior were not clearly known. We suspect the presence of a strain induced birefringence.

c. Transfer tube, flow controller, and temperature controller: Liquid He from a He vessel is delivered to the cryostat by a vacuum-insulated TTL transfer tube. A VC30 flow control console consisting of a vacuum gauge, a needle valve and a flow meter is used to control the flow rate of the liquid He from the transfer tube into the cryostat. From the transfer tube, liquid He is transferred down the length of the cryostat in the vacuum space to a heat exchanger section. The heat exchanger is fitted with a 27 ohm Rhodium-Iron resistance sensor and heater. An ITC4 temperature controller connecting to the sensor and heater is used to measure and control the temperature of the sample chamber. During an experiment, due to laser heating, the actual temperature of the

crystal may be a few degrees Kelvin higher than the temperature read from the temperature controller display panel.

3.3.1.4 Spectrometer and Detection System

a. Spectrometer

Scattered light collected is analysed by a Spex Industries model 1403 double monochromator. The spectrometer has an f-number of 7.8 and a focal length of 0.85 m. Finely ruled holographic gratings with 1800 grooves/mm are used. Similar to the case of a Dove prism mentioned in 3.3.1.2, these gratings have spectral response that depends on the polarization of the incident light. For this reason in every Raman scattering experiment, a polarization scrambler was placed in front of the Dove prism to correct for the different polarization efficiencies in both the Dove prism and the spectrometer. The spectral range of the spectrometer covers between approximately 300 and 1000 nm. A stepper motor inside the monochromator was controlled by a Spex Compudrive control unit which drove the system through a selected spectral region. Typical scan rate was 0.01 cm^{-1}/s.

In most Raman scattering experiments, slit widths were set at 250 microns for the entrance and exit slit widths. The intermediate slits are widely open. This setting results in a spectral bandpass of approximately between 2.5 and 3 cm^{-1} for the 514 nm and 488 nm excitations. The entrance and exit slits were closed down to 150 microns in cases the intensities of the ERS transitions were being swamped by the intensity of the Rayleigh scattered light, which happened when the spectral positions of these transitions were in the vicinity of the laser excitation.

b. Detection system

A high gain, low dark count, photo-electrically cooled Hamamatsu model R375 photomultiplier (PMT) tube was placed against the spectrometer's normal exit slit to collect light dispersed by the spectrometer. The voltage across the tube was 1000 V. The tube was placed in a housing which had water flowing at a rate of 2 liters/minute. The spectral range of the tube is 150 nm to 850 nm.

The photon signals from the photomultiplier tube were amplified by a factor of five by a Stanford Research model SR445 fast preamplifier and measured with a Stanford Research model SR400 photon counter. Most noise signals were rejected by setting the photon counter's discriminator level at about 6 V. Real signals were converted into NIM pulses, transferred to a PC 386 computer and then counted by a Tennelec/Nucleus Multi-Channel Scaler card, which was controlled by a program called MCS. The background count rate of the PMT tube when the spectrometer's entrance and exit slits are both 200 μm is approximately 200 count/sec. The data was stored in $5^1/_4$ inches floppy disks as binary files, which were then converted into ASCII files by a program called SPM2ASC. The ERS transitions intensities were analysed using a GRAMS program and plotted using an ORIGIN program.

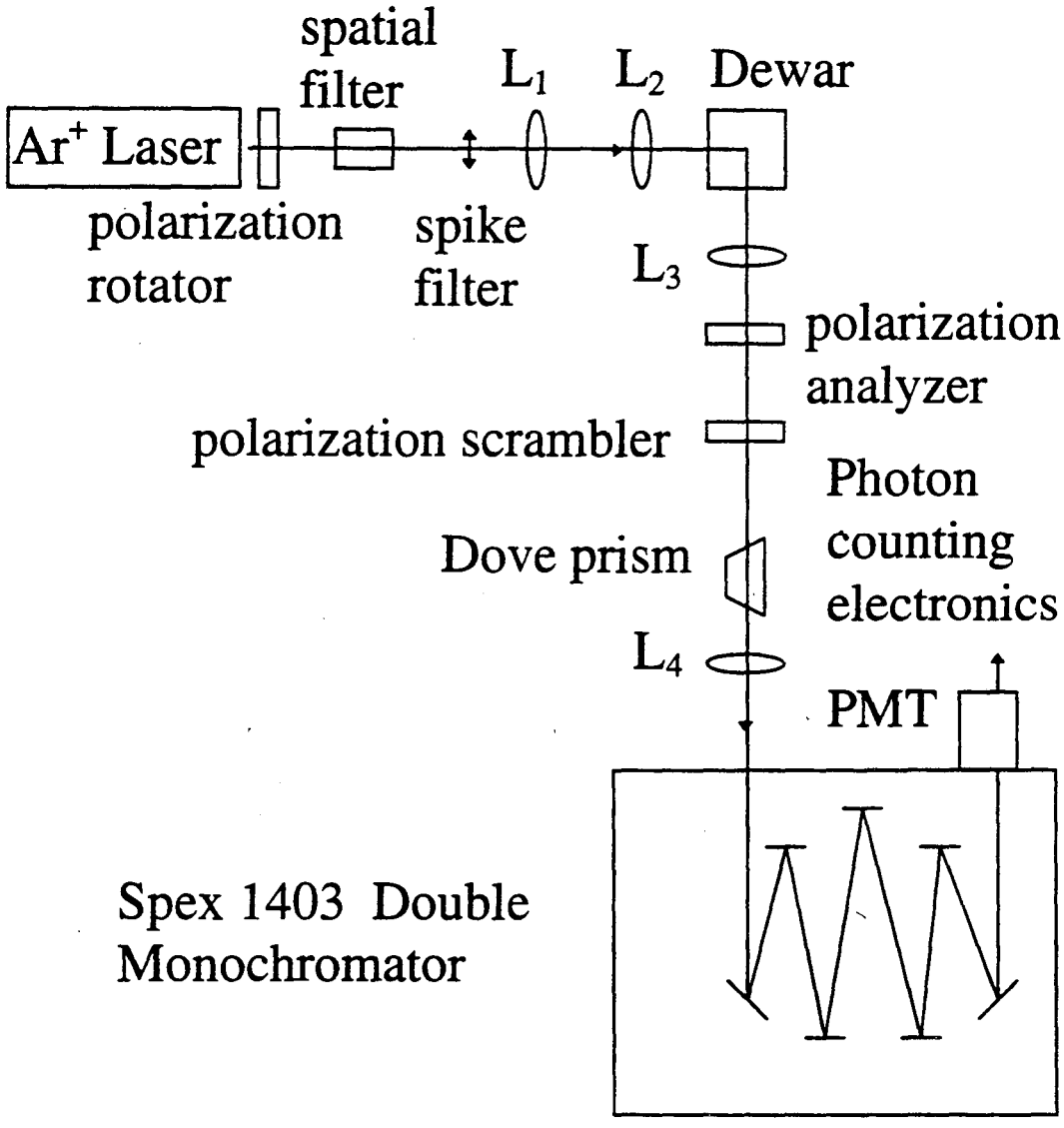

Fig. 3.2: Experimental set up in ERS measurements

3.3.2 Experimental Procedure

Experimentally, Raman lines are determined from one of the following criteria:

a. The Raman lines always appear with the same frequency shift relative to the laser excitation frequency, irrespective of the excitation.

b. The Raman intensities have their own polarization dependence characteristic of the corresponding Raman transitions. Phonon lines have their own polarization dependent curves which are generally different from electronic Raman curves.

c. Due to thermal population, electronic Raman transition intensities decrease as the temperature increases. Phonon intensities are only slightly dependent on temperature.

The polarization dependence spectra were obtained by the following procedure. A total of 45 scans were recorded, each corresponding to a polarization state of the incident and scattered light. The incident polarization angle θ_1 was initially set to 0°, while the scattered polarization angle θ_2 was incremented for each successive scan by 22.5°, from 0 to 180°. Then θ_1 was incremented to 22.5°, and the process repeated until θ_1 reached 90°. For calibration purposes, a pair of electronic Raman and phonon scattering spectra with similar polarization dependence curves were taken concurrently for each polarization state (θ_1,θ_2) of the incident and scattered light.

The observed linewidths were fitted using the computer program GRAMS. Most ERS transitions were fitted with Gaussians. For the phonon modes, approximately above 99 % Gaussian and less than 1% Lorentzian produced the best fits. The linewidths of phonon modes in the vanadate crystals vary between 2 cm^{-1} (E_g^1) to 20 cm^{-1} (A_{1g}^1). The linewidths of ERS transition are typically between 3 - 6 cm^{-1}.

The calibration was performed as follows. The observed intensities of the phonon mode selected for calibration were fitted using a least square fit analysis with the predicted polarization dependence functions given in section 3.2. Since the polarization dependence expressions for phonon modes always contain only one term, which is a constant multiplied by a simple function of θ_1 and θ_2, the constant factor in these expressions could be served as the fitting parameter. The best fit value of this fitting parameter would provide the fitted values for the phonon intensities for each polarization state (θ_1,θ_2). Each observed phonon intensity value corresponding to one polarization state (θ_1,θ_2) was then divided by the fitted value corresponding to that state. This ratio for each polarization state is called the scale factor for that state. For each polarization state, the observed ERS intensity was divided by the scale factor associated with that state. The final results were the calibrated ERS intensity values. By fitting these values to the theoretical polarization dependent curves, we obtained the best fitted value for the F_1/F_2 ratio. The following diagram summarizes the calibration procedure.

Calibration Diagram

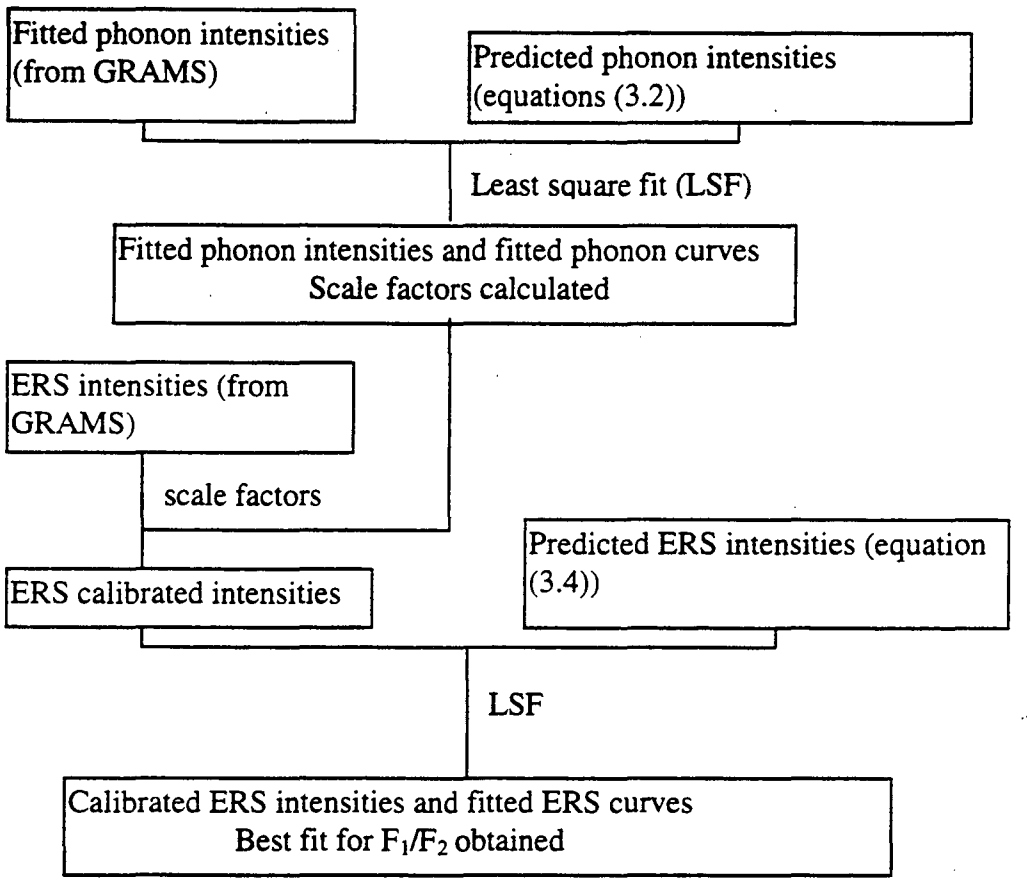

In the calibration procedure mentioned above it was assumed that the phonon curves were accurately described by the theory and that no interactions other than pure phonon scattering were involved. As will be reported in the discussion section, good agreement was found between observed and predicted phonon polarization dependent curves, justifying our use of the phonon data for calibration. Once a good fit for phonon intensities has been obtained, calibrating the ERS data using the phonon data may reduce systematic errors, since both ERS and phonon scattering data were taken with an

identical experimental set up, and therefore would suffer approximately the same systematic errors. In ERS experiments imperfect alignment of the crystal, defects in optical devices, multiple reflections from optical surfaces and the spectrometer's grating, all contribute to systematic errors in the observed data. Calibration procedures using the known behavior of the phonon modes would be more critical if these errors are significant, such as in the case where good crystal alignment is not possible or when the optical devices being used introduce unwanted polarization dependent behavior.

3.4 Two-Photon Absorption - Experimental Aspects

3.4.1 Crystal Samples

The Eu^{3+}:$LuPO_4$ sample was grown by L. A. Boatner and M. M. Abraham from the Oak Ridge National Laboratory. It has the form of a plate with dimensions of $0.2 \times 1 \times 6$ mm^3 . The nominal Eu^{3+} concentration is approximately 6 mole %.

The Cm^{3+}:$LuPO_4$ sample was grown by doping a single crystal of $LuPO_4$ with almost isotopically pure ^{248}Cm using a high-temperature melt [11,12]. It was relatively small, with dimensions of 0.5 x 2.0 x 1.0 mm^3. The nominal Cm^{3+} concentration is estimated to be less than 0.1 mole %. This radioactive sample was sealed in a quartz ampoule under a partial pressure of helium for containment purposes.

3.4.2 Absorpsion Measurements

Absorption measurements of Eu^{3+} in $LuPO_4$ have been carried out with a Cary 17 spectrophotometer and with a Xe lamp source and the Spex monochromator. The Cary data were taken at room temperature as a quick check of the concentration of the crystal and the approximate energy levels of the $^5D_0$, $^5D_1$, and $^5D_2$ multiplets. The Xe

lamp gives the absorption spectra of Eu^{3+}:$LuPO_4$ and the energy levels in the region of interest at 4K. Four filters were used in the absorption measurements using the Xe lamp. Light from the lamp is fitered by water and 4-96 and 4-76 Corning color filters. The intensity of filtered light passing through the crystal inside the Oxford cryostat is further reduced by a neutral density filter. The slit were open with slitwidths of 70 μm.

Absorption, excitation, and emission measurements of Cm^{3+} in $LuPO_4$ have been reported by Sytsma et al [13].

3.4.3 TPA Experimental Setup

Figure 3.3 shows the setup for the TPA experiments. In all Eu^{3+}:$LuPO_4$ experiments and most Cm^{3+}:$LuPO_4$ experiments the excitation source was a Lambda Physik Scanmate optical parametric power oscillator (OPPO). This laser is a hybrid optical parametric oscillator (OPO), which uses a small dye oscillator as a seed laser, and was pumped by the third harmonic output of a Spectra Physics model GCR-3 Nd:YAG laser. The output beam was passed through a 2-64 color filter. It had a sufficiently broad transverse mode for a Spectra Physics model 310-21 polarization rotator to be used to change the excitation polarization. The maximum excitation power used was 1mJ/pulse. A 25 cm quartz lens was used to focus the beam onto the crystal. A Hamamatsu R928 photomultiplier tube (PMT) was placed against the window of the cryostat to detect the fluorescence from the sample. Depending on the fluorescence wavelength, appropriate color and line filters were placed between the PMT and the window of the cryostat to filter the scattered light. The signal from the PMT was

preamplified by a Stanford Research model SR445 fast preamplifier and then measured using a Standford Research model SR400 gated photon counter. If a strong signal was detected, neutral density filters were used to avoid pulse pile-up.

The TPA spectra of Eu^{3+} in $LuPO_4$ were obtained using the OPPO laser with C540A dye for the $^7F_0$ - $^5D_2$ transitions and C503 dye for the $^7F_0$ - $^5D_0$ transition. A 4-94 and a 3-68 colour filter were used to allow transmission of the fluorescence from these TPA transitions but effectively blocking the infrared scattered light from the excitation. In each TPA polarized scan, steps of .01 nm were used, with 10 pulse integrations and the photon counter's gate delay and width set at 100 μs and 5 ms, respectively. For Cm^{3+} in $LuPO_4$, the TPA spectra of the $^8S_{7/2}$ - $^6D_{7/2}$ transitions at 17800 cm^{-1} and the $^8S_{7/2}$ - $^6P_{5/2}$ transitions were obtained using the OPPO laser with a C540 dye, and the TPA spectra of the $^8S_{7/2}$ - $^6D_{7/2}$ transitions at 27900 cm^{-1} were obtained using a Spectra Physics PDL-3 dye laser with LDS750 dye as the excitation source. A 2-73 color filter and a 602-10 nm line filter were used to select the transmission of the $^6D_{7/2}$-$^8S_{7/2}$ fluorescence. Steps of .004 nm were used in each polarized scan, with 20 pulse integration. The gate delay and the width of the photon counter in the Cm^{3+}:$LuPO_4$ experiments were set at 1 μs and 2 ms, respectively, according to the lifetime of the excited state of Cm^{3+}, which is approximately 500 μs.

All the experiments, unless otherwise stated, were conducted at a temperature of 4.2 K in an Oxford Instruments model CF1204 optical cryostat. The actual sample temperature may be 1 or 2 K higher due to the absorption of laser energy. Resistive coils

and an Oxford Instruments model ITCV4 temperature controller were sometimes used to raise the sample temperature.

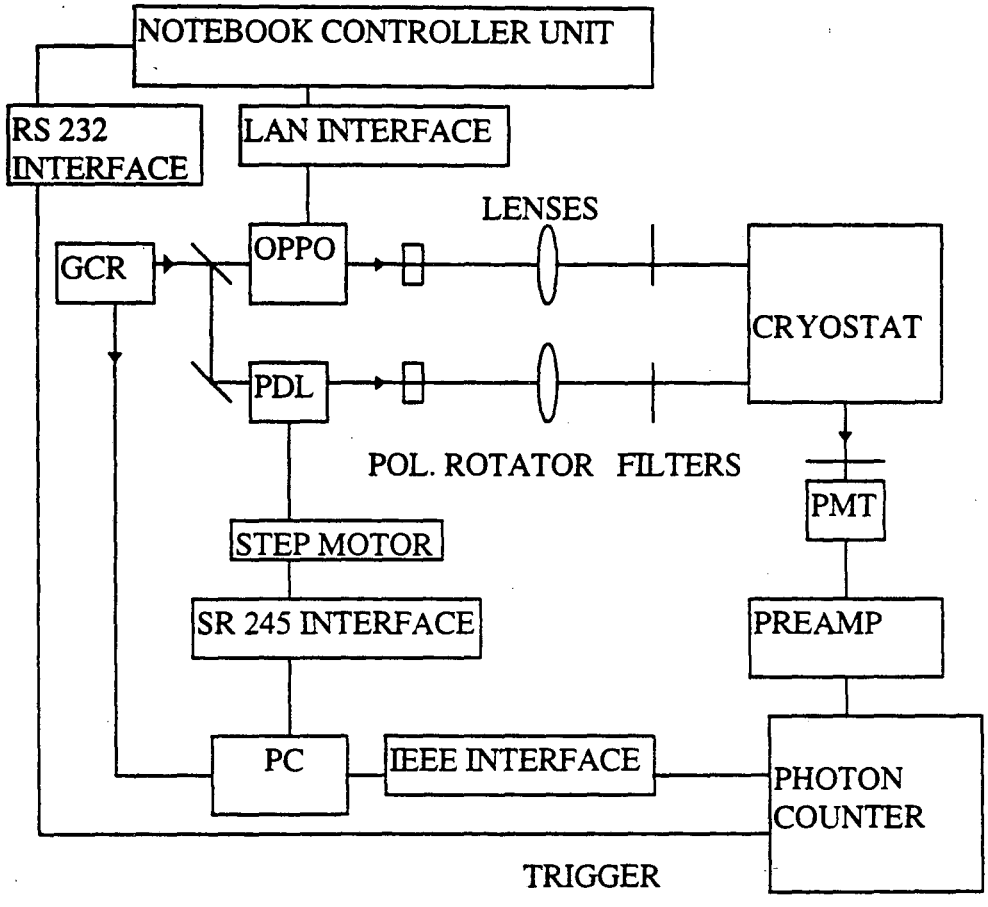

Fig. 3.3: Experimental set up in TPA intensity measurements

References

[1] P. C. Becker et al., Phys. Rev. B **31**, 8102 (1985).

[2] P. C. Becker, Ph.D. thesis, University of California, Berkeley, 1986.

[3] J. D. Axe, Phys. Rev. **136A**, 42 (1964).

[4] J. A. Koningstein and O. Mortensen, Phys. Rev. 168, 75 (1968), J. Opt. Soc. Am. **58**, 1208 (1968).

[5] L. Smentek-Mielczarek, Phys. Rev. B **46**, 14467 (1992); J. Chem. Phys. **94**, 5369 (1991); Phys. Rev. B **40**, 6499 (1989); Phys. Rev. B, **40**, 2019 (1989); Phys. Rev. **46**, 14467 (1992); Phys. Rev. **46**, 14453 (1992).

[6] R. R. Andronenko, S. I. Andronenko, A. N. Bazhan, Phys. Sol. State **36**, 1302 (1994).

[7] T. Hayhurst, G. Shalimoff, J. G. Conway, N. Edelstein, L.A. Boatner, and M. M. Abraham, J. Chem. Phys. **76**, 3960 (1982).

[8] P. Tanner and N. Edelstein, Chem. Phys. Lett. **152**, 140 (1988).

[9] A. A. Kaminskii, in *Laser Crystals* (Springer-Verlag, 1981), p. 130.

[10] D. E. Wortman, R. Leavitt, and C. A. Morrison, J. Phys. Chem. Solids **35**, 591 (1974).

[11] L.A. Boatner, G.W. Beall, M.M. Abraham, C.B. Finch, R.J. Floran, P.G. Huray, and M. Rappaz, "*Management of Alpha-Contaminated Wastes*", p. 114, IAEA-SM-245/73, International Atomic Energy Agency, Vienna (1981).

[12] M. Rappaz, L.A. Boatner, and M.M. Abraham, *J. Chem. Phys.* **73**, 1045 (1980).

[13] J. Sytsma, K. Murdoch, N. Edelstein, L. Boatner, and M Abraham, Phys. Rev. B **52**, 12668 (1995).

Chapter 4

Polarization Dependence of Phonon Scattering and Electronic Raman Scattering Intensities in $PrVO_4$, $NdVO_4$, $ErVO_4$, and $TmVO_4$

4.1 Raman Spectroscopy of $PrVO_4$

4.1.1 Pr^{3+}- Selection Rules

The open shell configuration of Pr^{3+} is $4f^2$. The point group symmetry of Pr^{3+} in $PrVO_4$ is D_{2d}. Since Pr^{3+} has an even number of active electrons, its electronic states are labeled by the irreducible representations Γ_1, Γ_2, Γ_3, Γ_4, and Γ_5 of D_{2d}.

The ground multiplet of Pr^{3+} is $^3H_4$. The decomposition of the ground multiplet into irreducible representations is given by $2\Gamma_1 + \Gamma_2 + \Gamma_3 + \Gamma_4 + 2\Gamma_5$. The ground crystal field state has the symmetry Γ_3. The selection rules and Raman activity for the Raman transitions originating in the ground state are described in table 4.1. Fluorescence measurements and Raman spectra of the ground multiplet of Pr^{3+} in $PrVO_4$ have been reported by Bleaney et al. [1], and the corresponding wavefunctions have been given by Andronenko et al. [2].

Table 4.1: Selection rules and Raman activity of ERS transitions originating in the ground state of Pr^{3+} in $PrVO_4$.

Transition	Scattering tensor symmetry	Raman activity α_q^t
$\Gamma_3 \leftrightarrow \Gamma_1$	Γ_3	$\alpha_2^2, \alpha_{-2}^2$
$\Gamma_3 \leftrightarrow \Gamma_2$	Γ_4	$\alpha_2^2, \alpha_{-2}^2$
$\Gamma_3 \leftrightarrow \Gamma_3$	Γ_1	α_0^2
$\Gamma_3 \leftrightarrow \Gamma_4$	Γ_2	α_0^1
$\Gamma_3 \leftrightarrow \Gamma_{5x}$ $\Gamma_3 \leftrightarrow \Gamma_{5y}$	Γ_{5x} Γ_{5y}	α_1^2, α_1^1 $\alpha_{-1}^2, \alpha_{-1}^2$

4.1.2 Pr^{3+}- Polarization Dependence Functions

Taking into account the necessary transformation given in (3.1), the polarization dependence curves corresponding to the Raman activity listed in table 4.1 are given in table 4.2.

We now determine the values of the non-zero matrix elements of $\alpha_q^{(t)}$ for Pr^{3+} in $PrVO_4$. The wavefunctions were obtained from a crystal-field fit [3] with the crystal field parameters given by Andronenko et al [2]. The wavefunctions for the ground multiplet of Pr^{3+} in $PrVO_4$ are listed in table 4.3. Table 4.4 lists the nonzero values of α_q^t, which were calculated using the second-order theory of Axe, and the polarization dependence functions for the corresponding transitions. Table 4.5 displays the predicted values of transition intensities taken in ZZ, XY, XZ, and ZY polarized scans relative to the ZY polarized intensity of the Γ_3 - Γ_5 transition at 85 cm^{-1}. The predicted values are expressed in terms of $\tau = F_1/F_2$.

Table 4.2: Polarization dependence functions for ERS transitions originating in the ground state of Pr^{3+} in $PrVO_4$.

Transition	Polarization dependence curves
$\Gamma_3 \leftrightarrow \Gamma_1$	$(1/4)(\alpha_2^2 + \alpha_{-2}^2)^2 \sin^2\theta_1 \sin^2\theta_2$
$\Gamma_3 \leftrightarrow \Gamma_2$	0
$\Gamma_3 \leftrightarrow \Gamma_3$	$(2/3)\,(\alpha_0^2)^2 \cos^2\theta_1 \cos^2\theta_2$
$\Gamma_3 \leftrightarrow \Gamma_4$	$(1/2)(\alpha_0^1)^2 \sin^2\theta_1 \sin^2\theta_2$
$\Gamma_3 \leftrightarrow \Gamma_{5x}$	$(1/8)[(\alpha_1^2)^2 + (\alpha_1^1)^2]\,[\sin^2(\theta_2-\theta_1) + \sin^2(\theta_2+\theta_1)]$ $+ \alpha_1^2\alpha_1^1 \sin(\theta_2-\theta_1)\sin(\theta_2+\theta_1)$
$\Gamma_3 \leftrightarrow \Gamma_{5y}$	$(1/8)[(\alpha_{-1}^2)^2 + (\alpha_{-1}^1)^2]\,[\sin^2(\theta_2-\theta_1) + \sin^2(\theta_2+\theta_1)]$ $- \alpha_{-1}^2\alpha_{-1}^1 \sin(\theta_2-\theta_1)\sin(\theta_2+\theta_1)$

Table 4.3: Wavefunctions for the ground multiplet of Pr^{3+} in $PrVO_4$.

Calculated Energy (cm^{-1})(*) and Symmetry	Wavefunction $\sum_{J,J_z} a(J,J_z)\ {}^{2S+1}L_J(J_z)$
0 (Γ_3)	.707 $^3H_4$ (2) + .707 $^3H_4$ (-2)
35 (Γ_1)	.53 $^3H_4$ (4) + .53 $^3H_4$ (-4) + .67 $^3H_4$ (0)
85 (Γ_{5x})	.92 $^3H_4$ (-1) + .37 $^3H_4$ (3)
(Γ_{5y})	.92 $^3H_4$ (1) + .707 $^3H_4$ (-3)
171 (Γ_2)	.707 $^3H_4$ (4) - .707 $^3H_4$ (-4)
195 (Γ_4)	.707 $^3H_4$ (2) - .707 $^3H_4$ (-2)
343 (Γ_1)	.474 $^3H_4$ (4) + .474 $^3H_4$ (-4) - .75 $^3H_4$ (0)
409 (Γ_{5x})	-.92 $^3H_4$ (3) + .37 $^3H_4$ (-1)
(Γ_{5y})	-.92 $^3H_4$ (-3) + .37 $^3H_4$ (1)

(*) From the crystal field fit.

Table 4.4. Polarization dependencies of ERS transition intensities in the $^3H_4$ ground multiplet of Pr^{3+} in $PrVO_4$.

Transitions (cm^{-1})	Non-zero α_q^t	Polarization Dependencies $\lvert\alpha_{21}\rvert^2$
0-35	$\alpha_2^2 = \alpha_{-2}^2 = .118F_2$	$.014\, F_2^2 \sin^2\theta_1 \sin^2\theta_2$
0-84	$\alpha_1^2 = .0313F_2$, $\alpha_1^1 = -.346F_1$	$2.45\times10^{-4}\, F_2^2\, [(\sin^2\theta_3 + \sin^2\theta_4)(1+123.2\,\tau^2) - 44.4\,\tau \sin\theta_3 \sin\theta_4]$ (*)
0-171	$\alpha_2^2 = \alpha_{-2}^2 = .05F_2$	0
0-195	$\alpha_0^1 = .261F_1$	$.017\, F_1^2 \sin^2\theta_1 \sin^2\theta_2$
0-343	$\alpha_2^2 = \alpha_{-2}^2 = -.062F_2$	$.017\, F_1^2 \sin^2\theta_1 \sin^2\theta_2$
0-409	$\alpha_1^2 = .145F_2$, $\alpha_1^1 = .122F_1$	$5.25\times10^{-3}\, F_2^2\, [(\sin^2\theta_3 + \sin^2\theta_4)(1+.706\,\tau^2) + 3.36\,\tau \sin\theta_3 \sin\theta_4]$ (*)

(*) $\theta_3 = \theta_2 - \theta_1$, $\theta_4 = \theta_1 + \theta_2$, $\tau = F_1/F_2$.

A particular ERS transition of interest is the first Γ_3 - Γ_5 transition at 85 cm^{-1}. From table 4.2, the Raman scattering intensity corresponding to this transition can be written

$$
\begin{aligned}
&\lvert\alpha_{e_2e_1}(\Gamma_3 \rightarrow \Gamma_5)\rvert^2 = \\
&\quad \frac{1}{4}\{[\alpha_1^2 \sin(\theta_2+\theta_1) + \alpha_1^1 \sin(\theta_2-\theta_1)]^2 + [\alpha_1^1 \sin(\theta_2+\theta_1) + \alpha_1^2 \sin(\theta_2-\theta_1)]^2\} \\
&\quad + \frac{1}{4}\{[\alpha_{-1}^2 \sin(\theta_2+\theta_1) - \alpha_{-1}^1 \sin(\theta_2-\theta_1)]^2 + [-\alpha_{-1}^1 \sin(\theta_2+\theta_1) + \alpha_{-1}^2 \sin(\theta_2-\theta_1)]^2\},
\end{aligned}
\tag{4.1}
$$

where α_q^t 's denote the matrix elements of the $\alpha_q^{(t)}$ tensors, $\langle\Gamma_5|\, \alpha_q^{(t)} |\Gamma_3\rangle$.

Noting the fact that the squared amplitude must be the same for ERS transitions coming from a singlet to each state of the doubly degenerate level, equation (4.1) becomes

$$|\alpha_{e_2e_1}(\Gamma_3 \rightarrow \Gamma_5)|^2 =$$
$$\frac{1}{2}\{[\alpha_1^2 \sin(\theta_2+\theta_1)+\alpha_1^1 \sin(\theta_2-\theta_1)]^2+[\alpha_1^1 \sin(\theta_2+\theta_1)+\alpha_1^2 \sin(\theta_2-\theta_1)]^2\}. \quad (4.2)$$

If we define $a=\frac{\alpha_1^2}{\alpha_1^1}=-\frac{\alpha_{-1}^2}{\alpha_{-1}^1}=-.09\frac{F_2}{F_1}=\frac{-.09}{\tau}$, (4.3)

the squared amplitude of the scattering tensor for the transition becomes:

$$|\alpha_{e_2e_1}(\Gamma_3 \rightarrow \Gamma_5)|^2 =$$
$$\frac{(\alpha_1^1)^2}{2}\{[\sin^2(\theta_2+\theta_1)+\sin^2(\theta_2-\theta_1)](a^2+1)+4a\sin(\theta_2+\theta_1)\sin(\theta_2-\theta_1)\}. \quad (4.4)$$

Let

$$f(\theta_1,\theta_2)=\frac{1}{2}\{[\sin^2(\theta_2+\theta_1)+\sin^2(\theta_2-\theta_1)](a^2+1)+4a\sin(\theta_2+\theta_1)\sin(\theta_2-\theta_1)\}. \quad (4.5)$$

We now keep θ_1 fixed at values incremented by 22.5° and determine the scattered intensity with respect to θ_2. For each value of θ_1:

$$f(0,\theta_2)=(a+1)^2\sin^2\theta_2$$

$$f(\pm 22.5°,\theta_2)=.85(a+1)^2\sin^2\theta_2+.15(a-1)^2\cos^2\theta_2$$

$$f(\pm 45°,\theta_2)=\frac{1}{2}(a^2+1-2a\cos 2\theta_2)$$

$$f(\pm 67.5°,\theta_2)=.85(a-1)^2\cos^2\theta_2+.15(a+1)^2\sin^2\theta_2$$

$$f(\pm 90°, \theta_2) = (a-1)^2 \cos^2 \theta_2 \tag{4.6}$$

Table 4.5: Predicted values of relative linestrengths of ERS transitions in the $^3H_4$ ground multiplet of Pr^{3+} in $PrVO_4$.

ERS transitions (cm^{-1})	ZZ polarized	XY polarized	XZ polarized	ZY polarized
35	0	$\frac{28}{(1+11.1\tau)^2}$	0	0
85	0	0	$\left(\frac{1-11.1\tau}{1+11.1\tau}\right)^2$	1
171	0	0	0	0
195	0	$\frac{34\tau^2}{(1+11.1\tau)^2}$	0	0
343	0	$\frac{8}{(1+11.1\tau)^2}$	0	0
409	0	0	$21\left(\frac{1+.84\tau}{1+11.1\tau}\right)^2$	$21\left(\frac{1-.84\tau}{1+11.1\tau}\right)^2$

4.1.3 $PrVO_4$ - Experimental Raman Spectra

Table 4.6 displays all phonon modes observed for the $PrVO_4$ crystal at room temperature and at 4.2 K. These phonon modes were assigned based on their polarization dependent behavior described in equations (3.2). Figures 4-1 and 4-2 show the unpolarized spectra for the phonon and ERS transitions in $PrVO_4$ between 30 and 450 cm^{-1}, which were taken at 293 and 4.2 K, respectively, using the 514 nm excitation line. The capital Arabic symbols represent the phonon modes, and the capital Greek symbols represent the ERS transitions. Only two electronic levels at 84 cm^{-1} and 344 cm^{-1} were observed, both of which were assigned to the symmetry representation Γ_5, as their intensities were strongest in XZ and ZY scans, where XZ and ZY correspond to the polarization states (θ_1=0, θ_2=90) and (θ_1=90, θ_2=0), respectively [4]. The assignment for the first doublet transition is in good agreement with reported fluorescence data [1], in which the first doublet level was assigned at 84 cm^{-1}. Our assignment for the second ERS transition, however, disagrees with the predicted assignment given by Andronenko et al. [2]. In their published paper, a single transition should have appeared at approximately 343 cm^{-1}, and a second doublet transition should have been observed at 409 cm^{-1}. Our theoretical assignments using a crystal field calculation [3] showed that the first and second doublet transitions would be located at 70 cm^{-1} and 373 cm^{-1}, respectively. The difference in energy levels between theory and observation should not be overemphasized, as we note that the predicted energy levels come from a crystal-field fit which included only two empirical energy levels. The remaining three ERS transitions of the ground multiplet predicted by this crystal field

calculation are either absent or too weak to be clearly identified as ERS. No other electronic lines were found in either polarized or unpolarized scans using the 488 nm, 496 nm, and 501 nm excitation lines.

Table 4.6. Frequencies (cm^{-1}) and symmetries of the Raman-active phonons in $PrVO_4$ at 297 K and 4.2 K.

Tem.(K)	E_g^1	B_{1g}^1	E_g^2	E_g^3	B_{1g}^2	B_{2g}^1	A_{1g}^1	E_g^4	B_{1g}^3	B_{1g}^4	E_g^5	A_{1g}^2
297	113	122	150	233	261	a	381	a	470	792	805	869
4.2	116	115	152	231	260	a	377	a	469	797	807	872

a: not observed

For calibration purpose, polarization dependence spectra have been recorded for the phonon mode at 807 cm^{-1}, due to the similarity in character between this phonon mode and the ERS transition at 84 cm^{-1} and the comparatively large oscillator strength of the phonon mode. ERS polarization dependence spectra were obtained for the first doublet transition at 84 cm^{-1}, whose intensity is strong enough for reliable polarization measurements. The phonon lines in Fig. 4-2 are located away from the electronic line at 84 cm^{-1} and do not seem to show an electron-phonon coupling effect. Figures 4-3 and 4-4 show the ZZ, XY, XZ, and ZY polarized spectra for the phonon mode at 807 cm^{-1} and for the ERS transition at 84 cm^{-1}, respectively. The uncertainty for the recorded spectral positions of the phonon and ERS transitions is less than 0.5 cm^{-1}, and the maximum relative error on the intensity measurements is about 10 percent.

The ERS intensities were calibrated and fitted using the calibration procedure described in chapter three. Fig. 4-5 shows the intensities of the phonon mode E_g at 807

cm^{-1} and its corresponding predicted curves described in equations (3.3), with the constant factor obtained from a least square fit (see section 3.3.2 for more detail on the fitting procedure). Fig. 4-6 displays the calibrated polarization dependencies for the ERS transition at 84 cm^{-1} and the corresponding fitted curves from equations (4.6). In equations (4.6), the fitted value of $a = \alpha_1^2/\alpha_1^1$ appearing in the polarization dependence functions was obtained from the least square fit of the ERS data to the corresponding functions in equations (4.6). The observed and predicted data in fig. 4-5 and 4.6 were scaled in such a way that the maximum values of the predicted data are always 100.

The observed data for the polarization dependent ERS and phonon spectra agree extremely well with prediction. This agreement seems to stem from the fact that the polarization dependence form of the scattering tensor described in expression (3.4) has been obtained purely from group theoretical consideration (see chapter 2). The Judd-Ofelt-Axe approximation was not introduced until the evaluation of the ratio α_1^2/α_1^1 in terms of $\tau = F_1/F_2$, which appears later in equation (4.4). Thus when applying equation (3.4) for the particular rare earth material, one should substitute the values of α_q^t's in terms of F_t only after the fit has been performed, especially when there exists more than two nonvanishing α_q^t's in equation (3.4).

Two fitted values of α_1^2/α_1^1 for the doublet transition at 84 cm^{-1} were extracted from the least square fit analysis using a total of 45 data points. These fitted values are the quadratic solutions of equation (4.4) and were found to be -0.0865 and -11.57. The corresponding values of τ are 1.04 and 0.0078, respectively. Taking into account only the d-configuration and assuming $E_{df}(Pr^{3+}) = 50{,}000\ cm^{-1}$ and $\hbar\omega = 20000\ cm^{-1}$, the

calculated values for $a = \alpha_1^2/\alpha_1^1$ and τ are -0.175 and .52, respectively (see equations (3.11) and (4.3)). The fact that one of the fitted values of τ (and a) only differs by a factor of 2 with prediction from the second-order perturbation theory of Axe demonstrates the dominance of the d-configuration in accounting for the two-photon intensities in $PrVO_4$.

Table 4.7 compares the observed and predicted relative linestrengths for the case $\tau = 1.03$. From tables 4.5 and 4.7 it is clear that a value $\tau \simeq 1$ explains rather well the inherently weak observed linestrengths and hence the absence of most of the ERS transitions originating in the ground state. For example, equating $(1- .84\tau)$ in table 4.5 to zero for the absence of the transition at 344 cm^{-1} in the ZY polarization gives a value of $\tau \simeq 1.2$.

Table 4.7: Comparison between predicted and observed relative linestrengths of ERS transitions in the $^3H_4$ ground multiplet of Pr^{3+} in $PrVO_4$ for the case $\tau = 1.03$.

ERS transitions (cm^{-1})		ZZ -polarized		XY-polarized		XZ-polarized		ZY-polarized	
Thry. *	Exp.	Cal.	Obs.	Cal.	Obs.	Cal.	Obs.	Cal.	Obs.
35	-	0	-	.18	-	0	-	0	-
85	84	0	-	0	-	.7	.71	1	1
171	-	0	-	0	-	0	-	0	-
195	-	0	-	.23	-	0	-	0	-
343	-	0	-	.05	-	0	-	0	-
409	344	0	-	0	-	.47	.25	.002	-

(-) Not observed

(*) From the crystal field fit

From the analysis above we conclude that the value of τ is most likely near unity. The other value of τ coming from the fit is very close to zero and does not fit the observed intensities and is thus considered non-physical. This result is in contradiction with the finding of Becker et al [5,6], who reported that $\tau = F_1/F_2 \simeq -0.03$ for most ERS transitions in the ground multiplet of $TmPO_4$. From the deduced small value for τ, Becker et al suggested the possibly important role of the excited g-configuration in making contribution to two-photon intensities [7]. As we can see from equation (3.13), if only the d-orbital configuration is taken into account, and using the values of R and E_d given by the Hartree-Fock calculation of the free-ions, the ratio F_1/F_2 is approximately 0.25 for Tm^{3+}, which is an order of magnitude larger than their observed values. Becker et al. asserted that a value of magnitude -0.03 for this ratio can only be obtained when the second term of the numerator in equation (3.13) is comparable to the first term, which indicates the g-orbital configuration might play an important role in two-photon processes. Our analysis for $PrVO_4$ has shown on the contrary that only the contribution from the d-orbital configuration is sufficient to account for most transition intensities in the ground multiplet and the prediction is especially excellent for the polarization dependent behavior of the ERS transition at 84 cm^{-1} in $PrVO_4$.

It remains to consider other possible contributions to the ERS intensities. These contributions include third- and fourth-order effects such as spin-orbit, crystal-field, ligand polarization, and electron correlation. Using the spin-orbit constants for Pr^{3+} given in table 3.1, we have computed the third-order spin-orbit contribution for the ERS

transitions in the ground multiplet. These contributions turn out to be at most a magnitude order smaller than the second-order contributions and therefore would not affect the result obtained above. For Pr^{3+} the considerably large second-order term associated with $<^3H_4\|U^{(2)}\|^3H_4>$ for the $^3H_4$ ground multiplet compared with the third-order term associated with $<^3H_4\|U^{(2)}W^{(11)0}\|^3H_4>$ and the relatively small spin-orbit constant both contribute to the small contribution of the third-order spin-orbit effect relative to the second order contribution. Table 4.8 summarizes the third-order spin-orbit contributions relative to the second-order contributions for the doublets at 84 cm^{-1} and 344 cm^{-1}.

Table 4.8: Relative magnitude of third-order spin-orbit to second-order contributions for ERS transitions in $PrVO_4$.

Transition (cm^{-1})	$\frac{(\alpha_1^2)^{3rd}}{(\alpha_1^2)^{2nd}}$	$\frac{(\alpha_1^1)^{3rd}}{(\alpha_1^1)^{2nd}}$	$\left(\frac{\alpha_1^2}{\alpha_1^1}\right)^{2nd}$	$\left(\frac{\alpha_1^2}{\alpha_1^1}\right)^{ot}$	$\left(\frac{\alpha_1^2}{\alpha_1^1}\right)^{fitted}$	τ^{2nd}	τ^{fitted}
84	-.036	-.072	-.175	-.181	-.089	.52	1.04
344	-.036	-.072	2.32	2.4	1	.52	1.2

Although we were not able to compute all third- and fourth-order contributions corresponding to other effects, we do not expect significant changes in our analysis given thus far. First, the polarization behavior will look exactly the same when higher order terms are added into the second order term. This is because the polarization dependence for these transitions only depend on one variable, namely $a=\alpha_1^2/\alpha_1^1$, which is related to $\tau = F_1/F_2$. Adding higher order terms only changes the computed values of a and τ, but the general expression of the polarization functions will be the same.

Secondly, as pointed above, unless the second-order term is negligibly small, which is not the case for Pr^{3+}, in general the contributions to the ERS intensities would decrease rapidly beyond the second order, therefore the values of a and τ should not be very different from the second order values when higher-order terms have been added. This is not the case for Gd^{3+}, whose leading contribution to two-photon intensities is zero in the second order. In this case, adding the third or higher order contributions would drastically change the result, as nicely demonstrated by Downer et al. [8,9].

In summary we conclude that the second-order theory of Axe is sufficient to explain the observed intensities in all transitions originating in the ground state of the $^3H_4$ ground multiplet of Pr^{3+} in $PrVO_4$. The polarization dependence formalism given in chapter 2 predicts extremely well the polarization dependent behavior of the observed phonon and ERS intensities. The phonon polarized intensities of a phonon mode can be used to calibrate the ERS intensities whose polarization dependent behavior is similar to that of the phonon line. The fitted value of the F_1/F_2 ratio for one transition (84 cm^{-1}) for Pr^{3+} is found to be approximately unity, which is half of the predicted value using the second-order theory and taking into account only the d-orbital configuration.

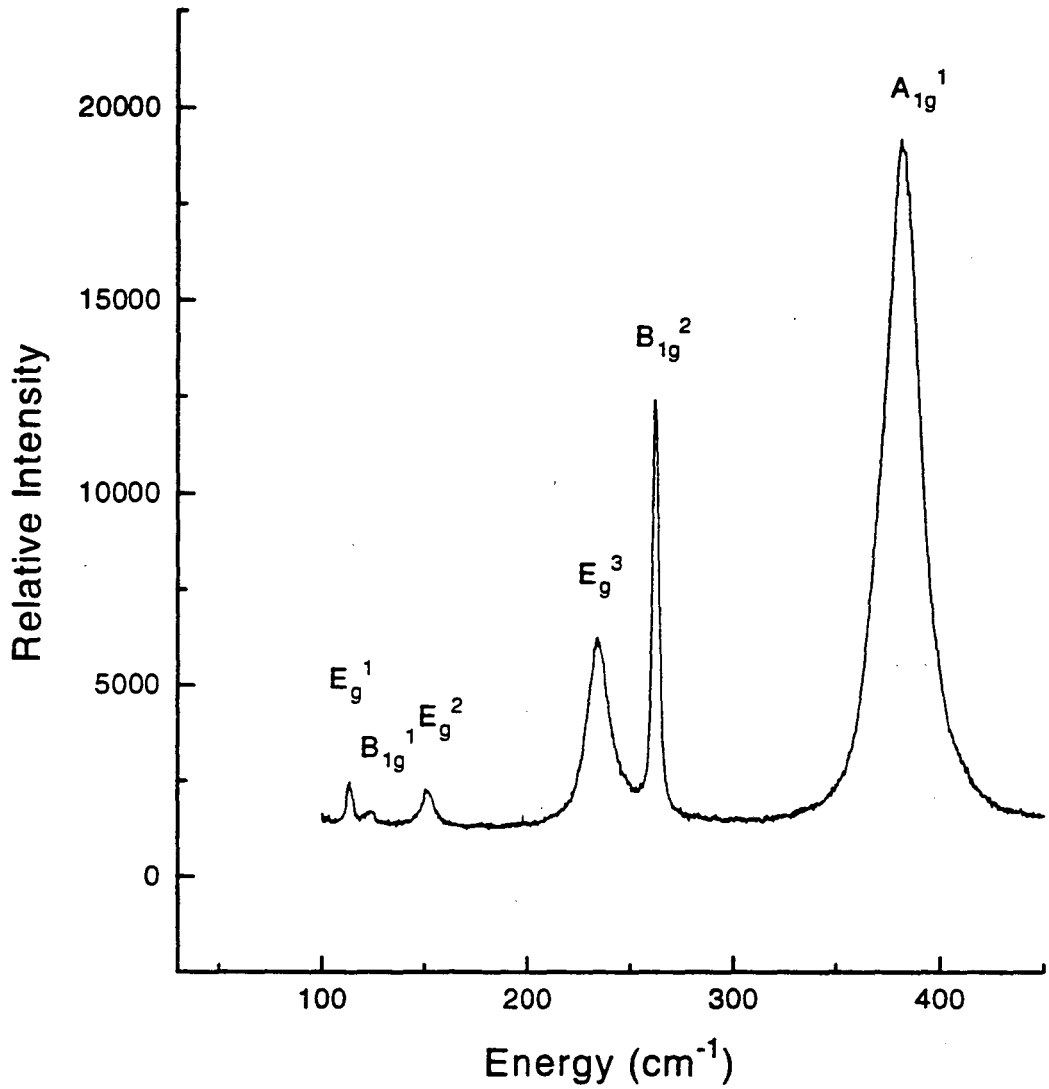

Fig. 4-1: Room temperature, unpolarized phonon spectra of $PrVO_4$, using the 514 nm excitation line.

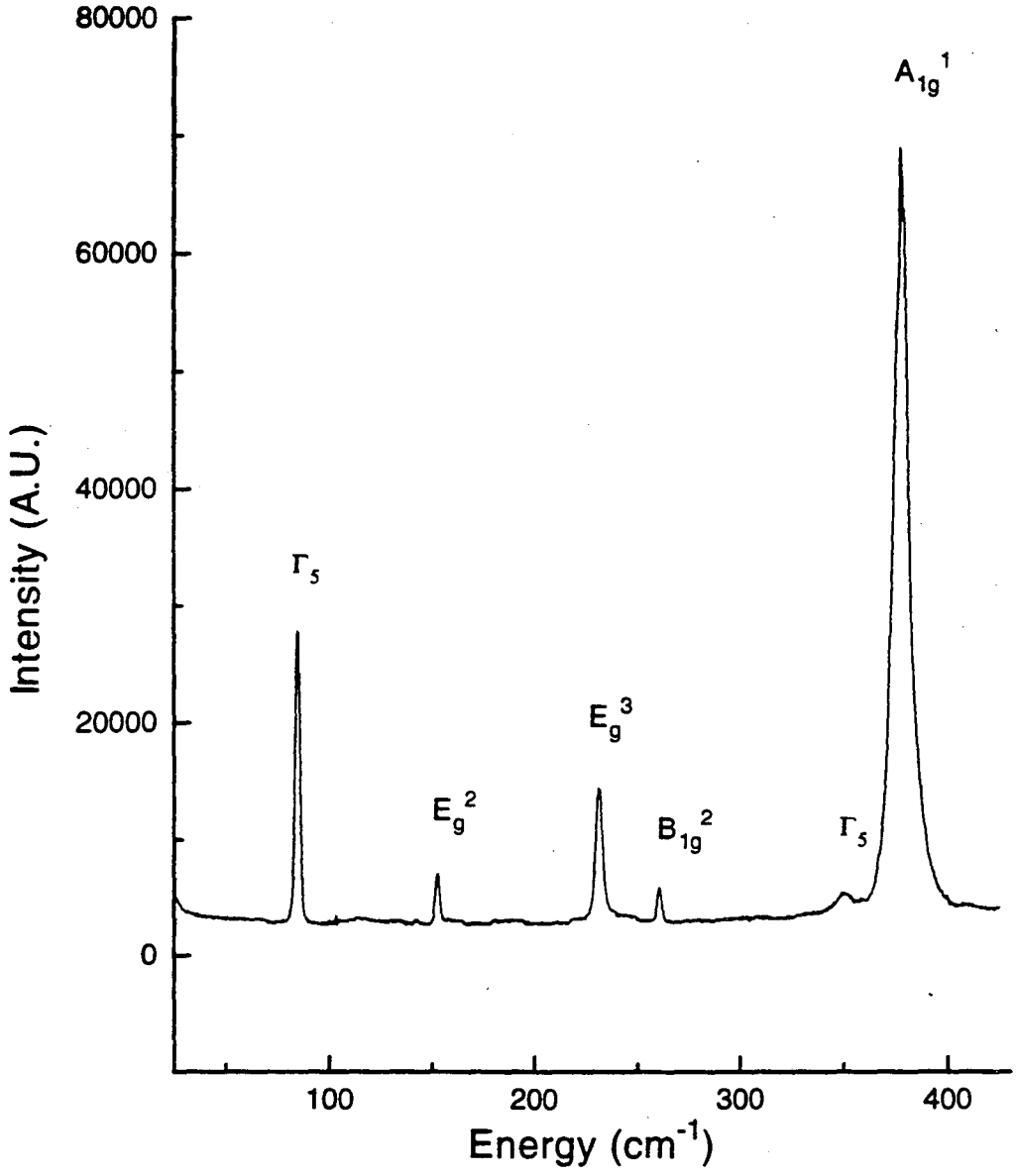

Fig. 4-2: Low temperature, unpolarized ERS spectrum of $PrVO_4$, using the 514 nm excitation line.

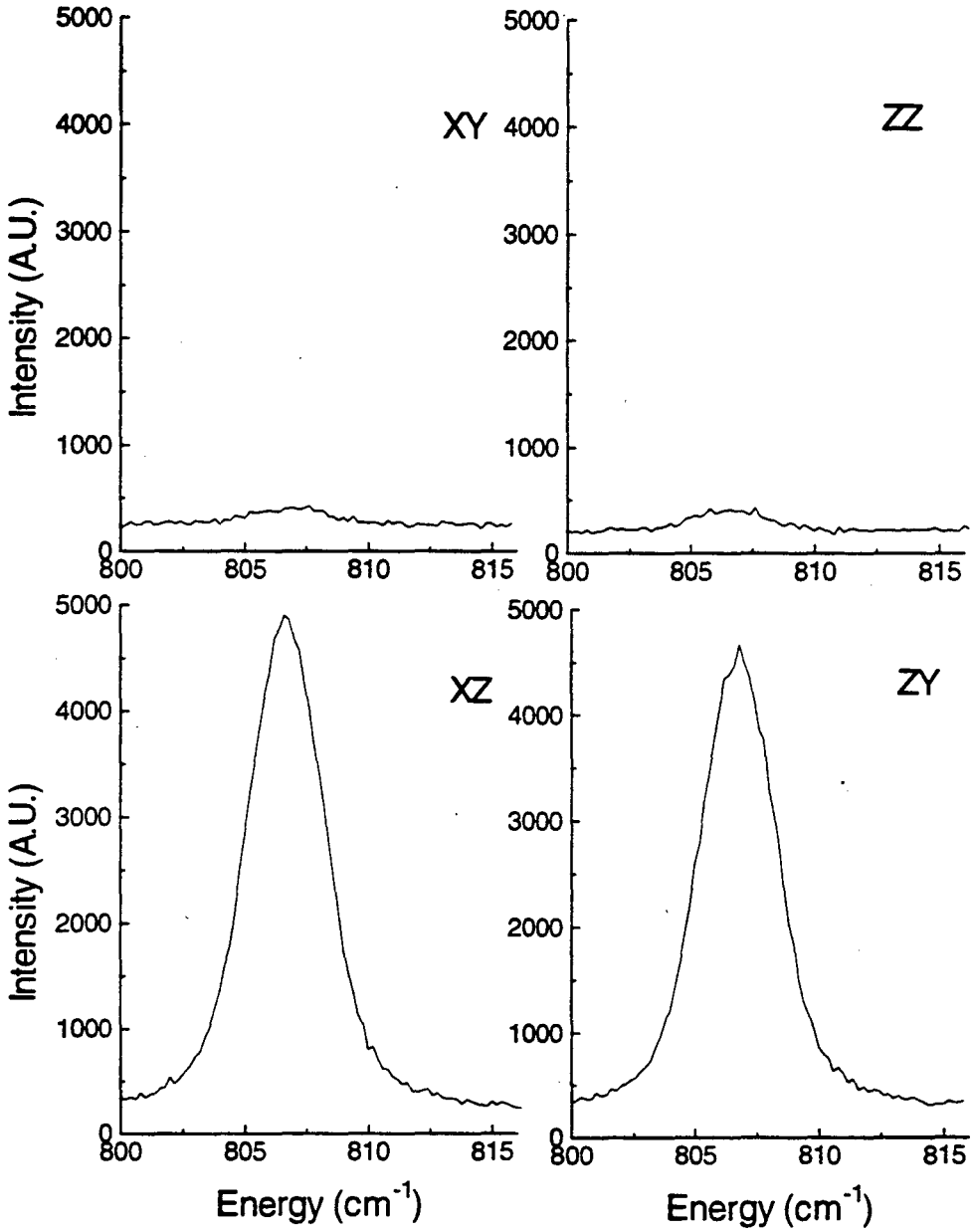

Fig. 4-3: Polarized phonon scattering spectra of $PrVO_4$ at 4.2 K, using the 514 nm excitation line.

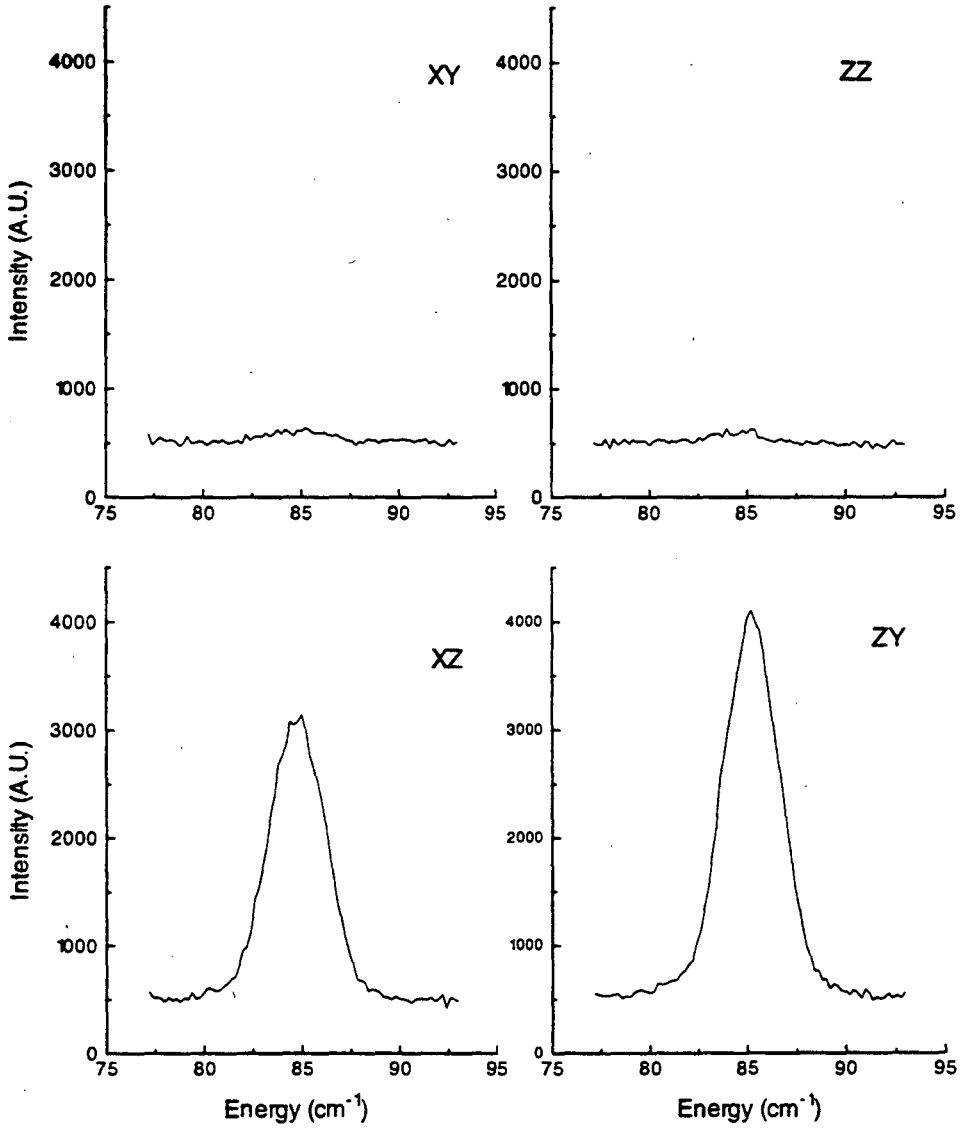

Fig. 4-4: Polarized ERS spectra of $PrVO_4$ at 4.2 K, using the 514 nm excitation line.

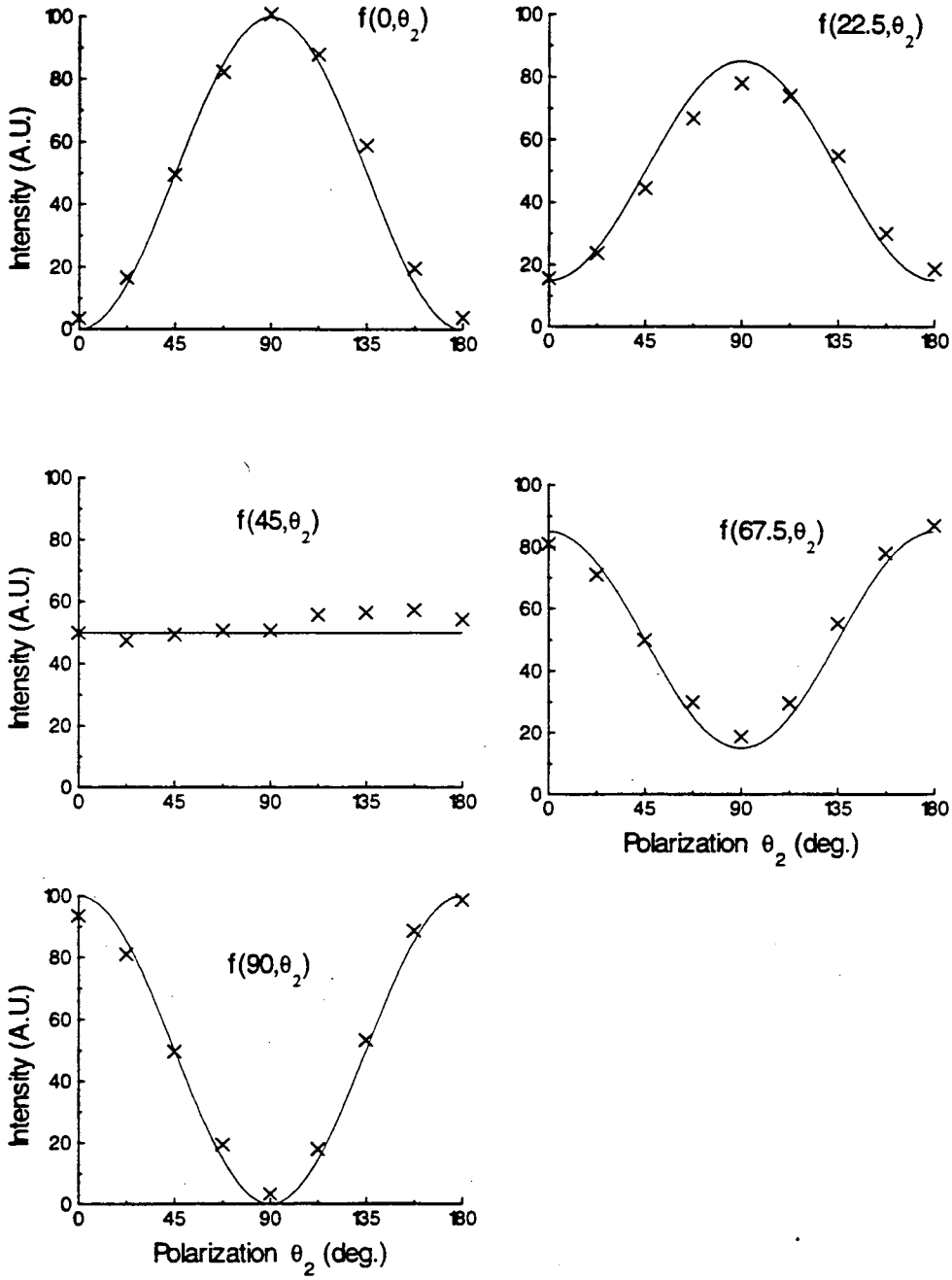

Fig. 4-5: Polarization dependence spectra of the phonon mode E_g at 807 cm^{-1} in $PrVO_4$ at 4.2 K. Solid lines represent the fitted curves using equations 3.3; crosses represent the experimental data.

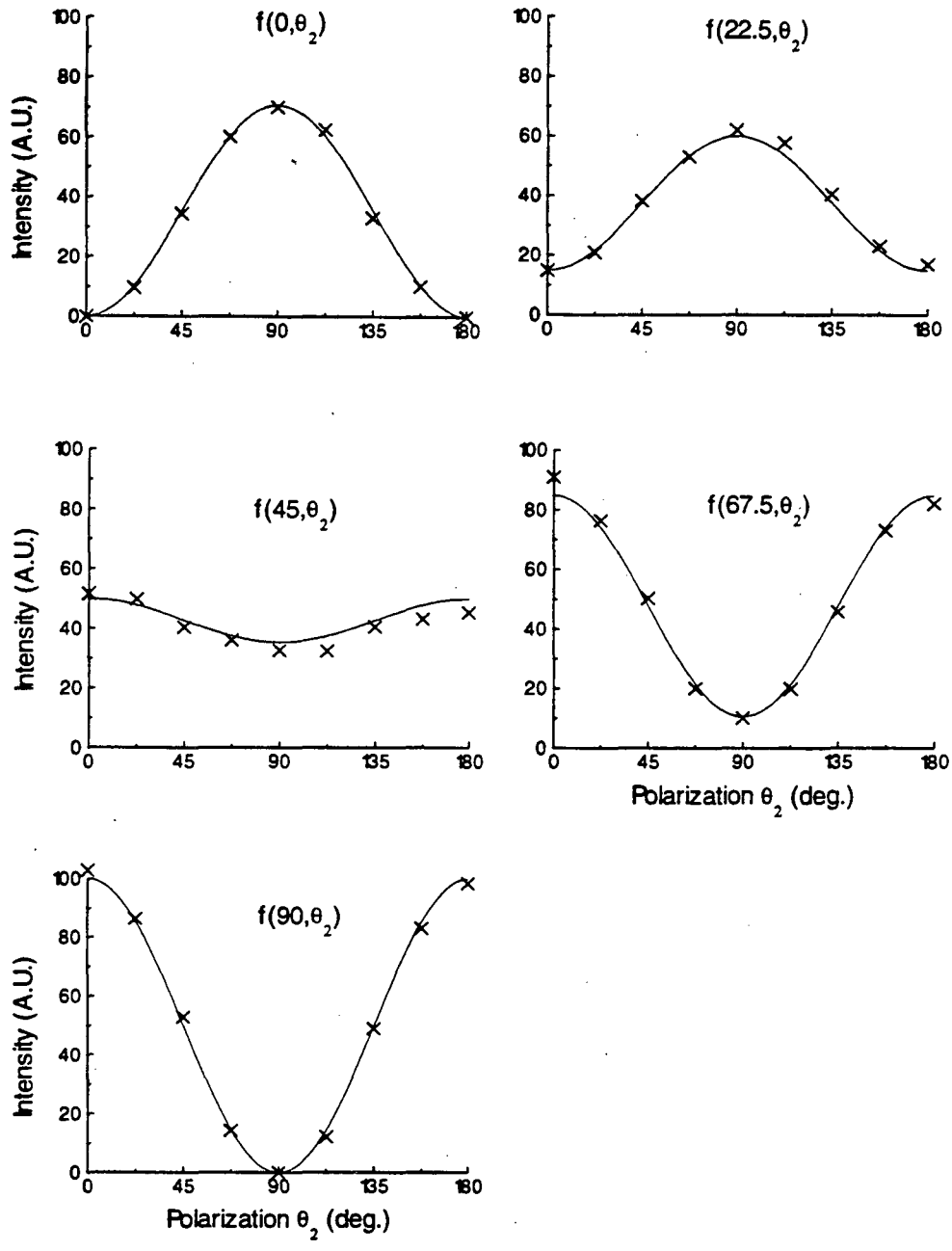

Fig. 4-6: Polarization dependence spectra of ERS transition at 84 cm^{-1} of Pr^{3+} in $PrVO_4$ at 4.2 K. Solid lines represent the fitted curves using equations 4.6; crosses represent the calibrated data.

4.2 Raman Spectroscopy of $NdVO_4$

4.2.1 Nd^{3+}- Selection Rules

Nd^{3+} has the open shell configuration $4f^3$. The point group symmetry of Nd^{3+} in $NdVO_4$ is D_{2d}. Since Nd^{3+} has an odd number of active electrons, the electronic states of the ion are labeled by the irreducible representations Γ_6 and Γ_7 of D_{2d}. All the electronic levels of Nd^{3+} are thus doubly degenerate Kramers' states. The crystal field energy levels and wavefunctions of Nd^{3+} in YVO_4 have been fully established by Tanner and Edelstein [10].

The ground multiplet of Nd^{3+} is $^4I_{9/2}$. The decomposition of the ground multiplet into irreducible representations is given by $3\Gamma_7 + 2\Gamma_6$. The ground crystal field state has the symmetry Γ_7. The selection rules and Raman activity for the Raman transitions originating in the ground state of Nd^{3+} are described in table 4.9.

Table 4.9: Selection rules and Raman activity of ERS transitions originating in the ground state of Nd^{3+} in $NdVO_4$.

Transition	Scattering tensor symmetry	Raman activity α_q^t
$\Gamma_7 \leftrightarrow \Gamma_7$	$\Gamma_1 + \Gamma_2$	α_0^1, α_0^2
$\Gamma_7^K \leftrightarrow \Gamma_7^K$ (*)	$\Gamma_1 + \Gamma_2$	α_0^1, α_0^2
$\Gamma_7^K \leftrightarrow \Gamma_7$	Γ_{5x}(**)	α_1^2, α_1^1
$\Gamma_7 \leftrightarrow \Gamma_7^K$	Γ_{5y}	$\alpha_{-1}^2, \alpha_{-1}^2$
$\Gamma_7 \leftrightarrow \Gamma_6$	$\Gamma_3 + \Gamma_4$	$\alpha_2^2, \alpha_{-2}^2$
$\Gamma_7^K \leftrightarrow \Gamma_6^K$	$\Gamma_3 + \Gamma_4$	$\alpha_2^2, \alpha_{-2}^2$
$\Gamma_7^K \leftrightarrow \Gamma_6$	Γ_{5x}	α_1^2, α_1^1
$\Gamma_7 \leftrightarrow \Gamma_6^K$	Γ_{5y}	$\alpha_{-1}^2, \alpha_{-1}^2$

(*)Γ and Γ^K represent the members of a Kramers doublet.

(**)Γ_{5x} and Γ_{5y} represent the states of a Γ_5 doublet.

4.2.2 Nd^{3+}- Polarization Dependence Functions

From table 4.9 we can construct the polarization behavior for ERS transitions in $NdVO_4$. Table 4.10 lists the two curves corresponding to $\Gamma_7 \leftrightarrow \Gamma_7$ and $\Gamma_7 \leftrightarrow \Gamma_6$ transitions.

In order to determine the values of the non-zero matrix elements of $\alpha_q^{(t)}$ for Nd^{3+} in $NdVO_4$, we use the wavefunctions given by Tanner and Edelstein [10]. These wavefunctions were obtained from a crystal field fit using the observed energy levels of Nd^{3+} diluted in YVO_4:Nd^{3+}. The wavefunctions for the $^4I_{9/2}$ ground multiplet of Nd^{3+} in YVO_4:Nd^{3+} are listed in table 4.11. The polarization dependencies of ERS transition intensities in the $^4I_{9/2}$ ground multiplet of Nd^{3+} are given in table 4.12, and the

intensities relative to the ZZ polarized intensity of the first transition at 115 cm^{-1} are given in Table 4.13.

Table 4.10: Polarization dependence functions for ERS transitions originating in the ground state of Nd^{3+} in $NdVO_4$.

Transition	Polarization dependence curves
$\Gamma_7 \leftrightarrow \Gamma_7$	$(\alpha_0^1)^2 \sin^2\theta_1 \sin^2\theta_2 + (4/3)(\alpha_0^2)^2 \cos^2\theta_1 \cos^2\theta_2$ $+ (1/4)[(\alpha_1^2)^2 + (\alpha_1^1)^2][\sin^2(\theta_2-\theta_1) + \sin^2(\theta_2+\theta_1)]$ $+ \alpha_1^2\alpha_1^1 \sin(\theta_2-\theta_1)\sin(\theta_2+\theta_1)$
$\Gamma_7 \leftrightarrow \Gamma_6$	$(1/2)(\alpha_2^2 + \alpha_{-2}^2)^2 \sin^2\theta_1 \sin^2\theta_2$ $+(1/4)[(\alpha_1^2)^2 + (\alpha_1^1)^2][\sin^2(\theta_2-\theta_1) + \sin^2(\theta_2+\theta_1)]$ $+ \alpha_1^2\alpha_1^1 \sin(\theta_2-\theta_1)\sin(\theta_2+\theta_1)$

Table 4.11: Wavefunctions for the ground multiplet of Nd^{3+} in $NdVO_4$.

Calculated Energy (cm^{-1}) and Symmetry	Wavefunction $\sum_{J,J_z} a(J,J_z)\ {}^{2S+1}L_J(J_z)$
0 (Γ_7)	$.773\ {}^4I_{9/2}(1/2) - .606\ {}^4I_{9/2}(-7/2)$
108 (Γ_7)	$-.768\ {}^4I_{9/2}(-7/2) - .603\ {}^4I_{9/2}(1/2)$
175 (Γ_6)	$.825\ {}^4I_{9/2}(3/2) - .525\ {}^4I_{9/2}(-5/2)$
219 (Γ_7)	$-.981\ {}^4I_{9/2}(9/2) + .166\ {}^2H2_{9/2}(9/2)$
437 (Γ_6)	$-.83\ {}^4I_{9/2}(-5/2) - .524\ {}^4I_{9/2}(3/2)$

Table 4.12. Polarization dependencies of ERS transition intensities in the $^4I_{9/2}$ ground multiplet of Nd^{3+} in $NdVO_4$.

Transitions (cm^{-1})	Non-zero α_q^t	Polarization Dependencies $\lvert\alpha_{21}\rvert^2$
0-108	$\alpha_0^2 = .0395F_2$, $\alpha_0^1 = -.259F_1$ $\alpha_1^2 = 0$, $\alpha_1^1 = .229F_1$	$.002\ F_2^2\ [\cos^2\theta_1 \cos^2\theta_2 + 33\ \tau^2 \sin^2\theta_1 \sin^2\theta_2$ $+6.55\ \tau^2(\sin^2\theta_3 + \sin^2\theta_4)]$
0-175	$\alpha_1^2 = -.004F_2$, $\alpha_1^1 = .432F_1$ $\alpha_2^2 = -.053F_2$, $\alpha_{-2}^2 = .045F_2$	$3\times10^{-5}\ F_2^2\ [\sin^2\theta_1 \sin^2\theta_2 - 58\ \tau \sin\theta_3 \sin\theta_4$ $+(\sin^2\theta_3 + \sin^2\theta_4)(.13 + 1566\ \tau^2)]$ (*)
0-219	$\alpha_1^2 = .041F_2$, $\alpha_1^1 = .175F_1$	$7.2\times10^{-3}\ F_2^2\ [\tau \sin\theta_3 \sin\theta_4$ $+(\sin^2\theta_3 + \sin^2\theta_4)(.059 + 1.06\ \tau^2)]$
0-437	$\alpha_1^2 = -.046F_2$, $\alpha_1^1 = -.003F_1$ $\alpha_2^2 = -.015F_2$, $\alpha_{-2}^2 = -.029F_2$	$9.5\times10^{-4}\ F_2^2\ [\sin^2\theta_1 \sin^2\theta_2 + .15\ \tau \sin\theta_3$ $\sin\theta_4$ $+(\sin^2\theta_3 + \sin^2\theta_4)(.56 + .009\ \tau^2)]$

(*) $\tau = F_1/F_2$, $\theta_3 = \theta_2 - \theta_1$, $\theta_3 = \theta_2 + \theta_1$

Table 4.13: Predicted values of relative linestrengths of ERS transitions in the $^4I_{9/2}$ ground multiplet of Nd^{3+} in $NdVO_4$.

ERS transitions (cm^{-1})	ZZ polarized	XY polarized	XZ polarized	ZY polarized
108	1	$33\ \tau^2$	$35\ \tau^2$	$35\ \tau^2$
175	0	0.015	$47(\tau - .009)^2$	$47(\tau + .009)^2$
219	0	0	$7.6(\tau + .23)^2$	$7.6(\tau - .23)^2$
437	0	.475	$.008(\tau + 8.3)^2$	$.008(\tau - 8.3)^2$

4.2.3 $NdVO_4$ - Experimental Raman Spectra

The observed phonon modes in $NdVO_4$ are listed in table 4.14. All the phonon modes except the B_{2g}^1 mode were clearly identified by their polarization dependent behavior. According to equations (3.2), a phonon mode of B_{2g} character can not be observed for the crystal orientation specified in our ERS setup. At room temperature, however, a weak line was observed at 375 cm^{-1} for the XY scan, and no feature appears between 375 cm^{-1} and 385 cm^{-1} for the XZ and ZY scans. At 4.2 K the observed linewidth of the A_{1g}^1 mode at 380 cm^{-1} is unusually large in an unpolarized scan, which suggests the observation of two superimposing phonon modes with approximately 2 cm^{-1} apart. These observations prompted us to assign the Raman line at 375 cm^{-1} to B_{2g}^1, whose intensity may arise from the leakage through imperpect crystal orientation. The E_g^4 mode has never been observed. Polarized spectra of ERS and phonon transition intensities in $NdVO_4$ were recorded at room temperature and at 4.2 K using the 488 nm excitation line. The crystal field energy levels for the $^4I_{9/2}$, $^2K_{13/2}$, and $^2G_{9/2}$ multiplets of Nd^{3+} in YVO_4 are shown in figure 4-7. Fig 4-8 shows the unpolarized spectrum for the Raman transitions between 90 cm^{-1} and 490 cm^{-1} in $NdVO_4$, which was taken at 4.2 K using the laser excitation at 476 nm. The line appearing at 358 cm^{-1} in fig 4-8 is absent in unpolarized spectra using other laser excitation lines and therefore assigned as an extraneous peak.

Three ERS transitions were observed and labeled by their energies in fig 4-8. These lines were assigned according to their predicted polarization dependent behavior given in tables 4.10 and 4.12. The intensity of the first transition at 101 cm^{-1} is strongest

when $\theta_1 = \theta_2 = 90^0$ and weakest, but not zero, when $\theta_1 = \theta_2 = 0^0$, which is consistent with the first $\Gamma_7 \leftrightarrow \Gamma_7$ transition predicted to be at 115 cm^{-1}. The intensity of the second transition at 169 cm^{-1} is zero when $\theta_1 = \theta_2 = 0^0$, relatively weak when $\theta_1 = \theta_2 = 90^0$, and strongest when $\theta_1 = 90$ and $\theta_2 = 0^0$ or when $\theta_1 = 0$ and $\theta_2 = 90^0$. The intensity of the third transition at 178 cm^{-1} is zero when $\theta_1 = \theta_2 = 0^0$ or when $\theta_1 = \theta_2 = 90^0$, and strongest when $\theta_1 = 90$ and $\theta_2 = 0^0$ or when $\theta_1 = 0$ and $\theta_2 = 90^0$. We thus assign the second and the third transitions to the second and third $\Gamma_7 \leftrightarrow \Gamma_6$ transitions predicted to be at 182 cm^{-1} and 226 cm^{-1}, respectively. Figures 4-9, 4-10, and 4-11 show the ZZ, XY, XZ, and ZY polarized spectra for the A_{1g}^2 phonon mode at 875 cm^{-1}, the ERS transition at 101 cm^{-1}, and the E_g^2 phonon mode at 151cm^{-1} and two ERS transitions at 169 cm^{-1} and 178 cm^{-1}, respectively.

Table 4.14. Frequencies (cm^{-1}) and symmetries of the Raman-active phonons in $NdVO_4$ at 297 and 4.2 K.

	E_g^1	B_{1g}^1	E_g^2	E_g^3	B_{1g}^2	B_{2g}^1	A_{1g}^1	E_g^4	B_{1g}^3	B_{1g}^4	E_g^5	A_{1g}^2
297 K	113	123	148	237	260	375	381	a	472	795	808	871
4.2 K	111	121	151	242	259	378	380	a	473	797	810	873

a: not observed

Polarization dependence spectra have been recorded for the A_{1g}^2 mode at 875 cm^{-1} and for the observed electronic transitions at 101, 169, and 178 cm^{-1}. Calibration was not performed for these ERS intensities because the polarization curves associated with the phonon modes are considerably different from those associated with the ERS transitions. Figures 4-12, 4-13, 4-14 and 4-15 display the experimental polarization

dependencies of the A_{1g}^2 mode and the ERS transitions at 101, 169, and 178 cm^{-1}, respectively. These experimental curves are plotted in the same graph as the predicted curves given in equations 3.2 and table 4.10.

The best fitted data using a least square fit program come from the ERS transition at 101 cm^{-1}. Since $\alpha_1^2=0$ for this transition, we only obtain the fitted values for α_1^1/α_0^1, α_1^1/α_0^2, and α_0^1/α_0^2. Using the relations of α_q^t in terms of τ given in table 4.12, two values of τ can be extracted from the fitted values of α_1^1/α_0^2 and α_0^1/α_0^2. These values of τ were in turn compared with the predicted values, which were obtained from the ab-initio second-order theory of Axe which takes into account only the d-configuration. The fitted value of $|\tau|$ is found to be approximately 0.48, comparing with the predicted value of $\tau = 0.43$ assuming $E_{df} = 60{,}000$ cm^{-1} and $\hbar\omega = 20{,}000$ cm^{-1} (see equation 3.13). The fitted value for α_1^1/α_0^1 was also compared with the calculated value given in table 4.12. These values differ by less than 10 per cent. Table 4.15 summarizes the comparison discussed thus far for the transition at 101 cm^{-1}. The maximum relative error on the intensity measurements for this transition is about 20 percent.

The other two ERS transitions have weaker intensities, and their spectral positions are close to one another and to a strong E_g^2 phonon mode at 151 cm^{-1}, which make it very difficult for accurate intensity measurements. As a result the fits for these transitions are poor and the fitted values for τ are not consistent, which are discounted as unreliable results.

Table 4.15: Comparison of the fitted and calculated values for the relative magnitudes of α_q^t's for the ERS transition in $NdVO_4$ at 101 cm^{-1}.

Transition (101 cm^{-1})	α_1^2	$\left(\frac{\alpha_0^1}{\alpha_1^1}\right)^2$	$\left(\frac{\alpha_0^1}{\alpha_0^2}\right)^2, \tau$	$\left(\frac{\alpha_1^1}{\alpha_0^2}\right)^2, \tau$
Fitted Values	0	.733	10.2, ±.488	7.4, ±.471
Calculated Values	0	.784	8.0, .43	6.2, .43

We can now use the fitted value of τ from the transition at 101 cm^{-1} to predict the intensities of other transitions in the $^4I_{9/2}$ ground multiplet. Table 4.16 compares the predicted and observed relative intensities for different transitions for the case $\tau = 0.48$. As we can see, the agreement between theory and experiment is excellent for all transitions in the $^4I_{9/2}$ ground multiplet of $NdVO_4$. Similar to the case of $PrVO_4$, this agreement provides another vindication for the second-order theory of Axe. Since the number of nonvanishing α_q^t's associated with a transition between two Kramers' states is generally greater than that associated with a transition between two non-Kramers' states, ERS intensities corresponding to transitions between Kramers' states such as that of Nd^{3+} provides a stronger test for Axe's theory than those corresponding to transitions between non-Kramers' states. Excellent agreement found between theory and experiment in the case of $NdVO_4$ has thus been important for the verification of the second order theory.

Table 4.16. Comparison between predicted and observed relative ERS transition intensities in the $^4I_{9/2}$ ground multiplet of Nd^{3+} in $NdVO_4$ for the case $\tau = 0.48$

ERS transitions (cm^{-1})		ZZ -polarized		XY-polarized		XZ-polarized		ZY-polarized	
Thry.*	Exp.	Cal.	Obs.	Cal.	Obs.	Cal.	Obs.	Cal.	Obs.
107	101	1	1	7.6	7.5	3.0	2.5	3.0	2.6
175	169	0	0	.015	0	10	7.5	11.2	7.9
219	178	0	0	0	0	3.8	4.5	1.9	2.2
427	-	0	-	.48	-	.6	-	.5	-

(-) Not observed

(*) From the crystal field fit

Table 4.17 shows the relative magnitude of the third-order spin-orbit contribution relative to the second-order. As in the case of $PrVO_4$, the third-order spin-orbit contribution was found to be relatively small compared to the second-order contribution, and the caculated values for α_q^t would only change slightly when the third-order term was included (compare, for example, tables 4.15 and 4.17). Since Nd^{3+} is a Kramers doublet, it is expected that all $\Gamma_7 \leftrightarrow \Gamma_7$ transitions should at least have different polarization dependence curves when higher order terms are taken into account, because of the presence of the α_0^0 term. For Nd^{3+} in $NdVO_4$, however, due to the negligibly small J-mixing in the states of the ground multiplet, α_0^0 vanishes (chapter 2), and the polarization dependence curves will look the same when higher order terms are included. This small J-mixing in the states of the ground multiplet, which is also found in $PrVO_4$, $ErVO_4$, and $TmVO_4$, is probably due to the small magnitude of the even rank

tensors of the crystal field present in vanadate crystals, which are responsible for the 4f configuration mixing into the 4f crystal field states. The relative magnitude of third-order spin-orbit to second-order contributions are given by

$$\frac{(\alpha_2^2)^{3rd}}{(\alpha_2^2)^{2nd}} = \frac{(\alpha_1^2)^{3rd}}{(\alpha_1^2)^{2nd}} = \frac{(\alpha_0^2)^{3rd}}{(\alpha_0^2)^{2nd}} = \frac{<{}^9I_{9/2}\| (\alpha^2)^{3rd} \|{}^9I_{9/2}>}{<{}^9I_{9/2}\| (\alpha^2)^{2nd} \|{}^9I_{9/2}>} = 0.036$$

and

$$\frac{(\alpha_1^1)^{3rd}}{(\alpha_1^1)^{2nd}} = \frac{(\alpha_0^1)^{3rd}}{(\alpha_0^1)^{2nd}} = \frac{<{}^9I_{9/2}\| (\alpha^1)^{3rd} \|{}^9I_{9/2}>}{<{}^9I_{9/2}\| (\alpha^1)^{2nd} \|{}^9I_{9/2}>} = 0.0395$$

for all transitions in the $^4I_{9/2}$ ground multiplet of Nd^{+3} in $NdVO_4$ (chapter 2).

Table 4.17: Relative magnitudes of (α_q^t) for the ERS transition in $NdVO_4$ at 101 cm^{-1}. Calculated values $(\alpha_q^t)^{tot}$ is the sum of the third-order spin-orbit and second-order contributions.

Transition 101 cm^{-1}	$\left(\frac{(\alpha_0^1)}{(\alpha_1^1)}\right)^2$	$\left(\frac{(\alpha_1^1)}{(\alpha_0^2)}\right)^2$	$\left(\frac{(\alpha_0^1)}{(\alpha_0^2)}\right)^2$
Fitted	.733	7.4	10.2
Calculated (total)	.78	6.28	8.05

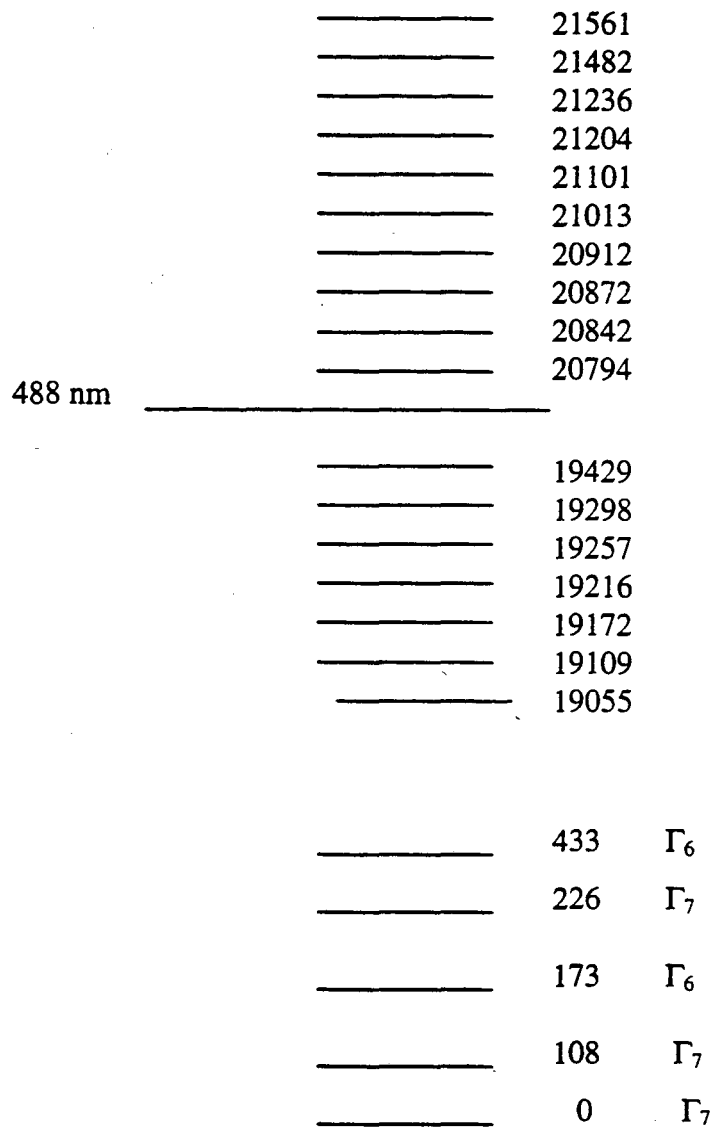

Fig. 4-7: Crystal-field levels of the $^4I_{9/2}$, $^2G_{9/2}$, $^2K_{13/2}$, and $^2K_{15/2}$ multiplets of Nd^{3+} in $NdVO_4$ [10].

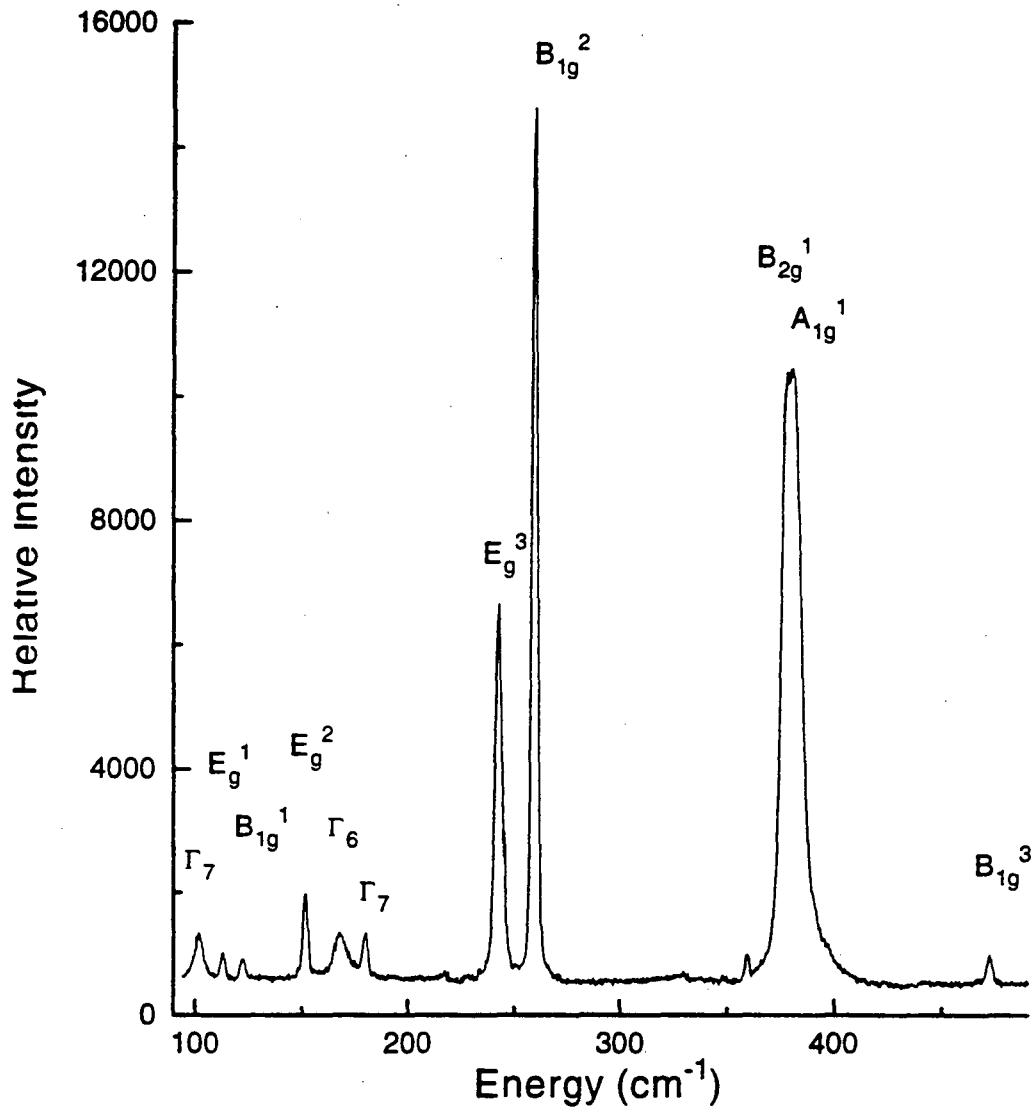

Fig. 4-8: Unpolarized ERS spectrum of $NdVO_4$ at 4.2 K, using the 476 nm excitation line.

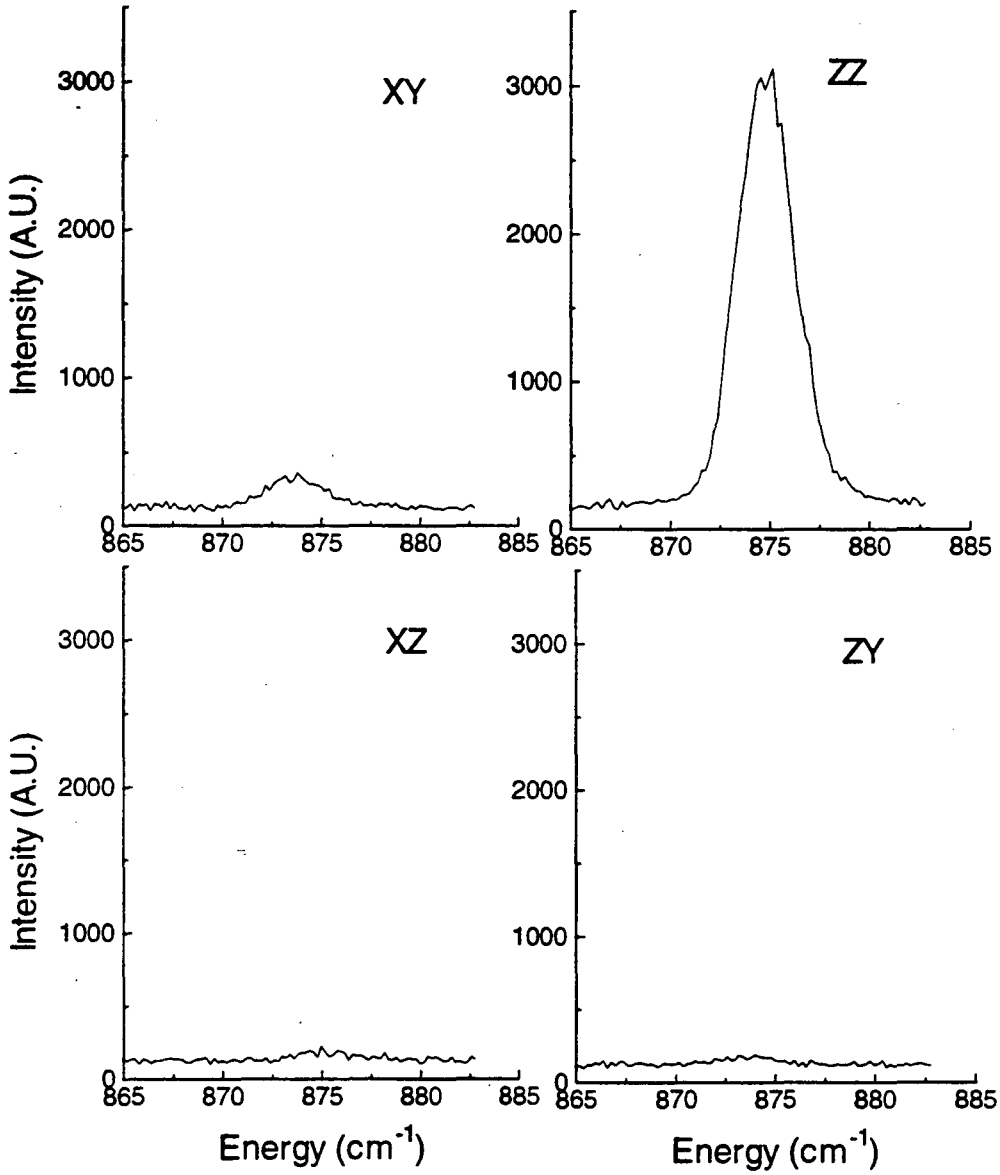

Fig. 4-9: Polarized phonon spectra of the A_{1g}^2 mode of $NdVO_4$ at 4.2 K, with excitation at 488 nm.

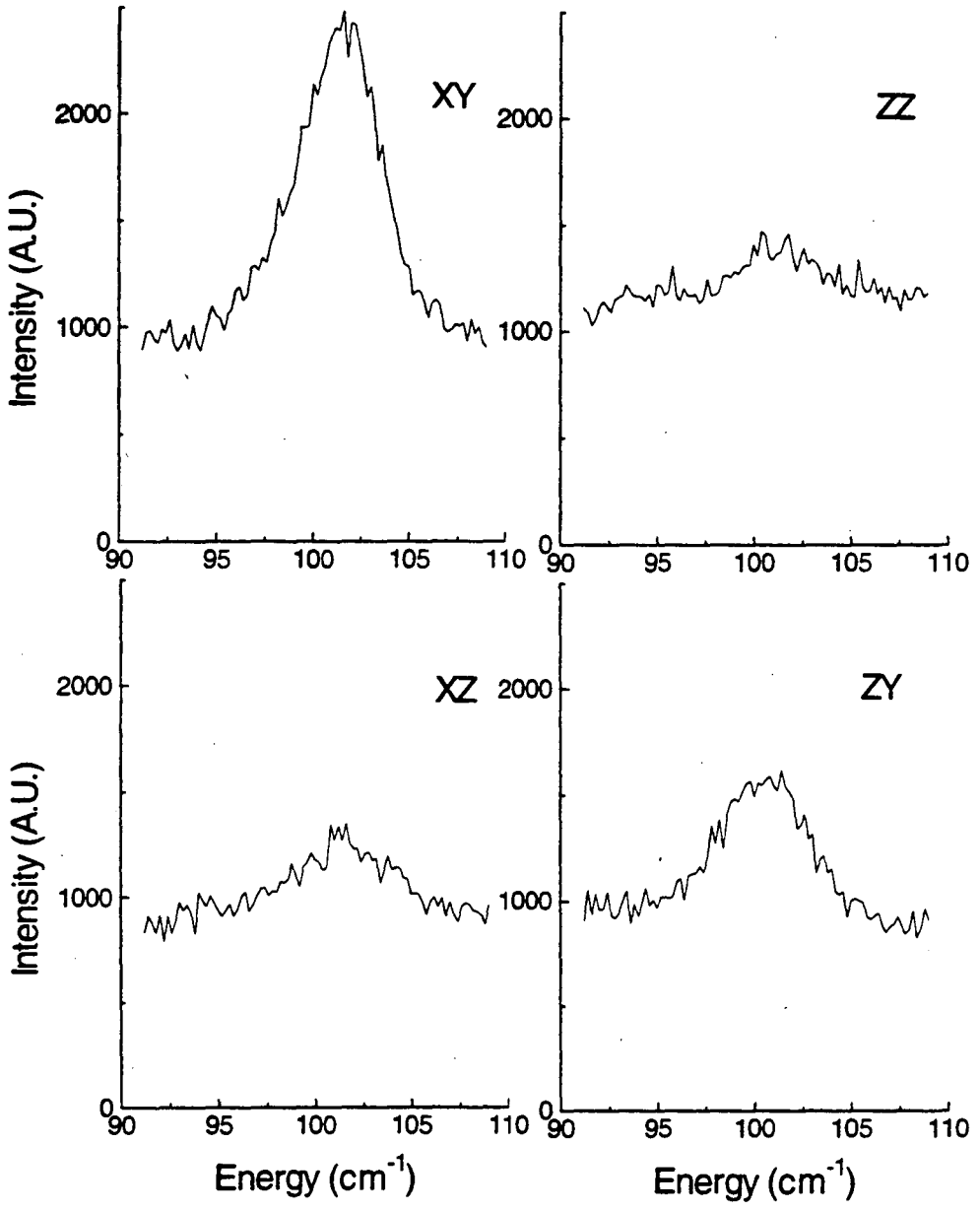

Fig. 4-10: Polarized ERS spectra of the 101 cm^{-1} transition of Nd^{3+} in $NdVO_4$ at 4.2 K, with excitation at 488 nm.

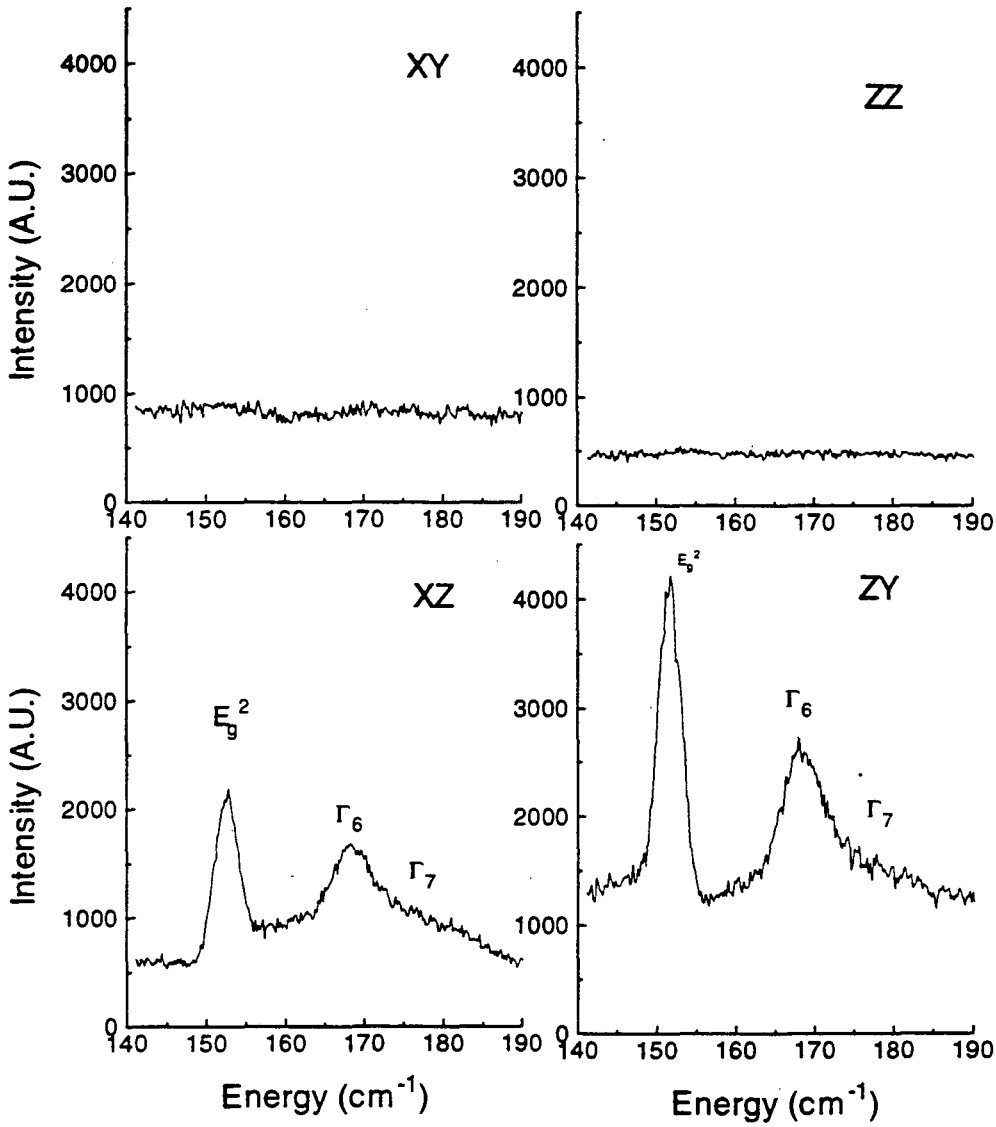

Fig. 4-11: Polarized Raman spectra of the 168 cm^{-1} and 178 cm^{-1} transitions of Nd^{3+} in $NdVO_4$ at 4.2 K, with excitation at 488 nm.

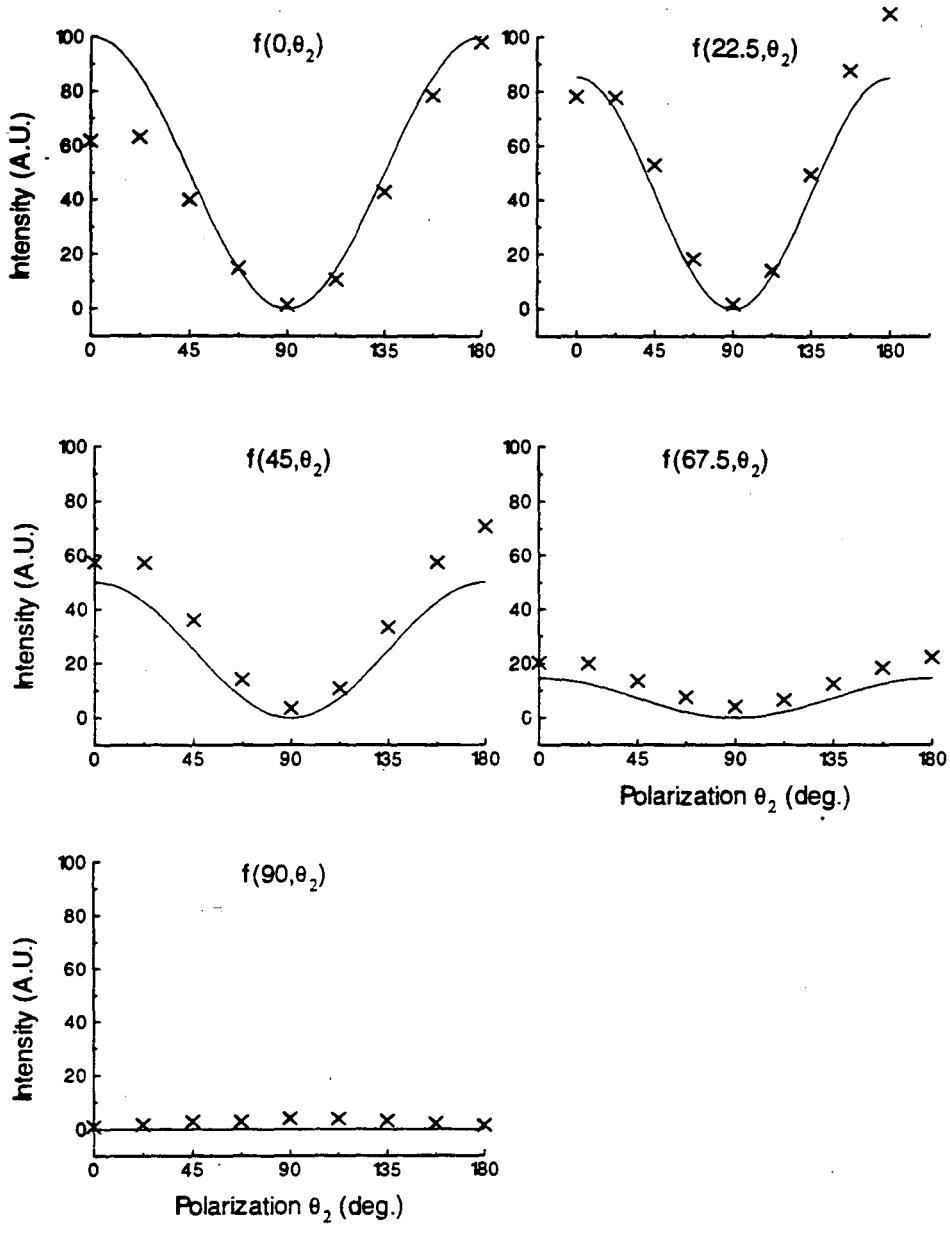

Fig. 4-12: Polarization dependence spectra of the A_{1g}^2 mode at 875 cm^{-1} in $NdVO_4$ at 4.2 K. Solid lines represent the fitted curves using equations 3.2; crosses represent the experimental data.

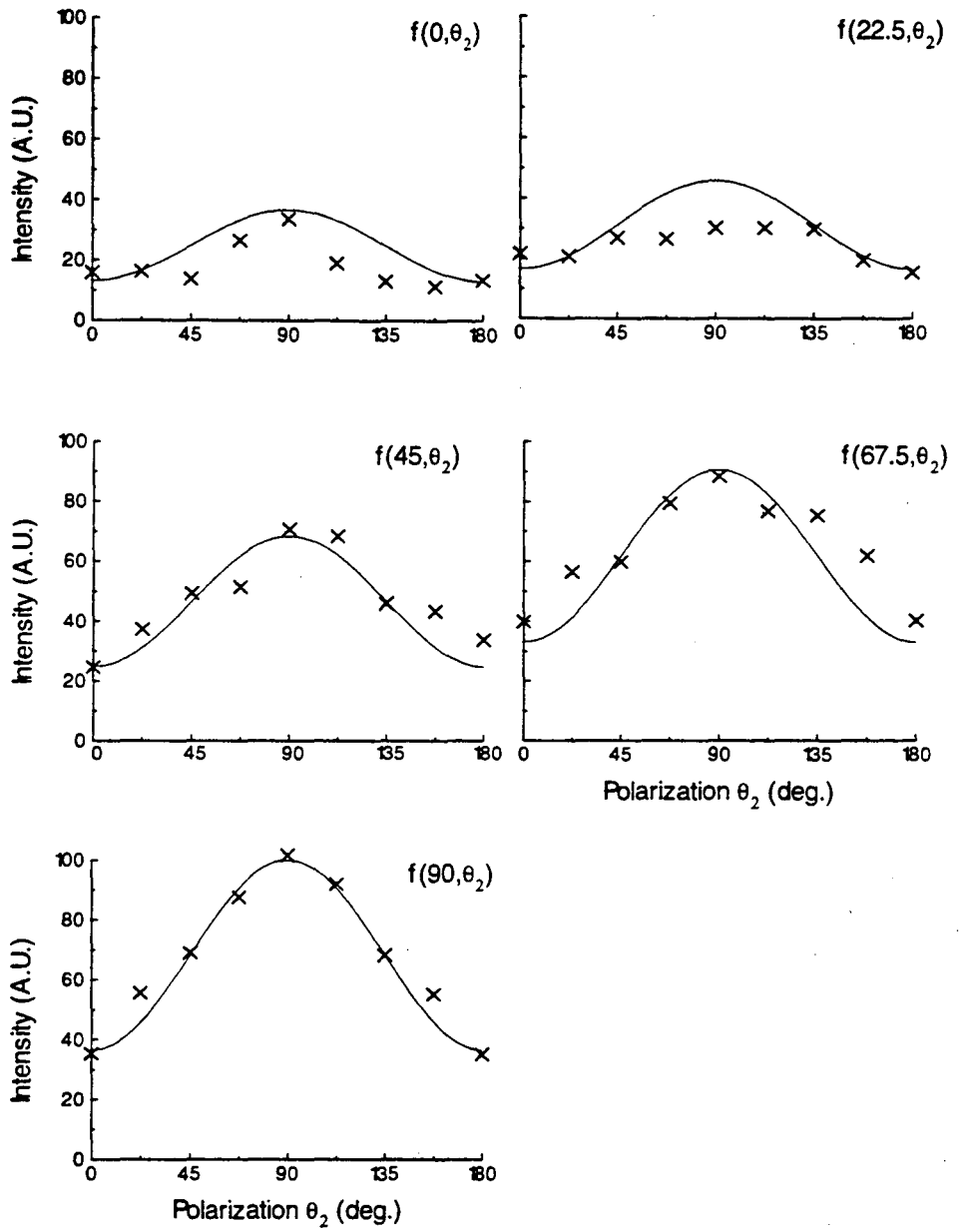

Fig. 4-13: Polarization dependent ERS spectra of the 101 cm^{-1} transition of Nd^{3+} in $NdVO_4$ at 4.2 K. Solid lines represent the fitted curves using Table 4.10; crosses represent the experimental data.

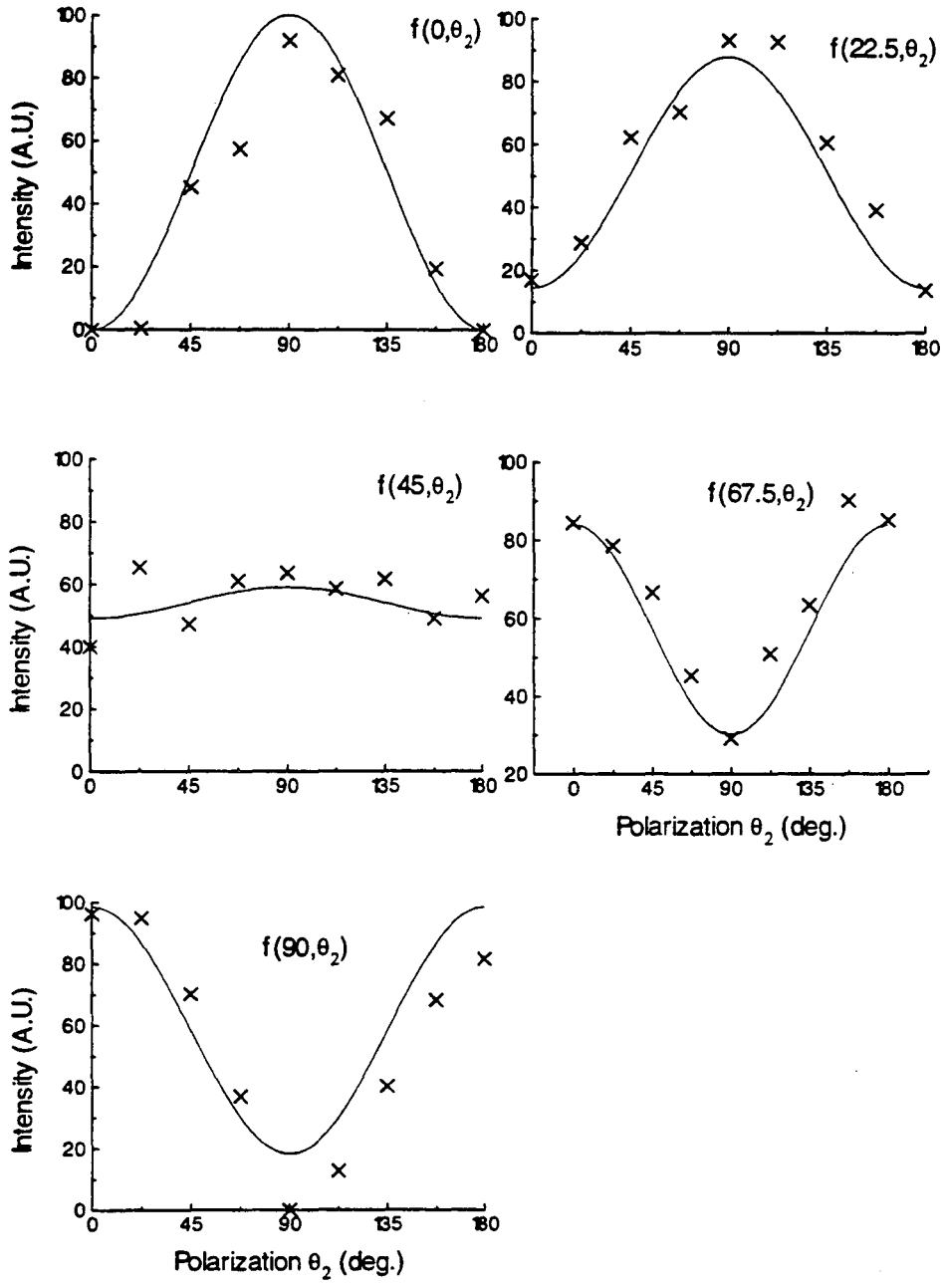

Fig. 4-14: Polarization dependent ERS spectra of the 169 cm^{-1} transition of Nd^{3+} in $NdVO_4$ at 4.2K. Solid lines represent the fitted curves using Table 4.10; crosses represent the experimental data.

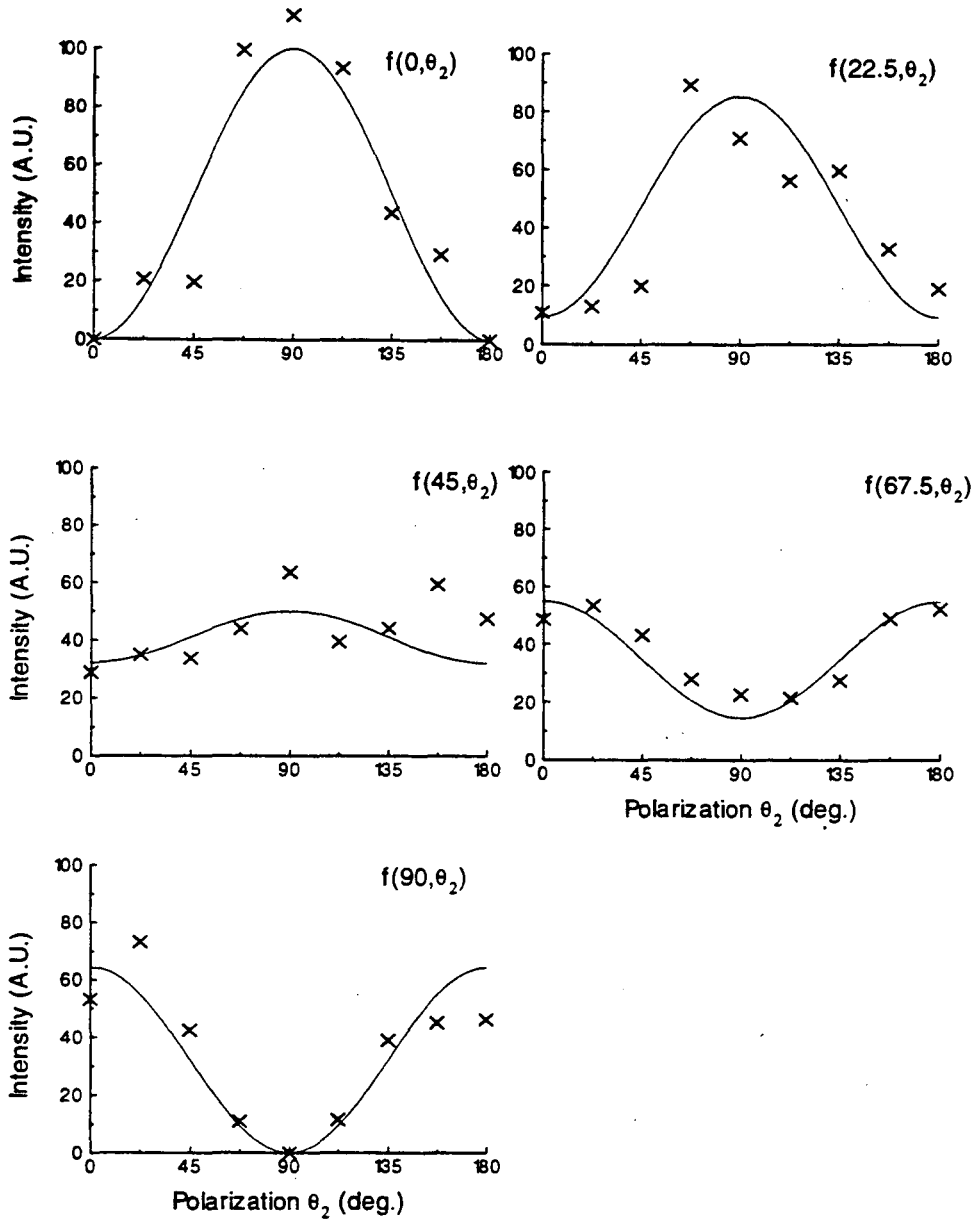

Fig. 4-15: Polarization dependent ERS spectra of the 178 cm^{-1} transition of Nd^{3+} in $NdVO_4$ at 4.2 K. Solid lines represent the fitted curves using Table 4.10; crosses represent the experimental data.

4.3 Raman Spectroscopy of $ErVO_4$

4.3.1 Er^{3+}- Selection Rules

Er^{3+} has eleven 4f electrons, three short of a full shell, which makes Er^{3+} formally equivalent to Nd^{3+}. The point group symmetry of Er^{3+} in $ErVO_4$ is D_{2d}. The doubly degenerate Kramers states of Er^{3+} are thus labeled by the irreducible representations Γ_6 and Γ_7 of D_{2d}. The optical absorption spectrum and crystal field fit of Er^{3+}in dilluted YVO_4 (the ratio of Er^{3+} to Y^{3+} is between 1:100 to 1:100) have been fully reported first by Kuse [11] and the crystal field fit was subsequently modified by Kaminski et al [12].

The ground multiplet of Er^{3+} is $^4I_{15/2}$. The decomposition of the ground multiplet into irreducible representations is given by $4\Gamma_7 + 4\Gamma_6$. The ground crystal field state has the symmetry Γ_7. The selection rules and Raman activity for the Raman transitions originating in the ground state of Er^{3+} are described in table 4.9.

4.3.2 Er^{3+}- Polarization Dependence Functions

The general polarization behavior for ERS transitions of Er^{3+} in $ErVO_4$ is similar to that of Nd^{3+} in $NdVO_4$, which is shown in table 4.10. Using the wavefunctions given by Kaminskii et al [12], we can determine determine the values of the non-zero matrix elements of $\alpha_q^{(t)}$ for Er^{3+} in $ErVO_4$. The wavefunctions for the $^4I_{15/2}$ ground multiplet of Er^{3+} in YVO_4:Er^{3+} are listed in table 4.18. The polarization

dependencies of ERS transition intensities in the $^4I_{15/2}$ ground multiplet of Er^{3+} are given in table 4.19, and the relative polarized intensities are given in table 4.20.

Table 4.18: Wavefunctions for the ground multiplet of Er^{3+}

Calculated Energy (cm^{-1}) and Symmetry	Wavefunction $\sum_{J,J_z} a(J,J_z)\ {}^{2S+1}L_J(J_z)$
0 (Γ_7)	-.793 $^4I_{15/2}$ (-7/2) - . 415 $^4I_{15/2}$ (9/2) +.327 $^4I_{15/2}$ (1/2) +. 25 $^4I_{15/2}$ (-15/2)
44 (Γ_7)	-.833 $^4I_{15/2}$ (9/2) + . 374 $^4I_{15/2}$ (-7/2) -.35 $^4I_{15/2}$ (-15/2) +. 117 $^4I_{15/2}$ (1/2)
48 (Γ_6)	-.798 $^4I_{15/2}$ (-5/2) - . 503 $^4I_{15/2}$ (3/2) -.242 $^4I_{15/2}$ (11/2) +. 145 $^4I_{15/2}$ (-13/2)
75 (Γ_7)	.886 $^4I_{15/2}$ (-15/2) +.366 $^4I_{15/2}$ (-7/2) -.217 $^4I_{15/2}$ (9/2)
147 (Γ_6)	.866 $^4I_{15/2}$ (11/2) - . 386 $^4I_{15/2}$ (-5/2) +.234 $^4I_{15/2}$ (3/2) +. 132 $^4I_{15/2}$ (-13/2)
255 (Γ_6)	-.787 $^4I_{15/2}$ (-13/2) +. 506 $^4I_{15/2}$ (3/2) +.295 $^4I_{15/2}$ (11/2) +.087 $^4I_{15/2}$ (-5/2)
288 (Γ_6)	.637 $^4I_{15/2}$ (3/2) +. 559 $^4I_{15/2}$ (-13/2) +.42 $^4I_{15/2}$ (-5/2) +. 274 $^4I_{15/2}$ (-11/2)
319 (Γ_7)	-.793 $^4I_{15/2}$ (-7/2) - . 415$^4I_{15/2}$ (9/2) +.327 $^4I_{15/2}$ (1/2) +. 25$^4I_{15/2}$ (-15/2)

Table 4.19: Polarization dependencies of ERS transition intensities in the $^4I_{15/2}$ ground multiplet of Er^{3+} in YVO_4.

Transitions (cm^{-1})	Non-zero α_q^t	Polarization Dependencies $\lvert\alpha_{21}\rvert^2$ (*)
0-43	α_0^2= .0043F_2, α_0^1= -.286F_1 α_1^2=.0386F_2 , α_1^1=-.235F_1	$2.5\times10^{-5}F_2^2$ [$\cos^2\theta_1\cos^2\theta_2$ + $3300\tau^2\sin^2\theta_1\sin^2\theta_2$ - $364\tau\sin^2\theta_3\sin^2\theta_4$ +$(567\tau^2+15)(\sin^2\theta_3+\sin^2\theta_4)$]
0-49	α_2^2=-.048F_2, α_{-2}^2=.0407F_2 α_1^2=.024F_2, α_1^1=.417F_1	2.6×10^{-5} F_2^2 [$\sin^2\theta_1\sin^2\theta_2$ +385τ $\sin\theta_3\sin\theta_4$ +$(1600\tau^2+5.5)(\sin^2\theta_3+\sin^2\theta_4)$]
0-75	α_0^2=-.0287F_2, α_0^1= .214F_1 α_1^2=.0204F_2, α_1^1=-.0086F_1	$1.1\times10^{-3}F_2^2$ [$\cos^2\theta_1\cos^2\theta_2$ + $.42\tau^2\sin^2\theta_1\sin^2\theta_2$ - $.158\tau\sin^2\theta_3\sin^2\theta_4$ +$(.016\tau^2+.096)(\sin^2\theta_3+\sin^2\theta_4)$]
0-147	α_2^2=.064F_2, α_{-2}^2=-.03F_2 α_1^2=.0405F_2, α_1^1=-.028F_1	$2.8\times10^{-4}F_2^2$ [$\sin^2\theta_1\sin^2\theta_2$ -$4\tau\sin\theta_3\sin\theta_4$ +$(.7\tau^2+1.5)(\sin^2\theta_3+\sin^2\theta_4)$]
0-255	α_2^2=-.01F_2, α_{-2}^2=-.0017F_2 α_1^2=-.01F_2, α_1^1=-.045F_1	$6.8\times10^{-5}F_2^2$ [$\sin^2\theta_1\sin^2\theta_2$ +$6.6\tau\sin\theta_3\sin\theta_4$ +$(7.3\tau^2+.37)(\sin^2\theta_3+\sin^2\theta_4)$]
0-288	α_2^2=-.031F_2, α_{-2}^2=-.006F_2 α_1^2=-.004F_2, α_1^1=-.061F_1	$6.6\times10^{-4}F_2^2$ [$\sin^2\theta_1\sin^2\theta_2$ +$.36\tau\sin\theta_3\sin\theta_4$ +$(1.4\tau^2+.0058)(\sin^2\theta_3+\sin^2\theta_4)$]
0-319	α_0^2=.012F_2, α_0^1=-.038F_1 α_1^2=-.005F_2, α_1^1=-.021F_1	$1.89\times10^{-4}F_2^2$ [$\cos^2\theta_1\cos^2\theta_2$ + $7.2\tau^2\sin^2\theta_1\sin^2\theta_2$ +$.56\tau\sin^2\theta_3\sin^2\theta_4$ +$(.56\tau^2+.033)(\sin^2\theta_3+\sin^2\theta_4)$]

(*) $\tau = F_1/F_2$, $\theta_3 = \theta_2 - \theta_1$, $\theta_3 = \theta_2 + \theta_1$

Table 4.20: Predicted values of relative linestrengths of ERS transitions in the $^4I_{15/2}$ ground multiplet of Er^{3+} in YVO_4.

ERS transitions (cm^{-1})	ZZ polarized	XY polarized	XZ polarized	ZY polarized
43	.95	$3100\,\tau^2$	$(5.5-32\,\tau)^2$	$(5.5+32\,\tau)^2$
48	0	1	$(3.3+56.6\,\tau)^2$	$(3.3-56.6\,\tau)^2$
75	42	$17.7\,\tau^2$	$(2.9-1.17\,\tau)^2$	$(2.9+1.17\,\tau)^2$
147	0	10.8	$(5.7-3.9\,\tau)^2$	$(2.9+3.9\,\tau)^2$
252	0	2.6	$(1.4+6.2\,\tau)^2$	$(1.4-6.2\,\tau)^2$
288	0	25.4	$(.5+8.4\,\tau)^2$	$(.5-8.4\,\tau)^2$
319	7.3	$53\,\tau^2$	$(.7+2.8\,\tau)^2$	$(.7-2.8\,\tau)^2$

4.3.3 $ErVO_4$ - Experimental Raman Spectra

The observed phonon modes in $ErVO_4$ are listed in table 4.21. Fig 4-16 shows the room temperature, unpolarized phonon spectrum of $ErVO_4$ between 90 and 550 cm^{-1}. As in the case of $NdVO_4$, the line at 380 cm^{-1} in fig 4-16 has unusually large linewidth (approximately 20 cm^{-1}) and may be the superposition of a A_{1g}^1 phonon mode and a very weak B_{2g}^1 mode appearing as an intensity leakage through imperfect orientation. The crystal field energy levels for the $^4I_{15/2}$, $^4F_{7/2}$, and $^4F_{5/2}$ multiplets of Er^{3+} in YVO_4 are shown in figure 4-17. The unpolarized spectrum for the Raman transitions between 30 cm^{-1} and 300 cm^{-1} in $ErVO_4$ is shown in fig 4-18, which was taken at 4.2 K using the laser excitation at 498 nm. The 488 nm excitation line is in resonance with the $^4F_{7/2}$ multiplet (see figure 4-17) and therefore was not used in non-resonant intensity measurements. Two ERS transitions were found at 43 and 252 cm^{-1}.

Their respective polarized spectra at 4K using the 476 nm excitation line are shown in figures 4-19 and 4-20. The line apearing at 275 cm^{-1} in fig. 4-18 is absent in spectra using 476 nm excitation line and was assigned as an extraneous peak. The line at 43 cm^{-1} in figures 4-18 and 4-19 only appeared in XZ, XY, and ZY Raman spectra at low temperature and was assigned to an $\Gamma_7 \leftrightarrow \Gamma_7$ electronic transition, which was predicted at 44 cm^{-1}. The assignment for the ERS line at 252 cm^{-1} was more ambiguous. The intensity of the line at 252 cm^{-1}, which is approximately the same position for the E_g^3 phonon mode observed at room temperature, was enhanced when the temperature drops below 77K, and weak intensities were observed in the XY scans, which should not have been observed for the E_g^1 phonon mode. The same degree of enhancement at low temperature was also found in the case of the B_{1g}^1 mode at 157 cm^{-1} (e.g. compare fig 4-16 and 4.18). For the line at 157 cm^{-1}, however, intensity is strongest in the XY scan, and zero intensity was found in the ZZ, XZ, or ZY, which indicates the absence of polarization leakage. Comparing with the expected polarization dependence curve for the ERS transition at 252 cm^{-1}, we conclude there possibly exists an $\Gamma_7 \leftrightarrow \Gamma_6$ electronic transition superposed on an E_g phonon mode at 252 cm^{-1}. Fig 4-21 displays the temperature evolution spectrum for this Raman peak at 4, 20, 77, 140, 210, and 297 K, using the 488 nm excitation line. The polarized spectra for this transition at 4K using the 476 nm excitation line is shown in fig 4-21.

The intensities for the ERS transition superposed on the B_{1g}^2 phonon mode at 252 cm^{-1} could not be accurately determined and therefore were not used for polarization dependence analysis. Fig 4-22 shows the experimental polarization

dependencies of the ERS transition at 43 cm^{-1}. Calibration using the phonon polarization dependence curves was not performed for the ERS intensities. The experimental curves are plotted in the same graph as the predicted curves given in table 4.10.

Table 4.21: Frequencies (cm^{-1}) and symmetries of the Raman-active phonons in $ErVO_4$ at 297 and 4.2 K.

Tem. (K)	E_g^1	B_{1g}^1	E_g^2	E_g^3	B_{1g}^2	B_{2g}^1	A_{1g}^1	E_g^4	B_{1g}^3	B_{1g}^4	E_g^5	A_{1g}^2
297	105	117	156	251	261	a	380	a	489	820	838	894
4.2	109	118	157	252	260	a	383	a	480	723	840	898

a: not observed

Table 4.22 compares the experimentally fitted values of the relative α_q^t's for the transition at 43 cm^{-1} and the predicted values with α_q^t's given in table 4.19, which were predicted from Axe's second order theory, assuming E_{df} = 100,000 cm^{-1} and $\hbar\omega$ = 20,000 cm^{-1}. The best fitted value of τ is found to be approximately 1.0. In comparing the fit for this transition and the transitions at 101 cm^{-1} in the case of $NdVO_4$ and 84 cm^{-1} in the case of $PrVO_4$, we note that the transition at 43 cm^{-1} is close to the laser excitation, and the peak intensity is weakest among the three, which resulted in more uncertainty in the fit for the transition at 43 cm^{-1} in $ErVO_4$. The maximum relative error on the intensity measurements for this transition is about 25 percent.

Table 4.23 compares the predicted and observed relative intensities for different transitions in $ErVO_4$ for the case τ = 1.0. The predicted relative intensities among transitions seem to account for the abscence of most transitions in $ErVO_4$ except the

ERS transition predicted to be located at 48 cm^{-1}, which was predicted to be at least as strong as the transition at 43 cm^{-1}. Whether or not this transition might be located below 40 cm^{-1} is unclear, since the strong background scattering intensity from the laser excitation in the energy range below 40 cm^{-1} make it impossible to detect the existence of ERS transitions located below 40 cm^{-1}. Also the polarization dependencies of the peak at 43 cm^{-1} matched better with the predicted transition at 44 cm^{-1} than that at 48 cm^{-1}, which eliminates the possibility for identifying the latter with the observed peak at 43 cm^{-1}.

Table 4.22: Comparison of the fitted and calculated values for the relative magnitudes of α_q^t's for the ERS transition in $ErVO_4$ at 43 cm^{-1}.

Transition (43 cm^{-1})	Fitted Values	Calculated Values (second-order)	Calculated Values (second-order)
$\left(\frac{\alpha_0^1}{\alpha_0^2}\right)^2, \tau$	2618, ±0.771	277, 0.25	4424, 1.0
$\frac{\alpha_1^2\alpha_1^1}{(\alpha_0^2)^2}, \tau$	-96.1, .261	-123, 0.25	-491, 1.0
$\frac{\alpha_1^2\alpha_1^1}{(\alpha_0^1)^2}, \tau$	-0.0489, 2.25	-0.44, 0.25	-0.11, 1.0
$\frac{(\alpha_1^2)^2+(\alpha_1^1)^2}{(\alpha_0^2)^2}, \tau$	2124, ±0.828	267.3, 0.25	3068, 1.0
$\frac{(\alpha_1^2)^2+(\alpha_1^1)^2}{(\alpha_0^1)^2}, \tau$	0.811, ±0.364	0.97, 0.25	0.69, 1.0
$\frac{(\alpha_1^2)^2+(\alpha_1^1)^2}{\alpha_1^1\alpha_1^2}, \tau$	16.6, 2.7 or 0.01	2.2, 0.25	6.3, 1.0

We now consider the possible ERS contribution from the third-order spin-orbit interaction. Taking into account only the d-configuration, the third-order spin-orbit contribution was found to be approximately a magnitude order smaller than the second-order contribution, and would not significantly affect the second order results. Because the states of the ground multiplet in $ErVO_4$ are highly pure in J, the third-order α_0^0's vanish for all states of the ground multiplet. The negligibly small J,L,S mixing is also responsible for the relatively small third order contribution in $ErVO_4$. Comparison between the relative magnitudes of (α_q^t)'s calculated from both second and third order contributions and the corresponding fitted values for the ERS transition in $ErVO_4$ at 43 cm^{-1} are listed in table 4.24. The relative magnitude of third-order spin-orbit to second-order contributions in $ErVO_4$ are given by

$$\frac{(\alpha_2^2)^{3rd}}{(\alpha_2^2)^{2nd}} = \frac{(\alpha_1^2)^{3rd}}{(\alpha_1^2)^{2nd}} = \frac{(\alpha_0^2)^{3rd}}{(\alpha_0^2)^{2nd}} = \frac{<{}^9I_{9/2}|| \ (\alpha^2)^{3rd}||{}^9I_{9/2}>}{<{}^9I_{9/2}|| \ (\alpha^2)^{2nd}||{}^9I_{9/2}>} = -0.131 \quad \text{and}$$

$$\frac{(\alpha_1^1)^{3rd}}{(\alpha_1^1)^{2nd}} = \frac{(\alpha_0^1)^{3rd}}{(\alpha_0^1)^{2nd}} = \frac{<{}^9I_{9/2}|| \ (\alpha^1)^{3rd}||{}^9I_{9/2}>}{<{}^9I_{9/2}|| \ (\alpha^1)^{2nd}||{}^9I_{9/2}>} = 0.03$$

for all transitions in the ${}^4I_{15/2}$ ground multiplet of Er^{+3} in $ErVO_4$.

Table 4.23: Comparison between predicted and observed relative ERS transition intensities in the $^4I_{15/2}$ ground multiplet of Er^{3+} in $ErVO_4$ for the case $\tau = 1.0$.

ERS transitions (cm^{-1})		ZZ -polarized		XY-polarized		XZ-polarized		ZY-polarized	
Thry.*	Exp.	Cal.	Obs.	Cal.	Obs.	Cal.	Obs.	Cal.	Obs.
44	43	1	0	3100	2080	700	700	1406	1052
48	-	0	-	1	-	3588	-	2841	-
75	-	42	-	18	-	3	-	15	-
147	-	0	-	11	-	3	-	17	-
255	252	0	0	3	u	129	u	23	u
288	-	0	-	25	-	79	-	62	-
319	-	7	-	0.5	-	12	-	4	-

(-) Not observed

(u) Unknown, due to superposed phonon intensities

(*) From the crystal field fit

Table 4.24: Relative magnitudes of (α_q^t) for the ERS transition in $ErVO_4$ at 43 cm^{-1}. Calculated values $(\alpha_q^t)^{tot}$ is the sum of the third-order spin-orbit and second-order contributions, with only the d-configuration taken into account.

Transition 43 cm^{-1}	Fitted Values	Calculated Values (second and third order)
$\left(\frac{\alpha_0^1}{\alpha_0^2}\right)^2$	2618	328
$\frac{\alpha_1^2\alpha_1^1}{(\alpha_0^2)^2}$	-96.1	-146
$\frac{\alpha_1^2\alpha_1^1}{(\alpha_0^1)^2}$	-0.0489	-0.37
$\frac{(\alpha_1^2)^2+(\alpha_1^1)^2}{(\alpha_0^2)^2}$	2124	290
$\frac{(\alpha_1^2)^2+(\alpha_1^1)^2}{(\alpha_0^1)^2}$	0.811	0.9
$\frac{(\alpha_1^2)^2+(\alpha_1^1)^2}{\alpha_1^1\alpha_1^2}$	16.6	2.0

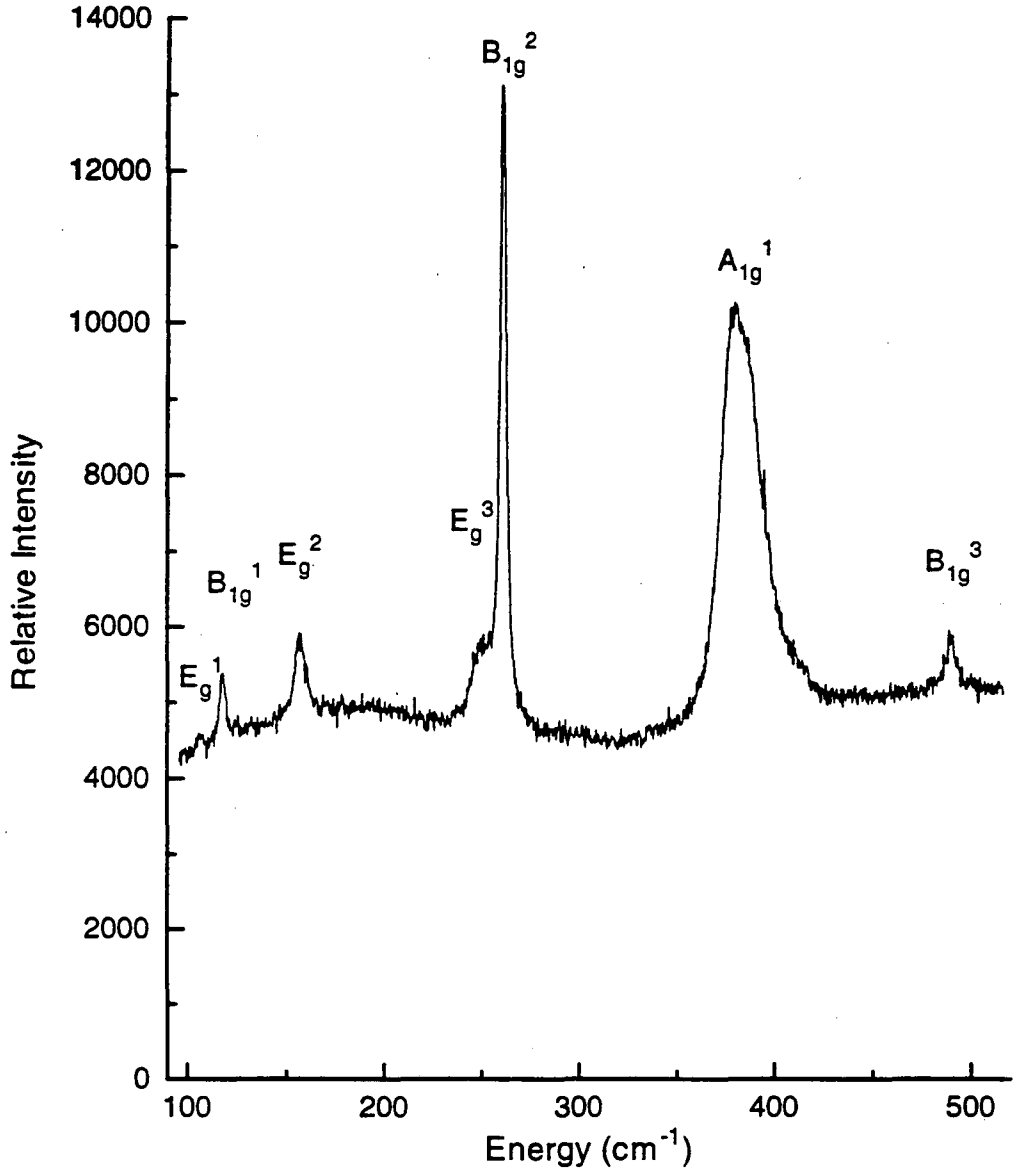

Fig. 4-16: Unpolarized phonon spectrum of $ErVO_4$ at 297 K, using the excitation line at 496 nm. The full scale is 14000 counts per second for each scan.

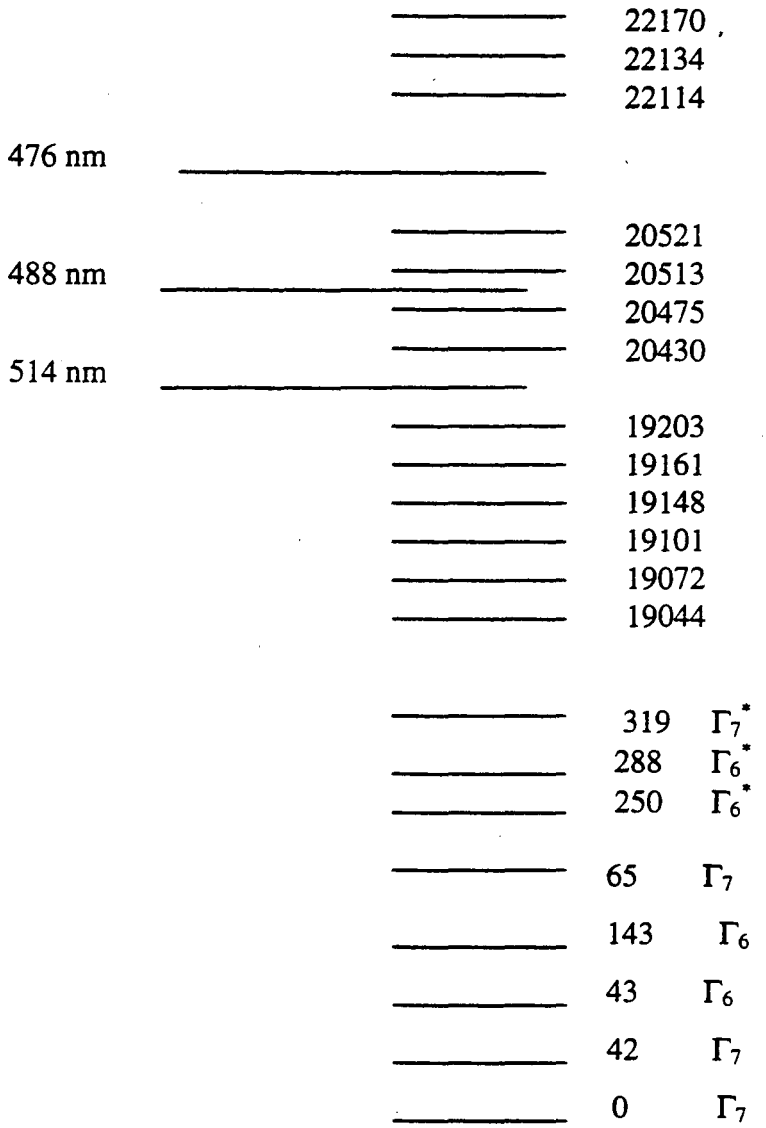

Fig. 4-17: Crystal field levels for the multiplets $^4I_{15/2}$, $^2H_{11/2}$, $^4F_{7/2}$, and $^4F_{5/2}$ for Er^{3+} in $ErVO_4$ [11]. (*) From crystal field fit.

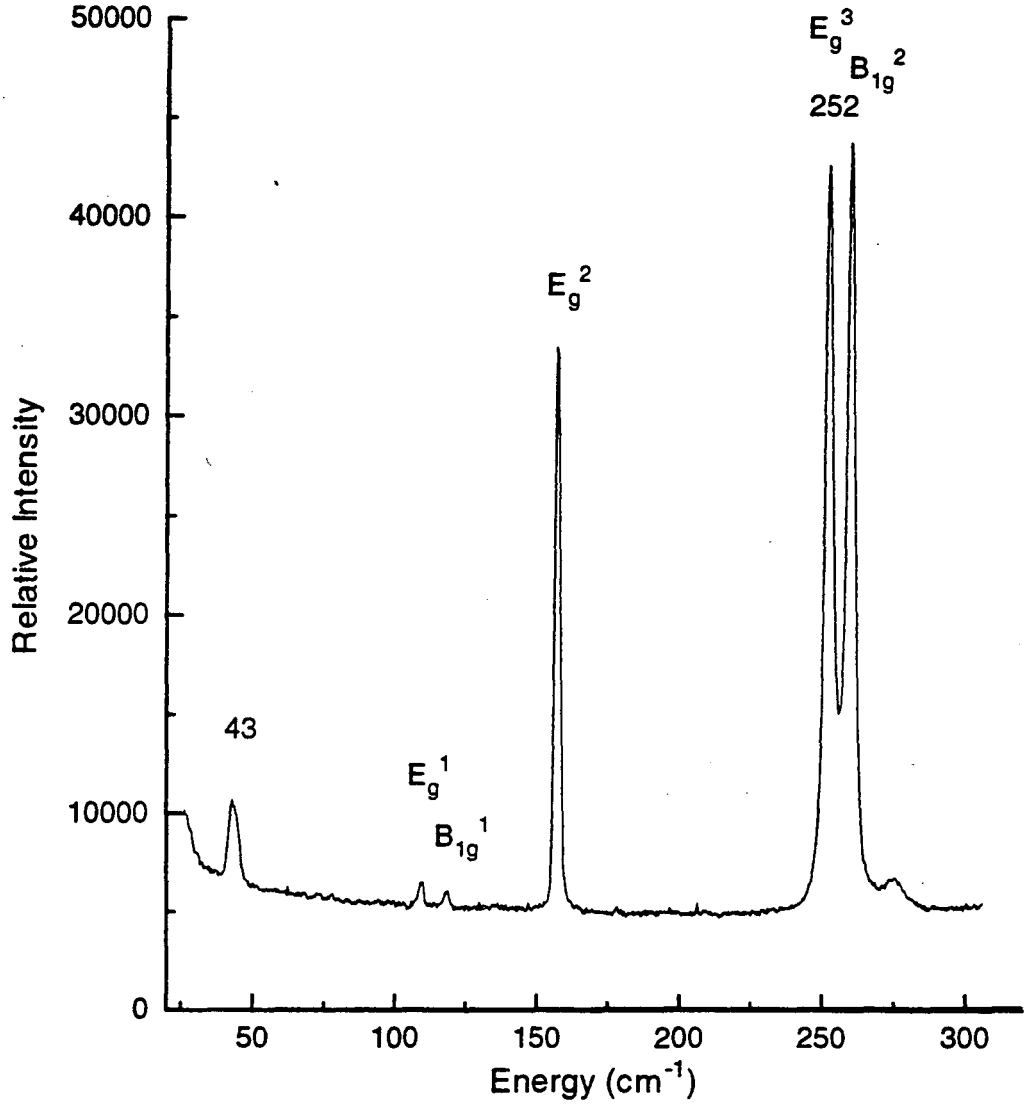

Fig. 4-18: Low temperature, unpolarized Raman spectrum of $ErVO_4$, using the 496 nm excitation line.

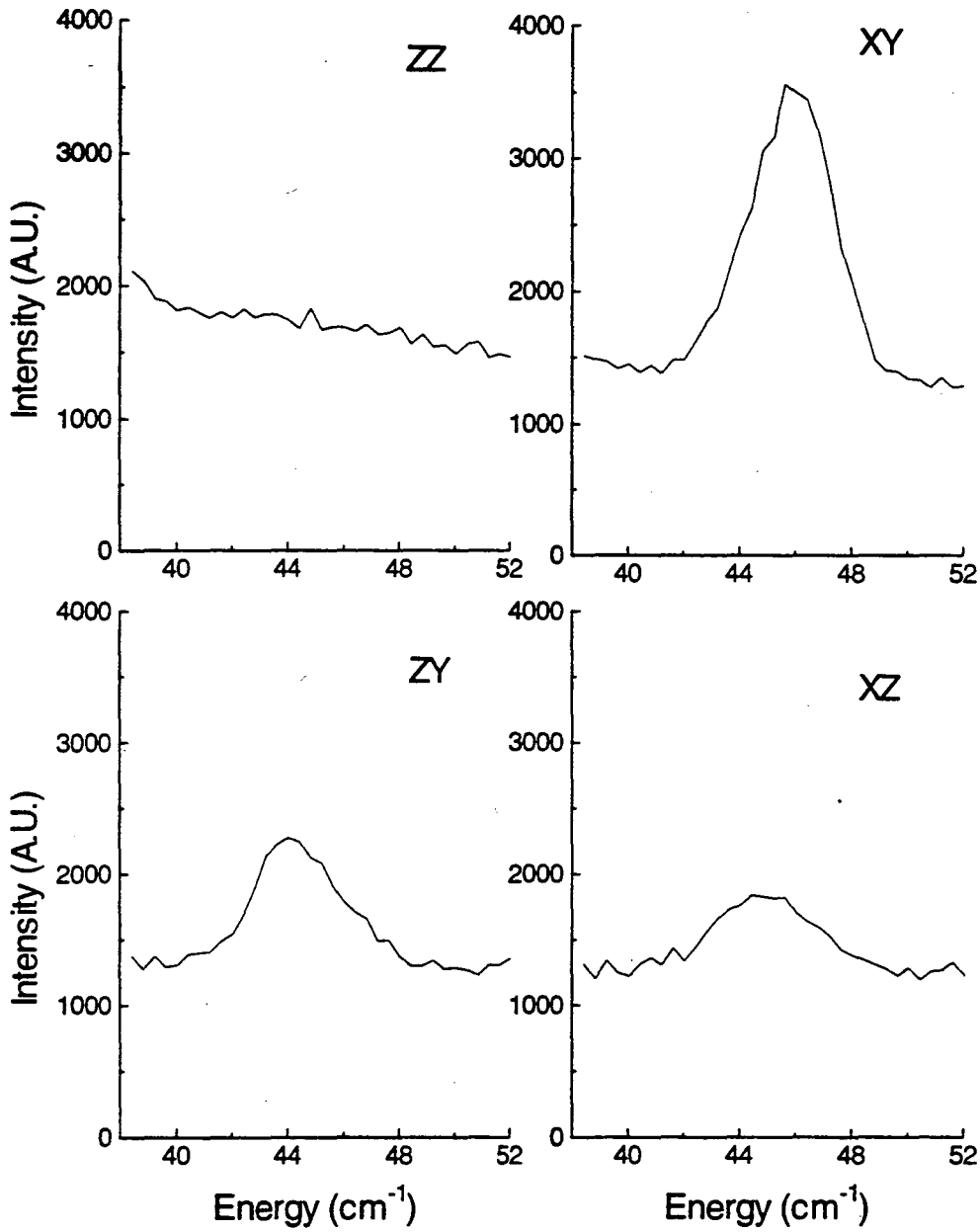

Fig. 4-19: Polarized ERS spectra of the 43 cm^{-1} transition of Er^{3+} in $ErVO_4$ at 4.2 K, with excitation at 476 nm.

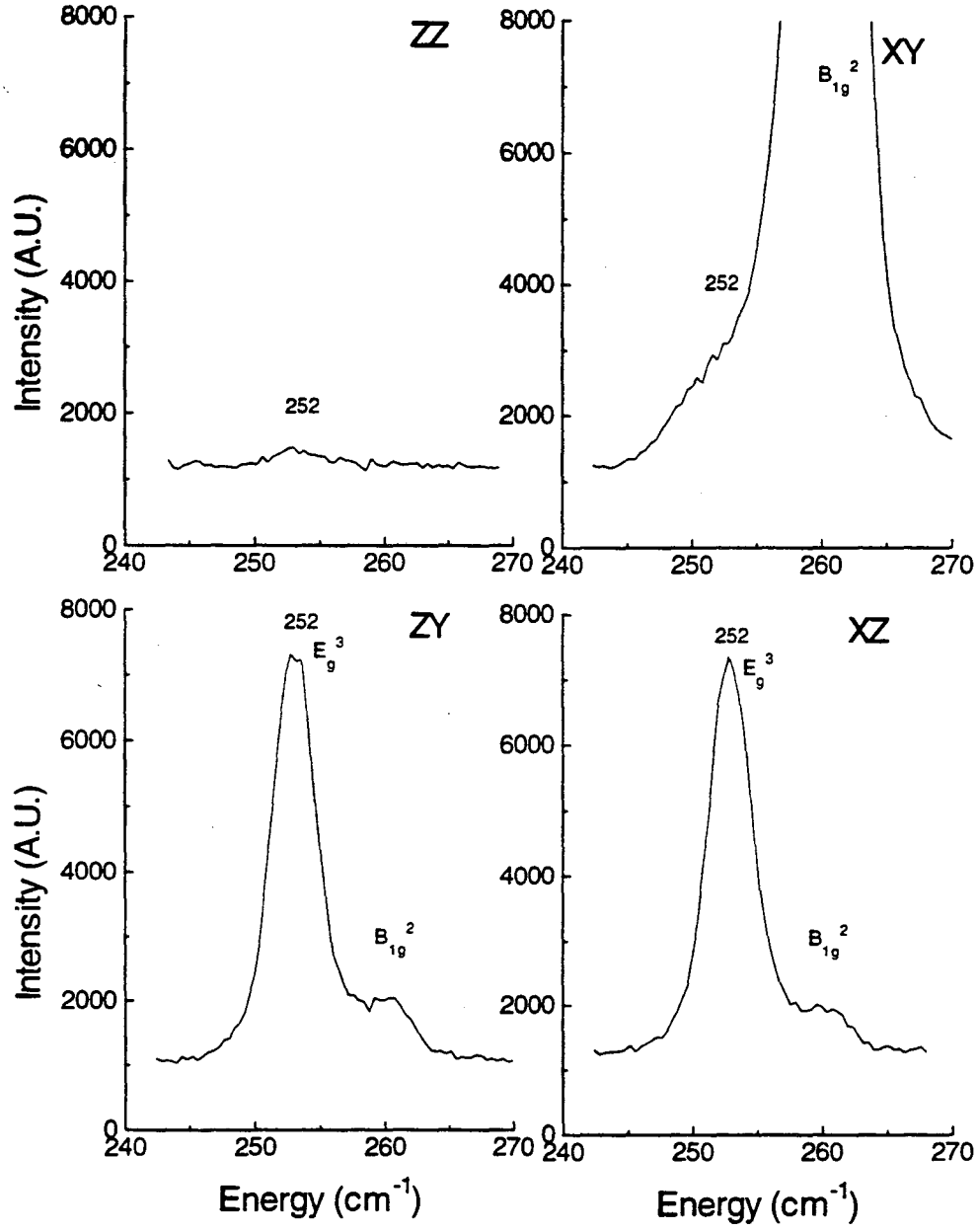

Fig. 4-20: Polarized ERS spectra of the 252 cm^{-1} transition of Er^{3+} in $ErVO_4$ at 4.2 K, with excitation at 476 nm.

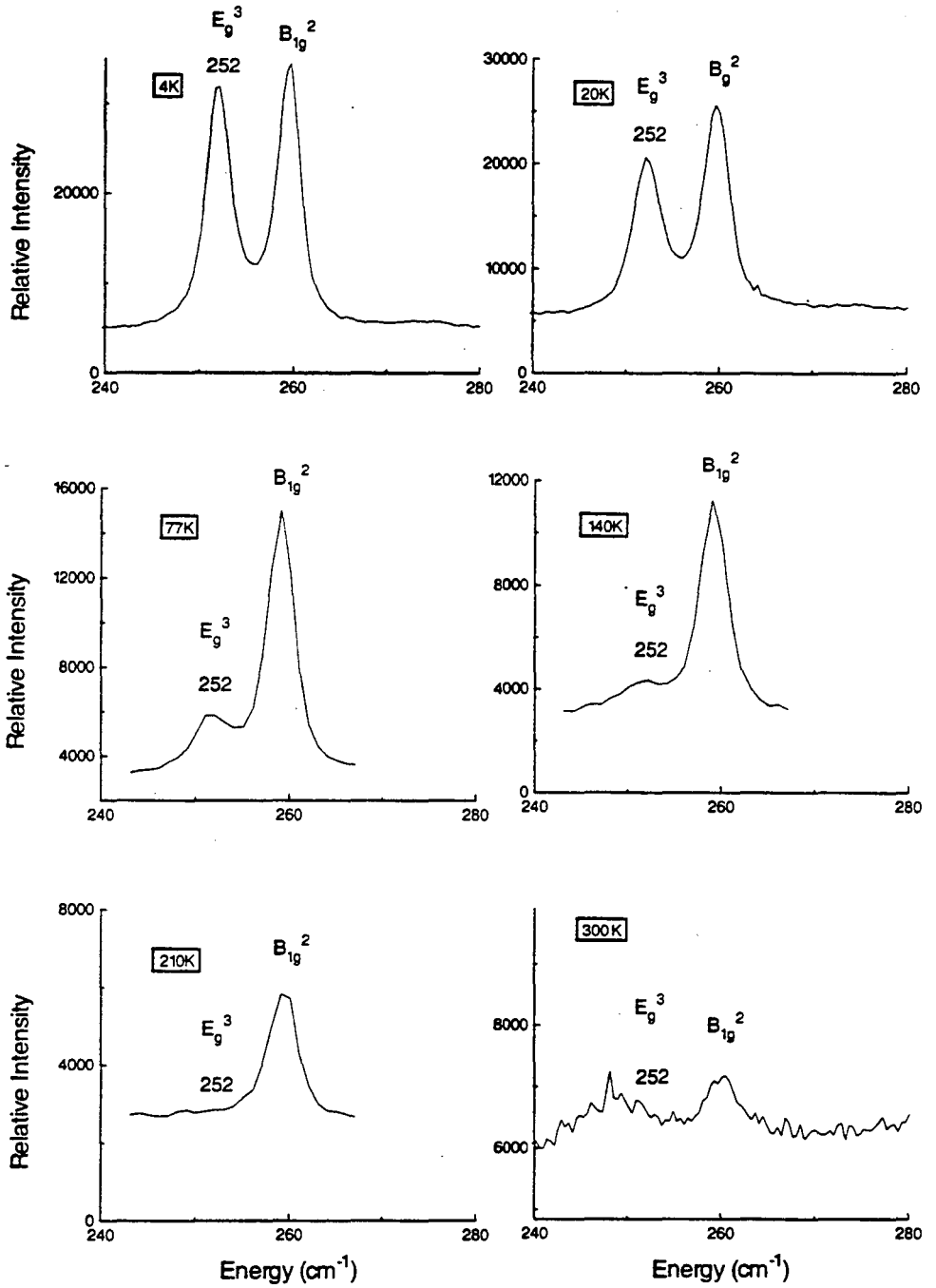

Fig. 4-21: Unpolarized ERS spectra of the 252 cm^{-1} transition of Er^{3+} in $ErVO_4$ as a function of temperature.

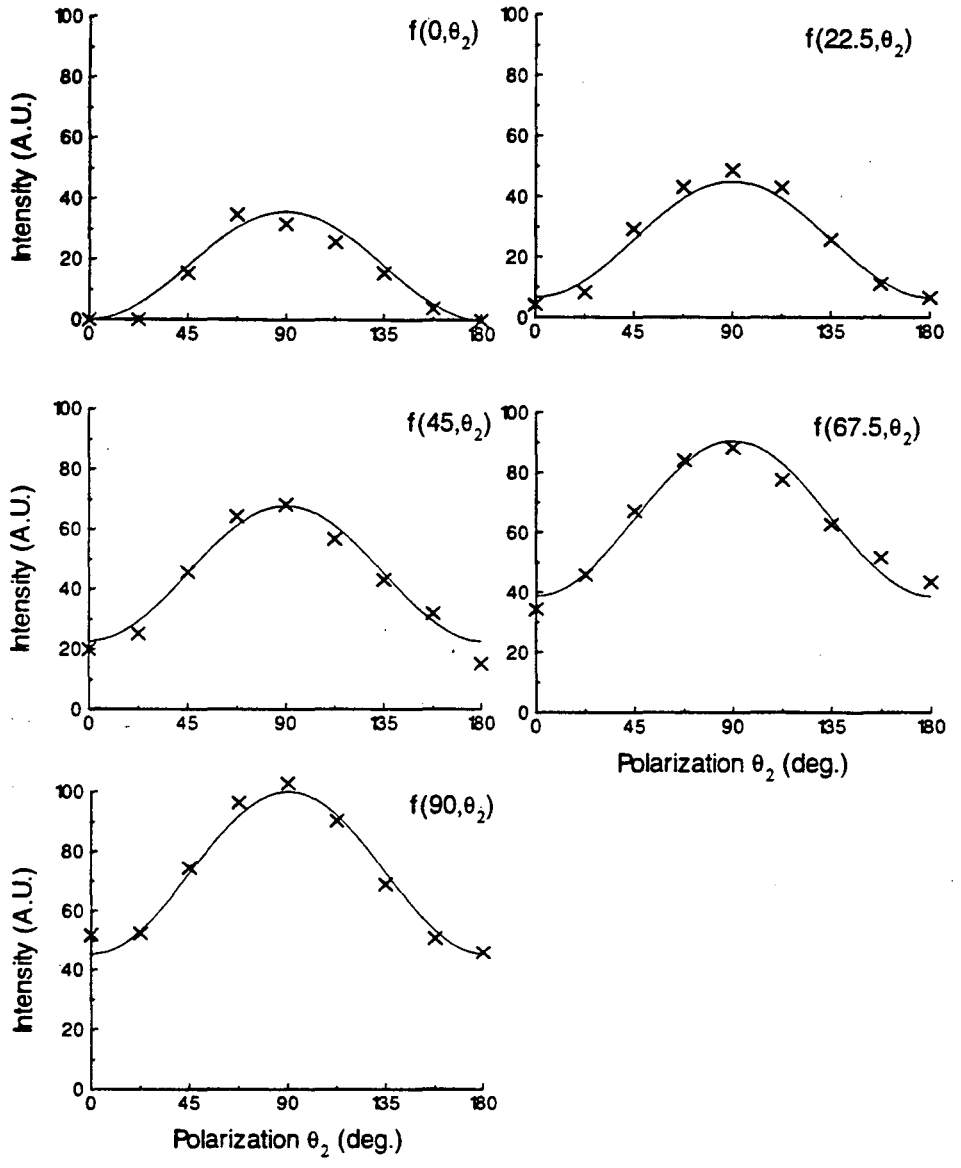

Fig. 4-22: Polarization dependence spectra of the 43 cm^{-1} transition of Er^{3+} in $ErVO_4$ at 4.2 K. Solid lines represent the fitted curves using Table 4.10; crosses represent the experimental data.

4.4 Raman Spectroscopy of $TmVO_4$

4.4.1 Tm^{3+}- Selection Rules

Tm^{3+} has twelve 4f electrons and two 4f holes, which is equivalent to Pr^{3+} which has two 4f electrons. The point group symmetry of Tm^{3+} in $TmVO_4$ is D_{2d}, and the crystal field states of Tm^{3+} are labeled by the irreducible representations Γ_1, Γ_2, Γ_3, Γ_4, and Γ_5 of D_{2d}. The absorption and fluorescence spectra and crystal field fit of Tm^{3+} in dilluted YVO_4 (the ratio of Tm^{3+} to Y^{3+} is between 1:100 to 1:5) have been reported first by Knoll [13]. An improved crystal field fit was later obtained by Wortman, Leavitt, and Morrison [14].

The ground multiplet of Tm^{3+} is $^3H_6$. The decomposition of the ground multiplet into irreducible representations is given by $3\Gamma_5+\Gamma_4+ 4\Gamma_3+2\Gamma_1$. The ground crystal field state has the symmetry Γ_5. The selection rules and Raman activity for the Raman transitions originating in the ground state of Tm^{3+} are described in table 4.25.

Table 4.25: Selection rules and Raman activity of ERS transitions originating in the ground state of Tm^{3+} in $TmVO_4$.

Transition	Scattering tensor symmetry	Raman activity α_q^t
$\Gamma_5 \leftrightarrow \Gamma_1$	Γ_5	α_1^2, α_1^1 $(\alpha_{-1}^2, \alpha_{-1}^1)$
$\Gamma_5 \leftrightarrow \Gamma_2$	Γ_5	α_1^2, α_1^1 $(\alpha_{-1}^2, \alpha_{-1}^1)$
$\Gamma_5 \leftrightarrow \Gamma_3$	Γ_5	α_1^2, α_1^1 $(\alpha_{-1}^2, \alpha_{-1}^1)$
$\Gamma_5 \leftrightarrow \Gamma_4$	Γ_5	α_1^2, α_1^1 $(\alpha_{-1}^2, \alpha_{-1}^1)$
$\Gamma_5 \leftrightarrow \Gamma_5$	$\Gamma_1+ \Gamma_2+ \Gamma_3+ \Gamma_4$	$\alpha_0^1, \alpha_0^2, \alpha_2^2, \alpha_{-2}^2$

4.4.2 Tm^{3+}- Polarization Dependence Functions

The general polarization behavior for ERS transitions of Tm^{3+} in $TmVO_4$ are given in table 4.26. Table 4.27 shows the wavefunctions for the ground multiplet of Tm^{3+} in $TmVO_4$ obtained from a crystal-field fit with the crystal field parameters given by Wortman et al. [14]. The nonzero α_q^t and the polarization dependence functions for the ERS transitions in the ground multiplet are shown in table 4.28. The relative polarized intensities of ERS transitions in the ground multiplet of $TmVO_4$ are given in table 4.29.

Table 4.26: Polarization dependence functions for ERS transitions originating in the ground state of Tm^{3+} in $TmVO_4$.

Transition	Polarization dependence curves
$\Gamma_5 \leftrightarrow \Gamma_5$	$(\alpha_0^1)^2 \sin^2\theta_1 \sin^2\theta_2 + (4/3)(\alpha_0^2)^2 \cos^2\theta_1 \cos^2\theta_2$ $+(1/2)(\alpha_2^2 + \alpha_{-2}^2)^2 \sin^2\theta_1 \sin^2\theta_2$
$\Gamma_5 \leftrightarrow \Gamma_1$ $\Gamma_5 \leftrightarrow \Gamma_2$ $\Gamma_5 \leftrightarrow \Gamma_3$ $\Gamma_5 \leftrightarrow \Gamma_4$	$(1/4)[(\alpha_1^2)^2 + (\alpha_1^1)^2][\sin^2(\theta_2-\theta_1) + \sin^2(\theta_2+\theta_1)]$ $+ \alpha_1^2\alpha_1^1 \sin(\theta_2-\theta_1)\sin(\theta_2+\theta_1)$, or $(1/4)[(\alpha_{-1}^2)^2 + (\alpha_{-1}^1)^2][\sin^2(\theta_2-\theta_1) + \sin^2(\theta_2+\theta_1)]$ $- \alpha_{-1}^2\alpha_{-1}^1 \sin(\theta_2-\theta_1)\sin(\theta_2+\theta_1)$

Table 4.27: Wavefunctions for the ground multiplet of Tm^{3+} in $TmVO_4$.

Calculated Energy (cm^{-1})(*) and Symmetry	Wavefunction $\sum_{J,J_z} a(J,J_z)\ {}^{2S+1}L_J(J_z)$
0 (Γ_5)	-.888 $^3H_6$ (5) + .408 $^3H_6$ (1) - .19 $^3H_6$ (-3)
30 (Γ_1)	-.643 $^3H_6$ (0) + .537 $^3H_6$ (4) +.537 $^3H_6$ (-4)
115 (Γ_3)	.617 $^3H_6$ (2) - .617 $^3H_6$ (-2) - .3385 $^3H_6$ (6) + .3385 $^3H_6$ (-6)
146 (Γ_5)	.6716 $^3H_6$ (-3) -.603 $^3H_6$ (1) - .42 $^3H_6$ (5)
150 (Γ_1)	.704 $^3H_6$ (-4) - .704 $^3H_6$ (4)
186 (Γ_3)	-.683 $^3H_6$ (6) -.683 $^3H_6$ (-6) +.17 $^3H_6$ (-2) +.17 $^3H_6$ (2)
221 (Γ_4)	.617 $^3H_6$ (-6) - .617 $^3H_6$ (6) - .3385 $^3H_6$ (2) + .3385 $^3H_6$ (-2)
306 (Γ_3)	.76 $^3H_6$ (0) + .4546 $^3H_6$ (4) + .4546 $^3H_6$ (-4)
341 (Γ_5)	.71 $^3H_6$ (-3) +.68 $^3H_6$ (1) + .1605 $^3H_6$ (5)
367 (Γ_3)	-.6828 $^3H_6$ (2) - .6828 $^3H_6$ (-2) - .17 $^3H_6$ (6) - .17 $^3H_6$ (-6)

(*) From the crystal field fit.

Table 4.28. Polarization dependencies of ERS transition intensities in the $^3H_6$ ground multiplet of Tm^{3+} in $TmVO_4$.

Transitions (cm^{-1})	Non-zero α_q^t	Polarization Dependencies $\lvert\alpha_{21}\rvert^2$ (*)
0-30	α_1^2=-.0812F_2, α_1^1=-.29F_1	$1.65\times10^{-3}\ F_2^2\ [(\sin^2\theta_3+\sin^2\theta_4)(1+12.67\tau^2)+14.2\tau\sin\theta_3\sin\theta_4]$
0-115	α_1^2=-.0576F_2, α_1^1=.214F_1	$8.3\times10^{-4}F_2^2[(\sin^2\theta_3+\sin^2\theta_4)(1+13.9\tau^2)-14.8\tau\sin\theta_3\sin\theta_4]$
0-146	α_2^2= .107, α_{-2}^2=-.0667F_2 α_0^2=-.088F_2, α_0^1=-.182F_1	$.0103\ F_2^2\ [\cos^2\theta_1\cos^2\theta_2+\sin^2\theta_1\sin^2\theta_2(3.2\tau^2+.078)$
0-150	α_1^2=.1426F_2, α_1^1=.1436F_1	$.005\ F_2^2\ [(\sin^2\theta_3+\sin^2\theta_4)(1+1.1\tau^2)+4\tau\sin\theta_3\sin\theta_4]$
0-186	α_1^2=-.115F_2, α_1^1=.151F_1	$.0033\ F_2^2\ [(\sin^2\theta_3+\sin^2\theta_4)(1+1.7\tau^2)-5.24\tau\sin\theta_3\sin\theta_4]$
0-221	α_1^2=-.091F_2, α_1^1= .041F_1	$.0021\ F_2^2\ [(\sin^2\theta_3+\sin^2\theta_4)(1+.2\tau^2)-1.8\tau\sin\theta_3\sin\theta_4]$
0-306	α_1^2=-.053 F_2, α_1^1=-.023F_1	$.0007\ F_2^2\ [(\sin^2\theta_3+\sin^2\theta_4)(1+.184\tau^2)+1.7\tau\sin\theta_3\sin\theta_4]$
0-341	α_2^2=.0241, α_{-2}^2=-.028 F_2 α_0^2=.05F_2, α_0^1=.003 F_1	$.0025\ F_2^2\ [\cos^2\theta_1\cos^2\theta_2+\sin^2\theta_1\sin^2\theta_2(3.6\tau^2+5.15)\times10^{-3}$
0-367	α_1^2=.015F_2, α_1^1=-.03F_1	$5.9\times10^{-5}F_2^2[(\sin^2\theta_3+\sin^2\theta_4)(1+3.8\tau^2)-7.7\tau\sin\theta_3\sin\theta_4]$

(*) $\theta_3=\theta_2-\theta_1$, $\theta_4=\theta_1+\theta_2$, $\tau=F_1/F_2$.

Table 4.29: Predicted values of relative linestrengths of ERS transitions in the $^3H_6$ ground multiplet of Tm^{3+} in $TmVO_4$.

ERS transitions (cm^{-1})	ZZ polarized	XY polarized	XZ polarized	ZY polarized
30	0	0	$.3(1+3.56\,\tau)^2$	$.3(1-3.56\,\tau)^2$
115	0	0	$.16(1-3.7\,\tau)^2$	$.16(1-3.7\,\tau)^2$
146	2	$2(.078+3.2\,\tau^2)$	0	0
150	0	0	$(1+1.05\,\tau)^2$	$(1-1.05\,\tau)^2$
186	0	0	$.65(1-1.3\,\tau)^2$	$.65(1+1.3\,\tau)^2$
221	0	0	$.41(1-.45\tau)^2$	$.41(1+.45\tau)^2$
306	0	0	$.24(1+.43\tau)^2$	$.24(1-.43\tau)^2$
341	.488	$1.8\times10^{-3}(1.4+\tau^2)$	0	0
367	0	0	0	0

4.4.3 $TmVO_4$ - Experimental Raman Spectra

Table 4.30 displays the observed phonon modes in $TmVO_4$ at room temperature and at 4.2 K. Phonon modes in $TmVO_4$ have been previously studied by Harley et al [15], whose reported phonon energies at 77 K are listed in the second row of table 4.30. Most of our assignments agree with Harley et al, except the phonon modes at 252, 260, and 265 cm^{-1}. We have assigned E_g^3, B_{1g}^2, and B_{2g}^2 to the phonon modes at 252, 260, and 265 cm^{-1}, according to their polarization behavior described in equations (3.2). The phonon intensities at 252 and 260 cm^{-1} were found to be strongest in the XZ (or ZY) and XY scans, respectively, when the beam is parallel with the crystallographic X axis of the crystal. When the crystallographic X axis is rotated at 45 degree with respect to

the incident beam, a phonon mode appears at 265 cm^{-1} with intensities strongest in the XY scans. Harley et al, however, reported a E_g^3 mode at 260 cm^{-1}, a B_{1g}^2 mode at 269 cm^{-1}, and a B_{2g}^1 mode at 262 cm^{-1}. The discrepancies may be the result of the ignorance of a 45 degree transformation of the scattering tensors in the work of Harley et al. Fig 4-23 and 4.24 show the unpolarized phonon and Raman spectra, respectively, of $TmVO_4$, with excitation lines at 514 nm and 488 nm. The phonon spectra were taken at room temperature and the Raman (both phonon and ERS) spectra were taken at 4K. Fig 4-25 shows the low temperature Raman spectra of $TmVO_4$ between 240 and 280 cm^{-1}, with the excitation lines at 497 and 488 nm, and with the crystal's crystallographic XY plane being rotated at 45 degree about the Z axis.

Table 4.30. Frequencies (cm^{-1}) and symmetries of the Raman-active phonons in $TmVO_4$ at 297, 77, and 4.2 K.

Tem.(K)	E_g^1	B_{1g}^1	E_g^2	E_g^3	B_{1g}^2	B_{2g}^1	A_{1g}^1	E_g^4	B_{1g}^3	B_{1g}^4	E_g^5	A_{1g}^2
297*	106	117	157	253	261	265	381	a	490	826	841	897
77 †	102	119	157	260	269	262	385	a	493	823	843	899
4.2 *	100	119	159	253	260	265	386	a	491	823	844	900

a: not observed

(*) This work

(†) Reference [15]

The crystal field splitting for the $^3H_6$ ground multiplet and $^1G_4$ multiplet of Tm^{3+} in $TmVO_4$ are shown in fig 4-26. Four electronic lines were observed at 119, 150, 183, and 881 cm^{-1}, two of which were identified as ERS transitions orginating in the $^3H_6$

ground multiplet of Tm^{3+} in $TmVO_4$. The lines at 119 cm^{-1} and 150 cm^{-1}, which were predicted to be at 115 and 150 cm^{-1}, were assigned to the $\Gamma_5 \leftrightarrow \Gamma_3$ and $\Gamma_5 \leftrightarrow \Gamma_1$ transitions, respectively. The ERS transition at 119 cm^{-1}, with linewidth approximately 2 cm^{-1}, is superposed on a weak B_{1g}^1 phonon line, which resulted in non-zero intensities in XY, XZ, ZY scans. The polarized spectra of this transition at 4K is shown in fig 4-27. The ERS transition at 150 cm^{-1} has a larger linewidth of approximately 5 cm^{-1} and has nonzero intensities in XZ and ZY scans. Its polarized spectra at 4K is shown in fig 4-28. The electronic line at 183 cm^{-1} has strongest intensities in XY scans and zero intensities in ZZ, XZ, and ZY scans. Note that there is no phonon B_{1g} mode at this frequency, and the $\Gamma_5 \leftrightarrow \Gamma_1$ transition predicted by the crystal field fit at 189 cm^{-1} would have zero intensities in XY scans, we conclude this observed ERS transition at 183 cm^{-1} might be due to an unknown impurity other than Tm^{3+}. The same conclusion is applied to the electronic line at 881 cm^{-1}, whose intensities are strongest in XZ and ZY scans. These two electronic lines, however, did not fit to any known ERS transitions of RE^{3+} in rare earth vanadates or phosphates reported to date. We therefore could not confirm the impurity origin of the lines at 183 and 881 cm^{-1}.

Polarization dependence measurements were performed for the E_g^2 phonon line at 155 cm^{-1} and the ERS line at 150 cm^{-1}. The phonon polarization dependence data were used to calibrate the ERS data at 150 cm^{-1}. The respective observed and predicted polarization dependence curves of these Raman lines at 155 and 150 cm^{-1} are shown in figures 4-29 and 4-30. The phonon predicted curves are described in equation 3.3. The $\Gamma_5 \leftrightarrow \Gamma_1$ transition at 150 cm^{-1} has the predicted curves described in equation 4.2, with

$$a\,(150\ \mathrm{cm}^{-1}) = \frac{\alpha_1^2}{\alpha_1^1} = .993\frac{F_2}{F_1} = \frac{.993}{\tau}, \tag{4.7}$$

Due to the slight overlap between the E_g^2 mode at 155 cm^{-1} and the ERS transition at 150 cm^{-1}, the intensity measurements of both of these Raman lines were very difficult. To obtain consistent fitted intensities, we kept the linewidths of the ERS transition fixed at 4.8 cm^{-1} and the phonon transition fixed at 10.0 cm^{-1}, with both being Gaussians fitted. The maximum error in these intensity fits were about 30 percent. The values of *a* extracted from the polarization dependence fit were 13.9 and .072, and the corresponding fitted values of τ were .0715 and 14.18.

Observed relative ERS intensities in the ground multiplets of $TmVO_4$ can be compared with prediction. Table 4.31 compares the observed and predicted intensities of ERS transitions in the ground multiplet of $TmVO_4$ relative to the ZY-polarized intensity of the transition at 150 cm^{-1} for the case τ = .072. Only approximately three fourths of the transition intensities were accurately accounted for.

Finally we determine the third-order spin-orbit contribution for the transitions in the ground $^3H_6$ multiplet of Tm^{3+} in $TmVO_4$. The relative magnitude of third-order spin-orbit to second-order contributions for the transition at 150 cm^{-1} given in table 4.32 is less 0.1. As expected, inclusion of the third order spin-orbit interaction in the total ERS intensity only results in marginal agreement with the intensity obtained from the fit. The magnitude of (α^t) in $TmVO_4$ calculated from the third-order spin-orbit contribution relative to that calculated from the second-order theory are given by

$$\frac{<{}^3H_6 \| (\alpha^2)^{3rd} \| {}^3H_6>}{<{}^3H_6 \| (\alpha^2)^{2nd} \| {}^3H_6>} = 0.086$$

and

$$\frac{<^3H_6 || (\alpha^1)^{3rd} || ^3H_6>}{<^3H_6 || (\alpha^1)^{2nd} || ^3H_6>} = 0.03$$

for all transitions in the $^3H_6$ ground multiplet of Tm^{+3} in $TmVO_4$.

Table 4.31: Comparison between predicted and observed relative linestrengths of ERS transitions in the $^3H_6$ ground multiplet of Tm^{3+} in $TmVO_4$ for the case $\tau = .072$.

ERS transitions (cm^{-1})		ZZ -polarized		XY-polarized		XZ-polarized		ZY-polarized	
Thry.*	Exp.	Cal.	Obs.	Cal.	Obs.	Cal.	Obs.	Cal.	Obs.
30	-	0	-	0	-		-		-
115	119	0	-	0	u	.09	.08	.25	.3
146	-	2	-	.18	-	0	-	0	-
150	150	0	.25	0	-	1.15	1.1	.85	.85
186	-	0	-	0	-	.5	-	.78	-
221	-	0	-	0	-	.38	-	.44	-
306	-	0	-	0	-	.25	-	.23	-
341	-	.5	-	.002	-	.008	-	.011	-
367	-	0	-	0	-	0	-	0	-

(-) Not observed

(u) Unknown

(*) From the crystal field fit

Table 4.32: Comparison of the relative magnitudes of (α_q^t) obtained from calculation using the second-order theory, third-order spin-orbit, and from the fit for the transition at 150 cm^{-1} in $TmVO_4$.

Transition (150 cm^{-1})	Second	Total	Fitted
$\left(\frac{\alpha_1^2}{\alpha_1^1}\right)$	4	3.8	14

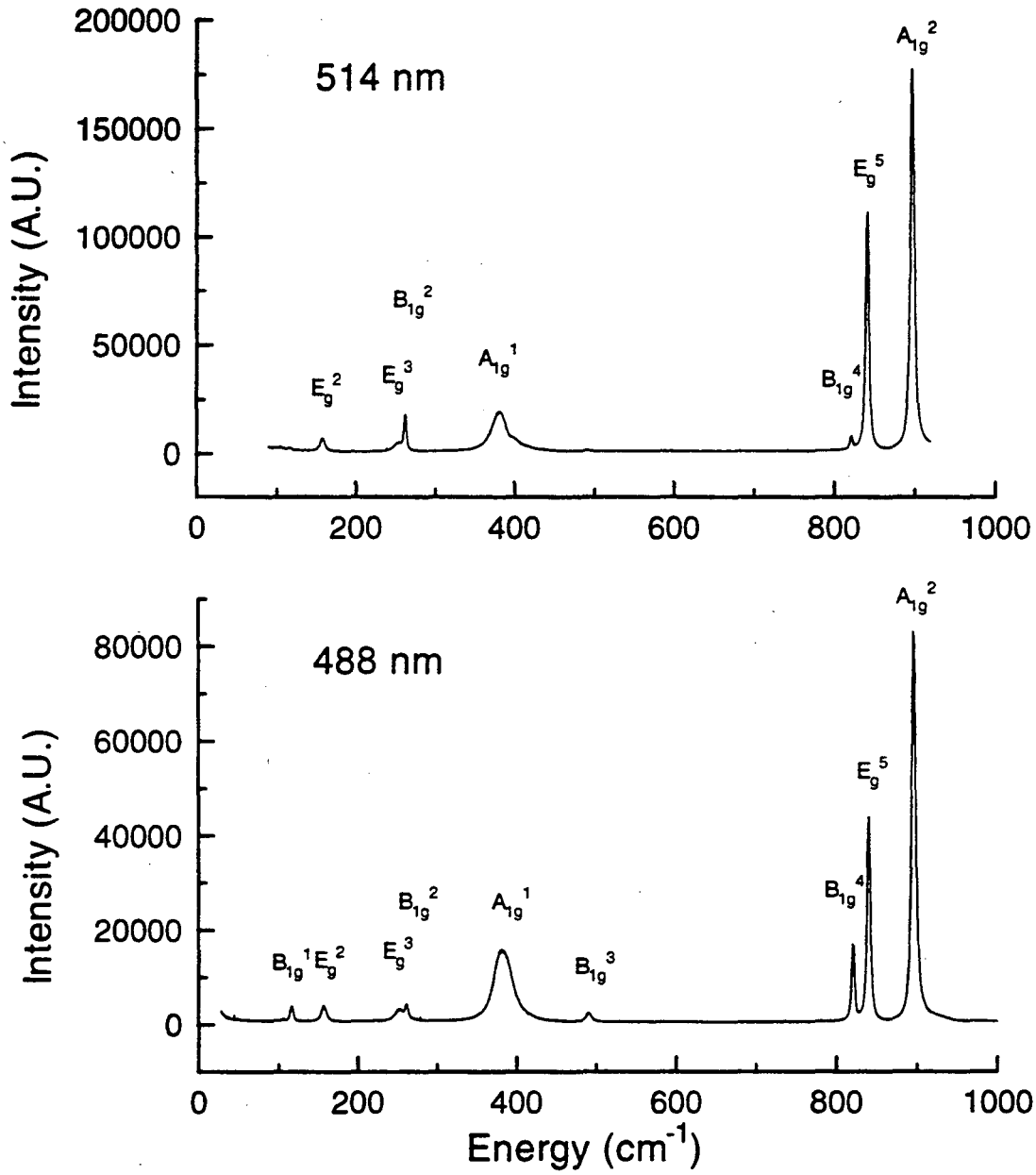

Fig. 4-23: Unpolarized phonon spectra of $TmVO_4$ at 293 K, with the laser excitation at 514 nm and 488 nm.

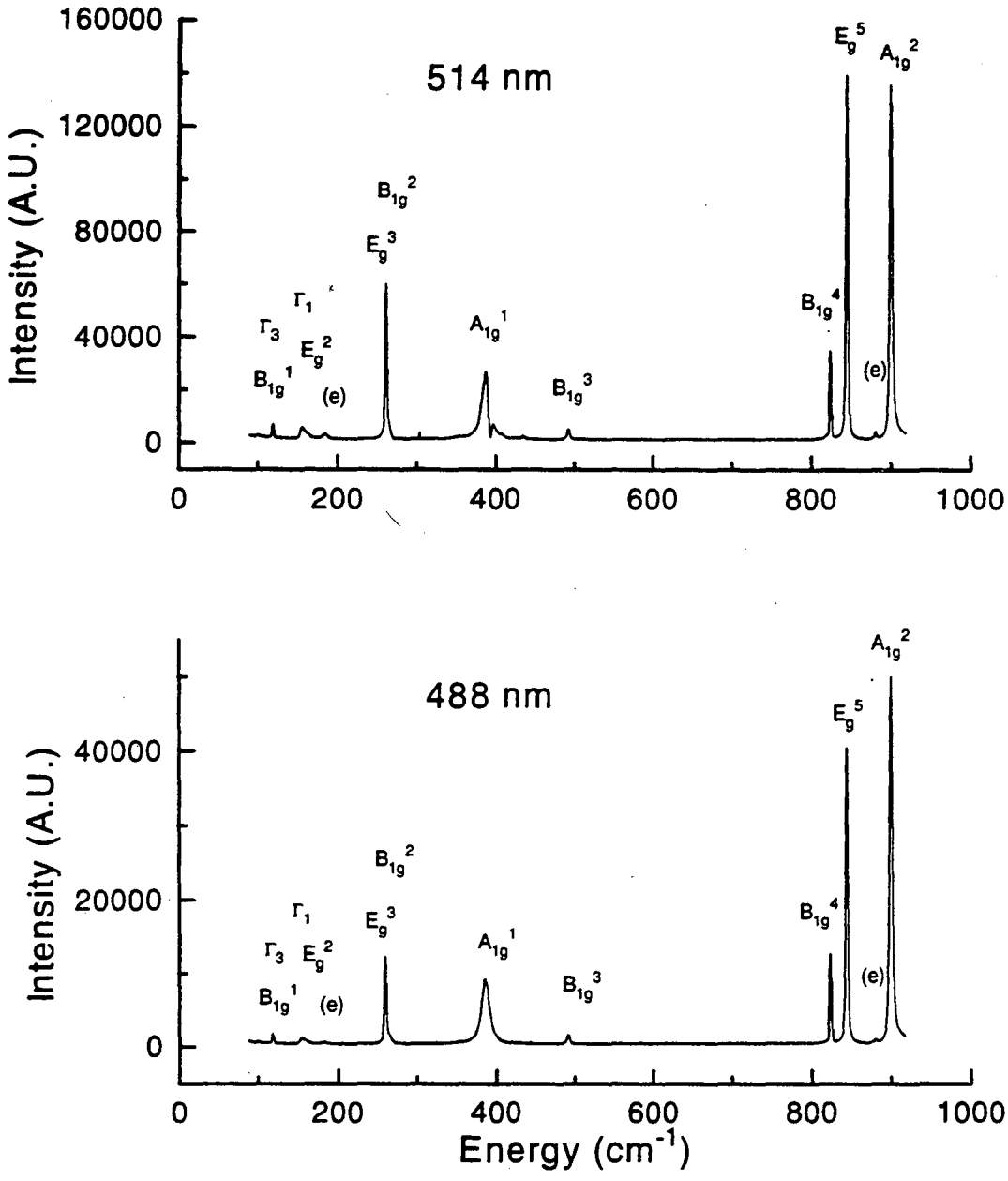

Fig. 4-24: Unpolarized Raman spectra of $TmVO_4$ at 4 K, with the laser excitation at 514 nm and 488 nm. The electronic lines are characterized by the Greek symbols, except the lines labeled by (e) at 183 and 881 cm^{-1}, whose origins and symmetries are unknown.

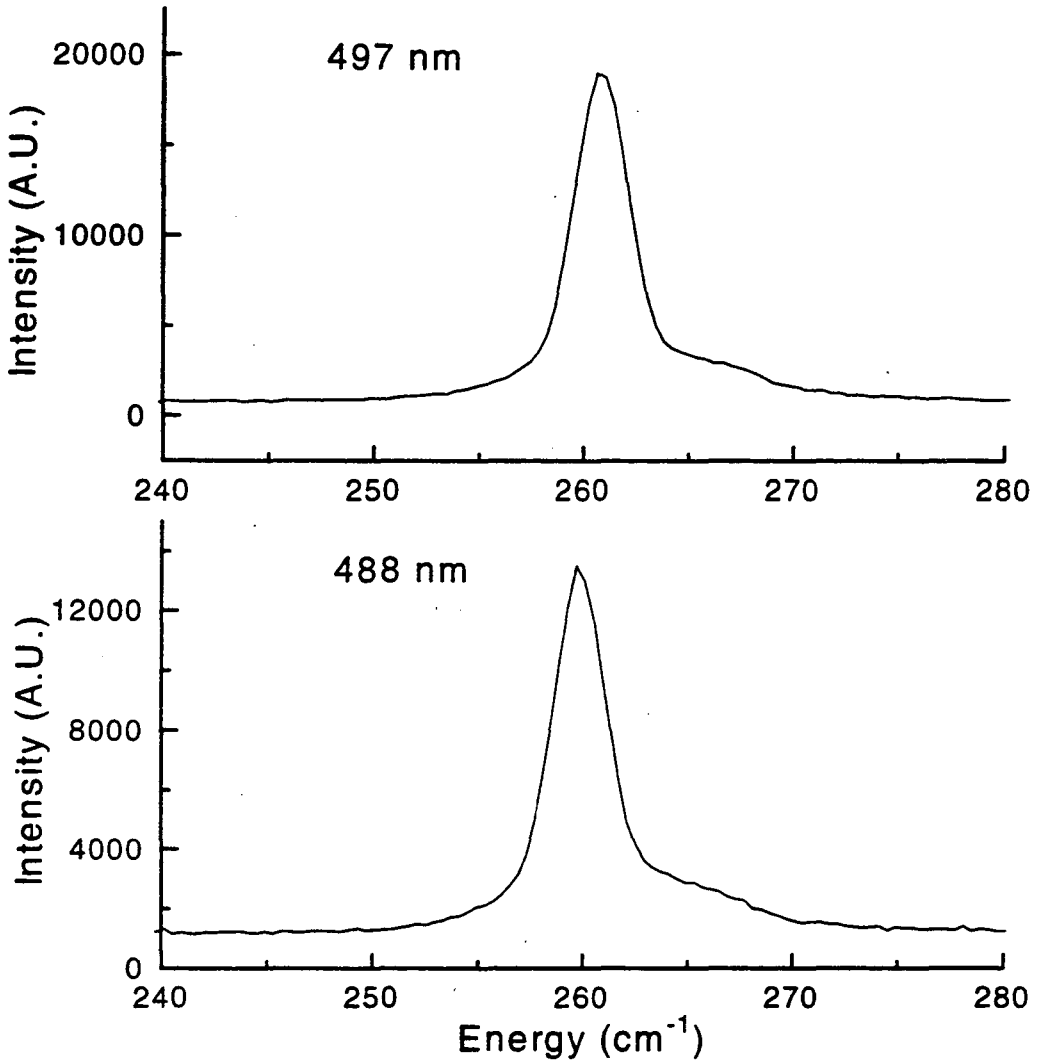

Fig. 4-25: Unpolarized Raman spectra of $TmVO_4$ at 4.2 K, with laser excitation at 497 nm and 488 nm. The crystal XY plane was rotated at 45 degree about the Z-axis.

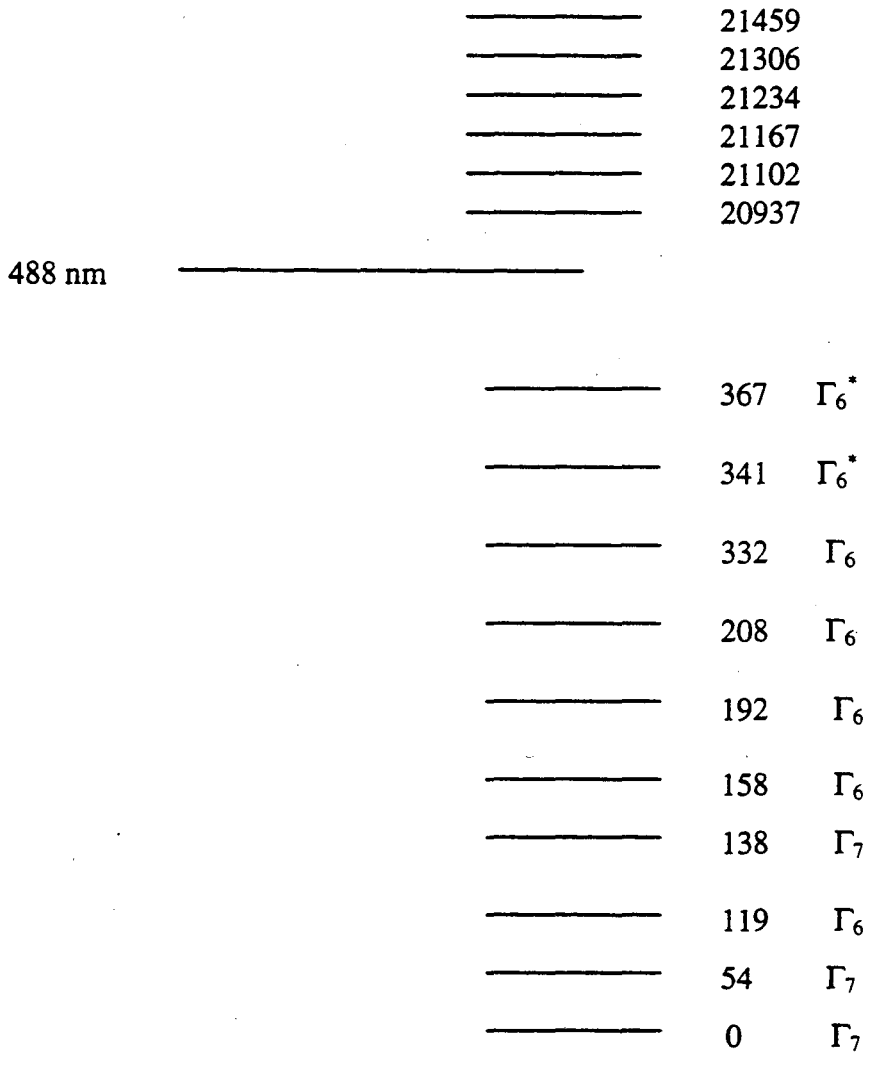

Fig. 4-26: Crystal field levels of the $^3H_6$ and $^1G_4$ multiplets of Tm^{3+} in $TmVO_4$ [13].

(*) crystal field fit

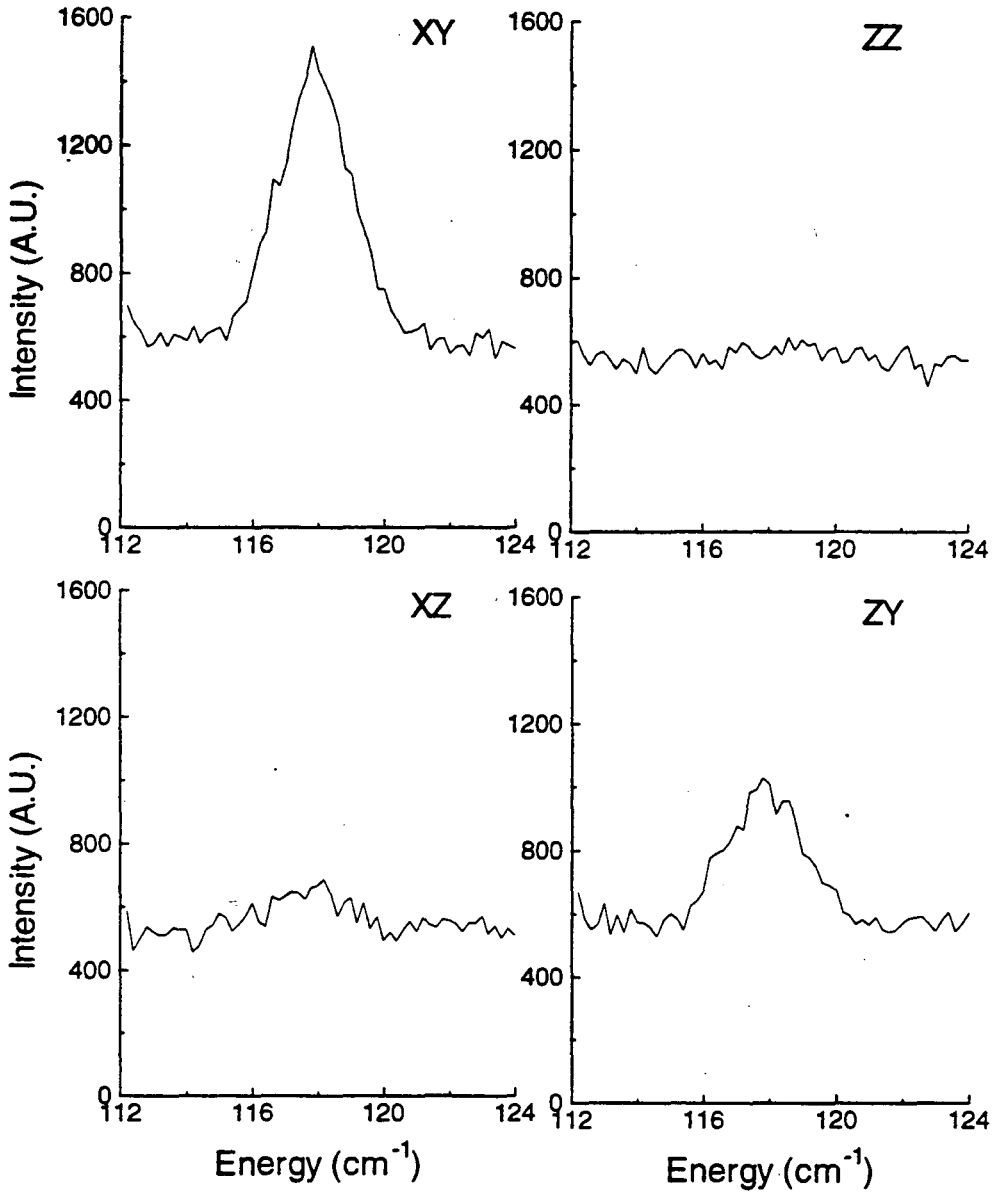

Fig. 4-27: Polarized ERS spectra of the 115 cm^{-1} transition of Tm^{3+} in $TmVO_4$ at 4.2 K, with excitation at 488 nm.

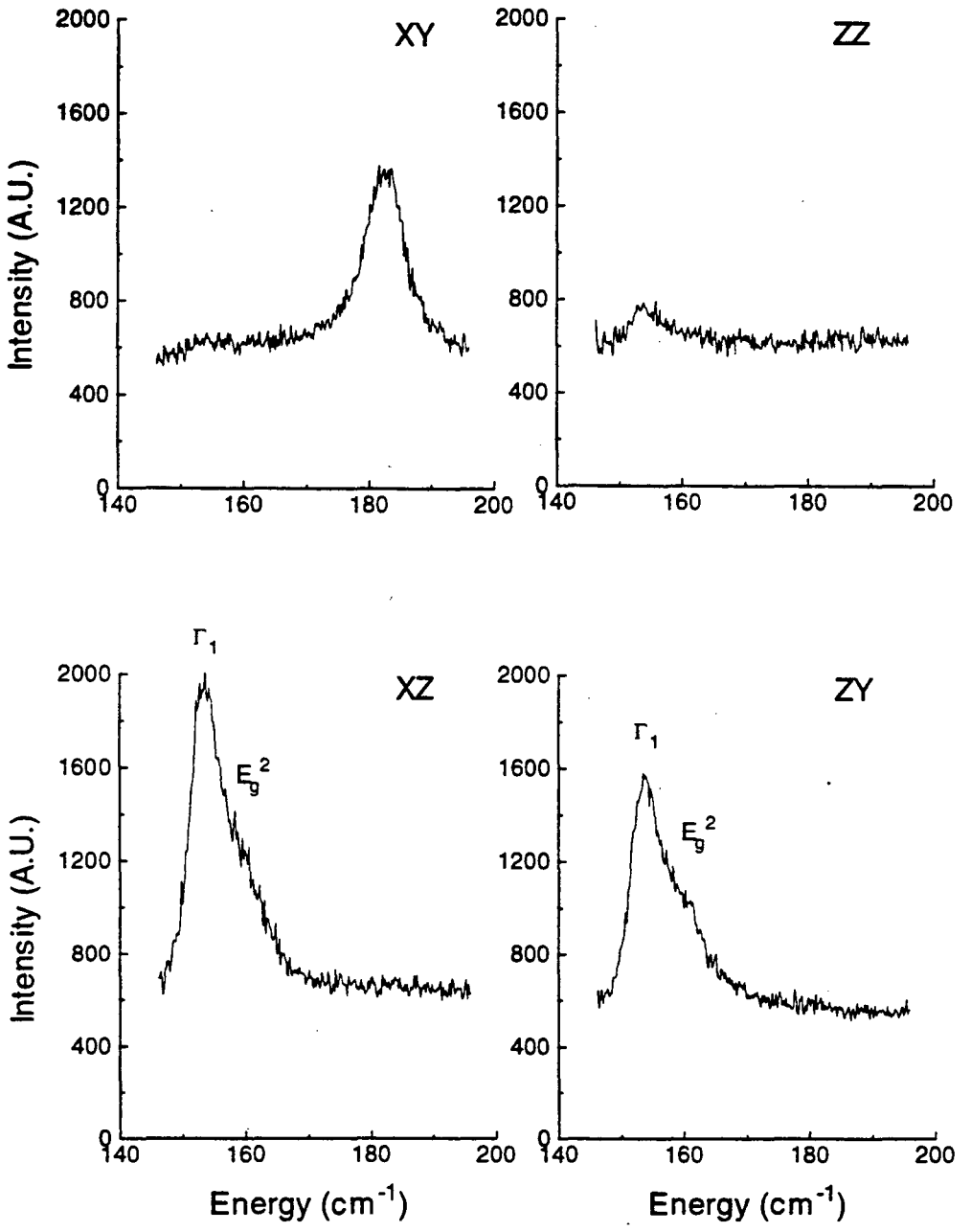

Fig. 4-28: Polarized Raman spectra of the 150 cm^{-1} transition of Tm^{3+} in $TmVO_4$ at 4.2 K, with excitation at 488 nm.

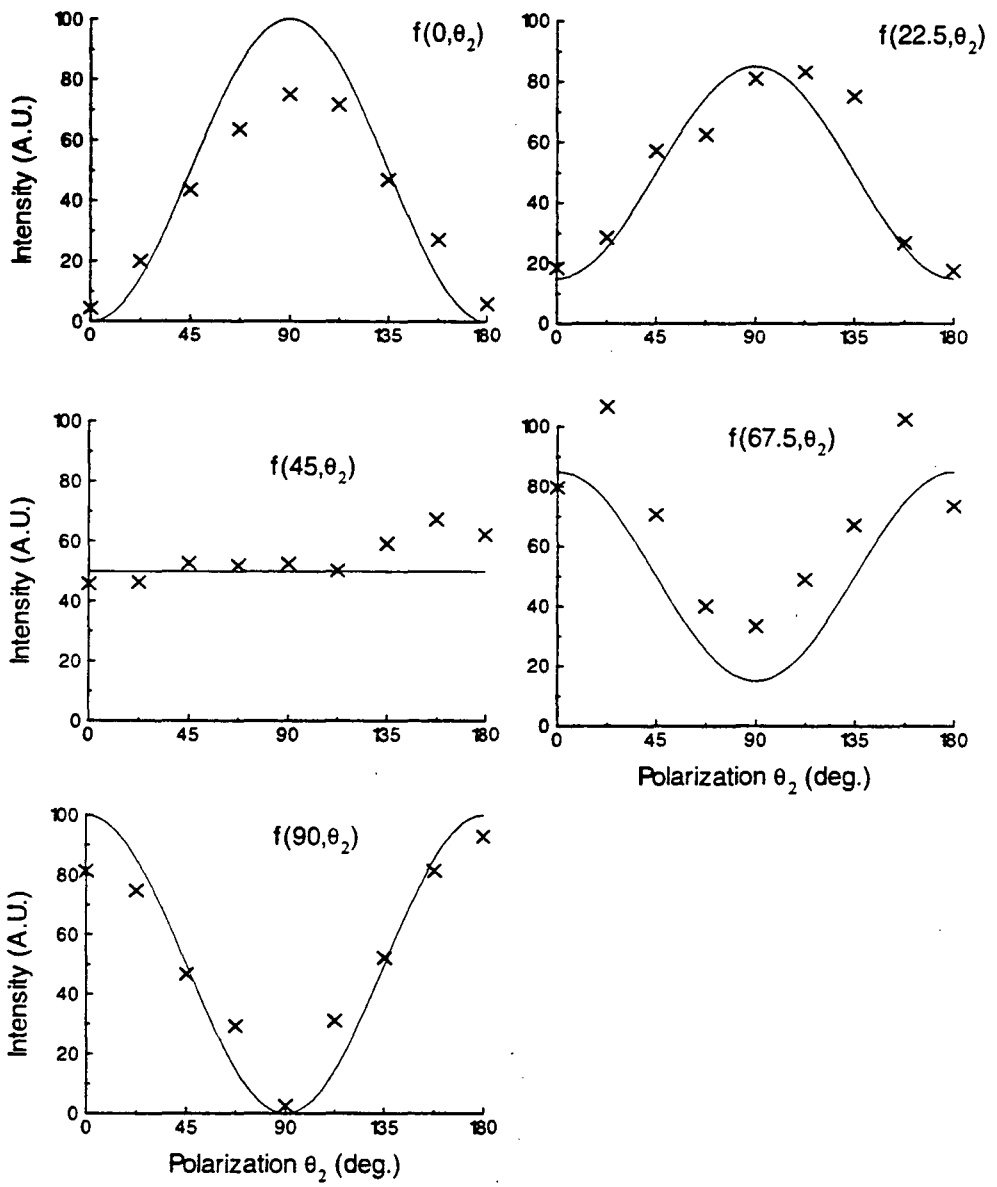

Fig. 4-29: Polarization dependent phonon spectra of the E_g^2 at 155 cm^{-1} of $TmVO_4$ at 4.2 K. Solid lines represent the fitted curves using equations 3.3; crosses represent the experimental data.

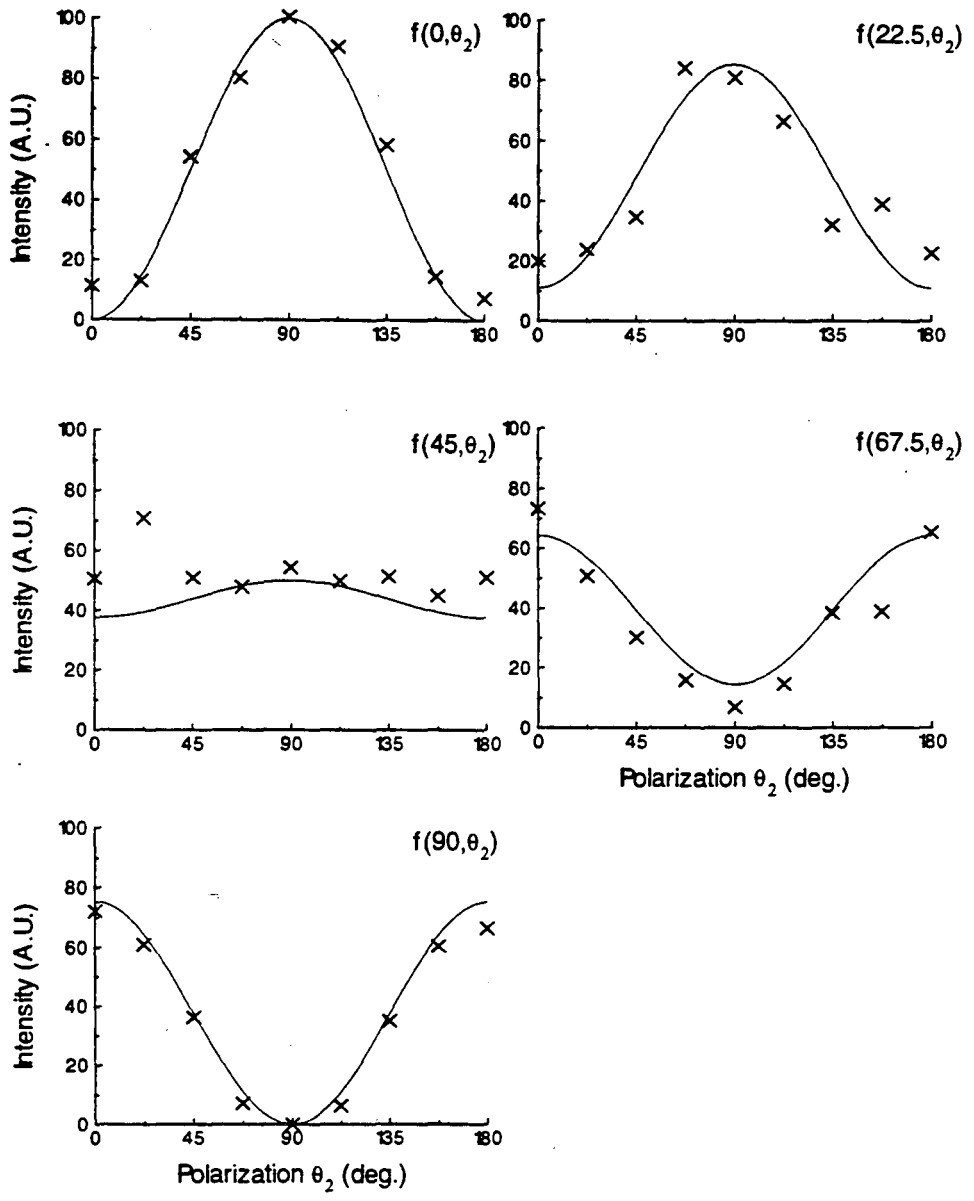

Fig. 4-30: Polarization dependent ERS spectra of the 150 cm^{-1} transition of Tm^{3+} in $TmVO_4$ at 4.2 K. Solid lines represent the fitted curves using equations 4.2; crosses represent the experimental data.

4.5 Summary

We have reported polarization dependent ERS measurements for the ground multiplets of Pr^{3+}, Nd^{3+}, Er^{3+}, and Tm^{3+} in vanadate crystals. The agreement between relative intensities obtained from prediction by the second-order theory and from observation was excellent in the case of $PrVO_4$ and $NdVO_4$ and only marginal in the case of $ErVO_4$ and $TmVO_4$. The third-order spin-orbit contributions were found to be approximately a magnitude order less than the second-order contributions in all cases and therefore did not affect the general results obtained from the second-order calculations. The best fitted value of τ for $PrVO_4$, $NdVO_4$, $ErVO_4$, and $TmVO_4$ were 1.0, 0.48, 1.0, and 0.07, respectively. These values of τ were in contrast with the considerably small fitted values for τ in Er^{3+}: YPO_4 and Tm^{3+}: YPO_4 reported by Becker et al [6,7]. The near unity values of τ in the case of Pr^{3+}, Nd^{3+}, and Er^{3+} in vanadate crystals have confirmed the validity of the Axe's theory taking into account only the d-configuration in accounting for the ERS intensities.

In all four cases the use of the polarization dependence technique has proved to be important in determining the symmetries and origins of the ERS spectral lines. The polarization dependence theory developed in chapter two has been extremely accurate in predicting the intensities of one of the ERS transitions in $PrVO_4$, whose linestrengh is sufficiently strong for accurate intensity measurements. The factor of two difference between the observed value of τ and the value of τ predicted by theory was probably due to the lack of accurate wavefunctions of the ground multiplet of $PrVO_4$, as we observed

that the only crystal field fits reported to date came from only a few lines of the ground multiplet and that there has been no reported spectroscopic work on higher multiplets of $PrVO_4$. As for $NdVO_4$, the highly accurate and complete crystal field fit reported by Tanner and Edelstein [10] has probably been responsible for excellent agreement between theory and experiment on the value of τ. Poorer agreements in the case of $ErVO_4$ and $TmVO_4$ were partially due to difficulties in intensity measurements, which arised from either interference of neighboring Raman lines or the Rayleigh excitation line.

We conclude that Axe's theory was sufficient to account for a majority of ERS intensities in our experimental studies on rare-earth doped vanadate crystals. Further work should be done on host materials doped with rare earth ions of different site symmetries than D_{2d}. Polarization dependence should always be done whenever possible, as the technique has shown to be superior than the currently used polarization technique in ERS experiments, in which only ZZ, XZ, ZY, and XY scans were performed. If the wavefunctions of the transitions considered are known, relative intensities can be obtained using the procedures mentioned in chapter two and three. When only the symmetries of the transitions were known, general polarization dependence functions can be obtained from table 2.1. The experimental procedure described in chapter three should be used as a guideline in polarized Raman scattering experiments. In our Raman set up we have tried to eliminate all the interfering factors that might possibly alter the intensities of the incident and scattered light. For example, by putting the polarization scrambler in front of the Dove prism to depolarize the

scattered light, we have avoided the polarization dependent response of both the Dove prism and the spectrometer. Previous polarized Raman scattering experiments reported have overlooked the device-polarization dependent effects and might have been the source of disagreement between theory and observation.

References

[1] B. Bleaney et al., J. Phys. C: Solid State Phys. **11**, 3059 (1978).

[2] R. R. Andronenko, S. I. Andronenko, A. N. Bazhan, Phys. Sol. State **36**, 1302 (1994).

[3] N. Edelstein, private communication.

[4] We have used Koningstein and Mortensen's notation here, in which the letters in subscript represent the polarizations of the and incident light.

[5] P. C. Becker et al., Phys. Rev. B **31**, 8102 (1985).

[6] P. C. Becker, Ph.D. thesis, University of California, Berkeley, 1986.

[7] P. C. Becker, N. Edelstein, B. R. Judd, R. C. Leavitt, and G. M. S. Lister, J. Phys. C **18**, L1063 (1985).

[8] M. C. Downer, A. Bivas, and N. Bloembergen, Opt. Commun. **41**, 335 (1982).

[9] M. C. Downer and A. Bivas, Phys. Rev. B **28**, 3677 (1983).

[10] P. Tanner and N. Edelstein, Chem. Phys. Lett. **152**, 140 (1988).

[11] D. Kuse, Z. Phys. **203**, 49 (1967).

[12] A. A. Kaminskii, in *Laser Crystals* (Springer-Verlag, 1981), p. 130.

[13] K. D. Knoll, Phys. Stat. Sol. B**45**, 553 (1971).

[14] D. E. Wortman, R. Leavitt, and C. A. Morrison, J. Phys. Chem. Solids **35**, 591 (1974).

[15] R.T. Harley, W. Hayes, and S.R. Smith, J. Phys. C: Solid State Phys. **5**, 1501 (1972).

Chapter 5

Polarization Dependence of Two-Photon Absorption Transition Intensities in Eu^{3+}:$LuPO_4$ and Cm^{3+}:$LuPO_4$.

The main motivation for studying the polarization dependent behavior of TPA transitions in Eu^{3+}:$LuPO_4$ and Cm^{3+}:$LuPO_4$ is to investigate the role of α_0^0 contributing to the TPA intensities. TPA was observed to the $^5D_0$ and $^5D_2$ levels of Eu^{3+} and to the $^6D_{7/2}$ levels at 16800 cm^{-1}, $^6P_{5/2}$ levels, and the $^6D_{7/2}$ levels at 27900 cm^{-1} of Cm^{3+}. The second-order contributions to the TPA intensities were found to be relatively small for these levels in Eu^{3+} and Cm^{3+}. As a result, the corresponding non-zero α_0^0 terms calculated in the third-order are expected to give at least a comparable if not dominant contribution compared to the second order terms. Polarization dependent behavior of the transitions for which α_0^0 is nonzero is also expected to drastically change by inclusion of the third-order interaction.

5.1 Introduction

Traditionally, polarization dependent TPA spectra have been analyzed using Bader and Gold's formulae derived from group theoretical methods in the frame work of the second order perturbation theory [1]. The main disadvantage of Bader and Gold's polarization dependence functions, however, is the presence of a number of phenomenological parameters, which often weakens the predictive capability of the

theory. Other polarization dependence formalisms have been developed by Makhanek et al [2,3] and by Kibler, Gacon, and coworkers [4-7]. Makhanek et al's theory has been developed within the second-order theory framework and could not be extended to include higher order interactions. Kibler et al theory, apparently due to its complexity, has been applied to only a few rare earth systems. Applying Judd-Ofelt-Axe's approximation [8-10], the Kibler-Gacon's second order results can be expressed in terms of only one parameter, which can be further estimated when proper approximations are made. Their third order analysis [6], however, is based exclusively on a few phenomenological constants, similar to those given in the Bader and Gold theory.

Recently Gacon et al reported experimental results in which Bader and Gold's theory has failed to predict the polarization dependence behavior of the reported TPA transitions. Gacon et al found that several of the TPA transitions in $Eu(OH)_3$ and Eu^{3+}:$LuPO_4$ have a constant background which is non zero for all polarization angles θ between the three-fold c axis and the beam polarization direction [11,12]. By fitting the experimental curves with the polarization dependence functions coming from a phenomenological model with a constant being added, agreement with theory was restored. The origin of the constant, which appeared to be an arbitrary complex number in the expression of the scattering amplitude, has never been explained in their papers.

Prompted by Gacon et al's observation we have investigated several TPA transitions in Eu^{3+}:$LuPO_4$ and Cm^{3+}:$LuPO_4$. The observed data were interestingly similar to what have been observed by Gacon et al. For those transitions for which

second-order contributions are significantly small, a constant background was observed. In addition the Cm^{3+} data have shown curious isotropic polarization dependent behavior in nearly all of the observed transitions. Both the origin of the constant background observed in Eu^{3+} and Cm^{3+} and the lack of anisotropy observed in Cm^{3+} will be explained in this chapter as the theory of the two-photon scattering amplitude developed in the time-dependent perturbation framework is reexamined. The few transitions which display neither the nonzero background nor isotropy have their polarization dependent behavior and relative intensities which can be explained by the second-order theory of Axe. It is interesting to note that the lowest among the TPA transitions to the $^5D_2$ multiplet of Eu^{3+}:$LuPO_4$ was predicted to have zero intensity when the crystal plane is oriented at 0° or 90° with respect to the incident excitation beam but have nonzero intensity when the crystal is rotated at other angles with respect to the beam direction about the z-axis. This was observed exactly as predicted. When the crystal was rotated at 45° with respect to the incident beam, a strong line appeared with energy, polarization behavior and relative transition intensities with other transitions agreeing with prediction. The transition disappeared when the crystal plane was perpendicular with the incident beam.

5.2 TPA Spectroscopy of Eu^{3+} in $LuPO_4$

5.2.1 Eu^{3+}- Selection Rules

The open shell configuration of Eu^{3+} is $4f^6$. The host lattice $LuPO_4$ has the tetragonal zircon-type structure with space group D_{4h}^{19}. The site symmetry of Eu^{3+} in

$LuPO_4$ is D_{2d}. The electronic states of Eu^{3+} are labeled by the irreducible representations Γ_1, Γ_2, Γ_3, Γ_4, and Γ_5 of D_{2d}.

The ground state of Eu^{3+} is $^7F_0$, which has the symmetry Γ_1. The selection rules and Raman activity for the TPA transitions originating in the ground state are described in table 5.1. Emission and absorption spectra of Eu^{3+} in YPO_4 have been reported by Brecher et al. [13]. The crystal field wavefunctions for Eu^{3+} in $LuPO_4$ are provided by Piehler and Kim [14].

Table 5.1: Selection rules and Raman activity of TPA transitions originating from the ground state of Eu^{3+} in $LuPO_4$

Transition	TPA scattering tensor symmetry	Raman activity α_q^t
$\Gamma_1 \leftrightarrow \Gamma_1$	Γ_1	α_0^0, α_0^2
$\Gamma_1 \leftrightarrow \Gamma_2$	Γ_2	none
$\Gamma_1 \leftrightarrow \Gamma_3$	Γ_3	$\alpha_2^2, \alpha_{-2}^2$
$\Gamma_1 \leftrightarrow \Gamma_4$	Γ_4	$\alpha_2^2, \alpha_{-2}^2$
$\Gamma_1 \leftrightarrow \Gamma_{5x}$ $\Gamma_1 \leftrightarrow \Gamma_{5y}$	Γ_{5x} Γ_{5y}	α_1^2 α_{-1}^2

5.2.2 Polarization Dependence Functions

The polarization dependence functions corresponding to the TPA $^7F_0 \rightarrow {}^5D_J$ transitions are listed in table 5.2.

The wavefunctions for the states of the $^7F_0$ and ^5D_J multiplets of Eu^{3+} in $LuPO_4$ are listed in table 5.3. These wavefunctions were obtained from a crystal field fit using the crystal field parameters provided by Piehler et al [14]. The nonzero values of α_q^t

calculated in the second-order and the corresponding polarization dependence functions for the $^7F_0 \rightarrow {}^5D_J$ transitions are listed in table 5.4. Taking into account only the d-configuration and using E_d=100,000 cm^{-1}, ζ_d=1330 cm^{-1} , the second- and spin-orbit third-order contributions for the $^7F_0 \rightarrow {}^5D_J$ transitions are shown in table 5.5. The predicted values of TPA transition intensities are provided in tables 5.6 and 5.7 for the case $\theta = 0°, 45°, 90°$ when $\varphi = 45°$ and $\varphi \neq 45°$, respectively.

Table 5.2: Polarization dependence curves for the TPA $^7F_0 \rightarrow {}^5D_J$ transitions of Eu^{3+} in $LuPO_4$.

Transition	Polarization dependence functions
$\Gamma_1 \leftrightarrow \Gamma_1$	$[-\frac{1}{\sqrt{3}}\alpha_0^0 + (\frac{3\cos^2\theta - 1}{\sqrt{6}})\alpha_0^2]^2$
$\Gamma_1 \leftrightarrow \Gamma_2$	0
$\Gamma_1 \leftrightarrow \Gamma_3$	$(1/4)(\alpha_2^2 + \alpha_{-2}^2)^2 \sin^4\theta \cos^2 2\varphi$
$\Gamma_1 \leftrightarrow \Gamma_4$	$(1/4)(\alpha_2^2 - \alpha_{-2}^2)^2 \sin^4\theta \sin^2 2\varphi$
$\Gamma_1 \leftrightarrow \Gamma_{5x}$	$(1/4)(\alpha_1^2)^2 \sin^2 2\theta$

Table 5.3: Wavefunctions for the $^7F_0$ and ^5D_J multiplets of Eu^{3+} in $LuPO_4$.

Multiplet	Calculated Energy (cm^{-1})	Symmetry	Wavefunction $\sum_{J,J_z} a(J,J_z)\ {}^{2S+1}L_J(J_z)$
$^7F_0$	0	Γ_1	-.963 $^7F_0$ (0) +.188 $^5D1_0$ (0)-.167 $^5D3_0$ (0) + .039 $^7F_2$ (0) -.006 $^5D1_2$ (0)+.005 $^5D3_2$ (0)
$^5D_0$	17181	Γ_1	.244 $^7F_0$ (0) +.55 $^5D1_0$ (0) -.672 $^5D3_0$ (0)
$^5D_1$	18940	Γ_5	.216 $^7F_1$ (1) +.576 $^5D1_1$ (1) -.71 $^5D3_1$ (1)
	18959	Γ_2	.216 $^7F_1$ (0) +.577 $^5D1_1$ (0) -.71 $^5D3_1$ (0)
$^5D_2$	21403	Γ_3	.119 $^7F_2$ (-2) +.422 $^5D1_2$ (-2) -.518 $^5D3_2$ (-2) + .119 $^7F_2$ (2) +.422 $^5D1_2$ (2) -.518 $^5D3_2$ (2)
	21423	Γ_5	.168 $^7F_2$ (1) +.597 $^5D1_2$ (1) -.734 $^5D3_2$ (1)
	21440	Γ_1	-.168 $^7F_2$ (0) -.597 $^5D1_2$ (0) +.734 $^5D3_2$ (0)
	21450	Γ_4	-.119 $^7F_2$ (-2) -.422 $^5D1_2$ (-2) +.518 $^5D3_2$ (-2) + .119 $^7F_2$ (2) +.422 $^5D1_2$ (2) -.518 $^5D3_2$ (2)

Table 5.4. Polarization dependencies of TPA intensities for the $^7F_0 \rightarrow {}^5D_J$ transitions of Eu^{3+} in $LuPO_4$ (second order contributions).

Transitions (cm^{-1})*		Non-zero α_q^t	Polarization Dependencies $\lvert\alpha_{21}\rvert^2$
$^7F_0$ - $^5D_0$	0-17181	α_0^2= -.0016 F_2	$4.3\times10^{-7}\ F_2^2\ (3\cos^2\theta-1)^2$
$^7F_0$ - $^5D_1$	0-18940	none	0
	0-18959	none	0
$^7F_0$ - $^5D_2$	0-21403	$\alpha_2^2 = \alpha_{-2}^2$=.0188 F_2	$3.5\times10^{-4}\ F_2^2\ \sin^4\theta\ \cos^2 2\varphi$
	0-21423	α_1^2=-.0266 F_2	$3.53\times10^{-4}\ F_2^2\ \sin^2 2\theta$
	0-21440	α_0^2=-.0266 F_2	$1.18\times10^{-4}\ F_2^2\ (3\cos^2\theta-1)^2$
	0-21450	$\alpha_2^2 = -\alpha_{-2}^2$=.0188 F_2	$3.5\times10^{-4}\ F_2^2\ \sin^4\theta\ \sin^2 2\varphi$

(*) Energies calculated from the crystal field fit.

Table 5.5. Polarization dependencies of TPA intensities for the $^7F_0 \rightarrow {}^5D_J$ transitions of Eu^{3+} in $LuPO_4$ (second and third order contributions).

Transitions (cm^{-1})*	Non-zero $\alpha_q^t \times 10^{-7}$	Polarization Dependencies $\lvert\alpha_{21}\rvert^2 \times 10^{-14}$
$^7F_0 - {}^5D_0$ 0-17181	$\alpha_0^2 = -.11$, $\alpha_0^0 = 6.0$	$2.0\times10^{-2}\,(24.4+\cos^2\theta)^2$
$^7F_0 - {}^5D_1$ 0-18940	none	0
0-18959	none	0
$^7F_0 - {}^5D_2$ 0-21403	$\alpha_2^2 = \alpha_{-2}^2 = 1.3$	$1.8\,\sin^4\theta\,\cos^2 2\varphi$
0-21423	$\alpha_1^2 = -1.9$	$1.81\,\sin^2 2\theta$
0-21440	$\alpha_0^2 = -1.9$, $\alpha_0^0 = .2$	$.44\,(3.5\cos^2\theta - 1)^2$
0-21450	$\alpha_2^2 = -\alpha_{-2}^2 = 1.3$	$1.8\,\sin^4\theta\,\sin^2 2\varphi$

(*) Energies calculated from the crystal field fit.

Table 5.6: Predicted values of relative TPA intensities for the $^7F_0 \rightarrow {}^5D_J$ transitions of Eu^{3+} in $LuPO_4$ for the case $\varphi = 45°$

TPA transitions (cm^{-1})*	$\theta = 0°$		$\theta = 45°$		$\theta = 90°$	
	Second order	Total ($2^{nd}+3^{nd}$)	Second order	Total ($2^{nd}+3^{nd}$)	Second order	Total ($2^{nd}+3^{nd}$)
$^7F_0 - {}^5D_0$						
0-17181	10^{-2}	7.2	0	6.9	10^{-3}	6.6
$^7F_0 - {}^5D_1$						
0-18940	0	0	0	0	0	0
0-18959	0	0	0	0	0	0
$^7F_0 - {}^5D_2$						
0-21403	0	0	0	0	0	0
0-21423	0	0	1.0	1.0	0	0
0-21440	1.3	1.5	.08	.14	.33	.24
0-21450	0	0	.25	.25	1.0	1

(*) Energies calculated from the crystal field fit.

Table 5.7: Predicted values of relative TPA intensities for the $^7F_0 \rightarrow {}^5D_J$ transitions of Eu^{3+} in $LuPO_4$ for the case $n = \cos^2 2\varphi \neq 0°$ ($n = 1$ when $\varphi = 0°$)

TPA transitions (cm^{-1})*	$\theta = 0°$		$\theta = 45°$		$\theta = 90°$	
	Second order	Total ($2^{nd}+3^{nd}$)	Second order	Total ($2^{nd}+3^{nd}$)	Second order	Total ($2^{nd}+3^{nd}$)
$^7F_0 - {}^5D_0$						
0-17181	10^{-2}	7.2	0	6.9	10^{-3}	6.6
$^7F_0 - {}^5D_1$						
0-18940	0	0	0	0	0	0
0-18959	0	0	0	0	0	0
$^7F_0 - {}^5D_2$						
0-21403	0	0	n/4	n/4	n	n
0-21423	0	0	1.0	1.0	0	0
0-21440	0	1.5	0	.14	0	.24
0-21450	0	0	(1-n)/4	(1-n)/4	1-n	1-n

(*) Energies calculated from the crystal field fit.

5.2.3 Eu^{3+} in $LuPO_4$ - Experimental TPA Spectra

The set up for TPA experiments was described in chapter three. For the case $\varphi = 45°$, the wavevector of the incident photon, $\mathbf{k}_i$, is perpendicular to the crystallographic XY plane of the crystal, and its polarization vector, $\mathbf{e}_i$, varies in the ZX plane (see figure 3.1 for the definition of X,Y, and Z directions with respect to the **c** axis of the crystal). When the crystal's largest surface is perpendicular to the incident wavevector ($\varphi = 45°$), TPA was observed to the $^5D_0$ level at 17186 cm^{-1}, which was assigned to the Γ_1, and to the $^5D_2$ levels at 21412, 21422, and 21458 cm^{-1}, which were assigned to the Γ_5, Γ_1 and Γ_4, respectively. The TPA transition to the lowest level of the $^5D_2$ multiplet which was

absent in the TPA spectra for the case $\varphi = 45^\circ$ was observed as predicted at 21371 cm^{-1} when the crystal is rotated about the **c** axis at 45° from the original position described above. We thus assigned this level to the Γ_3 symmetry. Taking into account the indices of refraction of the phosphate crystals [15], this latter configuration is equivalent with a rotation about the **c** axis with a rotation angle $\cong 22^\circ$ ($\varphi = 23^\circ$). The polarized spectra of the TPA transition to $^5D_2$ for the case $\varphi = 45^\circ$ and 23° are shown in figures 5.1 and 5.2. Figure 5.3 shows the experimental polarization dependence curves for the TPA transitions to the $^5D_0$ and $^5D_2$ multiplets, which were plotted in the same graph as the predicted curves whose polarization functions calculated in the second and third order were listed in table 5.5. The values of the experimental intensities were not calibrated with respect to the curves of the laser dyes being used.

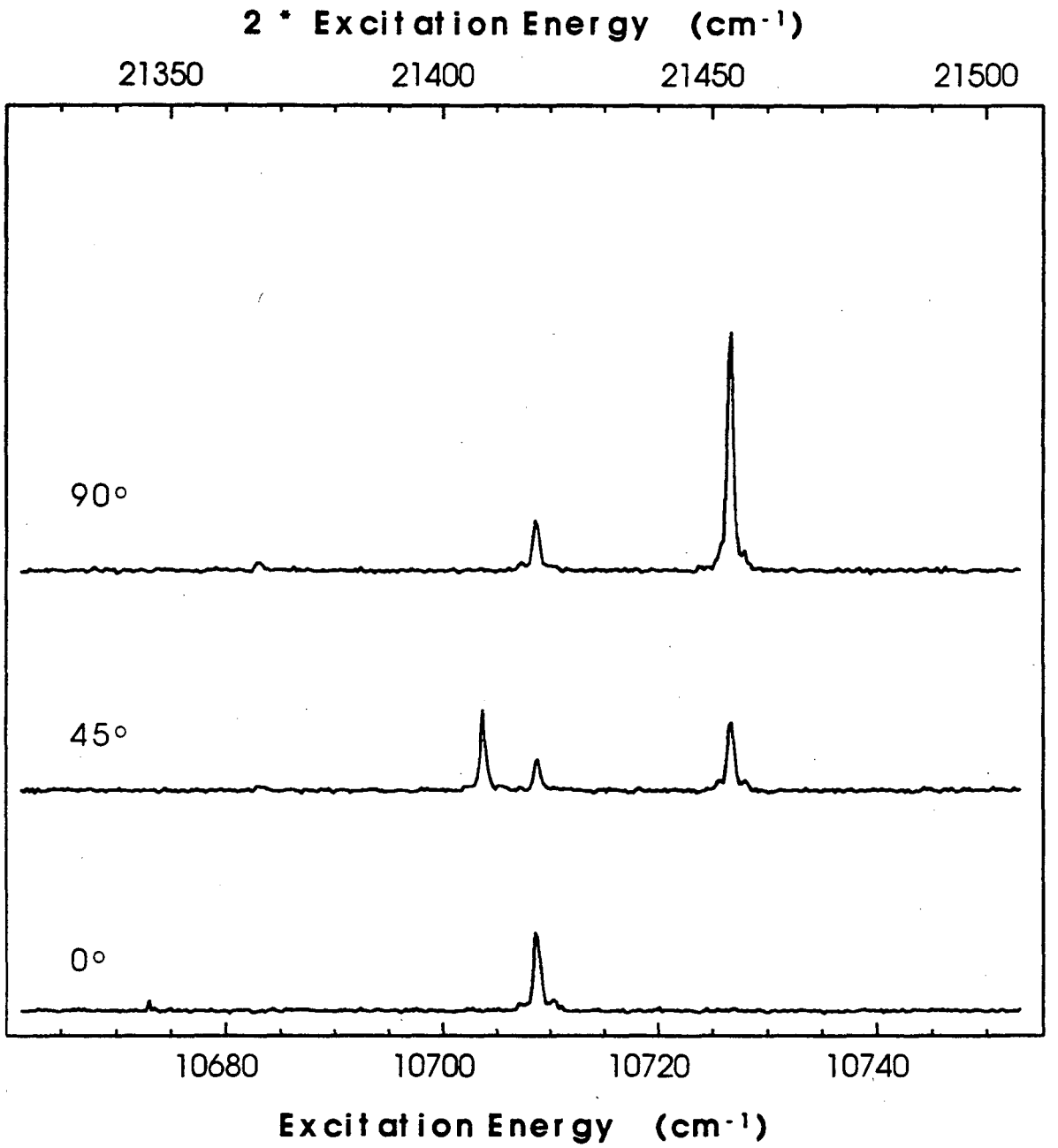

Fig. 5.1: Polarized spectra of the TPA transitions to the $^5D_2$ multiplet at 4.2 K ($\varphi = 45^\circ$).

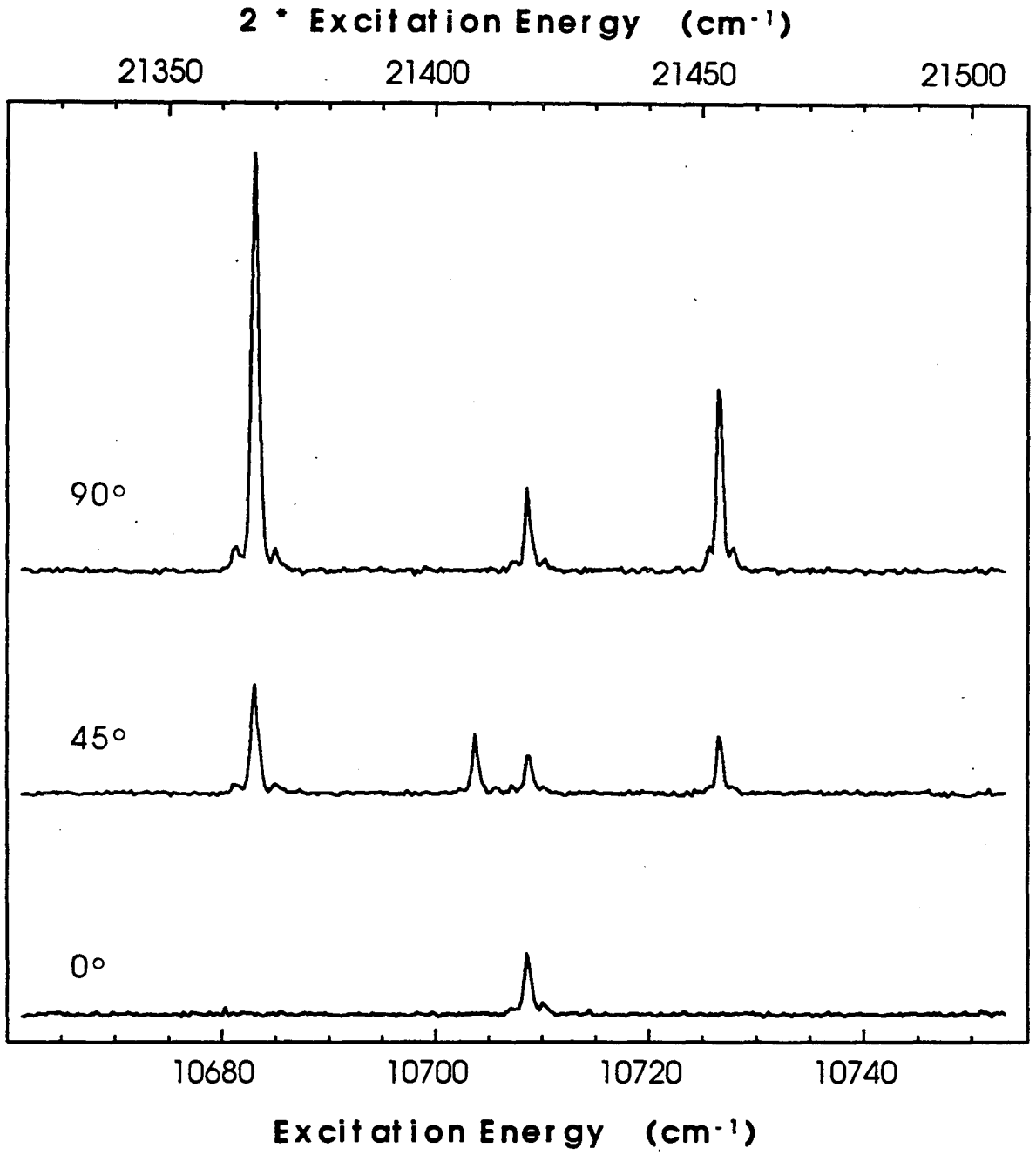

Fig 5.2: Polarized spectra of the TPA transitions to the $^5D_2$ multiplet at 4.2 K ($\varphi = 23°$).

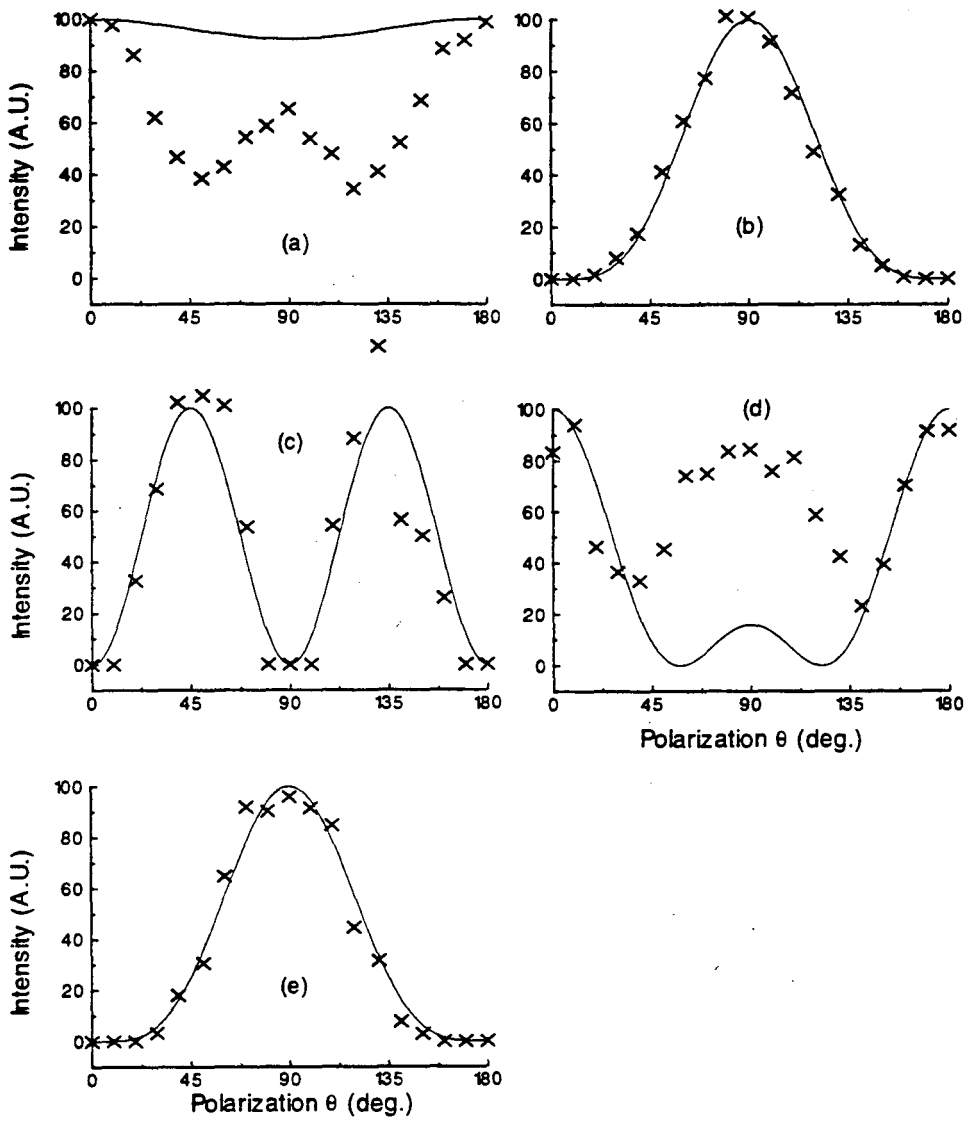

Fig. 5-3: Experimental (crosses) and predicted (solid line) polarization behavior of the $^7F_0$ - $^5D_0$ and $^5D_2$ transitions. (a) $^7F_0$ - $^5D_0$ (17186 cm^{-1}), (b) $^7F_0$ - $^5D_2(1)$ (21371 cm^{-1}), (c) $^7F_0$ - $^5D_2(2)$ (21412 cm^{-1}), (d) $^7F_0$ - $^5D_2(3)$ (21422 cm^{-1}), and (e) $^7F_0$ - $^5D_2(4)$ (21458 cm^{-1}).

For the TPA transitions to the Γ_3, Γ_5 and Γ_4 levels of the $^5D_2$ multiplet, which correspond to the $^7F_0 \rightarrow {}^5D_2(1,2,4)$ transitions, respectively, the experimental polarization dependence curves agreed well with prediction from second order theory. This relatively good agreement between theory and experiment deserves further attention. As explained in chapter two, the polarization dependencies listed in table 5.2, which were derived from a Raman scattering mechanism, could also be derived using the Bader and Gold theory [1]. As discussed in chapter two, the two methods are equivalent. In the case of the Bader and Gold theory, their polarization dependence formulae were derived using the group theoretical method. The derivation leading to the formulae given in table 5.2 was obtained using the properties of the second-rank irreducible scattering tensors and group theory. The relative intensities among various transitions, which were not given in Bader and Gold theory, were obtained using the second-order Axe theory. For these transitions second-order contribution should be sufficient, since the third-order spin-orbit contribution was found to be at least two magnitude order smaller than the second-order contribution. Tables 5.8 and 5.9 compare the theoretical and experimental values for the relative intensities corresponding to these levels for the case $\varphi = 45^\circ$ and $\varphi = 23^\circ$ and 35°, respectively. Agreement with theoretical values was marginal for the observed relative intensities. A factor of three difference between theory and observation was found for the for the case $\varphi = 45^\circ$, and an order magnitude difference between theory and observation was found for the Γ_1 - Γ_4 transition for the case $\varphi = 23^\circ$. For the Γ_1 - Γ_5 transition, the difference between theory and observation can be traced back to the ratio $[\alpha_1^2(\Gamma_5)/\alpha_2^2(\Gamma_3 \text{ or } \Gamma_4)]^2$. This ratio in

turn depends on the coefficients of the initial and final eigenfunctions. With more accurate fits for the crystal wavefunctions of Eu^{3+} in $LuPO_4$, a smaller gap between theory and observation may be obtained for this transition. For the Γ_1 - Γ_4 transition, the gap between prediction and observation comes mainly from the factor $\cos^2 \varphi$. A fit to the observed intensities with $\cos^2 \varphi$ being treated as a fitting parameter shows much better agreement would be found if $\varphi = 35^\circ$ (table 5.9).

Serious discrepancies between theory and observation were found for the TPA transitions to the Γ_1 levels of the $^5D_0$ and $^5D_2$ multiplets. For these transitions second-order contributions were found to be relatively small, being comparable to or smaller than the third-order spin-orbit contributions. For the Γ_1 transition of the $^5D_0$ multiplet, the predicted intensities incorporating the second- and third-order spin-orbit contribution vanish twice when θ changes from 0 to 180 degree. The observed intensities, however, are nonzero for all values of θ. For the Γ_1 transition of the $^5D_2$ multiplet, both the predicted and experimental intensities are nonzero for all values of θ. The theoretical curvature nevertheless was significantly different from the observed. It is obvious that even inclusion of the comparatively large third-order spin-orbit effect was not sufficient to account for both the relative intensities and the observed nonzero background in the TPA polarization dependencies. Good agreement with observation, however, was restored if the expression of the matrix elements of the scattering tensors described in chapter two contained both real and complex values. Figure 5.4 shows the fitted curves for these transitions using the revised formula $(A+B\cos^2\theta)^2$, where A is complex , and B is real. The imaginary part of A turned out to account for the

approximately constant background observed, since $(Re(A)+Im(A)+B\cos^2\theta)^2=(Re(A)+B\cos^2\theta)^2+[Im(A)]^2$, where $[Im(A)]^2$ is the non-zero background.

Table 5.8: Comparison of predicted and observed values of relative TPA intensities for the $^7F_0 \rightarrow {}^5D_2(1,2,4)$ transitions of Eu^{3+} in $LuPO_4$ for the case $\varphi=45°$.

TPA transitions (cm^{-1})*		$\theta = 0°$ Cal. ($2^{nd}+3^{nd}$)	$\theta = 0°$ Obs.	$\theta = 45°$ Cal. ($2^{nd}+3^{nd}$)	$\theta = 45°$ Obs.	$\theta = 90°$ Cal. ($2^{nd}+3^{nd}$)	$\theta = 90°$ Obs.
$^7F_0$ - $^5D_2$	0-21371	0	0	0	0	0	0
	0-21412	0	0	1.0	.3	0	0
	0-21458	0	0	.25	.28	1.0	1.0

(*) Observed energies

Table 5.9: Comparison of predicted and observed values of relative TPA intensities for the $^7F_0 \rightarrow {}^5D_2(1,2,4)$ transitions of Eu^{3+} in $LuPO_4$ for the case $\varphi = 23°$ and $35°$.

TPA transitions (cm^{-1})*	$\theta = 0°$ Cal. ($2^{nd}+3^{nd}$)	$\theta = 0°$ Obs.	$\theta = 45°$ Cal. ($2^{nd}+3^{nd}$)	$\theta = 45°$ Obs.	$\theta = 90°$ Cal. ($2^{nd}+3^{nd}$)	$\theta = 90°$ Obs.
$^7F_0$ - $^5D_2$, $\varphi = 23°$						
0-21371	0	0	.21	.4	.86	1.5
0-21412	0	0	1.0	.22	0	0
0-21458	0	0	.035	.23	.14	.75
$^7F_0$ - $^5D_2$, $\varphi = 35°$						
0-21371	0	0	.17	.18	.67	.67
0-21412	0	0	1.0	.1	0	0
0-21458	0	0	.08	.1	.33	.33

(*) Observed energies

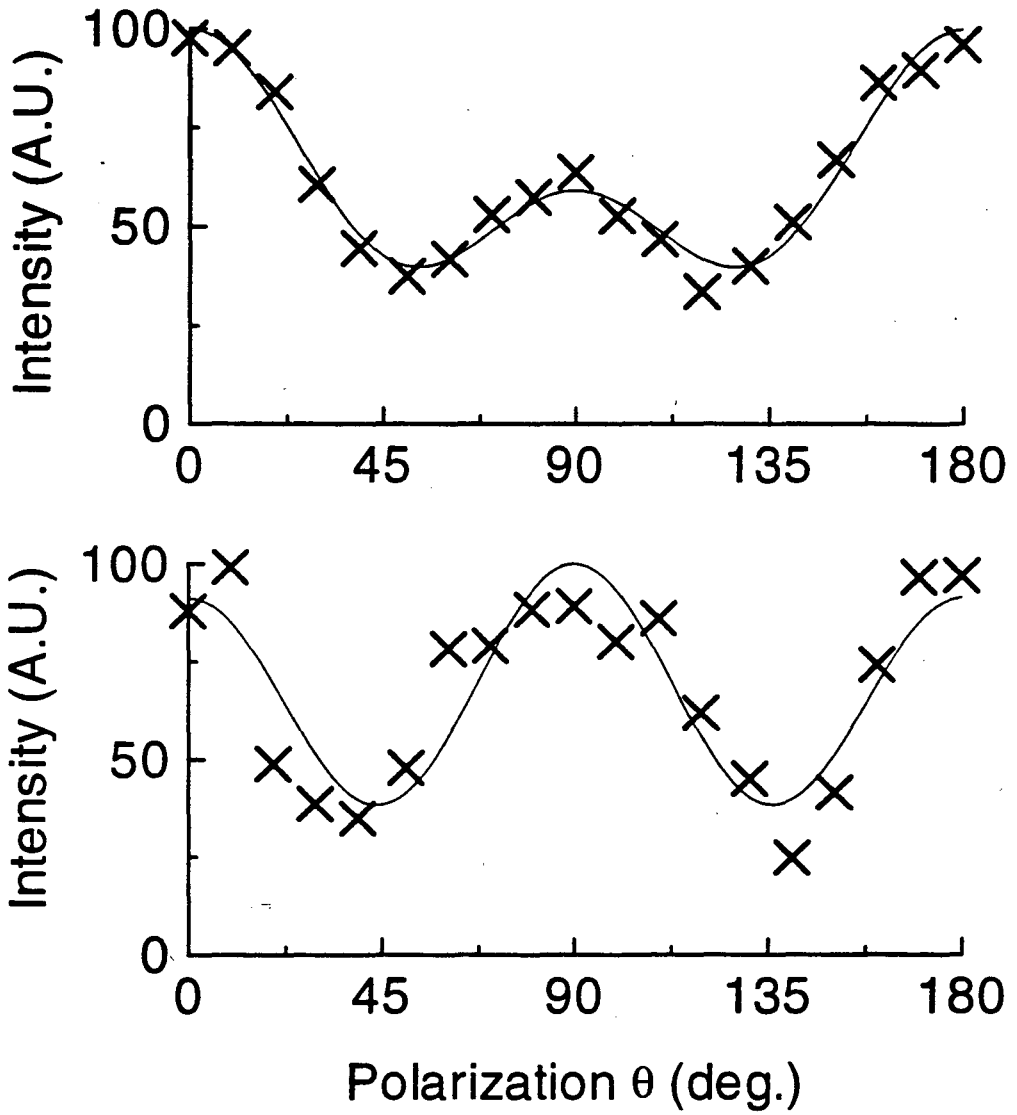

Fig. 5-4: Experimental (crosses) and fitted (solid line) polarization behavior of the $^7F_0(1)$ - $^5D_0(1)$ and $^5D_2(3)$ transitions.

The complex number A appearing in the TPA transition intensity expression has first been noticed by Gacon et al [6,11,12]. In their report a non-zero background was observed in the polarization dependence curves for TPA transitions to the Γ_1 level of the $^5D_0$ multiplet of Sm^{3+} in BaClF [6] and of Eu^{3+} in $LuPO_4$ [11] and $Eu(OH)_3$ [12] and to the Γ_5 level of the $^5D_2$ multiplet of Eu^{3+} in $Eu(OH)_3$ [12]. Using a phenomenological model, they expressed the TPA transition intensities which contained a complex parameter responsible for the non-zero constant background. The origin of the non-zero background, however, was not explained in their model, whose expression is equivalent to $(Re(A)+B\cos^2\theta)^2 + [Im(A)]^2$, our fitted formula mentioned earlier. We will now offer a qualitative explanation for the existence of this non-zero background.

Let Im(A) now denote the total imaginary contribution to the two-photon transition amplitude. We note that the two photon transition amplitude given in chapter two was obtained in the electric dipole approximation scheme. Expansion beyond the electric dipole approximation was discussed in chapter one. If we include the electric quadrupole in expression (1.48), the TPA amplitude expression will contain both the real and non-zero imaginary values. A similar case is found where only circular polarization is used, since the magnetic dipole term would differ the electric dipole term by a pure imaginary constant. We will illustrate the last two points by denoting by (E1) the electric dipole term in the matrix element M_{ab} appearing in the second-order expression (1.45), i(E2) the electric quadrupole term, and i(M1) the magnetic dipole term for the case of circular polarization, where (E1), (E2), and (M1) are real. Including (E1), (E2), and (M1), the numerator in (1.45) will contain the terms (E1)(E1),

(M1)(M1), (E2)(E2), i(E1)(E2), and i(E1)(M1). Only the last two terms (E1)(E2) and (E1)(M1) would contribute to the Im(A) term discussed above.

Another source contributing to Im(A) is the $i(\mathbf{k}_1 + \mathbf{k}_2)\cdot < i|\mathbf{D}|f >$ term in the first-order two-photon transition amplitude expression given in (1.42). When the ground states i and f are mixed with states of configurations with parity opposite to that of the ground configuration, this term gives non-zero contribution to Im(A). Finally, under resonant excitation, the factor $i\Gamma_j$ appearing in the denominator of (1.45) may also contribute to Im(A).

We now compare the magnitudes of the terms contributing to Im(A). For two-photon transitions with non-resonant excitation, the term associated with Γ_j would be negligible. As explained in chapter one, the $i(\mathbf{k}_1 + \mathbf{k}_2)\cdot < i|\mathbf{D}|f >$ term is smaller than the second-order electric-dipole term by a factor of 10^{-5} and can also be neglected. We are left with the terms (E1)(M1) and (E1)(E2). There are several pathways through two-photon transitions via (E1)(M1) and (E1)(E2). Consider, for example, the expressions

$$\sum_{5d} \frac{< 4f|\mathbf{m}|5d >< 5d|\mathbf{D}|4f >}{\hbar(\omega_{df} - \omega)}, \quad \sum_{5d} \frac{< 4f|\mathbf{D}|5d >< 5d|\mathbf{m}|4f >}{\hbar(\omega_{df} - \omega)},$$

$$\sum_{4f} \frac{< 4f|\mathbf{m}|4f >< 4f|\mathbf{D}|4f >}{\hbar(\omega_{ff} - \omega)}, \text{ and } \sum_{4f} \frac{< 4f|\mathbf{D}|4f >< 4f|\mathbf{m}|4f >}{\hbar(\omega_{ff} - \omega)}. \tag{5.1}$$

Comparing each term of (5.1) with the second order electric dipole expression

$$\sum_{5d} \frac{< 4f|\mathbf{D}|5d >< 5d|\mathbf{D}|4f >}{\hbar(\omega_{df} - \omega)} \tag{5.2}$$

it is easy to see that the first two terms of (5.1) are negligible, since <4f|m|5d> is smaller than <4f|m|4f> by a factor of 10^{-3}, which in turn is smaller than <4f|D|5d> by a factor of 10^{-2}. The last two terms of (5.1) are much larger than the first two. The denominators of the last two terms of (5.1) can be of the order of a few hundred wavenumbers, which is smaller than the denominator of (5.2) by a factor of 10^{-3}, and their numerators are smaller than the numerator of (5.2) by a factor of 10^{-5}. Their magnitude could be approximately two order of magnitudes smaller than the second-order electric dipole term. When the denominators of these terms are sufficiently small, their total magnitude could be comparable to the second-order electric dipole term, if the latter is sufficiently small.

Having established the (E2)(E1) and (M2)(M1) terms as the dominant contributions to Im(A) we can rewrite the scattering amplitude for TPA from the same source (see, for example, equations (2.2) and (1.48)) as follows:

$$
\begin{aligned}
< i|\alpha_{\mathrm{TPA}}|f >= & -\sum_{j\in 5d}\left[\frac{\langle i|\hat{\mathbf{e}}_2\cdot\mathbf{D}\,|j\rangle\langle j|\hat{\mathbf{e}}_1\cdot\mathbf{D}|f\rangle}{\hbar\omega_j-\hbar\omega}\right] \\
& -\frac{ie\omega}{2c}\sum_{j\in 5d}\left[\frac{\langle i|\hat{\mathbf{k}}_2\cdot\mathbf{DD}\cdot\hat{\mathbf{e}}_2|j\rangle\langle j|\hat{\mathbf{e}}_1\cdot\mathbf{D}|f\rangle}{\hbar\omega_j-\hbar\omega}\right]-\sum_{j'\in 4f}\left[\frac{\langle i|(\hat{\mathbf{k}}_2\times\hat{\mathbf{e}}_2)\cdot\mathbf{m}|j'\rangle\langle j'|\hat{\mathbf{e}}_1\cdot\mathbf{D}|f\rangle}{\hbar\omega_{j'}-\hbar\omega}\right],
\end{aligned}
\tag{5.3}
$$

where the first, second, and last terms correspond to the (E1)(E1), (E2)(E1), and (M1)(E1) contributions, respectively. The polarization dependent TPA expression for the scattering amplitude is given by (see equation 2.24)

$$
\alpha_{21}=\sum_{t=0}^{2}\sum_{q=-t}^{t}\lambda_q^t\alpha_q^{(t)}+\alpha(\mathrm{E2})+\alpha(\mathrm{M1}),
\tag{5.4}
$$

where the second and third terms in (5.4) represent the polarization dependence form of the second and third terms in (5.3). In our TPA experiments on Eu^{3+}:$LuPO_4$, the dominant contribution to Im(A) comes from the second term of (5.3). When the magnitude of this term is small compared to the (E1)(E1) term in (5.3), the former can be approximately independent of the polarization angles θ and φ. The matrix element of the TPA scattering amplitude between states of the 4f configuration becomes (compare, for example, with 3.26)

$$(4f|\alpha_{\mathrm{TPA}}|4f) = (4f|[-\frac{1}{\sqrt{3}}\alpha_0^{(0)} + (\frac{3\cos^2\theta - 1}{\sqrt{6}})\alpha_0^{(2)} - (\frac{e^{-i\varphi}}{2}\sin 2\theta)\alpha_1^{(2)} + (\frac{e^{i\varphi}}{2}\sin 2\theta)\alpha_{-1}^{(2)} + (\frac{e^{-2i\varphi}}{2}\sin^2\theta)\alpha_2^{(2)} + (\frac{e^{2i\varphi}}{2}\sin^2\theta)\alpha_{-2}^{(2)}]|4f) + iA, \tag{5.5}$$

where A is a real constant corresponding to the matrix element of the α(E2) term in (5.4). For a Γ_1 - Γ_1 transition the squared TPA amplitude is written

$$|(4f|\alpha_{\mathrm{TPA}}|4f)|^2 = |(4f|[-\frac{1}{\sqrt{3}}\alpha_0^{(0)} + (\frac{3\cos^2\theta - 1}{\sqrt{6}})\alpha_0^{(2)}]|4f) + iA|^2, \tag{5.6}$$

or

$$|(4f|\alpha_{\mathrm{TPA}}|4f)|^2 = |B + C\cos^2\theta + iA|^2, \tag{5.7}$$

where B,C, and A are real constants, with B and C corresponding to the matrix elements of the first and second terms on the right hand side of (5.6). As previously mentioned, the iA term in (5.7) might be responsible for the nonzero background observed in the Γ_1 - Γ_1 TPA transitions of Eu^{3+} in $LuPO_4$.

5.2.4 Conclusion

We have shown that when the second-order electronic-dipole contribution is sufficiently small, the relative contributions from the imagninary terms to the electronic dipole term may become significant. Among these imaginary terms, (E2)(E1) and (M1)(E1) have shown to be the dominant terms for the case of linear and circular polarizations, respectively. It should be noted that each of these imaginary terms have their own polarization dependencies which may not be the same as those given in table 2.1. When their relative magnitudes to the (E1)(E1) term are small, their total contribution may be approximated by a constant Im(A) added to the regular polarization dependence expressions for the (E1)(E1) term. Explicit evaluation of Im(A) for the case of Eu^{3+} in $LuPO_4$, however, was not performed, due to the difficulty in determining the values of the matrix elements <4f|D|4f> for Eu^{3+} with the 4f states being mixed with the 5d states via the odd-rank tensor of the crystal field Hamiltonian.

There are not many reports in the literature on the (M1E1) and (E2E1) terms contributing to TPA linestrengths in crystals doped with rare-earth ions. The studies of the contributions of the (M1E1) term to TPA linestrengths of rare-earth doped crystals to our best knowledge have been limited to the area known as two-photon circular dichroism [16-20]. One-photon circular dichroism [21,22] has been known for years, but observation of two-photon circular dichroic linestrengths of rare-earth compounds were reported only recently [20, 23]. The (E2E1) term may be responsible for the phase-shifted quadrupole second-harmonic contribution recently observed in Si(001) metal-oxide-semiconductor structures [24, 25]. Through our analysis above we have demonstrated for the first time that the (E2E1) term may be the main factor contributing

to the nonzero background observed in the polarization dependent TPA spectra of Eu^{3+} in $LuPO_4$.

5.3 TPA Spectroscopy of Cm^{3+} in $LuPO_4$

In this section we will present the polarization dependent TPA intensity measurements of Cm^{3+} in $LuPO_4$. Compared with Eu^{3+}, Cm^{3+} is a more ideal ion for studying the role of α_q^t's for several reasons. Firstly, due to the more spatial extension of the 5f wavefunctions into its crystalline environment compared to its 4f counterparts, the magnitude of the spin-orbit effect is larger for Cm^{3+} than for rare-earth ions. The third-order spin-orbit contribution is therefore expected to be more significant for Cm^{3+} than for rare-earth ions. Secondly, the second-order TPA contribution in Cm^{3+} is relatively small due to the vanishing value of the leading term $\langle f^7\ {}^8S\|U^{(2)}\|f^7\ {}^{2S+1}L_J\rangle$ in the expression of the TPA transition intensities originating from the ground ${}^8S_{7/2}$ multiplet. In fact this was the main reason why crystals doped with Gd^{3+} has displayed anomalous TPA linestrengths not accounted by the second-order theory [26-29]. By inclusion of the relatively comparable third-order spin-orbit and crystal-field contributions, agreement was restored between calculation and observation. Until now attention has been paid only to integrated TPA linestrength calculations on Gd^{3+}, since the extremely small splitting of the ${}^8S_{7/2}$ ground multiplet of Gd^{3+} (only a fraction of a wavenumber) made accurate intensity measurements for TPA Stark-to-Stark level transitions orinating from the ground manifold of Gd^{3+} virtually impossible to obtain. The larger crystal field interaction of the 5f wavefunctions allowed access to

observation of the ground state splittings for Cm^{3+} and hence measurements of Stark-to-Stark TPA linestrengths, which are essential for studying the role of α_q^t. In light of the discussion on the contributions from the imaginary terms in the TPA expressions in the previous section, TPA measurements on Cm^{3+} in $LuPO_4$ would provide important information for understanding the emerging role of these imaginary terms.

5.3.1 Cm^{3+}- Selection Rules

The trivalent Cm^{3+} ion has an open shell configuration $5f^7$. The lanthanide analogue of Cm^{3+}, Gd^{3+}, has a $4f^7$ electronic structure. Because of the greater spatial extension of the 5f wavefunctions, the interaction of the 5f electrons of Cm^{3+} with the environment is greater than that for Gd^{3+}. The free-ion spin-orbit coupling parameter for the 5f configuration of Cm^{3+} is about twice the value for the 4f configuration of Gd^{3+} or Eu^{3+}. The point group symmetry of Cm^{3+} in $LuPO_4$ is D_{2d}. The electronic states of Cm^{3+} are labeled by the irreducible representations Γ_6 and Γ_7 of D_{2d}.

Due to the large intermediate coupling effects, the ground state of Cm^{3+} is not pure $^8S_{7/2}$ state, but it is admixed with other states with the same value of J, but with different values of L and S. The ground state of Cm^{3+} in $LuPO_4$ is Γ_7. The selection rules and Raman activity for the TPA transitions originating in the ground state are described in table 5.10. EPR, emission and absorption measurements of Cm^{3+} in $LuPO_4$ have been reported by several research groups [30-32]. The crystal field wavefunctions for Cm^{3+} in $LuPO_4$ are provided by Sytsma et al [32].

Table 5.10: Selection rules and Raman activity of TPA transitions orginating from the ground state of Cm^{3+} in $LuPO_4$

Transition	Scattering tensor symmetry	Raman activity α_q^t
$\Gamma_7 \leftrightarrow \Gamma_7$	$\Gamma_1 + \Gamma_2$	α_0^0, α_0^2
$\Gamma_7^K \leftrightarrow \Gamma_7^K$ (*)	$\Gamma_1 + \Gamma_2$	α_0^0, α_0^2
$\Gamma_7^K \leftrightarrow \Gamma_7$	Γ_{5x}(**)	α_1^2
$\Gamma_7 \leftrightarrow \Gamma_7^K$	Γ_{5y}	α_{-1}^2
$\Gamma_7 \leftrightarrow \Gamma_6$	$\Gamma_3 + \Gamma_4$	$\alpha_2^2, \alpha_{-2}^2$
$\Gamma_7^K \leftrightarrow \Gamma_6^K$	$\Gamma_3 + \Gamma_4$	$\alpha_2^2, \alpha_{-2}^2$
$\Gamma_7^K \leftrightarrow \Gamma_6$	Γ_{5x}	α_1^2
$\Gamma_7 \leftrightarrow \Gamma_6^K$	Γ_{5y}	α_{-1}^2

(*)Γ and Γ^K represent the members of a Kramers doublet.

5.3.2 Polarization Dependence Functions

Polarization dependence functions for TPA transitions of Cm^{3+} in $LuPO_4$ are shown in table 5.11. The angles θ and φ were defined in chapter two where the expression for TPA intensities was given. The α_0^0 term is non-zero when third-order spin-orbit interaction is taken into account. Because of the non-zero value of the α_0^0 term calculated in the third order, the polarization dependence curves for $\Gamma_7 \leftrightarrow \Gamma_7$ transitions would look different when third-order spin-orbit effect is included. For TPA transitions between Kramers doublet states, the polarization dependent TPA linestrengths would generally depend on two or more non-zero α_q^t. Table 5.12 lists the crystal-field wavefunctions of Cm^{3+} in $LuPO_4$ for crystal-field levels of the $^8S_{7/2}$ ground multiplet, $^6D_{7/2}$ multiplet at 16800 cm^{-1}, $^6P_{5/2}$ multiplet, and $^6D_{7/2}$ multiplet at 27900

cm^{-1}. For each Kramers level only one state of the Kramers doublet is listed; the other Kramers conjugate state can be obtained using expressions (D6) and (D7) of chapter two. To avoid a potential ambiguity in the labeling of the multiplets, $^6D_{7/2}$ will be used to denote the multiplet at 16800 cm^{-1}, while $^6D_{7/2}'$ (distinguished by a prime) will be used for the multiplet at 27900 cm^{-1}. The nomenclature $^{2S+1}L_J(n)$ will be used to indicate the nth highest energy level in the multiplet $^{2S+1}L_J$. Using the crystal-field wavefunctions given in table 5.12, the polarization dependent TPA intensities can be expressed in terms of only one variable. The crystal field wavefunctions were obtained from a fit with 60 levels [32]. Due to the large intermediate coupling effect, a single eigenstate of Cm^{3+} would be composed of a large number of $^{2S+1}L_j$ states, where J is the same but L and S may be different. Only $^{2S+1}L_j$ states with sufficiently large coefficients (one percent or above) were used in the calculations. Adding smaller terms only changed the values of the corresponding α_q^t by less than one percent. The non-zero values of α_q^t calculated up to third order for various transitions in Cm^{3+}:$LuPO_4$ are shown in table 5.13. Their respective polarization dependencies are shown in table 5.14. Only transitions for which experimental data were obtained were listed in tables 5.13 and 5.14. We have assumed only the θ dependence, with φ taken to be 45^0. For different configurations corresponding to different values of φ, table 5.11 can be used.

Table 5.11: Polarization dependence curves for TPA transitions originating in the ground state of Cm^{3+} in $LuPO_4$.

Transition	Polarization dependence curves
$\Gamma_7 \leftrightarrow \Gamma_7$	$2[-\frac{1}{\sqrt{3}}\alpha_0^0+(\frac{3\cos^2\theta-1}{\sqrt{6}})\alpha_0^2]^2+\frac{\sin^2 2\theta}{2}(\alpha_1^2)^2$
$\Gamma_7 \leftrightarrow \Gamma_6$	$\frac{\sin^2 2\theta}{2}(\alpha_1^2)^2+\frac{\sin^4\theta}{2}\lvert e^{-2i\varphi}\alpha_2^2+e^{2i\varphi}\alpha_{-2}^2\rvert^2$

Table 5.12: Wavefunctions for various multiplets of Cm^{3+} in $LuPO_4$.

Calculated Energy (cm^{-1})	Symmetry	Wavefunction $\sum_{J,J_z} a(J,J_z)\ {}^{2S+1}L_J(J_z)$
$^8S_{7/2}$		
0.0	Γ_7	-.844 $^8S_{7/2}$(7/2) -.403 $^6P_{7/2}$(7/2)+.088 $^6D_{7/2}$(7/2) - .27 $^8S_{7/2}$(-1/2) -.13$^6P_{7/2}$(-1/2)+.028 $^6D_{7/2}$(-1/2)
3.0	Γ_6	.808 $^8S_{7/2}$(5/2) +.386 $^6P_{7/2}$(5/2) -.084 $^6D_{7/2}$(5/2) + .363 $^8S_{7/2}$(-3/2) +.173$^6P_{7/2}$(-3/2) -.038 $^6D_{7/2}$(-3/2)
14.6	Γ_7	-.27 $^8S_{7/2}$(7/2) -.13 $^6P_{7/2}$(7/2)+.028 $^6D_{7/2}$(7/2) - .844 $^8S_{7/2}$(-1/2) -.403 $^6P_{7/2}$(-1/2)+.088 $^6D_{7/2}$(-1/2)
15.4	Γ_6	.363 $^8S_{7/2}$(5/2) +.173 $^6P_{7/2}$(5/2) -.038 $^6D_{7/2}$(5/2) +.808 $^8S_{7/2}$(-3/2) +.386 $^6P_{7/2}$(-3/2) -.084 $^6D_{7/2}$(-3/2)
$^6D_{7/2}$		
16526	Γ_7	.233 $^8S_{7/2}$(7/2) -.25 $^6P_{7/2}$(7/2)+.27 $^6D_{7/2}$(7/2) +.225 $^8S_{7/2}$(-1/2) -.24$^6P_{7/2}$(-1/2)+.26 $^6D_{7/2}$(-1/2)
16565	Γ_6	.307 $^8S_{7/2}$(5/2) -.33 $^6P_{7/2}$(5/2)+.354 $^6D_{7/2}$(5/2) +.104 $^8S_{7/2}$(-3/2) -.113 $^6P_{7/2}$(-3/2)+.12 $^6D_{7/2}$(-3/2)
16992	Γ_7	.225 $^8S_{7/2}$(7/2) -.24 $^6P_{7/2}$(7/2)+.26 $^6D_{7/2}$(7/2) -.233 $^8S_{7/2}$(-1/2) +.25 $^6P_{7/2}$(-1/2)-.27 $^6D_{7/2}$(-1/2)
$^6P_{5/2}$		
19841	Γ_6	.46 $^6P_{5/2}$(5/2) -.4 $^6D_{5/2}$(5/2)+.16 $^6F_{5/2}$(5/2)+.16 $^4D6_{5/2}$(5/2) +.45 $^6P_{5/2}$(-3/2)-.39 $^6D_{5/2}$(-3/2) +.16 $^6F_{5/2}$(-3/2) +.15 $^4D6_{5/2}$(-3/2)

$^6D_{7/2}$'		
27869	Γ_6	-.05 $^6P_{7/2}$(5/2) -.06 $^6D_{7/2}$ (5/2) +.05 $^6F_{7/2}$ (5/2)
		-.04 $^6G_{7/2}$ (5/2) -.04 $^4D6_{7/2}$ (5/2) -.03 $^4D1_{7/2}$ (5/2)
		+ .36 $^6P_{7/2}$(-3/2)+.46 $^6D_{7/2}$ (-3/2) -.39 $^6F_{7/2}$ (-3/2)
		+.3 $^6G_{7/2}$ (-3/2) +.28 $^4D6_{7/2}$ (-3/2) +.21 $^4D1_{7/2}$ (-3/2)
27913	Γ_7	.19 $^6P_{7/2}$(7/2) +.24 $^6D_{7/2}$ (7/2) - .2 $^6F_{7/2}$ (7/2)
		+.155 $^6G_{7/2}$ (7/2) +.148 $^4D6_{7/2}$ (7/2) +.11 $^4D1_{7/2}$ (7/2)
		-.3 $^6P_{7/2}$(-1/2) -.39 $^6D_{7/2}$ (-1/2) +.32 $^6F_{7/2}$ (-1/2)
		-.25 $^6G_{7/2}$ (-1/2) -.24 $^4D6_{7/2}$ (-1/2) -.18 $^4D1_{7/2}$ (-1/2)
27971	Γ_6	-.36 $^6P_{7/2}$(5/2) -.46 $^6D_{7/2}$ (5/2) +.38 $^6F_{7/2}$ (5/2)
		-.3 $^6G_{7/2}$ (5/2) -.29 $^4D6_{7/2}$ (5/2) -.21 $^4D1_{7/2}$ (5/2)
		-.056 $^6P_{7/2}$(-3/2) -.07 $^6D_{7/2}$ (-3/2) +.058 $^6F_{7/2}$ (-3/2)
		-.046 $^6G_{7/2}$ (-3/2) -.044 $^4D6_{7/2}$ (-3/2) -.03 $^4D1_{7/2}$ (-3/2)
28023	Γ_7	-.3 $^6P_{7/2}$(7/2) -.38 $^6D_{7/2}$ (7/2) +.313 $^6F_{7/2}$ (7/2)
		-.25 $^6G_{7/2}$ (7/2) -.235 $^4D6_{7/2}$ (7/2) -.18 $^4D1_{7/2}$ (7/2)
		-.2 $^6P_{7/2}$(-1/2) -.254 $^6D_{7/2}$ (-1/2) +.21 $^6F_{7/2}$ (-1/2)
		-.17 $^6G_{7/2}$ (-1/2) -.16 $^4D6_{7/2}$ (-1/2) -.12 $^4D1_{7/2}$ (-1/2)

Table 5.13. Non-zero contributions of $\alpha_q^{(t)} = \langle i|\alpha_q^{(t)}|f\rangle$ for the $^8S_{7/2} \rightarrow {}^6D_{7/2}$, $^6P_{5/2}$ transitions of Cm^{3+} in $LuPO_4$ ($\varphi=45^0$).

Transitions (cm^{-1})	Second order $\alpha_q^t \times 10^{-7}$	Second and third order $\alpha_q^t \times 10^{-7}$
$^8S_{7/2}$ - $^6D_{7/2}$		
0 - 16526	α_0^2=1.36	α_0^2=1.93, α_0^0= 7.88
0 - 16565	α_2^2= –.226, α_{-2}^2=-.989, α_1^2=	α_2^2= –.32, α_{-2}^2=-1.4, α_1^2= 2.86
0 - 16992	2.01	α_0^2=3.0, α_0^0= 3.9
3 - 16526	α_0^2= 2.086	α_2^2= .93, α_{-2}^2=2.36, α_1^2= 1.73
	α_2^2= .655, α_{-2}^2=1.666, α_1^2= 1.22	
$^8S_{7/2}$ - $^6P_{5/2}$		
0 -19841	α_2^2= .243, α_{-2}^2=-1.27, α_1^2= -.96	α_2^2= .298, α_{-2}^2=-1.55, α_1^2= -1.18
3 - 19841	α_0^2= 1.534, α_1^2= -.568	α_0^2= 1.88, α_1^2= -.097
$^8S_{7/2}$ - $^6D_{7/2}$'		
0 - 27869	α_2^2= .559, α_{-2}^2=.968, α_1^2= -.526	α_2^2= .71, α_{-2}^2=1.23, α_1^2= -.67
0 - 27913	α_0^2=1.38	α_0^2=1.76, α_0^0= -1.54
3 - 27869	α_0^2=.393, α_1^2= 1.59	α_0^2=.5, α_0^0= 2.03, α_1^2= 2.03
3 - 27913	α_2^2= .637, α_{-2}^2=.99, α_1^2= 1.21	α_2^2= .812, α_{-2}^2=1.264, α_1^2= 1.54

Table 5.14: Polarization dependencies of TPA intensities for the $^8S_{7/2} \rightarrow {}^6D_{7/2}$, $^6P_{5/2}$ transitions of Cm^{3+} in $LuPO_4$ (φ=45^0).

Transitions (cm^{-1})	Second order $\lvert\alpha_{21}\rvert^2 x10^{14}$	Second and third order $\lvert\alpha_{21}\rvert^2 x10^{14}$
$^8S_{7/2}$ - $^6D_{7/2}$		
0 - 16526	$.616\,(3\cos^2\theta - 1)^2$	$11.1\,(2.26 - \cos^2\theta)^2$
0 - 16565	$.29\sin^4\theta + 2.02\sin^2 2\theta$	$.58\sin^4\theta + 4.1\sin^2 2\theta$
0 - 16992	$1.45\,(3\cos^2\theta - 1)^2$	$24\,(1 - 1.06\cos^2\theta)^2$
3 - 16526	$.511\sin^4\theta + .743\sin^2 2\theta$	$\sin^4\theta + 1.5\sin^2 2\theta$
$^8S_{7/2}$ - $^6P_{5/2}$		
0 -19841	$1.14\sin^4\theta + .46\sin^2 2\theta$	$1.7\sin^4\theta + .7\sin^2 2\theta$
3 - 19841	$.784(3\cos^2\theta - 1)^2 + .161\sin^2 2\theta$	$1.18(3\cos^2\theta - 1)^2 + .24\sin^2 2\theta$
$^8S_{7/2}$ - $^6D_{7/2}$'		
0 - 27869	$.0838\sin^4\theta + .138\sin^2 2\theta$	$.135\sin^4\theta + .224\sin^2 2\theta$
0 - 27913	$.6348\,(3\cos^2\theta - 1)^2$	$9.24\,(\cos^2\theta + .08)^2$
3 - 27869	$.05(3\cos^2\theta - 1)^2 + 1.26\sin^2 2\theta$	$2(.61\cos^2\theta - 1.38)^2 + 2.06\sin^2 2\theta$
3 - 27913	$.0623\sin^4\theta + .732\sin^2 2\theta$	$.1\sin^4\theta + 1.2\sin^2 2\theta$

5.3.3 Cm^{3+} in $LuPO_4$ - Experimental TPA Spectra

5.3.3.1 $^8S_{7/2}$ - $^6D_{7/2}$ Transitions

TPA was observed to three of the four levels of the $^6D_{7/2}$ multiplet (figure 5.5). Two transitions are observed to the $^6D_{7/2}(1)$ level, which are separated by 3.5 cm^{-1}. This is a ground-state splitting and identifies these transitions unambigously as originating from the two lowest $^8S_{7/2}$ levels. The fitted linewidths are 3.5 cm^{-1}, broader than the 2.3 cm^{-1} linewidth measured for single-photon absorption. Their polarization behavior is

unusual, with both transitions appearing surprisingly isotropic (figure 5.6). At higher temperatures a third transition was seen, originating from the third ground-state level. However, it was two weak to yield good line fits.

Two transitions were observed to the $^6D_{7/2}(2)$ level, separated by 7.9 cm^{-1}, originating from the first and third ground-state levels. Only one broad line, with a linewidth of 20.2 cm^{-1}, was observed to the $^6D_{7/2}(3)$ level. The originating level can not be determined definitively as no ground-state splittings are resolved. However, the strong polarization anisotropy suggests that this comprises absorption from mainly one level. As the intensity of this line decreases immediately when the sample is heated, this transition probably originates from the lowest ground-state level.

In addition to the electronic transitions, there are numerous minor excitation features in the spectra, which have reproducible structure. These were also observed in single-photon absorption (figure 5.7), and appear to be phonon bands coupling to the main electronic lines. Their displacements are in approximate agreement with phonon energies measured by Raman spectroscopy [33]. In the two-photon case, the features in the region 8400 to 8460 cm^{-1} appear strongest for σ-polarization excitation. This would suggest that they are coupled to the $^8S_{7/2}(1)$ - $^6D_{7/2}(2)$ transition, which appears strongly for σ-polarization excitation. Selection rules forbid phonon-assisted transitions in two-photon spectroscopy, which would explain the absence of the features above 17000 cm^{-1} seen in the single-photon spectra. However, the appearance of any phonon bands in two-photon spectra is unusual.

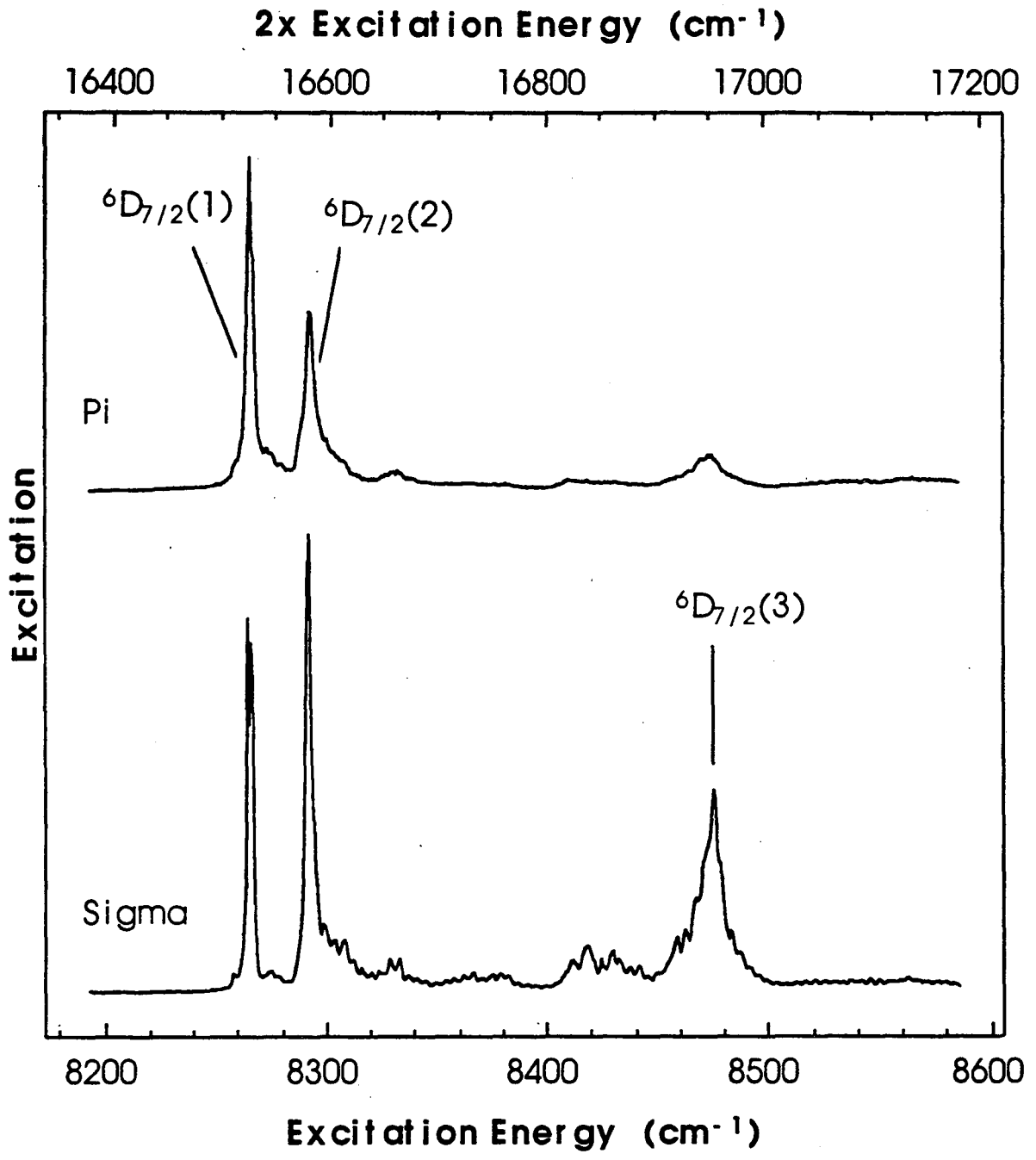

Fig. 5-5: Pi and sigma polarized spectra of the TPA transitions to the $^6D_{7/2}$ multiplet.

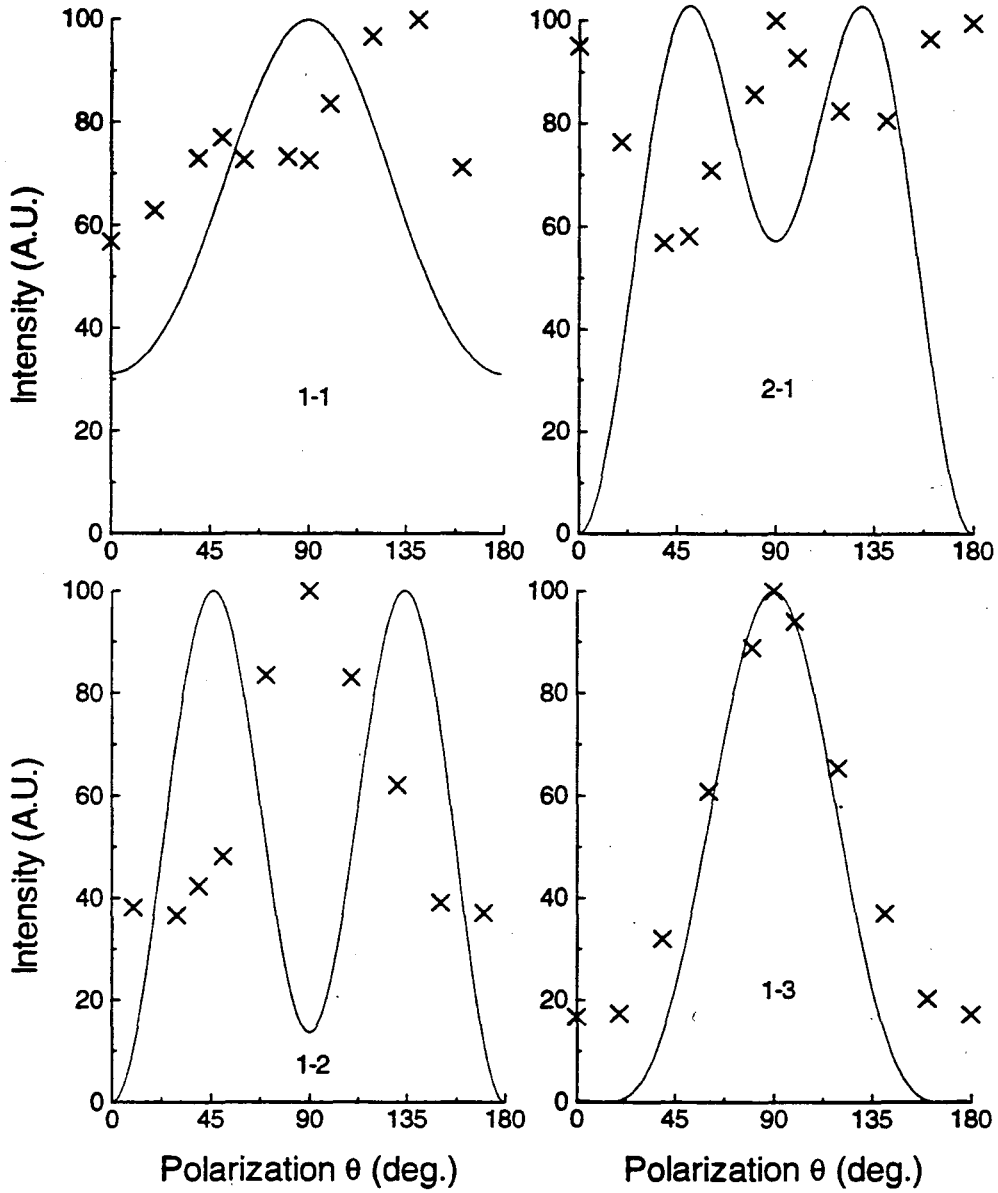

Fig. 5-6: Experimental (crosses) and predicted (solid line) polarization behavior of the $^8S_{7/2}$ - $^6D_{7/2}$ TPA transitions.

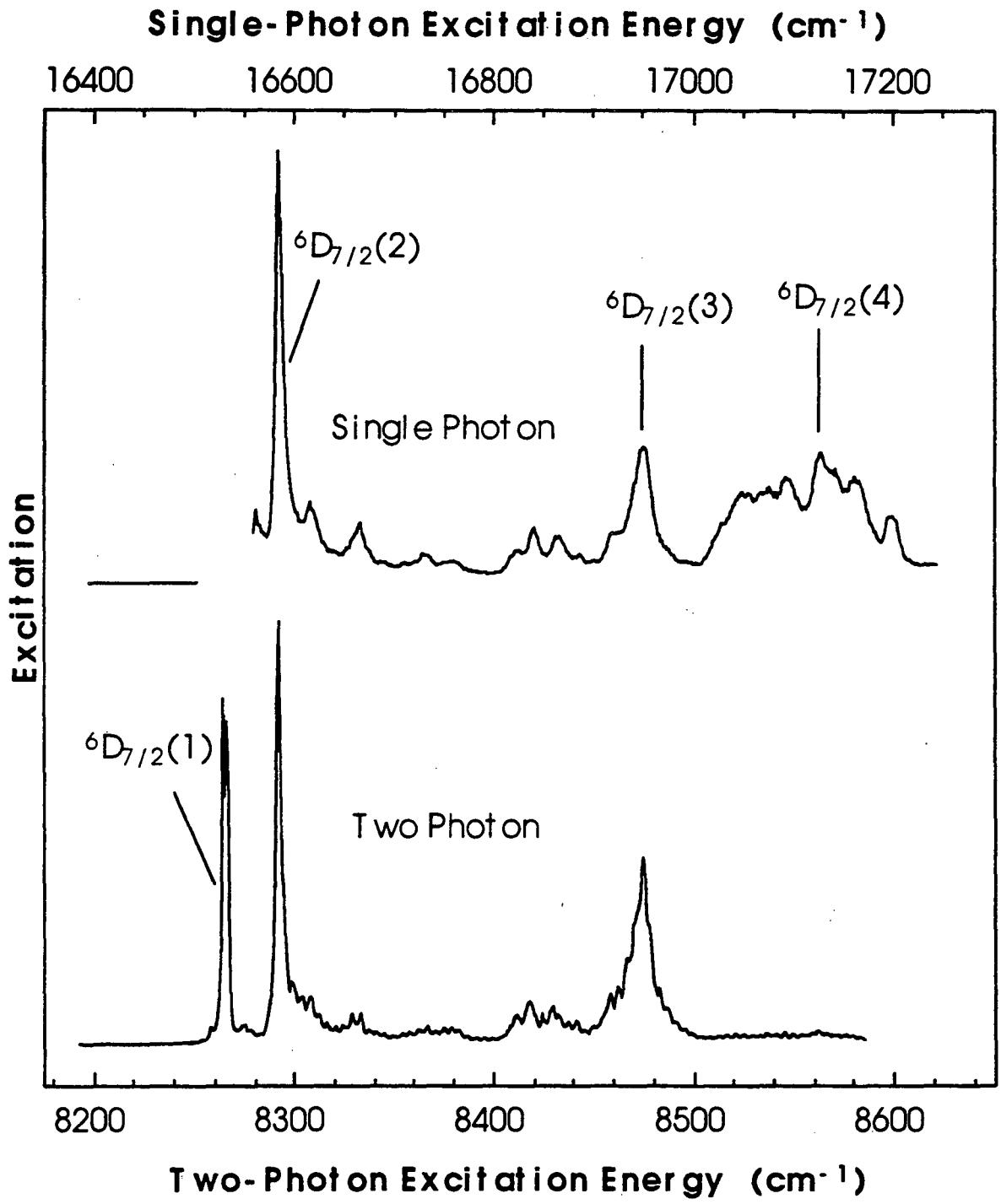

Fig. 5-7: Single-photon and two-photon absorption transitions to the four levels of the $^6D_{7/2}$ multiplet.

5.3.3.2 $^8S_{7/2}$ - $^6P_{5/2}$ Transitions

TPA was observed to two of the three levels of the $^6P_{5/2}$ multiplet (figure 5.8). Three distinct transitions can be discerned to the $^6P_{5/2}(1)$ level. Two of these originate from the two lowest levels of the ground state and are identified by their common splitting of 3.1 cm^{-1}. Their polarization behavior is plotted in Figure 5.9. The third transition could originate from either or both of the third and fourth ground-state levels, with a fitted displacement of 8.8 cm^{-1}. The line to the $^6P_{5/2}(3)$ level could not be resolved into its ground-state components, and its shape and intensity does not change appreciably with temperature.

Phonon bands are also observed in these two-photon excitation spectra. With the exception of the feature 20 cm^{-1} higher than the $^8S_{7/2}(1)$ - $^6P_{5/2}(1)$ transition, these are weaker than for single-photon excitation.

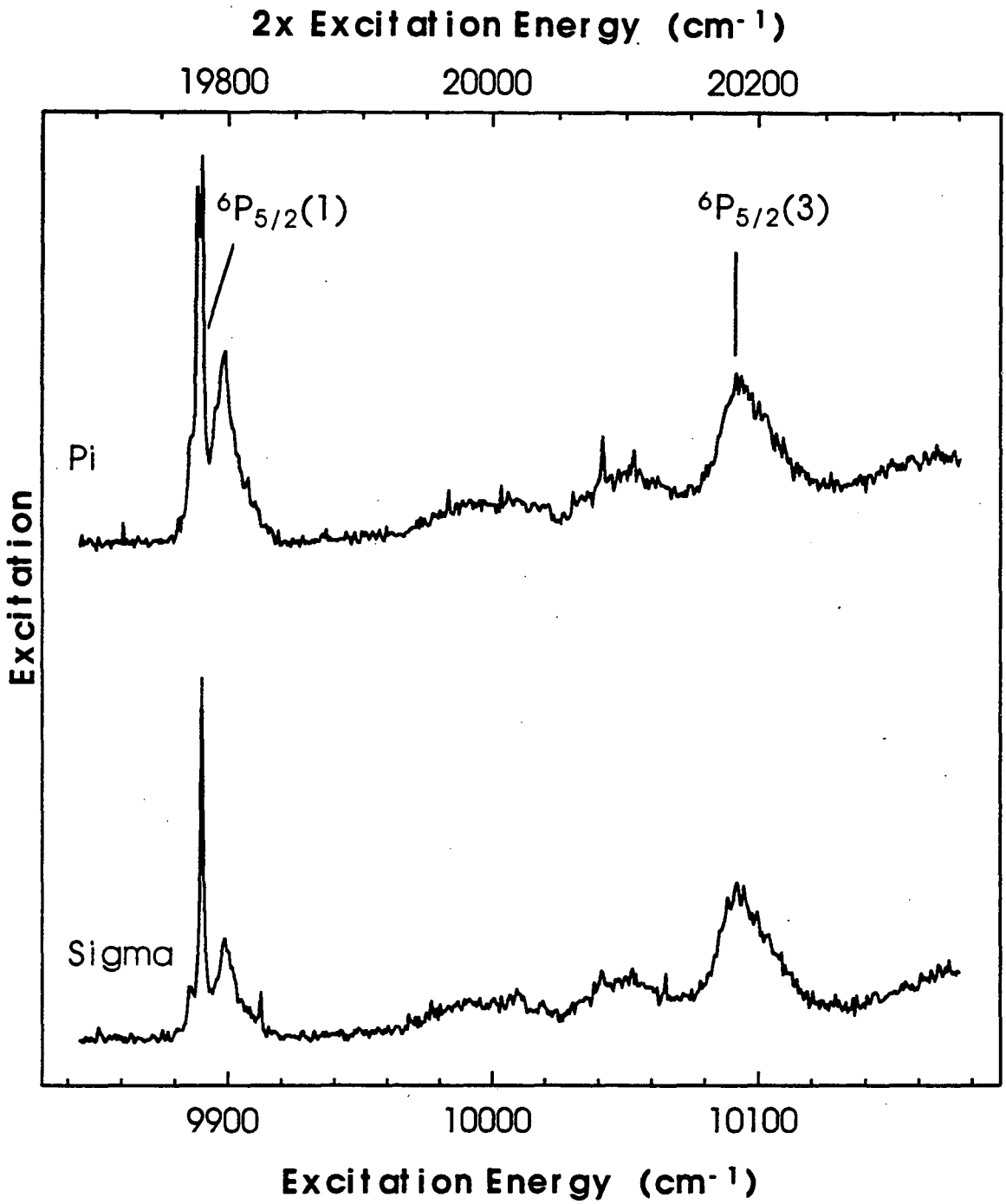

Fig. 5-8: Pi and sigma polarized spectra of the TPA transitions to the $^6P_{5/2}$ multiplet.

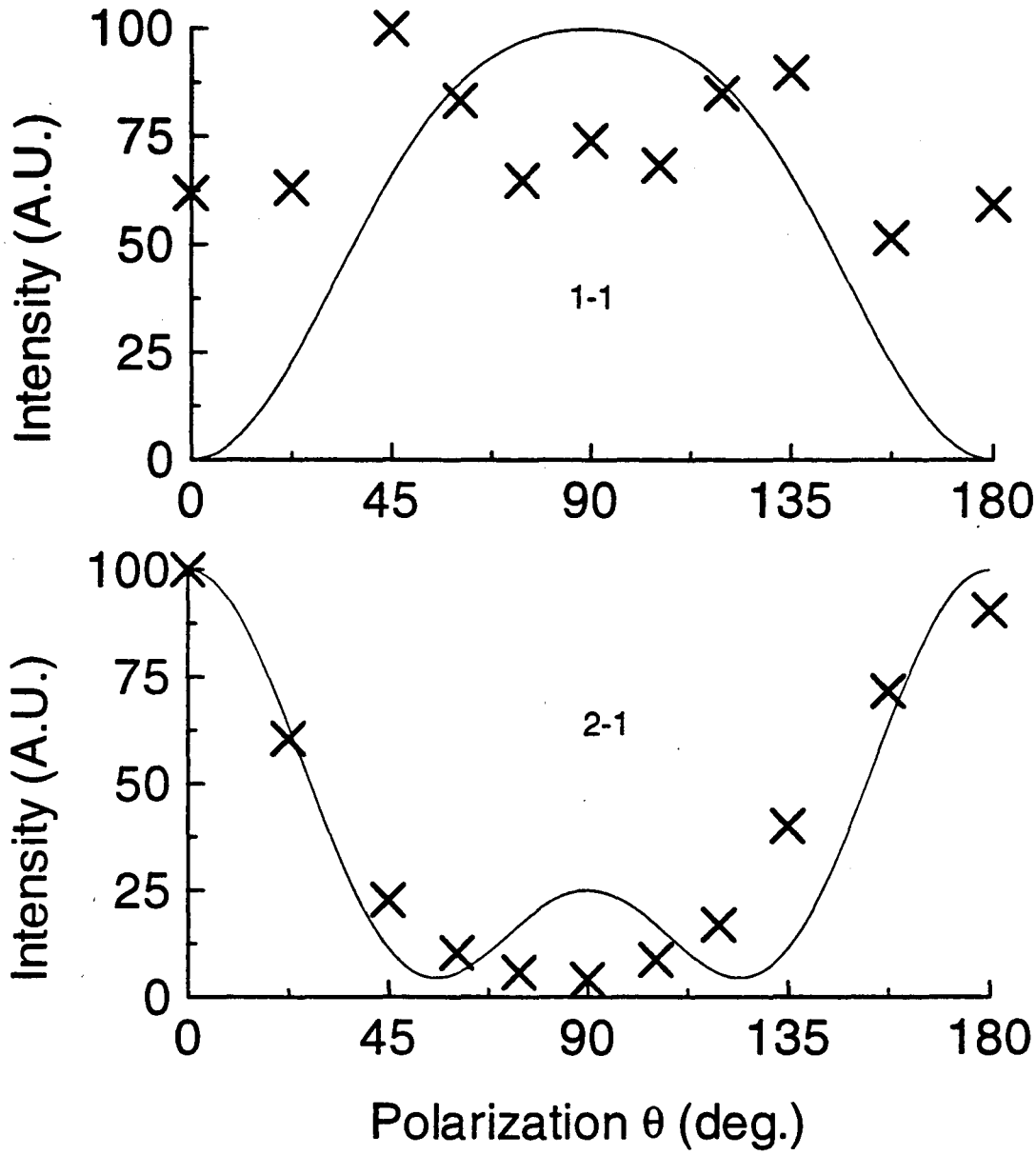

Fig. 5-9: Experimental (crosses) and predicted (solid line) polarization behavior of the $^8S_{7/2}$ - $^6P_{5/2}$ TPA transitions.

5.3.3.3 $^8S_{7/2}$ - $^6D_{7/2}$' Transitions

TPA was observed to all four crystal-field levels of the $^6D_{7/2}$' multiplet (Figure 5.10). Two of the transitions to the $^6D_{7/2}$'(1) level could be identified as originating from the two lowest levels of the ground state. There was an additional transition with a displacement of 9.1 cm^{-1}. These three transitions had fitted linewidths of 4.8 cm^{-1}. Similarly, both the transitions between the two lowest ground-state levels and the $^6D_{7/2}$'(2) level were identified. A third transition, with a displacement of 8.6 cm^{-1}, was also observed. The polarization behavior of these transitions is plotted in Figure 5.11.

A broad line was observed to each of the $^6D_{7/2}$'(3) and $^6D_{7/2}$'(4) levels. Neither of these could be resolved sufficiently to identify components originating from the different ground-state levels. Both of these exhibit rather isotropic polarization behavior. To test whether these transitions are really due to TPA, the excitation power dependence was measured for the lines to the $^6D_{7/2}$'(3) and $^6D_{7/2}$'(4) levels. In both cases the fluorescence intensity fitted well to a quadratic function, confirming their two-photon nature.

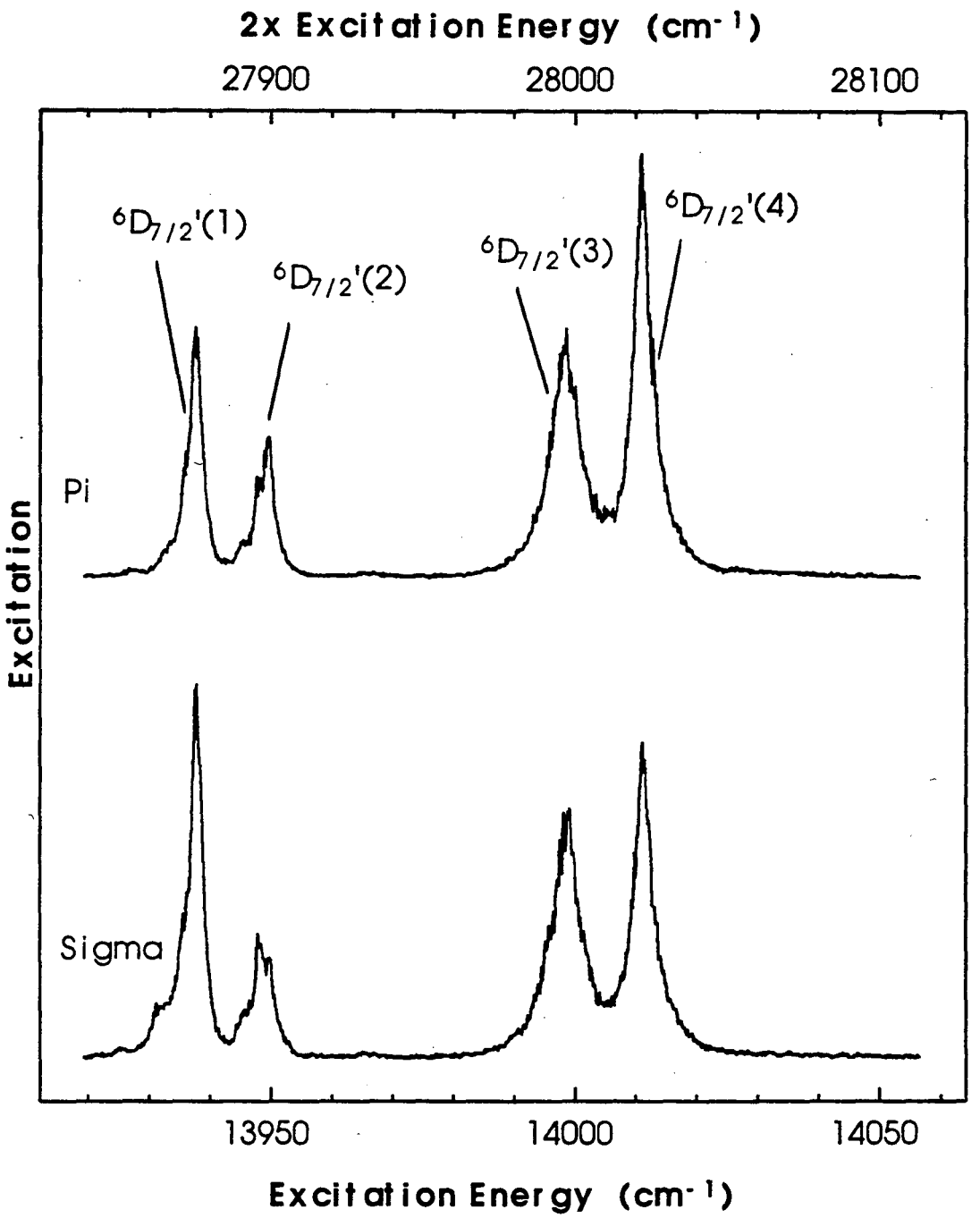

Fig. 5-10: Pi and sigma polarized spectra of the TPA transitions to the $^6D_{7/2}$' multiplet.

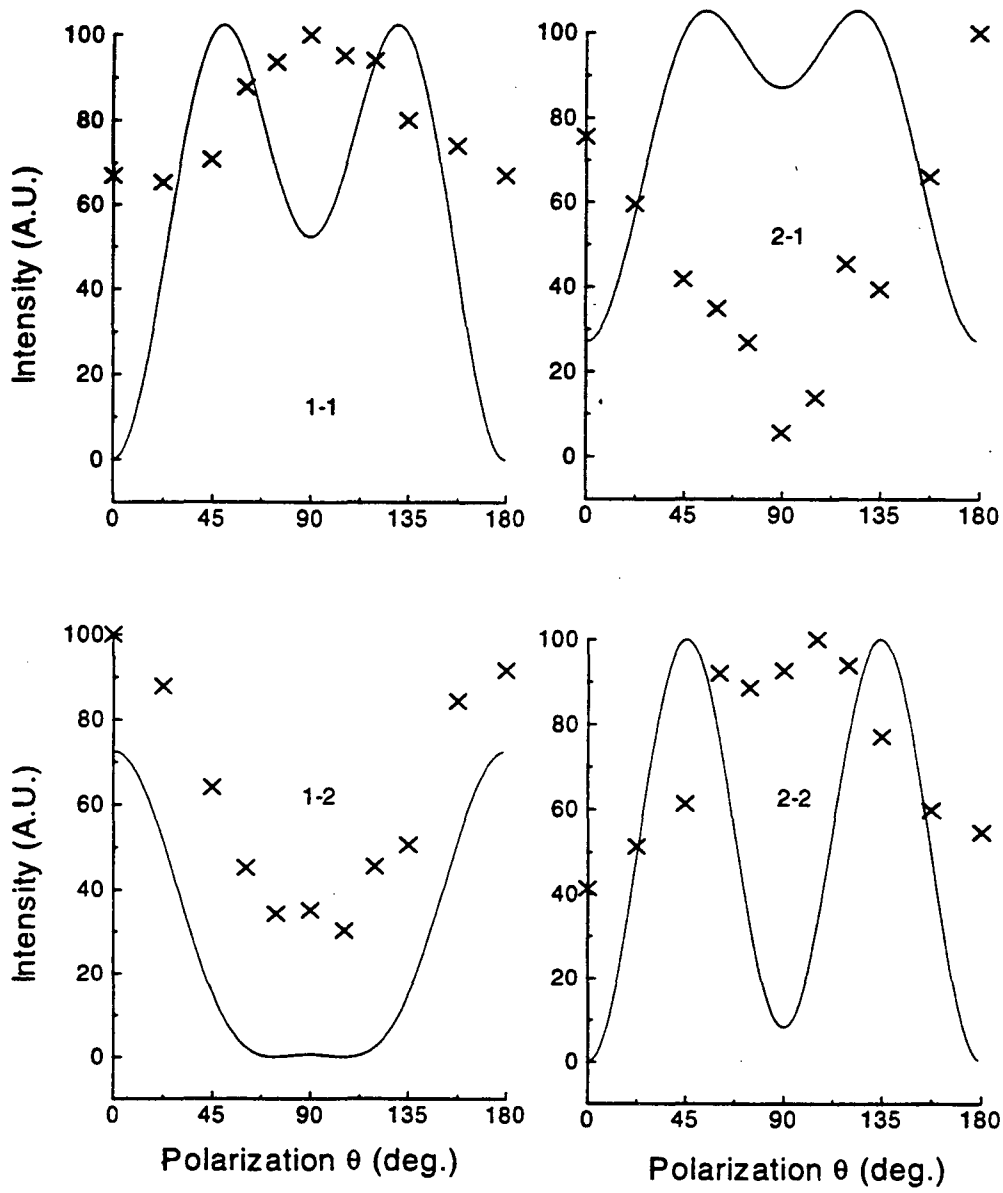

Fig. 5-11: Experimental (crosses) and predicted (solid line) polarization behavior of the $^8S_{7/2}$ - $^6D_{7/2}$' TPA transitions.

5.3.4 Discussion

Except for the $^8S_{7/2}(1)$ - $^6D_{7/2}(3)$, $^8S_{7/2}(2)$ - $^6P_{5/2}(1)$, and $^8S_{7/2}(1)$ - $^6D_{7/2}'(2)$ transitions, all of the TPA intensities of the transitions observed (figures 5-6, 5-9, and 5-11) are very different from the prediction of the theory (table 5.14) which includes the second and third-order spin-orbit effect. Varying the values of φ as shown in table 5.11 did not result in better fits. Most transitions are highly isotropic. The observed isotropic polarization behavior of the TPA transitions can be explained by noting that the second-order contributions in these transitions are relatively small, comparable to the third-order spin-orbit contributions. The quadrupolar (E2)(E1) term discussed in the previous section which is of approximately the same order of magnitude as the third-order contributions may now be comparable with the sum of the (E1)(E1) term and other third-order terms. This quadrupolar term, which is 90° out of phase with the (E1)(E1) term, would give rise to the non-zero background, or isotropic behavior of the observed TPA transitions. In transitions with small background shifts, the small contribution from the (E2)(E1) term may be regarded as a constant, independent of the polarization angles θ or φ. In transitions where the (E2)(E1) term is more appreciable, its dependence on θ and φ must be taken into account. The TPA amplitude for transitions between states of the 4f configurations can be written

$$\begin{aligned}(4f|\alpha_{\mathrm{TPA}}|4f) = (4f|[&-\frac{1}{\sqrt{3}}\alpha_0^{(0)} + (\frac{3\cos^2\theta - 1}{\sqrt{6}})\alpha_0^{(2)} \\ &-(\frac{e^{-i\varphi}}{2}\sin 2\theta)\alpha_1^{(2)} + (\frac{e^{i\varphi}}{2}\sin 2\theta)\alpha_{-1}^{(2)}]|4f) + iA\end{aligned} \tag{5.8}$$

for Γ_7 - Γ_7 transitions, and

$$(4f|\alpha_{TPA}|4f) = (4f|[-(\frac{e^{-i\varphi}}{2}\sin 2\theta)\alpha_1^{(2)} + (\frac{e^{i\varphi}}{2}\sin 2\theta)\alpha_{-1}^{(2)} + (\frac{e^{-2i\varphi}}{2}\sin^2\theta)\alpha_2^{(2)} + (\frac{e^{2i\varphi}}{2}\sin^2\theta)\alpha_{-2}^{(2)}]|4f) + iA' \tag{5.9}$$

for Γ_7 - Γ_6 transitions. Figure 5.12 shows the fit for six of the ten transitions observed with

$$A + (B\cos^2\theta + C)^2 + D\sin^2 2\theta \qquad \text{for } \Gamma_7 - \Gamma_7 \text{ transitions,} \tag{5.10}$$

and $$A' + B'\sin^4\theta + C'\sin^2 2\theta \qquad \text{for } \Gamma_7 - \Gamma_6 \text{ transitions,} \tag{5.11}$$

where A, B, C, D, A', B', and C' are positive fitting parameters.

The fits for the transitions shown in figure 5.12 are quite good. The other four transitions did not result in good fits using (5.10) and (5.11) and are not shown in fig. 5-12. The poor fits for these transitions are probably due to their large background which may slightly depend on the polarization angles. Explicit evaluation of their polarization dependence, however, is not available, due to the difficulty in determining the values of the term

$$\langle 4f|D|4f\rangle = \langle 4f|D|5d\rangle\langle 5d|V_{odd}|4f\rangle / (E_{5d} - E_{4f}) \tag{5.12}$$

which in turn depend on the values of $B_q^{(k)}$, with k odd [8,9]. Considering the experimental uncertainties such as the ambiguous measurement of the φ angle of the Cm sample and the difficulty in measuring the intensities of overlapping transitions, the excellent agreement between observation and prediction using (5.8) and (5.9) is surprising.

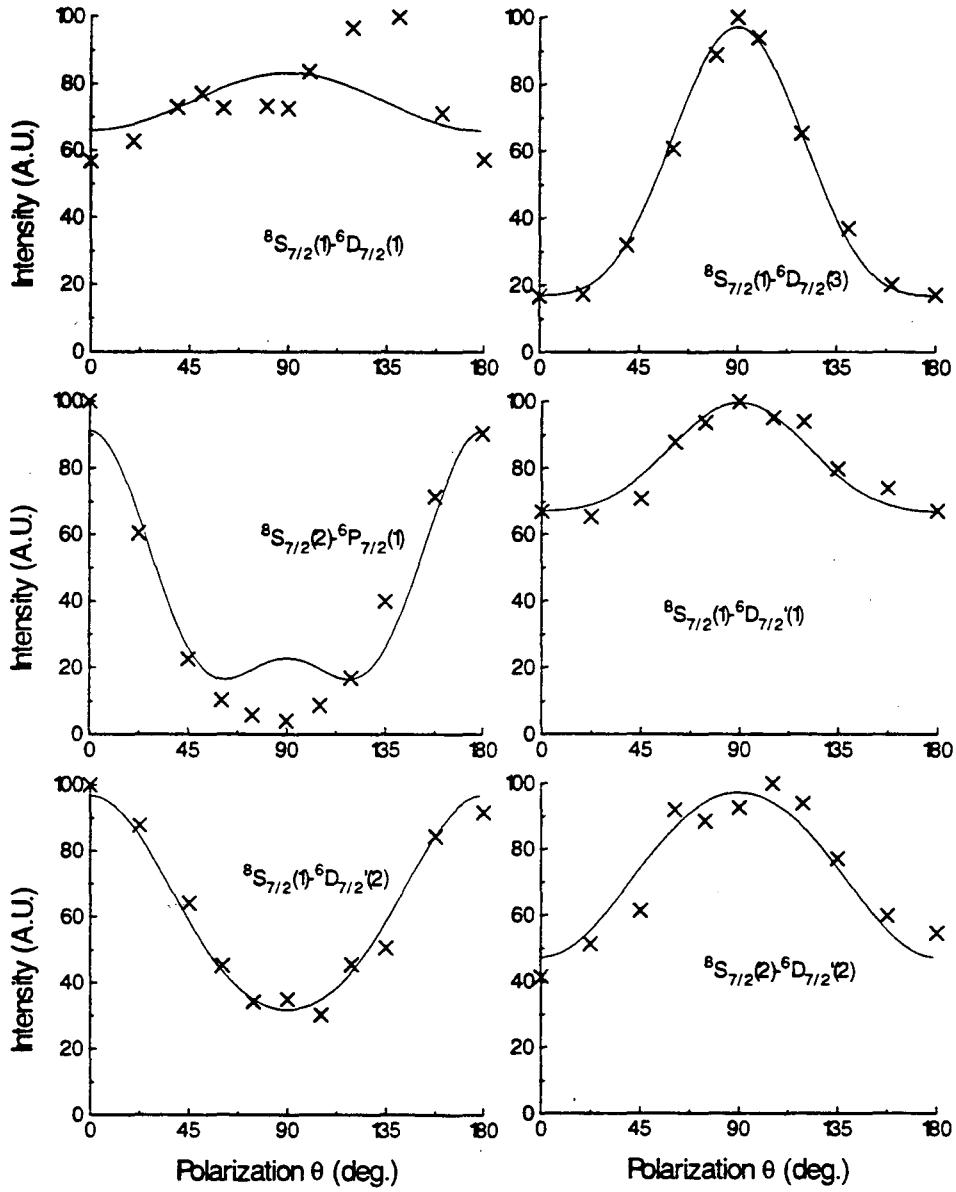

Fig. 5-12: Experimental (crosses) and fitted (solid line) polarization behavior of the $^8S_{7/2}$ - $^6D_{7/2}$, $^6P_{5/2}$, and $^6D_{7/2}$' transitions.

5.4 Summary

TPA have been observed to the crystal field levels of the $^5D_0$ and $^5D_2$ multiplets of Eu^{3+} in $LuPO_4$ and of the $^6D_{7/2}$, $^6P_{5/2}$, and $^6D_{7/2}$' multiplets of Cm^{3+} in $LuPO_4$. For transitions whose second-order contributions are sufficiently large, the polarization dependent behavior can be explained from the framework of the second-order theory. For transitions whose second-order contributions are comparable or smaller than third order contributions, one must add the contribution from the α_0^0 term. We have also shown that several imaginary terms of which the (E2)(E1) term is dominant, which have been ignored in TPA theoretical treatments up to the present, might account for the non-zero background observed in two transitions of Eu^{3+}:$LuPO_4$ and in most transitions of Cm^{3+} in $LuPO_4$. Thus in addition to the contribution from the α_0^0 term in TPA transitions of Eu^{3+} and Cm^{3+}, one must add the contributions from the (E2)(E1) term in order to account for the observed isotropic polarization behavior. When more empirical data for the values of $B_q^{(k)}$ (k odd) for $LuPO_4$ doped with Eu^{3+} and Cm^{3+} are available, explicit polarization dependencies can be obtained for the imaginary terms in (5.1).

The (E2)(E1) term has been shown to be the most important contributions to the Im(A) term discussed in section 5.2. The role of other terms should also be explored by studying systems for which these terms are dominant. For example, the contribution arising from the $i\Gamma_j$ term in (1.45) may become more significant for excitation at resonance. Resonant ERS [33-35] and TPA [36,37] experiments have been studied on $LuPO_4$ hosts doped with rare-earth ions. In these studies only conventional TPA techniques were used. Polarization dependence techniques developed from chapter two

to five in this thesis can be used as a new powerful tool to interpret the two-photon intensities coming from the resonant ERS and TPA transitions.

References

[1] T. R. Bader and A. Gold, Phys. Rev. B **45**, 2023 (1992).

[2] A. G. Makhanek, V. S. Korolkov, and L. A. Yuguryan, Phys. Stat. Sol. B **149**, 231 (1988).

[3] G. Makhanek and V. S. Korolkov, *Analytical Methods in Perturbation Theory of Quantum Mechanics* (Izd. Nauka I Tekhnika, Minsk 1982).

[4] J. C. Gâcon, J. F. Marcerou, M. Bouazaoui, B. Jacquier, and M. Kibler, Phys. Rev. B **40**, 2070 (1989).

[5] J. C. Gâcon, G. Grenet, J. C. Souillat, and M. Kibler, J. Chem. Phys. **69**, 868 (1978).

[6] J. C. Gâcon, B. Jacquier, J. F. Marcerou, M. Bouazaoui and M. Kibler, J. Lum. **45**, 162 (1990).

[7] J. Sztucki, M. Daoud, and M. Kibler, Phys. Rev. B **45**, 2023 (1992).

[8] B. R. Judd, Phys. Rev. **127**, 750 (1962).

[9] G. S. Ofelt, J. Chem. Phys. **37**, 511 (1962).

[10] J. D. Axe, Phys. Rev. **136A**, 42 (1964).

[11] R. Mahiou, J.C. Gacon, B. Jacquier, and R.L. Cone, J. Lum. **60 & 61**, 664 (1994).

[12] J. C. Gacon, M. Bouazaoui, B. Jacquier, M. Kibler, L.A. Boatner, and M. M. Abraham, Eur. J. Solid State Inorg. Chem. **28**, 113 (1991).

[13] C. Brecher, H. Samelson, R. Riley, and A. Lempicki, J. Chem. Phys. **49**, 3303 (1968).

[14] D. Piehler and D.S. Kim, unpublished work.

[15] A. Armbruster, R. Thoma, and H. Wehrle, Phys. Status Solidi A **24**, K71 (1974)..

[16] E. A. Power, J. Chem. Phys. **63**, 1348 (1975)

[17] I. Tinoco, J. Chem. Phys. **62**, 1006 (1975)

[18] J. Sztucki and W. Strek, J. Chem. Phys. **85**, 5547 (1986)

[19] T. Kundu et al, Phys. Rev. B **41**, 10911 (1990)

[20] K.E. Gunde and F.S. Richardson, Chem. Phys. **194**, 195 (1995)

[21] K. Nakanishi, N. Berova and R.W. Woody ed., *Circular dichroism. Principles and applications* (VCH, New York, 1994).

[22] N. Purdie and H.G. Brittain ed., *Analytical applications of circular dichroism* (Elsevier, Amsterdam, 1994).

[23] K.E. Gunde, G..W. Burdick, and F.S. Richardson, unpublished.

[24] J.I. Dadap et al., Phys. Rev. B **53**, 7067 (1996).

[25] M.C. Downer, private communication.

[26] M. C. Downer, A. Bivas, and N. Bloembergen, Opt. Commun. **41**, 335 (1982).

[27] B. R. Judd and D. R. Pooler, J. Phys. C **15**, 591 (1982).

[28] M. C. Downer, Ph. D. thesis, Harvard University, 1983.

[29] M. C. Downer and A. Bivas, Phys. Rev. B **28**, 3677 (1983).

[30] M.M. Abraham and L.A. Boatner, Phys. Rev. B **26**, 1434 (1982)

[31] W. K. Kot, N.M. Edelstein, M.M Abraham, and L.A. Boatner, Phys. Rev.B **48**, 12704 (1993).

[32] J. Sytsma, K.M. Murdoch, N.M. Edelstein, L.A. Boatner, and M.M. Abraham, Phys. Rev. B **52**, 12668 (1995).

[33] P.C. Becker, Ph.D. thesis, University of California at Berkeley, 1986.

[34] G.M. Williams, P.C. Becker, N. Edelstein, L.A. Boatner, and M.M. Abraham, Phys. Rev. B **40**, 1288 (1989).

[35] G. M. Williams, Ph.D. thesis, University of California, Berkeley, 1988.

[36] J. Huang, G. Liu, and R.L. Cone, Phys. Rev. B **39**, 6348 (1989).

[37] J. Huang, Ph.D. thesis, Montana State University, 1987.

Ernest Orlando Lawrence Berkeley National Laboratory
One Cyclotron Road | Berkeley, California 94720

Prepared for the U.S. Department of Energy under Contract No. DE-AC03-76SF00098